Catalytic Organometallic Anticancer Complexes

A Thesis Submitted for the Degree of Doctor of Philosophy

James Paul Charles Coverdale MChem (Hons)

Supervisors: Prof. Peter J. Sadler, FRS

Prof. Martin Wills

University of Warwick, Department of Chemistry

November 2017

Dedicated to the memory of Mark R. Coverdale

Table of contents

Chapter 2 - Materials, methods and instrumentation

Chapter 3 - Asymmetric catalytic osmium sulfonamide complexes

Acknowledgements

Since first exploring the chemistry of osmium(II) complexes during my master's degree, I was fortunate enough to continue my research as part of a PhD at Warwick University. To Professor Peter J. Sadler and Professor Martin Wills; I am immensely grateful for the opportunity, and the invaluable guidance and support you have offered me since I first started working in your labs in 2013.

Nothing in science comes easily, and I would like to thank Dr. Isolda Romero-Canelón and Dr. Carlos Sanchez-Cano for helping me become a better researcher; combining long hours, psycho-working style, and maintaining carefully-placed optimism. I have been lucky enough to work with you both around the world – Grenoble (France) and Guangzhou (China) – and I'm sure that we will remain close in the future; if not through science, then through food, gin and tonic. To Hannah, and our fantastic technicians Ji and Bindy; thank you for your time, energy, laughter and patience, both inside and outside of tissue culture. Since I began working in biology (sorry, Abraha), I have undoubtedly made some friends for life. I have been lucky enough to work alongside so many people from around the world; Khatija, Joan, Robbin, Mariana, Carol, Chloe and Yasmin – you have all helped to shape my research into the final form that has come together in this thesis. Thank you all for your encouragement, food breaks and expertise. I also would not have completed my research without the support of the Warwick Chemistry staff. Particularly, thank you to Dr. Lijiang Song and Phil Aston, who patiently endured my over-enthusiasm for ICP samples.

From beyond the lab, I would most like to thank my family and friends. Your unwavering love and support over the last three years have allowed me to follow my dreams, and for that I am truly grateful.

Declaration

I hereby declare that except where specific reference is made to other sources, the work contained in this thesis is the original work of the author. It has been composed by myself and has not been submitted, in whole or in part, for any other degree, diploma, or other qualification.

Some of the work presented in this thesis has been published:

1. J. P. C. Coverdale, C. Sanchez-Cano, G. J. Clarkson, R. Soni, M. Wills, P. J. Sadler, *Chem. Eur. J.*, 2015, **21**, 8043.
2. J. P. C. Coverdale, I. Romero-Canelón, C. Sanchez-Cano, G. J. Clarkson, M. Wills, P. J. Sadler, *Nature Chemistry*, Manuscript accepted.

James P. C. Coverdale

September 2017

Abstract

Half-sandwich complexes of ruthenium, iridium, and more recently osmium, have shown promise as anticancer agents. Many of these 'piano-stool' complexes appear to target the redox balance in cells. Separately, similar complexes have been investigated for the catalysis of hydrogenation reactions, with many examples achieving high turnover frequencies and enantioselectivities. This thesis is concerned with achieving *in cell* catalysis to increase drug potency and generate selectivity for cancer cells.

A series of eighteen Os(II) and Ir(III) complexes, of the type [M(η^x-arene)(diamine)] (Os-arene: *p*-cymene, biphenyl, or *m*-terphenyl; Ir-arene: Cp*, Cp^{xPh}, or Cp^{xBip}), were synthesised and fully characterised. The structures were derived from a Ru(II) transfer hydrogenation catalyst [Ru(η^6-*p*-cymene)(TsDPEN)], TsDPEN = *N*-tosyl-diphenyl-ethylenediamine. The complexes were isolated as 16-electron amido catalysts, which were highly stable in solution and upon storage, unlike their 16-electron Ru(II) counterparts, and were highly active for asymmetric transfer hydrogenation of ketones. Os complexes afforded enantiomerically-pure alcohols with high conversion and enantioselectivity (> 99%) at rates exceeding those of the existing Ru catalyst.

Two Os and Ir complexes were explored for the conversion of NADH to its oxidised form (NAD^+) under physiologically-relevant conditions. Antiproliferative activities determined in 14 human cell lines correlated with experimentally-determined hydrophobicities. Typically, Os catalysts were found to be more active than their Ir counterparts, though were internalised by cancer cells to a lesser degree, suggestive of a more potent *in-cell* mechanism of action. Structural modifications identified an apparent inert site of substitution on the sulfonamide substituent. Furthermore, their potency towards cancer cells was increased in combination with L-buthionine sulfoximine, an inhibitor of glutathione synthesis.

Acute *in vivo* toxicities were determined in zebrafish, and all compounds investigated exhibited lower toxicities than the Pt anticancer drug, cisplatin. The complexes were shown to generate reactive oxygen species (ROS) in cancer cells, and similarly generated ROS in zebrafish.

Transfer hydrogenation catalysis was explored under physiologically-relevant conditions using sodium formate as a biologically-compatible hydride source. Osmium complexes catalysed the reduction of pyruvate, a key metabolite in cells, to either L-lactate or D-lactate, selectively (*ca*. 83% *ee*). Upon co-administration of the catalyst and sodium formate, cancer cell proliferation was decreased by up to 13× (relative to cells treated with the catalyst alone), while no sodium formate effect was determined in non-cancerous cells. Importantly, the treatment of cells with a particular enantiomer of the Os catalyst and sodium formate facilitated the *in cell* reduction of pyruvate to D-lactate, providing, to the best of my knowledge, the first example of a synthetic catalyst carrying out asymmetric transfer hydrogenation chemistry in cells.

Conferences and courses attended

1. Bruker AVANCE/TopSpin NMR Course (Coventry, UK). January 2015.
2. Transferable skills in science (University of Warwick, UK). June 2015.
3. Postgraduate Chemistry Symposium (University of Warwick, UK). June 2015.
4. 10th International School of Organometallic Chemistry (Camerino, Italy). September 2015. Poster presentation.
5. RSC Dalton Division Joint Interests Group Meeting (University of Warwick, UK). March 2016. Poster presentation.
6. Postgraduate Chemistry Symposium (University of Warwick, UK). June 2016. Poster presentation.

Abbreviations

ATH	Asymmetric Transfer Hydrogenation
Bip	Biphenyl
BMEN	1,2-bis(4-methoxyphenyl)ethylenediamine
Bs	Benzenesulfonyl
BsDPEN	Benzenesulfonyl diphenylethylenediamine
(L)-BSO	L-Buthionine sulfoximine
CBP	Carboplatin (*cis*-diamine(cyclobutane-1,1-dicarboxylate-O,O')platinum(II))
CDDP	Cisplatin (*cis*-diamminedichloroplatinum(II))
COSY	Correlation Spectroscopy
Cp*	1,2,3,4,5-pentamethylcyclopentadienyl
Cp^{xPh}	Tetramethyl(phenyl)-cyclopentadienyl
Cp^{xBiPh}	Tetramethyl(biphenyl)-cyclopentadienyl
CTR1	Copper transporter protein 1
d	Doublet (NMR)
dd	Doublet of doublets (NMR)
ddw	Doubly deionized water
DFT	Density Functional Theory
DMEM	Dulbecco's Modified Eagle Medium
DNA	Deoxyribonucleic Acid
DPEN	1,2-diphenylethylenediamine
equiv.	Equivalents
ESI-MS	Electrospray ionization mass spectrometry

Fb	4-fluorobenzenesulfonyl
FbDPEN	4-fluorobenzenesulfonyl diphenylethylenediamine
FDA	Food and Drug Administration (U.S.A.)
GSH	Glutathione
HBSS	Hanks' Balanced Salt Solution
HR-MS	High resolution mass spectrometry
IC_{50}	Half-maximal inhibitory concentration
ICP-OES	Inductively-coupled plasma optical emission spectroscopy
ICP-MS	Inductively-coupled plasma mass spectrometry
LC_{50}	Half-maximal lethal concentration
$\lambda_{(ex/em)}$	Wavelength (excitation / emission)
m	Multiplet
m-terp	1,3-diphenylbenzene (*meta*-terphenyl)
MS	Mass spectrometry
m/z	Mass-to-charge ratio
NAD^+	Nicotine adenine dinucleotide (oxidised)
1,4-NADH	Nicotine adenine dinucleotide (reduced)
Ns	4-nitrobenzenesulfonyl
NsDPEN	4-nitrobenzenesulfonyl diphenylethylenediamine
NMR	Nuclear magnetic resonance
P-gp	P-glycoprotein
P21 (p21)	Tumour suppressor gene 21 (tumour suppressor protein 21)
P53 (p53)	Tumour suppressor gene 53 (tumour suppressor protein 53)
PBS	Phosphate-buffered saline
PI	Propidium iodide

ROS	Reactive oxygen species
RPMI-1640	Roswell Park Memorial Institute 1640
s	Singlet
SG	Singapore (zebrafish embryos)
SRB	Sulforhodamine B
SrbDPEN	2-(3-diethylamino-6-diethylazaniumylidene-xanthen-9-yl)-5-(N-(2-amino-1,2-diphenyl-ethyl)sulfonoyl)-benzenesulfonate
TCA	Trichloroacetic acid
Ts	Tosyl (4-methylbenzenesulfonyl)
TsBMEN	4-toluenesulfonyl-1,2-bis(4-methoxyphenyl)ethylenediamine
TsDPEN	4- toluenesulfonyl-1,2-diphenylethylenediamine
TU	Tübingen (zebrafish embryos)
UV-Vis	Ultraviolet-Visible spectroscopy
v/v	Volume / volume (percentage solution)
w/v	Weight / volume (percentage solution)

Cell lines studied in this thesis:

A2780	Human ovarian carcinoma
A2780cis	Human ovarian carcinoma (cisplatin-resistant)
A549	Human lung carcinoma
HCT116	Human colon carcinoma
HCT116-p21-/-	Human colon carcinoma (*P21*-deficient)
HCT116-p53-/-	Human colon carcinoma (*P53*-deficient)
HEPG2	Human hepatocellular carcinoma
MCF7	Human breast adenocarcinoma
OE19	Human oesophageal carcinoma
PC3	Human prostate adenocarcinoma
SK-OV-3	Human ovarian adenocarcinoma
SW626	Human ovarian adenocarcinoma
HOF	Human ovarian fibroblasts (non-cancerous primary cell line)
MRC5	Human lung fibroblasts (non-cancerous primary cell line)

Chapter 1

Introduction

1. Introduction

This thesis is concerned with the synthesis of novel Os(II) organometallic complexes of the general structure [Os(η^6-arene)(diamine)] which are active asymmetric transfer hydrogenation (ATH) catalysts. For comparison, structurally-similar Ir(III) η^5-Cp* complexes (Cp* = 1,2,3,4,5-cyclopentamethyl) were also synthesised. The complexes are derived from the reputable ruthenium(II) chemistry pioneered by Professor Ryoji Noyori. The catalytic cycle begins with the transference of hydride from a sacrificial donor molecule (such as formic acid) to the catalyst, forming a metal-hydride complex which can then go on to donate the hydride to a substrate acceptor molecule, affording the product in a highly enantioselective manner and with high conversion (Figure 1.3).[1, 2] Ruthenium(II) arene chlorido pre-catalysts of the general structure [Ru(η^6-arene)Cl(diamine)] are well-established,[1] however the apparent inertness of Os(II) allows the active 16-electron catalytic species [Os(η^6-arene)(diamine)] to be directly obtained, rather than isolation of a pre-catalyst which must first dissociate chloride. It is envisaged that the greater stability of osmium(II) transfer hydrogenation catalysts compared to ruthenium(II) will reduce catalyst degradation (trace Ru(0) is known to contaminate reduction products), while direct use of the active catalyst may be advantageous, achieving higher catalytic rates.

Highly potent Os(II) half-sandwich anticancer complexes have previously been identified, achieving nanomolar antiproliferative activities towards cancer cells in a non-catalytic manner.[3] Conversely, a catalytic metallodrug may be obtained by combining structural components from a known asymmetric hydrogenation catalyst and a potent anticancer complex in a single structure (Figure 1.1). *In vitro* catalysis may specifically target unique biochemical traits of a particular disease (e.g. the increased rate of glycolysis in cancer cells).[4]

The osmium(II) catalysts designed in this thesis are explored initially for the catalysis of simple aromatic ATH substrates (based on acetophenone) under forcing conditions in organic solvents (formic acid : triethylamine azeotrope), before exploring both the catalytic oxidation (NADH to NAD^+) and reduction (pyruvate to lactate) of important biomolecules under physiologically-relevant conditions (aqueous-phase reduction, bio-compatible hydride source). Ultimately, the catalysts are employed to carry out *in cell* reductions with high enantioselectivity, making use of new bio-orthogonal chemistry as a new strategy for inducing cell death.

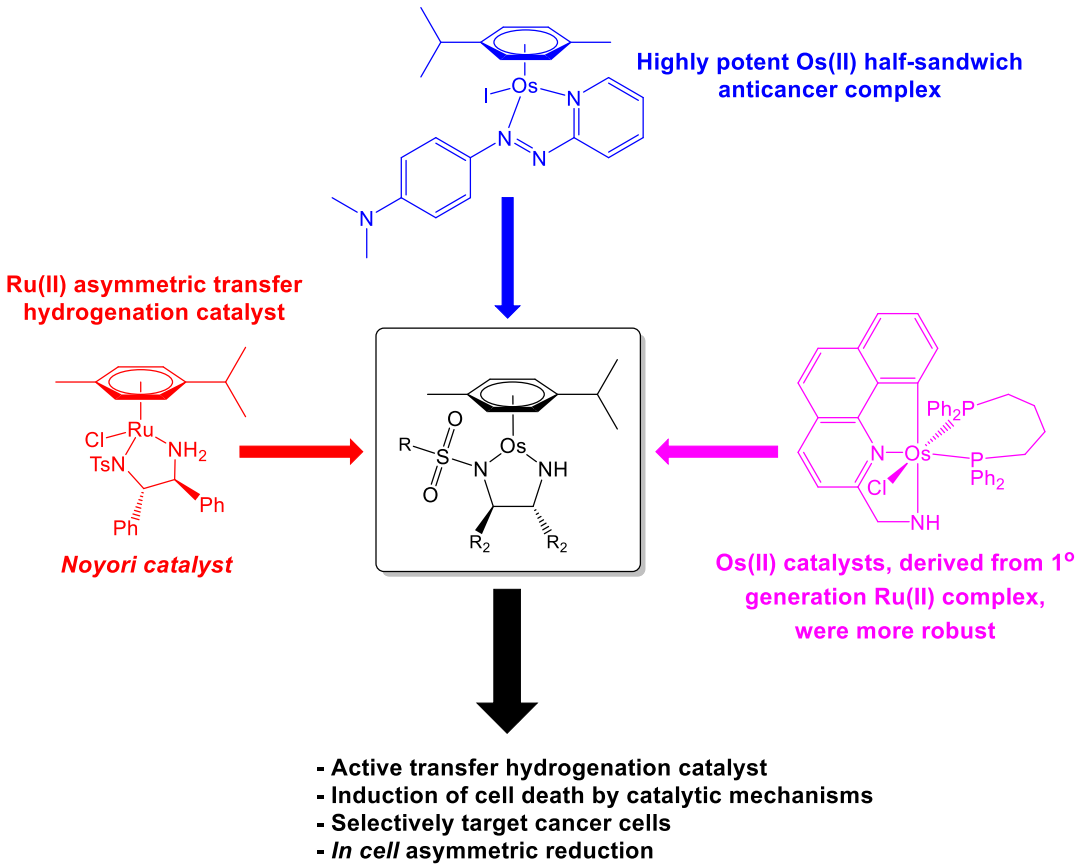

Figure 1.1. Rational design of Os(II) transfer hydrogenation catalysts for the treatment of cancer, based on existing catalyst technologies of Ru (**red**) and Os (**pink**), combined with the high potency of Os(II) arene anticancer complexes (**blue**). R = 4-methylphenyl, 4-methoxyphenyl, phenyl, 4-fluorophenyl, methyl; R_2 = phenyl or 4-methoxyphenyl.

1.1 Asymmetric transfer hydrogenation

Transfer hydrogenation reactions are a relatively recent advance in hydrogenation chemistry. This involves the relocation of hydrogen from a sacrificial donor molecule to an acceptor (target) transition metal complex, thereby providing a controlled route to reduce organic targets, and safer alternative to reactions involving the use of hydrogen gas under high pressure conditions.[1, 5] In the mid-20th century, iridium hydride complexes were shown to catalyse the reduction of unsaturated ketones to alcohols, using isopropanol as a sacrificial hydride donor.[6]

1.1.1 The Noyori ruthenium bifunctional catalyst

Prof. Noyori is often considered to be the pioneer of asymmetric transfer hydrogenation. His work, concerning catalysts capable of affording enantiomerically-pure alcohols (and later, imines) with high conversion, won the 2001 Nobel Prize in Chemistry. First-generation catalysts [Ru(BINAP)Cl_2(diamine)] (BINAP = 2,2'-bis(diphenylphosphino)-1,1'-binaphthyl) demonstrated high turnover frequency and enantioselectivity (> 99%) for the reduction of ketones (Figure 1.2a).[7] Studies demonstrated that the mechanism of hydrogenation was non-classical and occurred in an outer-sphere process, rather than the traditional [2+2] mechanism (Figure 1.2).[8]

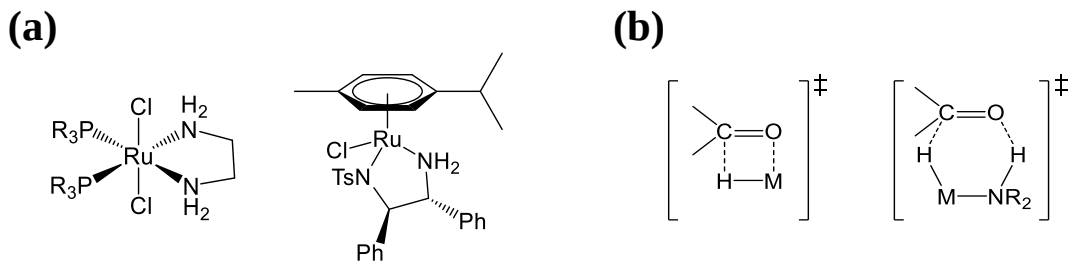

Figure 1.2. (a) First and second-generation Ru transfer hydrogenation catalysts, developed by Noyori and co-workers. (b) The Noyori bifunctional catalyst transfers H_2 to an acceptor (ketone) via a non-classical 6-membered transition state, rather than via a traditional [2+2] mechanism.[8]

The second-generation bifunctional half-sandwich complexes improved catalytic efficiency,[7] even though they share structural similarity with the first-generation catalysts in the chiral diamine (Figure 1.2a).[1, 2, 9-20] The catalytic mechanism for Noyori-type bifunctional catalysts has been studied in great depth, both experimentally and computationally.[9, 20-22] The complexes must first dissociate the chloride ligand, and are deprotonated by a base, forming the 16-electron complex [M(arene)(TsDPEN)], the active catalytic species. Note that the M^{2+} complex is still neutral overall due to the formation of two anionic nitrogen atoms on the bidentate ligand, which is reflected by the shorter metal-nitrogen bond length in the x-ray crystallographic structures. Upon addition of a sacrificial hydride donor (commonly formic acid or 2-propanol)[2, 15] the basic nitrogen atom is re-protonated, and a metal-hydride bond is formed, along with the elimination of the oxidised sacrificial molecule (carbon dioxide, if the donor was formic acid).[2, 15-26] The reverse process can then occur with the target hydrogen acceptor, transferring hydrogen from the hydride catalyst to the target via a 6-membered transition state (Figure 1.3). The entire catalytic process is considered outer sphere,[21-26] since neither the acceptor or donor molecules have any direct interaction with the metal centre. The system is reversible, and will carry out the thermodynamically favourable reduction. This can be influenced by the selection of formic acid as a hydride source, since after donation of hydrogen, carbon dioxide gas is released, effectively making the reaction irreversible.

The success of the Noyori transfer hydrogenation catalysts is down to the reaction achieving high enantiomeric excess when prochiral acceptor molecules are used. The geometry of the transition state, and subsequent enantioselectivity, is directed by the chirality of the bidentate diamine[17] and stabilised by favourable π-interactions with the η^6-arene of the catalyst (Figure 1.3).[2, 15-26]

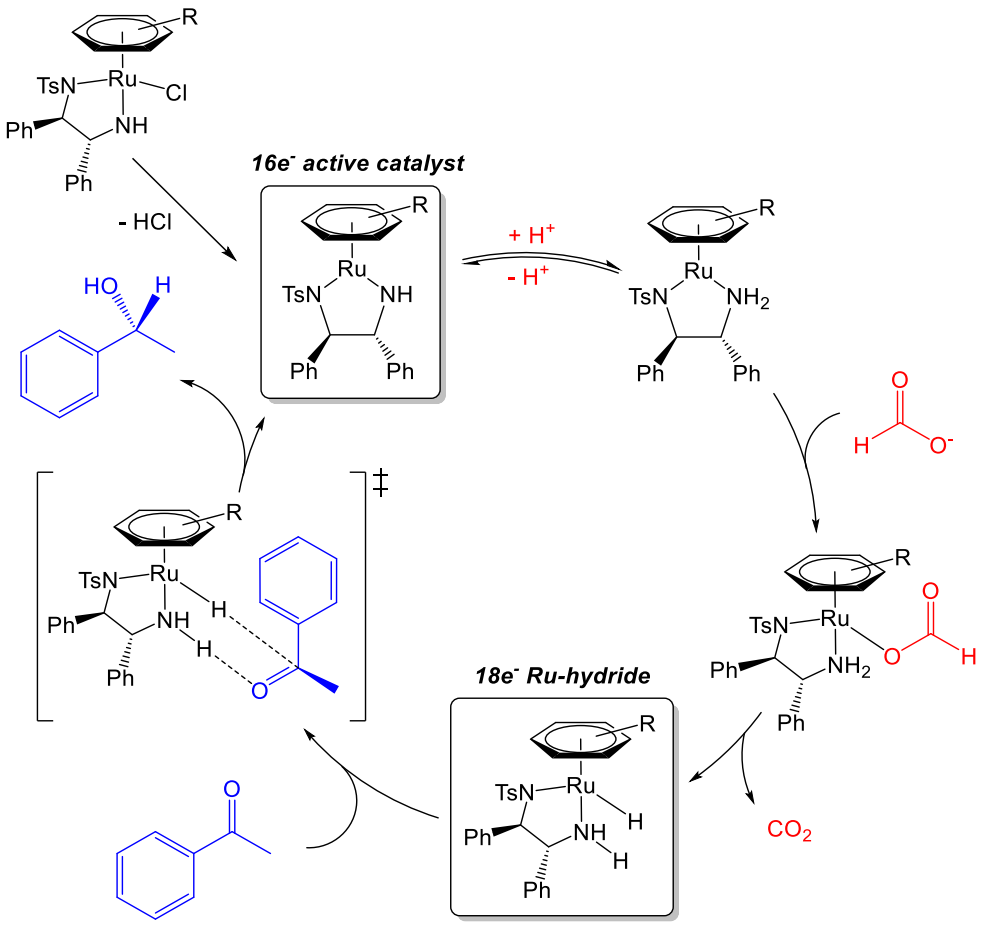

Figure 1.3. General mechanism for the asymmetric transfer hydrogenation of ketones using the Noyori 2nd generation bifunctional catalyst (hydrogen donor: formic acid; hydrogen acceptor: acetophenone).

Wills *et al*. modified the diamine component of the Noyori catalyst by alkylation of either nitrogen atom, forming a covalent "tether" between the diamine and the η^6-arene of the catalyst.[27, 28] This modification stabilised the catalyst further by constraining the pseudo-octahedral geometry of the chlorido pre-catalyst to be retained in the 16-electron active catalyst, resulting in higher reaction turnover frequencies and high conversions, whilst retaining the high enantioselectivity of the original Noyori catalyst.[28-30] Electron-rich amino-substituted ketones were readily reduced under aqueous conditions using the tethered ruthenium catalysts, however methoxy-substituted substrates proved more challenging.[31]

The analogous iridium(III) and rhodium(III) TsDPEN bifunctional catalysts were soon reported, from which other structurally-derived transfer hydrogenation catalysts were developed.[5, 32-38] In particular, the Rh(III) catalyst was found to be the most efficient catalyst for aqueous reduction of ketones using sodium formate as a hydride source.[32] Transfer hydrogenation catalysts using the bidentate ligand TsCYDN (N-tosyl-1,2-cyclohexadiamine) have been developed, and some out-perform the catalytic rate of TsDPEN analogues.[35] TsCYDN catalysts have also been used to carry out asymmetric reductions in water with sodium formate without the need for an inert atmosphere.[39] Noyori-type catalysts have also been immobilised on supports and polymers for both continuous-flow systems and ease of recyclability. The supported catalyst retained high catalytic activity with no loss of enantioselectivity.[39-42]

1.1.2 Osmium transfer hydrogenation catalysts

More recently, osmium transfer hydrogenation catalysts have been explored, despite osmium often being considered catalytically-inferior to other platinum group metals (Figure 1.4).[43] Osmium catalysts were largely pioneered by Baratta *et al*. who have worked extensively in the field of pincer complexes,[6] achieving extraordinarily high rates of reduction (up to 10^6 h^{-1} TOF) at very low catalyst loadings (0.005 mol%).[44-48] Other osmium catalysts containing a ferrocene moiety were found to out-perform ruthenium analogues, achieving up to 3×10^5 h^{-1} TOF (Figure 1.4).[49]

Various bidentate ligands have been explored to produce both chiral and achiral osmium catalysts.[50-52] Complexes with N,O-chelating ligands achieved high enantioselectivities, including cis-aminoindanol[53, 54] and L-α-amino carboxylate[55] complexes. Other N,N-ligands, including iminopyridine,[56] and pybox (pybox = 2,6-bis[4′-(*S*)-isopropyloxazolin-2′-yl]pyridine) have been explored.[57]

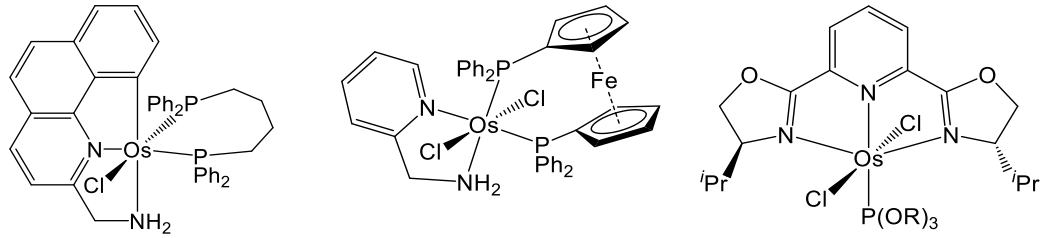

Os-pincer **Os-ferrocene** **Os-pybox**

Figure 1.4. Various osmium transfer hydrogenation catalysts. Pincer complexes,[44, 47] complexes conjugated to ferrocene,[49] and pybox ligands[57] all demonstrated high activity and enantioselectivity for the transfer hydrogenation of ketones.

Osmium derivatives of the Noyori first-generation ATH catalyst were explored, and were demonstrated to be more robust. [$OsCl_2$(diphosphine)(2-aminomethylpyridine)] catalysed the rapid transfer hydrogenation of acetophenone (TOF 5.7×10^5 h^{-1}), an order of magnitude greater than the ruthenium analogues.[47] Hydride complexes of osmium formed *in situ* have also been investigated for the transfer hydrogenation of acetophenone, showing high catalytic activity but low enantioselectivity.[43] Hydride complex *mer*-[$OsHCl(CO)(PR_3)_3$] achieved 70% conversion with 3.5% *ee* in isopropanol (356 K).[58] As well as the reduction of ketones to alcohols, osmium complexes have been used to catalyse the reduction of imines to amines,[43, 59] hydrogenation of olefins,[60] and the hydrogenation of esters to their corresponding alcohols, though were typically out-performed by their ruthenium analogues.[61]

Osmium catalysts have also been investigated for hydrogen-borrowing reactions.[62] Such reactions are highly similar to transfer hydrogenation chemistry, however the reagent itself acts as the hydrogen donor. A molecule (typically an alcohol) donates hydrogen to the catalyst molecule and is oxidised to the corresponding ketone, which can undergo a subsequent reaction (e.g. with an amine to form an imine). Hydrogen is then transferred back from the catalyst to reduce the final product (e.g. to an amine).

1.2 Metals in medicine

Inorganic chemistry provides a wealth of novel solutions to pharmaceutical challenges. Where organic compounds are typically restricted to linear, trigonal or tetrahedral coordination, the introduction of a metal centre allows access to new geometries, such as square planar, trigonal bipyramidal and octahedral. The central cobalt ion in cobalamin (Vitamin B_{12}) provides structure and functionality unmatched by an organic molecule. Inorganic metal ions can also access a vast range of oxidation states. For example, osmium may exist from -2 to +8. Since redox processes are key to many cellular pathways,[63] the tuneable redox potential of a metal-based drug may be advantageous to clinical success.

1.2.1 Historical use of metallodrugs

Metals have played an important role in treatments of diseases and illnesses over the ages. Gold has been used in medicine since ancient times, and may be traced back as early as 2500 BC. Preparations were particularly common in ancient China and India, and were used to treat a range of illnesses, ranging from diabetes mellitus to memory loss and asthma.[64] Since the 1920s, gold thiolates such as sodium 2-(auriosulfanyl)-3-carboxypropanoate (sodium aurothiomalate) and tetraacetyl-β-d-thioglucose gold(I) triethylphosphine (Auranofin) have been used for the treatment of rheumatoid arthritis, and are currently being explored for their anticancer activities.[65] Gold(I) N-heterocyclic carbene (NHC) metallodrugs have also earned popularity as potential anticancer agents. Many Au complexes have been shown to be potent TrxR (Thioredoxin reductase) inhibitors. An example is the di-carbene gold complex MC-3, which possess nanomolar IC_{50} values (21-67 nM) against pancreatic cancer cells (Figure 1.5).[66]

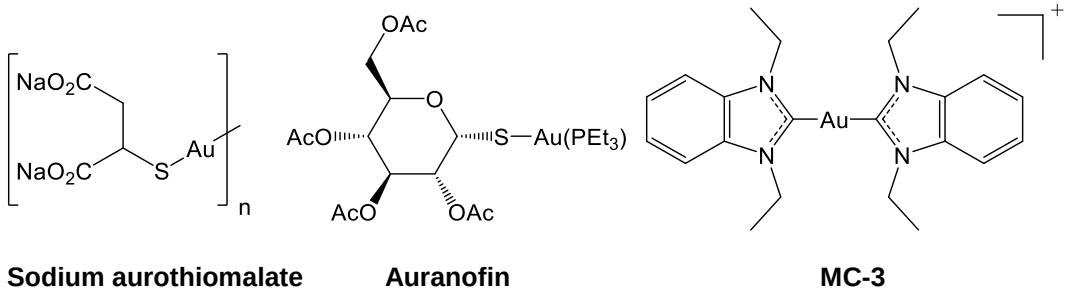

Sodium aurothiomalate **Auranofin** **MC-3**

Figure 1.5. Gold thiolates used for the treatment of rheumatoid arthritis (sodium aurothiomalate and Auranofin) alongside MC3, a potent apoptosis-inducing gold(I) N-heterocyclic carbene complex.[66]

Silver has also been used medicinally for thousands of years.[67] The ancient Romans and Greeks were known to have stored water in silver vessels, and made use of the antimicrobial properties of silver nitrate, which continues to be used during the modern day treatment of severe skin burns.[68] The antibacterial activity of silver ions is now well established,[67] and commonly feature in personal hygiene products. Recently, alkyl phosphine complexes of group 11 metals (copper, silver and gold) have been investigated for their *in vitro* antitumor activity, with mechanistic studies identifying interactions of the gold and silver complexes with thioredoxin reductase, while the copper complexes lead to proteasome inhibition.[69]

In 1907, a compound of arsenic was first synthesised and subsequently tested for activity against *spirochaetes*, a group of organisms found to cause syphilis, infections from which were highly prevalent in the early 20th century.[70] The compound, named "606" after its preparation number (also known as Arsphenamine or Salvarsan) continued to be widely used until penicillin became readily available after World War II.[70] In fact, a study conducted in 2005 reported the structure of "606" as a mixture of two structural isoforms, both of which led to the formation of the active compound $RAs(OH)_2$, where R = 3-amino-4-hydroxyphenyl.[71]

1.2.2 The discovery of cisplatin

In 1965, physicist Barnett Rosenberg (Michigan State University) observed inhibition of cell division as well as filamentous growth, up to 300× the usual length, in *E. coli*.[72] Electrolysis products formed from his platinum mesh electrodes and salt solution were found to be Peyrone's compound, *cis*-[$PtCl_2(NH_3)_2$], first synthesised in 1845.[73] The compounds molecular structure was elucidated in 1893 by Werner,[73, 74] and almost a century later, was found by Rosenberg to exhibit potential as an anticancer agent in rats, as reported in his 1969 publication: "*Platinum compounds: a new class of potent anti-tumor agents*".[72] Peyrone's compound (cis-diaminedichloroplatinum(II) / cisplatin) was first administered to a human patient in 1971, and became clinically available in 1978 under the brand name Platinol®.[73] The discovery of a pharmaceutically active metal-containing compound was so significant in that an entirely new area of bio-inorganic research emerged, involving the development of other novel metallodrugs. Cisplatin is also commonly found in combination therapies, such as administration with the anticancer drug paclitaxel (for the treatment of ovarian, breast, lung, head and neck cancers), fluorouracil (5FU, for the treatment of oral cancers)[75] and metformin (for the treatment of lung adenocarcinoma).[74, 76]

Cisplatin has since been used in the successful treatment of various cancers, including testicular, lung, breast, cervical and prostate cancers.[74] It is the mainline treatment for ovarian cancer, a highly prominent female gynaecological cancer with high mortality rates, often associated with late-stage diagnosis and poor detection.[76] However, platinum-resistant ovarian cancers are common, through either intrinsic or acquired resistance.[77-79] For this reason, this thesis will largely focus on a human ovarian carcinoma cell line (A2780) allowing for direct comparison between novel catalytic metallodrugs of osmium, and existing platinum-based treatments.

The DNA-targeting mechanism of action of cisplatin is commonly accepted. Cellular Pt uptake occurs via copper transporter proteins as well as a contribution from passive diffusion. The chloride ligands are labile, and once inside the cell, the lower intracellular chloride concentration favours chloride dissociation, allowing stepwise hydrolysis to afford the di-aqua complex $[Pt(NH_3)_2(OH_2)_2]^{2+}$ which can form 1,2-intra-strand cross-links with purine bases; typically, N7 of guanine (Figure 1.6). If the DNA cannot be successfully repaired, high-mobility group (HMG) proteins recognise and bind platinated DNA,[80] causing either apoptotic or necrotic cell death, depending on the cisplatin exposure time.[76, 81] The *cis* geometry of cisplatin is important, since its *trans* isomer is inactive as intra-strand adducts cannot form. While DNA adduct formation lacks specificity for cancer cells, metal complexes are commonly multi-targeting, which may increase cancer cell selectivity.[82, 83] Though only *ca*. 1% of cisplatin reaches the nucleus, the complex is also known to interact with many other biomolecules. The tripeptide GSH (Glu-Cys-Gly) is present at millimolar (1-10 mM) concentrations in mammalian cells, and has been shown to highly influence the efficacy of cisplatin.[84] GSH also chelates Cu^{2+} causing up-regulation of the copper transporter Ctr1, increasing Pt uptake. Conversely, GSH-Pt adducts may also facilitate Pt efflux via the multidrug resistance protein 2 (MRP2) efflux pump.[84, 85]

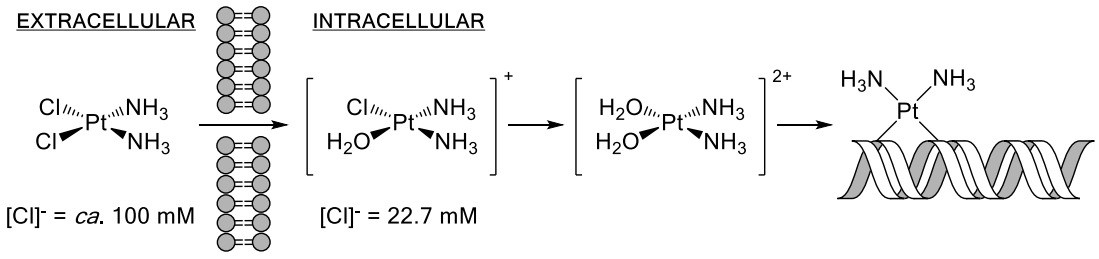

Figure 1.6. Cisplatin undergoes step-wise hydrolysis inside cells due to the lower cytosolic chloride concentration, forming aqua adducts (hydroxido complexes are also known). Protein and DNA adducts can then form (nucleus $[Cl^-]$ = 4 mM), causing apoptotic and necrotic cell death.

Despite the widespread use of cisplatin, dosage is limited due to the side effects in normal tissue; causing nausea, vomiting, hair loss, nephrotoxicity, neurotoxicity, and hearing loss.[74] Cisplatin resistance is also of clinical concern, which may be either intrinsic or acquired. Resistance mechanisms may include decreased cellular uptake, or increased efflux by membrane-bound transport ATPases such as MDR-1/2.[74, 86] To reduce off-target effects, Carboplatin was introduced in the 1980s, and possesses a bidentate carboxylate in the place of the two chlorido ligands.[73] Carboplatin is used for the treatment of lung, head and neck cancers, and does not exhibit the nephrotoxic effects of cisplatin, which may be associated with the lower reactivity and subsequent slower rate of DNA binding. The longer retention half-life of 30 hours (compared to 1.5-3.6 h for cisplatin) means that effects are longer-lasting. Other cisplatin-derived compounds (Figure 1.7) that have reached the clinic or clinical trials include Oxaliplatin (1999),[87] Heptaplatin (2005), Nedaplatin (1996) and Lobaplatin (2004).[88]

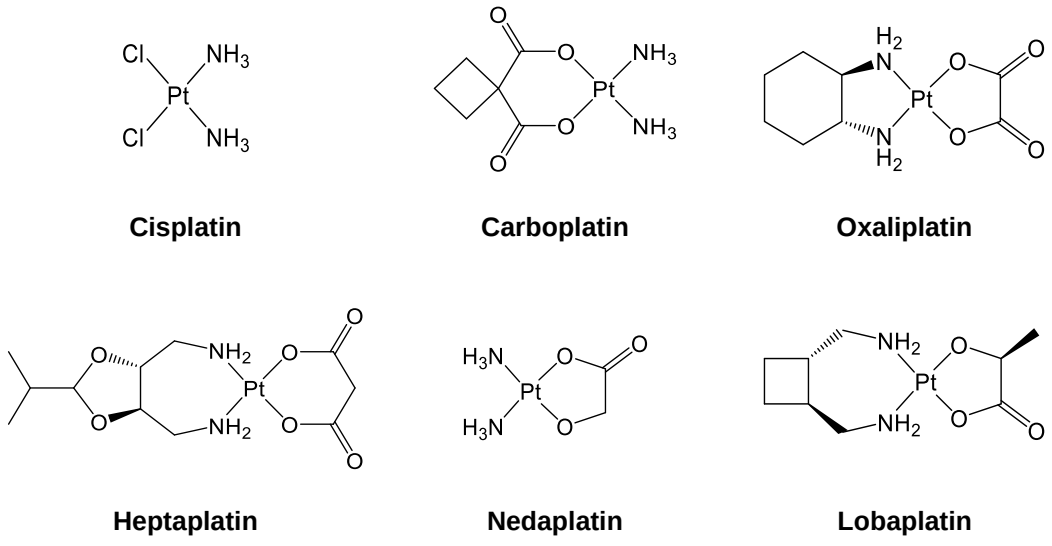

Figure 1.7. Six platinum(II) anticancer drugs. Cisplatin, carboplatin and oxaliplatin are established world-wide. Heptaplatin is approved for the treatment of gastric cancers in South Korea, Nedaplatin for the treatment of head and neck, testicular, lung, ovarian, cervical, and non-small-cell lung cancers in Japan, and Lobaplatin for the treatment of chronic myelogenous leukaemia in China.[88]

1.2.3 Platinum group metals in medicine

The six elements of the platinum group (Ru, Os, Rh, Ir, Pt, Pd) are chemically very similar. It is perhaps unsurprising that after the successes of Pt therapies, interests into the design of Ru complexes have grown exponentially over the last few decades. A Ru(III) complex, NKP-1339 (sodium *trans*-[tetrachloridobis(1*H*-indazole)ruthenate]), the sodium salt of KP1019 (Figure 1.8), is currently in phase II clinical trials.[89] The planar arrangement of chloride ligands around the octahedral Ru centre shows structural similarity to the square planar geometry of cisplatin. NKP-1339, like cisplatin, induces G_2/M arrest and apoptosis in cancer cells.[90] However unlike cisplatin, NKP-1339 disrupts the redox balance of the cell by generation of reactive oxygen species (ROS),[91] and also appears to target the endoplasmic reticulum.[90] In fact, the generation of ROS by metal complexes in cells is well documented, providing an alternative mechanism of action to DNA binding.[92-95] The contrasting mechanism provides evidence that both the chemical and biological properties of the complex may be modified by careful selection of suitable ligands, paired with a particular metal.

The analogous *cis*-osmium(III) complexes, derived from KP1019, have been prepared by the 1-electron reduction of precursor Os(IV) complexes.[96] The osmium complexes were found to not interact with amino acids or model nucleotides (such as 5'-guanosine monophosphate). While the Os(III) complexes exhibited lower antiproliferative activities than those of the parent Ru(III) compound, they showed selectivity for human melanoma cells (FemX), while the antiproliferative activities determined using KP1019 were comparable between all cell lines investigated.[97] Interestingly, though *trans*-[tetrachlorobis(1H-indazole)ruthenate(III)] (KP1019) and its *trans*-Os(III) isomer are known, at the time of writing, the *cis*-Ru(III) isomer is not isolable, while *cis*-osmium(III) isomer has recently been fully characterised.[96]

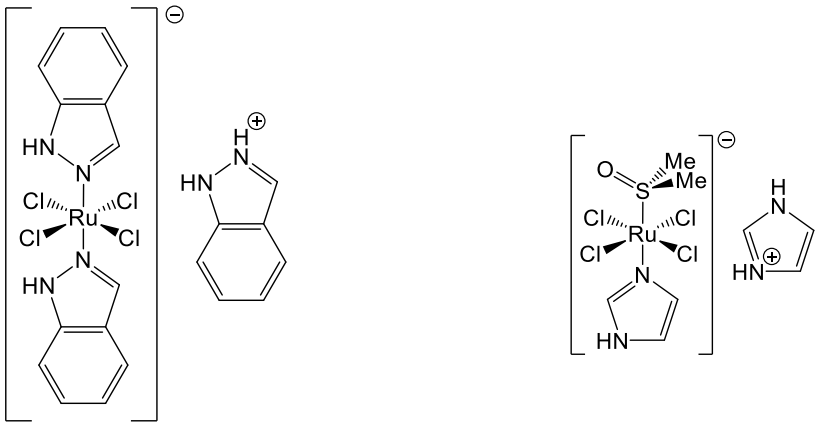

Figure 1.8. Anticancer Ru(III) complexes in clinic trials: (a) KP-1019,[91] (b) NAMI-A.[98]

A structurally similar ruthenium complex, NAMI-A (Figure 1.8) has been extensively studied.[89, 99, 100] The complex entered a phase I/II clinical study, in combination with gemcitabine, for the treatment of non-small cell lung cancers, however was only moderately tolerated in patients.[98] Similarly to KP1019, the osmium analogues of NAMI-A have also been investigated, prepared stepwise from osmium tetroxide.[101] As a third-row transition metal with slower exchange kinetics, osmium was previously discounted as a useful metal centre for a metallodrug. The osmium complexes did not undergo hydrolysis of the chloride ligands, unlike the ruthenium centre in NAMI-A, yet showed approximately an order of magnitude greater activity than the ruthenium counterparts.[101] In contrast, replacement of Ru for Os in KP1019 decreased antiproliferative activity, indicating that trends anticancer activity cannot be predicted upon metal exchange.

While NAMI-A and KP1019 were synthesised by selection of small-molecule ligands with properties that would benefit the overall complex, ruthenium complexes of natural products have also been explored, where the role of the metal centre allows access to unique structural architectures. Ruthenium protein kinase inhibitors based

on staurosporine have been synthesised (Figure 1.9).[102] These complexes exhibit high selectivity for particular tyrosine-protein kinases, specifically for the Abelson tyrosine kinase (Abl) which is known to be highly involved with cell growth processes. In fact, the complex was found to be inactive against a range of other kinases (e.g. PKC_{α}).[102] Interestingly, the IC_{50} (half-maximal inhibitory concentration) of the Ru complex was found to be *ca*. 10× lower than that of the free ligand (2 nM compared to 25 nM) towards the Abl, reinforcing the importance of the metal centre.

In recent years, "sandwich" structures have gained substantial interest. Such complexes are identified by the coordination of one (or many) η^5 or η^6- arene(s) to a central metal, which can act to stabilise the overall complex as well as providing a lipophilic region. Since the synthesis of the organo-iron compound, Ferrocene [$Fe(\eta^5\text{-}C_5H_5)_2$] in 1951,[103] structurally-derived sandwich complexes of ruthenium, osmium and iron have been conjugated to the anticancer compound Tamoxifen, increasing the potency towards breast cancer cells (Figure 1.9). Iron-conjugates of ferrocene were found to be more active than Os and Ru counterparts, demonstrating that the role of the ferrocene moiety was not purely structural.[104]

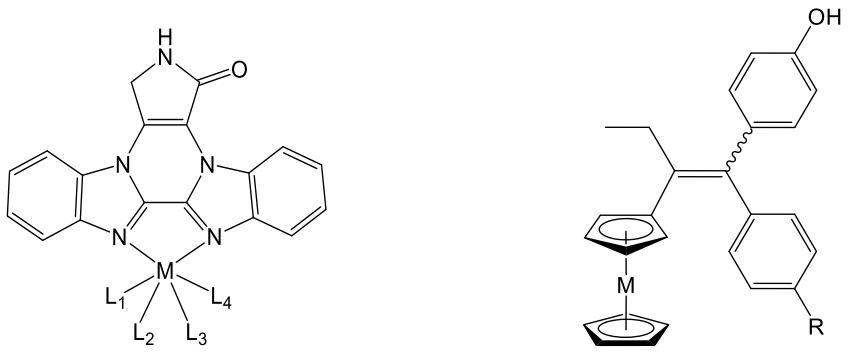

Protein kinase inhibitors
(M = Ru)

Tamoxifen derivatives
(M = Fe / Ru / Os)

Figure 1.9. Organometallic "sandwich" complexes derived from established anticancer compound Tamoxifen, and a ruthenium protein kinase inhibitor based on a natural product, staurosporine.

Half-sandwich "piano-stool" complexes [M(η^6-arene)(bidentate)(monodentate)] only possess one metal-coordinated arene, and typically adopt pseudo-octahedral geometry. Early examples of half-sandwich complexes with anticancer properties are the Ru compound RM-175 and its Os analogue, AFAP-51, with the general structure [M(η^6-biphenyl)(ethylenediamine)Cl]$^+$ (Figure 1.10).[105] Though the chemistry of Ru(II) and Os(II) ions is often considered similar, the Os complex was found to be 6× more potent than the Ru analogue. RM-175 (Ru) however showed high *in vivo* activity, leading to a reduction in metastases which was not found in the Os case.[105] In this example, there are meaningful biological implications resulting from the fine-tuning of the redox and kinetics by of the different metal centres. Sadler *et al*. developed a series of osmium and ruthenium azo/imino-pyridine complexes of the general formula [M(η^6-arene)(azo/imino-pyridine)(X)]$^+$ where X = Cl or I, that show high activity against cancer cells,[106] which were found to be higher for iodido complexes than their chloride analogues.[3] The complexes were shown to exhibit a new mechanism of action that differed from that of existing platinum therapies, since these complexes did not appear to undergo aquation nor bind to DNA.[3] The complexes also retained activity in Pt-resistant cells.[107] One Os complex in particular (FY26; Figure 1.10), has been shown to delay growth of human colon cancer xenografts in mice, with negligible toxicity.[108]

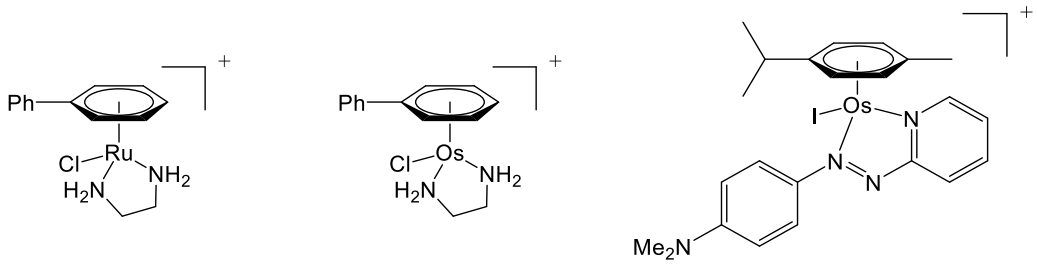

RM-175 **AFAP-51** **FY-26**

Figure 1.10. Anticancer Ru(II) and Os(II) complexes: (a) FY26, (b) RM-175, (c) AFAP-51. Hexafluorophosphate (PF_6^-) counter-ions not shown.

1.3 Cancer

In the UK, someone dies from cancer every two minutes.[109] Cancer is one of the most significant cause of death around the world,[110] and is particularly prevalent in developed countries. In Britain, cancer is now expected to affect around 1 in 2 people, with the lifetime risk for men slightly exceeding that for women.[109, 111] Cancers may result from inherited genetic traits, but it is estimated that up to 80% are caused by external factors such as radiation, carcinogenic chemicals or viruses.[112] Many cancers that were previously considered highly lethal (such as testicular cancer, Hodgkin's lymphoma, and some leukemias) are now effectively treatable with anticancer drugs.[86] However, while highly sensitive screening methods are detecting many cancers before they have metastasized, the battle against malignant cancers is expected to remain a key part of modern medicine.[86]

1.3.1 The origin of cancer

The six hallmarks of cancer, according to Hanahan and Weinberg, are growth-suppressor evasion, growth signaling self-sufficiency, becoming active for invasion and metastasis, enabling replicative immortality, the induction of angiogenesis and resisting cell death.[113]

In normal cells, proto-oncogenes code for proteins that play an important role in many cellular processes such as cell division, cell differentiation, and cell death. Over-production of these proteins leads to a loss of control over such cellular processes. Proto-oncogenes may become activated by mutations that either increase the expression level or activity to become oncogenes,[114] which may result in causing cancer.[112] Cells also possess anti-oncogenes, known as tumor suppressor genes. Inactivation of a tumor suppressor gene removes restrictions that regulate normal and

controlled cell proliferation. A key tumor suppressor gene (*P53*) encodes the transcriptional regulator protein p53, the absence of which greatly increases the occurrence of tumors.[112] After exposure to DNA-damaging agents, expression of p53 is increased, resulting in cell cycle arrest and apoptosis. Both the activity of the p53 protein and transcription of the *P53* gene are negatively regulated by the E3 ubiquitin ligase, Mdm2 (Figure 1.11). Mutations in *P53* are in fact the most common genetic alteration in human cancers.[115] Such mutations include: (a) deletion of the carboxyl-terminal domain, preventing p53 tetramer formation, (b) amino acid alteration in the DNA binding domain, preventing downstream gene activation, (c) overexpression of MDM2, stimulating the degradation of p53.[116]

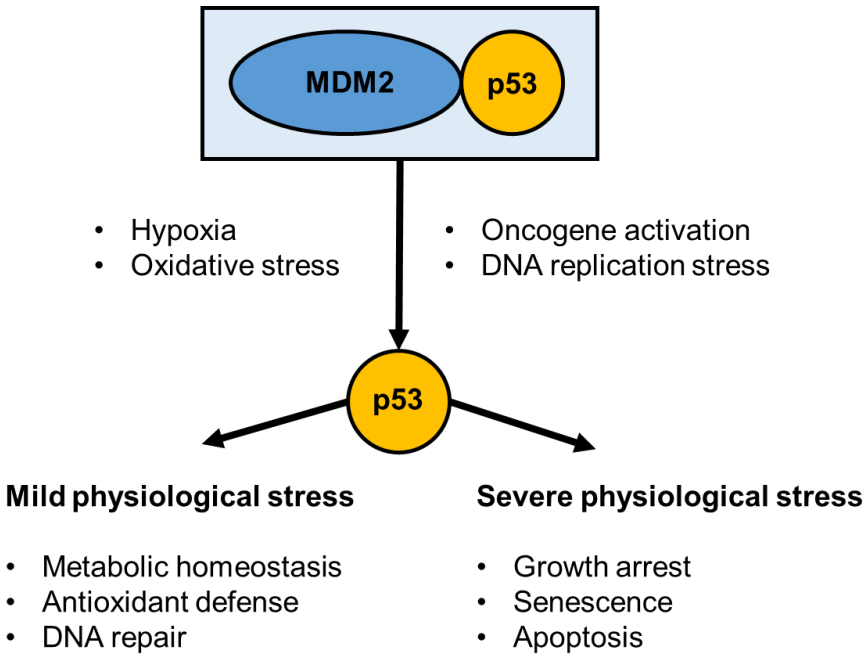

Figure 1.11. Simplified p53 pathway (adapted from A. J. Levine and M. Oren, 2009).[117] P53 is expressed after oncogene activation, DNA replication stress, hypoxia and oxidative stress; resulting in metabolic homeostasis, antioxidant defense and DNA repair; or in severe cases, growth arrest, senescence and apoptotic cell death.

Differences in the physiology and biochemistry of cancer cells compared to normal cells may facilitate selective targeting by novel anticancer agents. Physiologically, tumors typically are commonly hypoxic,[118] and have low extracellular pH as a result of lactate secretion.[119] These traits are commonly observed as microenvironments which are chemically-distinct from healthy tissue, and have led to interest in developing inactive pro-drugs that become activated by tumor physiology.[120] Such compounds typically contain *N*-oxides, quinones or transition metals, which are activated under hypoxic conditions. Tirapazamine, a di-*N*-oxide compound, demonstrated up to 200× more cytotoxicity in hypoxic cells.[121]

Biochemically, the metabolism of glucose in cancer cells differs from that in healthy cells.[122] Rapidly-proliferating cells require more ATP, a cellular energy source. While healthy cells metabolize glucose to pyruvate (via glycolysis) and subsequently oxidize pyruvate to carbon dioxide by oxidative phosphorylation, the 'Warburg Effect' summarises the observation that cancer cells display a preference for the reduction of pyruvate to lactate, rather than oxidation to carbon dioxide.[123] Only in the absence of oxygen would healthy cells utilise lactate production as a means of acquiring energy, since ATP production by glycolysis is far less efficient than by oxidative phosphorylation (2 molecules of ATP, compared to 36 molecules per glucose molecule).[4] For this reason, the consumption of glucose is significantly higher in cancer cells.[124] This glucose-dependence makes glycolysis a target for anticancer drug design, and in fact, many glycolytic inhibitors (2-deoxyglucose, lonidamine, 3-bromopyruvate, Imatinib) have been explored for use as anticancer agents.[124]

Furthermore, the availability of cellular reducing agents (e.g. NADH or NADPH) has been associated with the rate of proliferation,[125] making redox-based strategies an attractive method of selectively targeting cancer cells.[63, 126, 127]

1.3.2 Current treatment of cancer

Three treatment options are well established in the clinic, and are usually used in combination to achieve the best outcome for the patient. Surgical excision of a tumour is most commonly employed after size-reduction using radiotherapy or chemotherapy. Many existing chemotherapy agents target cellular replication processes, by damaging DNA or affecting key pathways involved with cell growth. Many of these targets are not unique to cancer cells, and drugs have little selectivity for cancerous cells over healthy cells that also have rapid rates of proliferation, such as the hair follicles, bone marrow and gastrointestinal tract cells;[128] resulting in a range of side-effects.

New targeted approaches to chemotherapy are required that exploit the unique biochemical properties of cancer cells. While cancer-specific drug delivery strategies can reduce off-target effects, research into future novel anticancer compounds may identify other chemotherapeutic targets, such as the previously discussed hypoxic environment,[120, 121] high rate of glycolysis,[124] and increased levels of oxidative stress[129] in cancer cells. By combining targeting monoclonal antibodies with an anticancer drug, antibody-drug conjugates increase the selectivity of existing therapies. Trastuzumab emtansine is the first FDA-approved conjugate, for use against human epidermal growth factor receptor 2 positive (HER2+) breast cancers.[130] Recent studies have also explored the potential of kinase inhibitors. Kinases are known to be crucial in many cell signalling pathways, including those associated with cancer (such as proliferation and cell survival mechanisms).[131] While highly potent (nanomolar IC_{50}), many of the inhibitors investigated lacked specificity for a particular kinase.[132] In addition, drug carriers; for example nanoparticles, liposomes and polymeric conjugates, have also been explored to improve delivery of cytotoxic agents specifically to cancer cells, while protecting the drug from deactivation.[128, 133]

1.4 Catalytic therapies

Though absorption, metabolism and excretion mechanisms of current pharmaceuticals have been thoroughly studied, the damage that may occur at high concentrations is a common clinical concern. By designing catalytic therapies, dosage could be dramatically reduced while achieving the same efficacy. For many diseases, including cancer, the redox balance in cells is known to differ from normal levels.[63, 134] Cellular redox homeostasis is mainly regulated by two co-factors; nicotine adenine dinucleotide (NAD), and flavin adenine dinucleotide (FAD), which catalytically transport hydride. Chemical mimics that can catalytically generate and transfer redox-active molecules may play a crucial role in future pharmaceuticals.

Catalysts are well-established in chemical synthesis to achieve reaction rates that would not be possible in their absence. Inorganic catalysts allow access to a range of redox potentials and coordination numbers. Ligands may be stabilising, substrate-directing, or participate in the catalytic cycle, and allow for the fine-tuning of the properties. However, many inorganic catalysts require inert atmospheres (to prevent metal oxidation) and particular solvents to circumvent catalyst deactivation. Advances are being made in the development of water-compatible catalysts,[5] which are advantageous when considering the development of catalytic medicines, which would be required to maintain activity in an aqueous cellular environment, and indeed many successful examples have been reported. Artificial protease complexes of cobalt(III) and copper(II) have been shown to catalytically cleave bovine serum albumin and myoglobin.[135] Suzuki-Miyaura cross-couplings and allylcarbamate cleavages have been carried out inside cells using palladium(0) nanoparticles.[136] Ruthenium catalysts have been used to uncage an active anticancer drug in HeLa cells,[137] and to uncouple the mitochondrial electron transport chain by *in situ* generation of 2,4-dinitrophenol.[138]

1.4.1 Oxidative catalytic therapies

The catalytic generation of reactive oxygen species (ROS), such as hydroxyl radicals $OH^{\bullet}$ and superoxide $O_2^{\bullet-}$ has been frequently identified for cells exposed to metal complexes.[56, 139] This is particularly important for the treatment of many conditions, including cancer, Alzheimer's disease and Parkinson's disease; where abnormal cellular redox balance is observed, offering a promising therapeutic target.[140] Methodical design and modification of ligands around the metal centre allows for fine tuning of the metal centre chemistry, to access physiologically-relevant redox couples.

Inhibition of thioredoxin reductase (TrxR), an enzyme known to be important in the regulation of cellular redox levels, has been demonstrated using ruthenium(II) arene complexes.[141] Ruthenium azopyridine complexes have been shown to catalytically oxidise glutathione (GSH), an important anti-oxidant molecule in cells, to glutathione disulphide (GSSG).[93] Iridium(III) catalysts have been successfully used catalytically oxide NADH,[142] and shown to increase the NAD^+/NADH ratio inside cancer cells (Figure 1.12).[143] While osmium(II) iminopyridine and azopyridine complexes have been also shown to generate reactive oxygen species in cells, the oxidation was not catalytic, and only iminopyridine complexes were capable of NADH oxidation (forming NAD^+) by abstraction of hydride, while azopyridine complexes could not.[106]

Superoxide dismutase (SOD) mimics have also been studied to catalyse the conversion of the superoxide radical to dioxygen and hydride peroxide, since SOD is considered one of the cell's primary defence mechanisms against oxidative stress.[144-146] Many transition metal-catalysed examples have been described, including OsO_4,[144] while more recent reports have explored the high activity of manganese(II) complexes. In particular, Mn(II) salen complexes and Mn(II) peptide complexes have been found to significantly reduce superoxide levels inside cells.[147, 148]

1.4.2 Reductive catalytic therapies

Transfer hydrogenation of NAD^+ to its reduced form (NADH) have been extensively studied using inorganic catalysts of ruthenium and iridium, in combination with sodium formate (or hydrogen gas).[149, 150] NADH mimics have also been used for reduction reactions in aqueous solution, and hydrogenation (regeneration) of the coenzyme mimics, using sodium formate, has been successfully described.[151] Non-asymmetric ruthenium *N*,*N*-bidentate piano-stool complexes [Ru(arene)Cl(tosyl-diamine)] have been used to reduce NAD^+ using sodium formate in an aqueous model,[152] and later inside cancer cells using a non-toxic concentration of sodium formate (Figure 1.12).[129]

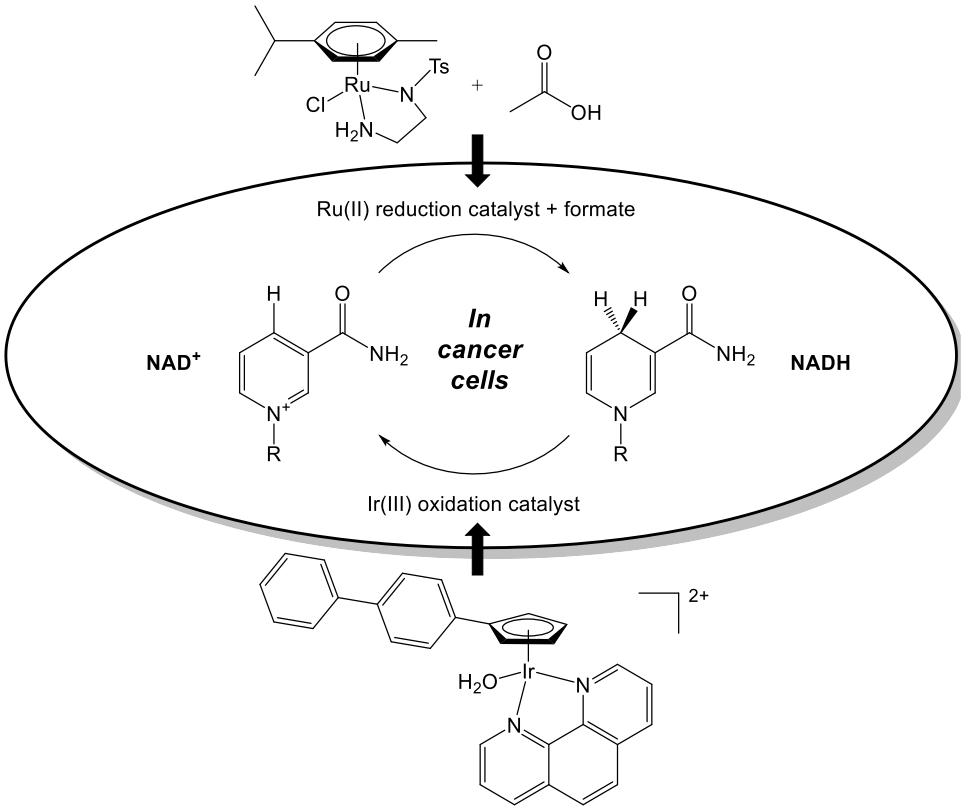

Figure 1.12. Modulation of the NAD^+/NADH ratio inside cancer cells by: (a) transfer hydrogenation (reduction) of NAD^+ to NADH using Ru ATH catalysts with sodium formate as a hydride source;[129] (b) catalytic oxidation of NADH (abstraction of hydride) by Ir(III) complexes.[143]

Stereoselective ruthenium(II) complexes have been assessed for both catalytic efficiency and antiproliferative activity in cells. Interestingly, highly potent complexes were found to be poor transfer hydrogenation catalysts, while promising catalysts were less effective against cancer cells.[153] Half-sandwich rhodium(III) Cp* complexes have been shown to reduce NAD^+ to NADH by ^{1}H-NMR in a model system, and can also rapidly convert pyruvate to lactate, using sodium formate as a hydride source, though the reduction is not enantioselective. In competition experiments, the rhodium complexes preferentially reduced NAD^+ over pyruvate.[154] Pyruvate reduction using ruthenium(II) bipyrimidine and iridium(III) phenanthroline complexes has also been studied by ^{1}H-NMR,[143] however no previous examples have demonstrated reduction of pyruvate by an osmium catalyst. Furthermore, at the time of writing, no examples have reported the selective reduction of pyruvate to L- or D-lactate with high enantioselectivity, nor the reduction of pyruvate inside cells.

The work in this thesis builds on the aforementioned examples to explore the antiproliferative activities of Os(II) and Ir(III) transfer hydrogenation catalysts against cancer cells, which are compared to current non-catalytic Pt therapies. Utilising the enantioselective properties of the catalyst, modulation of intracellular L- or D-lactate concentrations by asymmetric reduction of pyruvate inside cells are carried out using novel Os(II) complexes, generating selectivity for cancer cells over healthy cells. Such complexes are based on racemic Ru(II) catalysts previously described to carry out the reduction of NAD^+ to 1,4-NADH inside cells (using sodium formate as a hydride source). Furthermore, the reverse osmium(II)-catalysed reaction is explored by catalysing the oxidation of the co-enzyme and cellular hydride source 1,4-NADH to NAD^+ in a model system under biologically-relevant conditions (pH 7.4, aqueous-phase reduction).

1.5 Aims

This thesis aims to explore the novel catalytic and anticancer properties of 16-electron osmium(II) sulfonamide complexes of the general formula [Os(η^6-arene)(diamine)], where the η^6-arene is *para*-cymene, biphenyl or *meta*-terphenyl, and the diamine substituent contains a sulfonamide with various R group substituents.

- **Asymmetric transfer hydrogenation of ketones by an Os(II) catalyst**

Structurally similar ruthenium 16-electron complexes of the general form [Ru(η^6-arene)(diamine)] have previously been identified as the active species in the catalytic cycle for the transfer hydrogenation of ketones. In Chapter 3, the osmium complexes are assessed for their activity, including degree of enantioselectivity, for the transfer hydrogenation of asymmetric ketones (derived from acetophenone) to assess primary catalytic activity in organic solvent systems.

- **Conversion of the co-enzyme NADH to NAD^+ by an Os(II) catalyst**

In Chapter 4, the osmium(II) (and structurally-similar iridium(III)) sulfonamide catalysts are explored as catalysts for the oxidation of NADH, an important biological source of hydride. Furthermore, the primary anticancer activities are investigated in range of human cell lines to examine activity trends. As the compounds contain a xenobiotic element, cellular metal accumulation mechanisms and pathways, and cellular distribution patterns are reported, using representative compounds from the osmium(II) and iridium(III) series. The oxidation of NADH is known to generate downstream reactive oxygen species, which can be detected in cells.

- **Asymmetric reduction of pyruvate in cancer cells by an Os(II) catalyst**

Chapter 5 further explores the catalytic potential of the complexes *in vitro* by co-administering the catalyst with a source of hydride (sodium formate) to enhance antiproliferative potency. This effect is examined in both cancer cells and healthy cells (primary fibroblasts). Both enantiomers of Os(II) sulfonamide complex [Os(*p*-cymene)(TsDPEN)] are explored for their ability to catalyse the asymmetric reduction of pyruvate to L- or D-lactate in cells and in model systems, which are studied using time-dependent ^{1}H-NMR and enzymatic assays. Enzymes that are known to be over-expressed in certain cancer cells are also explored to selectively generate hydride *in situ*, further increasing the selectivity of the compounds for cancer cells.

- **Exploring the toxicity and mechanism of Os(II) complexes in zebrafish**

Lead osmium(II) anticancer complexes are explored in Chapter 6 for the first time *in vivo* using the zebrafish model (*Danio rerio)* to evaluate both acute aquatic toxicity as described in OECD guideline 236. Data are compared to results obtained with currently available anticancer drugs and other osmium(II) complexes which have shown clinical promise. Additionally, since production of reactive oxygen species was observed in cells, generation of ROS was investigated in whole-mount zebrafish to determine whether the observation is maintained in a whole live animal. ROS were visualised using confocal microscopy and a green-fluorescent ROS probe. To confirm the specific role of the metal complex, a red-fluorescent Os(II) complex derived from the sulfonamide series was designed, synthesised, fully characterised, and its biological activities assessed before co-imaging Os(II) complex (red) and ROS generation (green) in zebrafish.

1.6 References

1. R. Noyori and S. Hashiguchi, *Acc. Chem. Res.*, 1997, **30**, 97-102.
2. S. Hashiguchi, A. Fujii, J. Takehara, T. Ikariya and R. Noyori, *J. Am. Chem. Soc.*, 1995, **117**, 7562-7563.
3. Y. Fu, A. Habtemariam, A. M. B. H. Basri, D. Braddick, G. J. Clarkson and P. J. Sadler, *Dalton Trans.*, 2011, **40**, 10553-10562.
4. M. G. Vander Heiden, L. C. Cantley and C. B. Thompson, *Science*, 2009, **324**, 1029-1033.
5. X. Wu and J. Xiao, *Chem. Commun.*, 2007, 2449-2466.
6. D. Wang and D. Astruc, *Chem. Rev.*, 2015, **115**, 6621-6686.
7. T. Ohkuma, *Proc. Jpn. Acad. Ser. B Phys. Biol. Sci.*, 2010, **86**, 202-219.
8. C. A. Sandoval, T. Ohkuma, K. Muñiz and R. Noyori, *J. Am. Chem. Soc.*, 2003, **125**, 13490-13503.
9. S. E. Clapham, A. Hadzovic and R. H. Morris, *Coord. Chem. Rev.* , 2004, **248**, 2201-2237.
10. S. Gladiali and E. Alberico, *Chem. Soc. Rev.*, 2006, **35**, 226-236.
11. J. Václavík, P. Šot, B. Vilhanová, J. Pecháček, M. Kuzma and P. Kačer, *Molecules*, 2013, **18**, 6804-6828.
12. T. Ikariya and A. J. Blacker, *Acc. Chem. Res.*, 2007, **40**, 1300-1308.
13. C. Wang, X. Wu and J. Xiao, *Chem. Asian J.*, 2008, **3**, 1750-1770.
14. A. Robertson, T. Matsumoto and S. Ogo, *Dalton Trans.*, 2011, **40**, 10304-10310.
15. A. Fujii, S. Hashiguchi, N. Uematsu, T. Ikariya and R. Noyori, *J. Am. Chem. Soc.*, 1996, **118**, 2521-2522.

16. T. Ikariya, S. Hashiguchi, K. Murata and R. Noyori, *Org. Synth.*, 2005, **82**, 10-17.

17. T. Ikariya, K. Murata and R. Noyori, *Org. Biomol. Chem.*, 2006, **4**, 393-406.

18. N. Uematsu, A. Fujii, S. Hashiguchi, T. Ikariya and R. Noyori, *J. Am. Chem. Soc.*, 1996, **118**, 4916-4917.

19. M. Yamakawa, H. Ito and R. Noyori, *J. Am. Chem. Soc.*, 2000, **122**, 1466-1478.

20. R. Noyori, M. Yamakawa and S. Hashiguchi, *J. Org. Chem.*, 2001, **66**, 7931-7944.

21. D. A. Alonso, P. Brandt, S. J. M. Nordin and P. G. Andersson, *J. Am. Chem. Soc.*, 1999, **121**, 9580-9588.

22. C. P. Casey and J. B. Johnson, *J. Org. Chem.*, 2003, **68**, 1998-2001.

23. K.-J. Haack, S. Hashiguchi, A. Fujii, T. Ikariya and R. Noyori, *Angew. Chem., Int. Ed.*. 1997, **36**, 285-288.

24. P. Brandt, P. Roth and P. G. Andersson, *J. Org. Chem.*, 2004, **69**, 4885-4890.

25. J. W. Handgraaf and E. J. Meijer, *J. Am. Chem. Soc.*, 2007, **129**, 3099-3103.

26. P. A. Dub and T. Ikariya, *J. Am. Chem. Soc.*, 2013, **135**, 2604-2619.

27. R. Hodgkinson, V. Jurčík, A. Zanotti-Gerosa, H. G. Nedden, A. Blackaby, G. J. Clarkson and M. Wills, *Organometallics*, 2014, **33**, 5517-5524.

28. R. Soni, K. E. Jolley, G. J. Clarkson and M. Wills, *Org. Lett.*, 2013, **15**, 5110-5113.

29. D. Morris, A. Hayes and M. Wills, *J. Org. Chem.*, 2006, **71**, 7035-7044.

30. A. Hayes, D. Morris, G. Clarkson and M. Wills, *J. Am. Chem. Soc.*, 2005, **127**, 7318-7319.

31. R. Soni, T. H. Hall, B. P. Mitchell, M. R. Owen and M. Wills, *J. Org. Chem.*, 2015, **80**, 6784-6793.

32. X. Wu, X. Li, A. Zanotti-Gerosa, A. Pettman, J. Liu, A. J. Mills and J. Xiao, *Chem. Eur. J.*, 2008, **14**, 2209-2222.

33. T. Ohkuma, N. Utsumi, M. Watanabe, K. Tsutsumi, N. Arai and K. Murata, *Org. Lett.*, 2007, **9**, 2565-2567.

34. T. Thorpe, J. Blacker, S. M. Brown, C. Bubert, J. Crosby, S. Fitzjohn, J. P. Muxworthy and J. M. J. Williams, *Tetrahedron Lett.*, 2001, **42**, 4041-4043.

35. K. Murata, T. Ikariya and R. Noyori, *J. Org. Chem.*, 1999, **64**, 2186-2187.

36. X. Sun, G. Manos, J. Blacker, J. Martin and A. Gavriilidis, *Org. Process Res. Dev.*, 2004, **8**, 909-914.

37. Z. M. Heiden and T. B. Rauchfuss, *J. Am. Chem. Soc.*, 2009, **131**, 3593-3600.

38. C. Li, B. Villa-Marcos and J. Xiao, *J. Am. Chem. Soc.*, 2009, **131**, 6967-6969.

39. X. Wu, D. Vinci, T. Ikariya and J. Xiao, *Chem. Commun.*, 2005, 4447-4449.

40. W. Wang and Q. Wang, *Chem. Commun.*, 2010, **46**, 4616-4618.

41. X. Huang and J. Y. Ying, *Chem. Commun.*, 2007, 1825-1827.

42. C. M. Zammit and M. Wills, *Tetrahedron: Asymmetry*, 2013, **24**, 844-852.

43. G. Chelucci, S. Baldino and W. Baratta, *Acc. Chem. Res.*, 2015, **48**, 363-379.

44. W. Baratta, S. Baldino, M. J. Calhorda, P. J. Costa, G. Esposito, E. Herdtweck, S. Magnolia, C. Mealli, A. Messaoudi, S. A. Mason and L. F. Veiros, *Chem. Eur. J.*, 2014, **20**, 13603-13617.

45. W. Baratta, G. Bossi, E. Putignano and P. Rigo, *Chem. Eur. J.*, 2011, **17**, 3474-3481.

46. W. Baratta, F. Benedetti, A. Del Zotto, L. Fanfoni, F. Felluga, S. Magnolia, E. Putignano and P. Rigo, *Organometallics*, 2010, **29**, 3563-3570.

47. W. Baratta, M. Ballico, A. Del Zotto, K. Siega, S. Magnolia and P. Rigo, *Chem. Eur. J.*, 2008, **14**, 2557-2563.

48. A. Acosta-Ramirez, M. Bertoli, D. G. Gusev and M. Schlaf, *Green Chem.*, 2012, **14**, 1178-1188.

49. E. Putignano, G. Bossi, P. Rigo and W. Baratta, *Organometallics*, 2012, **31**, 1133-1142.

50. W. N. O Wylie, A. J. Lough and R. H. Morris, *Organometallics*, 2011, **30**, 1236-1252.

51. S. E. Clapham and R. H. Morris, *Organometallics*, 2005, **24**, 479-481.

52. R. Castarlenas, M. A. Esteruelas and E. Oñate, *Organometallics*, 2008, **27**, 3240-3247.

53. J. W. Faller and A. R. Lavoie, *Organometallics*, 2002, **21**, 3493-3495.

54. J. W. Faller and A. R. Lavoie, *Org. Lett.*, 2001, **3**, 3703-3706.

55. D. Carmona, F. J. Lahoz, P. García-Orduña, L. A. Oro, M. P. Lamata and F. Viguri, *Organometallics*, 2012, **31**, 3333-3345.

56. Y. Fu, R. Soni, M. J. Romero, A. M. Pizarro, L. Salassa, G. J. Clarkson, J. M. Hearn, A. Habtemariam, M. Wills and P. J. Sadler, *Chem. Eur. J.*, 2013, **19**, 15199-15209.

57. E. Vega, E. Lastra and M. P. Gamasa, *Inorg. Chem.*, 2013, **52**, 6193-6198.

58. C. Schlünken, Miguel A. Esteruelas, Fernando J. Lahoz, Luis A. Oro and H. Werner, *Eur. J. Inorg. Chem.*, 2004, **2004**, 2477-2487.

59. M. Rosales, J. Castillo, A. González, L. González, K. Molina, J. Navarro, I. Pacheco and H. Pérez, *Transit. Metal Chem.*, 2004, **29**, 221-228.

60. G. Chelucci, G. A. Pinna, G. Pinna, M. Solinas and B. Sechi, *Chinese J. Catal.*, 2016, **37**, 1824-1836.

61. D. Spasyuk, S. Smith and D. G. Gusev, *Angew. Chem. Int. Ed.*, 2012, **51**, 2772-2775.

62. G. Chelucci, *Coord. Chem. Rev.*, 2017, **331**, 1-36.

63. J. D. Pennington, T. J. C. Wang, P. Nguyen, L. Sun, K. Bisht, D. Smart and D. Gius, *Drug Resist. Update*, 2005, **8**, 322-330.

64. C. Corti and R. Holliday, *Gold: Science and Applications*, CRC Press, 2009.

65. F. Darabi, T. Marzo, L. Massai, F. Scaletti, E. Michelucci and L. Messori, *J. Inorg. Biochem.*, 2015, **149**, 102-107.

66. X. Cheng, P. Holenya, S. Can, H. Alborzinia, R. Rubbiani, I. Ott and S. Wölfl, *Mol. Cancer*, 2014, **13**, 221.

67. W. K. Jung, H. C. Koo, K. W. Kim, S. Shin, S. H. Kim and Y. H. Park, *Appl. Environ. Microbiol.*, 2008, **74**, 2171-2178.

68. D. J. Barillo and D. E. Marx, *Burns*, 2014, **40**, S3-S8.

69. C. Santini, M. Pellei, G. Papini, B. Morresi, R. Galassi, S. Ricci, F. Tisato, M. Porchia, M. P. Rigobello, V. Gandin and C. Marzano, *J. Inorg. Biochem.*, 2011, **105**, 232-240.

70. K. J. Williams, *J. R. Soc. Med.*, 2009, **102**, 343-348.

71. N. C. Lloyd, H. W. Morgan, B. K. Nicholson and R. S. Ronimus, *Angew. Chem. Int. Ed.*, 2005, **44**, 941-944.

72. B. Rosenberg, L. Vancamp, J. E. Trosko and V. H. Mansour, *Nature*, 1969, **222**, 385-386.

73. L. Kelland, *Nat. Rev. Cancer*, 2007, **7**, 573-584.

74. A. M. Florea and D. Büsselberg, *Cancers*, 2011, **3**, 1351-1357.

75. C. Andreadis, K. Vahtsevanos, T. Sidiras, I. Thomaidis, K. Antoniadis and D. Mouratidou, *Oral Oncol.*, 2003, **39**, 380-385.

76. S. Dasari and P. Bernard Tchounwou, *Eur. J. Pharmacol.*, 2014, **740**, 364-378.

77. Z. Ai, Y. Lu, S. Qiu and Z. Fan, *Cancer Lett.*, 2016, **373**, 36-44.

78. D.-W. Shen, L. M. Pouliot, M. D. Hall and M. M. Gottesman, *Pharmacol. Rev.*, 2012, **64**, 706-721.

79. R. J. Parker, A. Eastman, F. Bostick-Bruton and E. Reed, *J. Clin. Invest.*, 1991, **87**, 772-777.

80. U.-M. Ohndorf, M. A. Rould, Q. He, C. O. Pabo and S. J. Lippard, *Nature*, 1999, **399**, 708-712.

81. A. Sharma, A. Ramanjaneyulu, R. Ruma and M. R. Rajeswari, *DNA Cell Biol.*, 2009, **28**, 311-318.

82. C. S. Allardyce and P. J. Dyson, *Dalton Trans.*, 2016, **45**, 3201-3209.

83. U. Ndagi, N. Mhlongo and M. E. Soliman, *Drug Des. Devel. Ther.*, 2017, **11**, 599-616.

84. H. H. W. Chen and M. T. Kuo, *Met. Based Drugs*, 2010, **2010**, 430939.

85. P. V. Korita, T. Wakai, Y. Shirai, Y. Matsuda, J. Sakata, M. Takamura, M. Yano, A. Sanpei, Y. Aoyagi, K. Hatakeyama and Y. Ajioka, *Oncol. Rep.*, 2010, **23**, 965-972.

86. B. Alberts, A. Johnson, . and J. Lewis, *Molecular Biology of the Cell. 4th edition.*, Garland Science, New York, 2002.

87. J. Graham, M. Muhsin and P. Kirkpatrick, *Nat. Rev. Drug Discov.*, 2004, **3**, 11-12.

88. T. Boulikas, A. Pantos, E. Bellis and P. Christofis, *Cancer Therapy*, 2007, **5**, 537-583.

89. G. K. Gransbury, P. Kappen, C. J. Glover, J. N. Hughes, A. Levina, P. A. Lay, I. F. Musgrave and H. H. Harris, *Metallomics*, 2016, **8**, 762-773.

90. L. S. Flocke, R. Trondl, M. A. Jakupec and B. K. Keppler, *Investigat. New Drugs*, 2016, **34**, 261-268.

91. R. Trondl, P. Heffeter, C. R. Kowol, M. A. Jakupec, W. Berger and B. K. Keppler, *Chem. Sci.*, 2014, **5**, 2925-2932.

92. A. Maillet, S. Yadav, Y. L. Loo, K. Sachaphibulkij and S. Pervaiz, *Cell Death Dis.*, 2013, **4**, e653.

93. S. J. Dougan, A. Habtemariam, S. E. McHale, S. Parsons and P. J. Sadler, *Proc. Natl. Acad. Sci. U. S. A.*, 2008, **105**, 11628-11633.

94. W. Kandioller, E. Balsano, S. M. Meier, U. Jungwirth, S. Goschl, A. Roller, M. A. Jakupec, W. Berger, B. K. Keppler and C. G. Hartinger, *Chem. Commun.*, 2013, **49**, 3348-3350.

95. K. K. Kim, R. K. Singh, R. M. Strongin, R. G. Moore, L. Brard and T. S. Lange, *PLOS ONE*, 2011, **6**, e19049.

96. G. E. Buchel, S. Kossatz, A. Sadique, P. Rapta, M. Zalibera, L. Bucinsky, S. Komorovsky, J. Telser, J. Eppinger, T. Reiner and V. Arion, *Dalton Trans.*, 2017, **46**, 11925-11941.

97. P.-S. Kuhn, G. E. Büchel, K. K. Jovanović, L. Filipović, S. Radulović, P. Rapta and V. B. Arion, *Inorg. Chem.*, 2014, **53**, 11130-11139.

98. S. Leijen, S. A. Burgers, P. Baas, D. Pluim, M. Tibben, E. van Werkhoven, E. Alessio, G. Sava, J. H. Beijnen and J. H. M. Schellens, *Invest. New Drug*, 2015, **33**, 201-214.

99. M. Bacac, A. C. G. Hotze, K. v. d. Schilden, J. G. Haasnoot, S. Pacor, E. Alessio, G. Sava and J. Reedijk, *J. Inorg. Biochem.*, 2004, **98**, 402-412.

100. G. Sava, S. Zorzet, C. Turrin, F. Vita, M. Soranzo, G. Zabucchi, M. Cocchietto, A. Bergamo, S. DiGiovine, G. Pezzoni, L. Sartor and S. Garbisa, *Clin. Cancer. Res.*, 2003, **9**, 1898-1905.

101. B. Cebrián-Losantos, A. A. Krokhin, I. N. Stepanenko, R. Eichinger, M. A. Jakupec, V. B. Arion and B. K. Keppler, *Inorg. Chem.*, 2007, **46**, 5023-5033.

102. L. Zhang, P. Carroll and E. Meggers, *Org. Lett.*, 2004, **6**, 521-523.

103. T. J. Kealy and P. L. Pauson, *Nature*, 1951, **168**, 1039-1040.

104. H. Z. S. Lee, O. Buriez, F. Chau, E. Labbé, R. Ganguly, C. Amatore, G. Jaouen, A. Vessières, W. K. Leong and S. Top, *Eur. J. Inorg. Chem.*, 2015, **2015**, 4217-4226.

105. A. Bergamo, A. Masi, A. F. A. Peacock, A. Habtemariam, P. J. Sadler and G. Sava, *J. Inorg. Biochem.*, 2010, **104**, 79-86.

106. Y. Fu, M. J. Romero, A. Habtemariam, M. E. Snowden, L. Song, G. J. Clarkson, B. Qamar, A. M. Pizarro, P. R. Unwin and P. J. Sadler, *Chem. Sci.*, 2012, **3**, 2485-2494.

107. I. Romero-Canelón, L. Salassa and P. J. Sadler, *J. Med. Chem.*, 2013, **56**, 1291-1300.

108. S. D. Shnyder, Y. Fu, A. Habtemariam, S. H. van Rijt, P. A. Cooper, P. M. Loadman and P. J. Sadler, *Med. Chem. Comm.*, 2011, **2**, 666-668.

109. *Ovarian Cancer Statistics*, Cancer Research UK, 2014.

110. A. Jemal, F. Bray, M. Center, J. Ferlay, E. Ward and D. Forman, *CA-Cancer J. Clin.*, 2011, **61**, 69-90.

111. A. S. Ahmad, N. Ormiston-Smith and P. D. Sasieni, *Br. J. Cancer*, 2015, **112**, 943-947.

112. R. K. Murray, D. K. Granner, P. A. Mayes and V. W. Rodwell, *Harper's Biochemistry*, McGaw-Hill Medical, 25th edn., 2000.

113. D. Hanahan and R. Weinberg, *Cell*, 2011, **144**, 646-674.

114. H. Chial, *Nature Education*, 2008, **1**, 33.

115. M. Hollstein, D. Sidransky, B. Vogelstein and C. Harris, *Science*, 1991, **253**, 49-53.

116. B. Vogelstein, D. Lane and A. J. Levine, *Nature*, 2000, **408**, 307-310.

117. A. J. Levine and M. Oren, *Nat. Rev. Cancer*, 2009, **9**, 749-758.

118. J. M. Brown, in *Methods Enzymol.*, Academic Press, 2007, vol. 435, pp. 297–321.

119. Y. Kato, S. Ozawa, C. Miyamoto, Y. Maehata, A. Suzuki, T. Maeda and Y. Baba, *Cancer Cell Int.*, 2013, **13**, 89-89.

120. W. A. Denny, *Curr. Med. Chem. Anticancer Agents*, 2004, **4**, 395-399.

121. W. R. Wilson and M. P. Hay, *Nat. Rev. Cancer*, 2011, **11**, 393-410.

122. Y. Zhao, E. B. Butler and M. Tan, *Cell Death Dis.*, 2013, **4**, e532.

123. O. Warburg, *Science*, 1956, **123**, 309-314.

124. H. Pelicano, D. S. Martin, R. H. Xu and P. Huang, *Oncogene*, 2006, **25**, 4633-4646.

125. M. V. Liberti and J. W. Locasale, *Trends Biochem. Sci.*, 2016, **41**, 211-218.

126. I. Romero-Canelón, M. Mos and P. J. Sadler, *J. Med. Chem.*, 2015, **58**, 7874-7880.

127. I. Romero-Canelón and P. J. Sadler, *Inorg. Chem.*, 2013, **52**, 12276-12291.

128. E. Pérez-Herrero and A. Fernández-Medarde, *Eur. J. Pharm. Biopharm.*, 2015, **93**, 52-79.

129. J. J. Soldevila-Barreda, I. Romero-Canelón, A. Habtemariam and P. J. Sadler, *Nat. Commun.*, 2015, **6**, 6582.

130. E. Borcoman and C. Le Tourneau, *Curr. Opin. Oncol.*, 2016, **28**, 429-436.

131. S. Gross, R. Rahal, N. Stransky, C. Lengauer and K. P. Hoeflich, *J. Clin. Invest.*, 2015, **125**, 1780-1789.

132. K. Ghoreschi, A. Laurence and J. J. O'Shea, *Nat. Immunol.*, 2009, **10**, 356-360.

133. J. Vikas, J. Shikha and S. C. Mahajan, *Curr. Drug Deliv.*, 2015, **12**, 177-191.

134. E. O. Hileman, J. Liu, M. Albitar, M. J. Keating and P. Huang, *Cancer Chemother. Pharmacol.*, 2004, **53**, 209-219.

135. C. Perera-Bobusch, J. Hormann, C. Weise, S. Wedepohl, J. Dernedde and N. Kulak, *Dalton Trans.*, 2016, **45**, 10500-10504.

136. R. M. Yusop, A. Unciti-Broceta, E. M. V. Johansson, R. M. Sánchez-Martín and M. Bradley, *Nat. Chem.*, 2011, **3**, 239-243.

137. T. Völker, F. Dempwolff, P. L. Graumann and E. Meggers, *Angew. Chem. Int. Ed.*, 2014, **53**, 10536-10540.

138. M. Tomás-Gamasa, M. Martínez-Calvo, J. R. Couceiro and J. L. Mascareñas, *Nat. Commun.*, 2016, **7**, 12538.

139. Z. Liu, I. Romero-Canelón, B. Qamar, J. M. Hearn, A. Habtemariam, N. P. E. Barry, A. M. Pizarro, G. J. Clarkson and P. J. Sadler, *Angew. Chem. Int. Ed.*, 2014, **53**, 3941-3946.

140. U. Jungwirth, C. R. Kowol, B. K. Keppler, C. G. Hartinger, W. Berger and P. Heffeter, *Antioxid. Redox Signal.*, 2011, **15**, 1085-1127.

141. A. Casini, C. Gabbiani, F. Sorrentino, M. P. Rigobello, A. Bindoli, T. J. Geldbach, A. Marrone, N. Re, C. G. Hartinger, P. J. Dyson and L. Messori, *J. Med. Chem.*, 2008, **51**, 6773-6781.

142. A. J. Millett, A. Habtemariam, I. Romero-Canelón, G. J. Clarkson and P. J. Sadler, *Organometallics*, 2015, **34**, 2683-2694.

143. S. Betanzos-Lara, Z. Liu, A. Habtemariam, A. M. Pizarro, B. Qamar and P. J. Sadler, *Angew. Chem. Int. Ed.*, 2012, **51**, 3897-3900.

144. S. Goldstein, G. Czapski and A. Heller, *Free Radical Bio. Med.*, 2005, **38**, 839-845.

145. A. Tovmasyan, S. Carballal, R. Ghazaryan, L. Melikyan, T. Weitner, C. G. C. Maia, J. S. Reboucas, R. Radi, I. Spasojevic, L. Benov and I. Batinic-Haberle, *Inorg. Chem.*, 2014, **53**, 11467-11483.

146. I. Batinić-Haberle, J. S. Rebouças and I. Spasojević, *Antioxid. Redox Signal.*, 2010, **13**, 877-918.

147. O. Iranzo, *Bioorg. Chem.*, 2011, **39**, 73-87.

148. S. Miriyala, I. Spasojevic, A. Tovmasyan, D. Salvemini, Z. Vujaskovic, D. St. Clair and I. Batinic-Haberle, *Biochim. Biophys. Acta.*, 2012, **1822**, 794-814.

149. Y. Maenaka, T. Suenobu and S. Fukuzumi, *J. Am. Chem. Soc.*, 2012, **134**, 367-374.

150. J. Canivet, G. Süss-Fink and P. Štěpnička, *Eur. J. Inorg. Chem.*, 2007, **2007**, 4736-4742.

151. Y. Okamoto, V. Köhler, C. E. Paul, F. Hollmann and T. R. Ward, *ACS Catal.*, 2016, **6**, 3553-3557.

152. J. J. Soldevila-Barreda, P. C. A. Bruijnincx, A. Habtemariam, G. J. Clarkson, R. J. Deeth and P. J. Sadler, *Organometallics*, 2012, **31**, 5958-5967.

153. Y. Fu, C. Sanchez-Cano, R. Soni, I. Romero-Canelon, J. M. Hearn, Z. Liu, M. Wills and P. J. Sadler, *Dalton Trans.*, 2016, **45**, 8367-8378.

154. J. J. Soldevila-Barreda, A. Habtemariam, I. Romero-Canelón and P. J. Sadler, *J. Inorg. Biochem.*, 2015, **153**, 322-333.

Chapter 2

Materials, methods and instrumentation

2. Materials, methods and instrumentation

2.1 Materials

Osmium trichloride hydrate was purchased from Heraeus. Iridium trichloride hydrate was purchased from Precious Metals Online. Potassium hydroxide, magnesium sulphate and all non-dried solvents were obtained from Fischer Scientific. (1*R*,2*R*) and (1*S*,2*S*)-1,2-diphenylethylenediamine were purchased as optically pure compounds from Arran Chemical Company Ltd (Ireland). Reduced precursors (1,4-dihydro-biphenyl and 1,4-dihydro-*m*-terphenyl) were kindly provided by Khatija Bhayat, Dr. Russell Needham and Dr. Abraha Habtemariam (University of Warwick, UK). Deuterated solvents were purchased from Goss Scientific.

Reagents for biological experiments: acetic acid, CDDP (cisplatin), DMSO, sulforhodamine B and trichloroacetic acid were purchased from Sigma Aldrich as biological-grade reagents.

ICP standards for Os (hexachlorodiammonium osmate, 1000 ± 10 µg/mL in 15% v/v hydrochloric acid), Ru (ruthenium chloride, 1004 ± 5 µg/mL in 10% v/v hydrochloric acid), Ir (iridium chloride, 995 ± 4 µg/mL in 10% v/v hydrochloric acid) and Pt (TraceCERT® platinum, 1001 ± 2 mg/L in 5% w/w hydrochloric acid) were purchased from Inorganic Ventures and stored at 276 K. Sodium chloride (TraceSELECT®), thiourea (puriss) and ascorbic acid (BioXtra) were used for ICP experiments. Nitric acid (72% v/v) was freshly distilled and diluted with doubly deionized milliQ water (18.2 MΩ·cm at 298 K) to achieve a working concentration of 3.6% v/v.

All other reagents and solvents were purchased from Sigma Aldrich and used as received, unless specified otherwise.

2.1.1 Metal salt aquation analysis

A standard solutions of osmium trichloride was prepared (1 mM) assuming an anhydrous molecular weight, in 3.6% v/v nitric acid containing thiourea (10 mM) and ascorbic acid (100 mg/L). The stock solution was diluted in triplicate to achieve final working concentrations appropriate for ICP-OES analysis (*ca*. 300 ppb Os). The determined concentration of the solution was used to solve for *n* (the water of crystallisation), determined to be $n = 2.71$ (≈ 3).

2.1.2 Synthesis of dimer precursors

Osmium dimer precursors were synthesised following an adapted literature procedure for microwave synthesis of similar (Ru / Ir / Rh) metal dimer complexes.[1] All dimers were characterised by NMR and ESI-MS, and data matches previously reported results. Chain-extended iridium dimer compounds **$[Ir(Cp^{xPh})Cl_2]_2$** and **$[Ir(Cp^{xBip})Cl_2]_2$** (Figure 2.1) were kindly provided by Dr. Abraha Habtemariam.

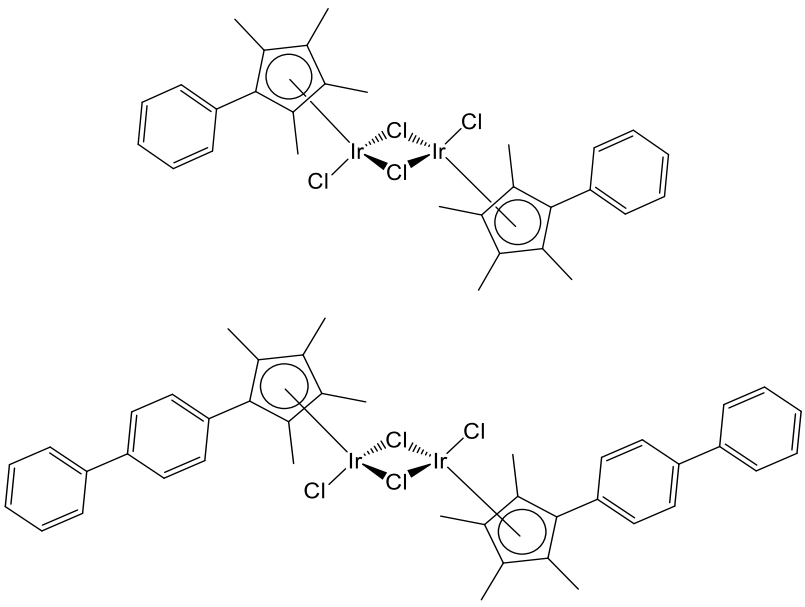

Figure 2.1. Chain-extended iridium dimer compounds $[Ir(Cp^{xPh})Cl_2]_2$ and $[Ir(Cp^{xBip})Cl_2]_2$.

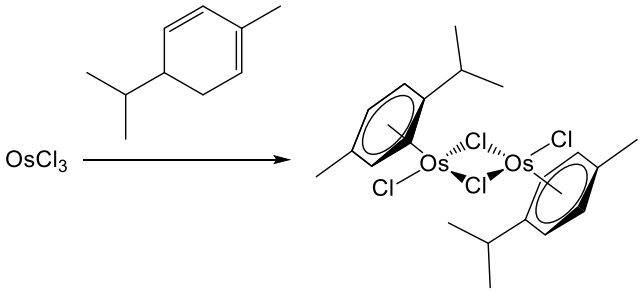

[Os(η^6-*p*-cymene)Cl$_2$]$_2$.[2] Osmium trichloride trihydrate (1.00 g, 2.8 mmol) was dissolved in degassed methanol (10 mL). To this was added α-phellandrene (3.8 g, 28 mmol) with stirring. The reaction vessel was placed in a CEM Discovery-SP microwave reactor for 10 min (413 K, 150 W, 250 psi). An orange solid precipitate was observed, which was washed with n-pentane (3 × 10 mL). The solid was washed with diethyl ether yielding a bright orange crystalline solid (863 mg, 1.1 mmol, 79%). ^{1}H NMR (300 MHz, $CDCl_3$, 25°C, TMS): δ=6.18 (d, 4H, ^3J(H,H)=5.0 Hz; Os-ArH), 6.02 (d, 4H, ^3J(H,H)=5.0 Hz; Os-ArH), 2.78 (sept, 2H, ^3J(H,H)=6.8 Hz; C*H*$(CH_3)_2$), 2.21 (s, 6H; Ar-CH_3), 1.29 (d, 12H, ^3J(H,H)=6.8 Hz; CH(C*H*$_3)_2$).

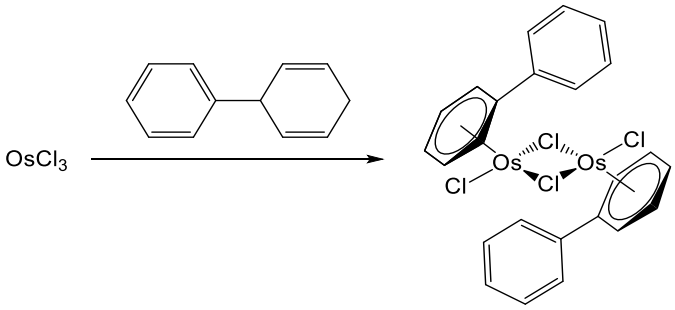

[Os(η^6-biphenyl)Cl$_2$]$_2$. The synthesis was carried out as described for the osmium *p*-cymene dimer using 3-phenyl-cyclohexa-1,4-diene (1.56 g, 10 mmol) in place of α-phellandrene. The solid was washed with n-pentane followed by diethyl ether to obtain the product as a dark orange amorphous solid (936 mg, 1.3 mmol, 81%). ^{1}H NMR (400 MHz, $CDCl_3$, 25°C, TMS): δ=7.69 (m, 4H; ArH), 7.47 (m, 6H; ArH), 7.29 (m, 2H; ArH) 6.65 (m, 2H; ArH), 6.32 (m, 6H; ArH).

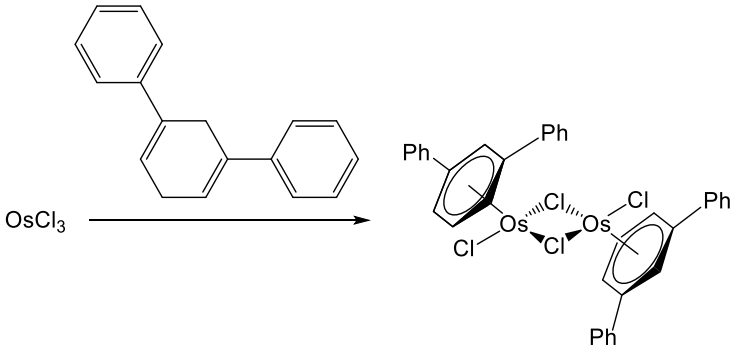

[Os(η^6-*m*-terphenyl)Cl$_2$]$_2$. To a solution of osmium trichloride trihydrate (287 mg, 0.82 mmol) in freshly distilled ethanol (20 mL) was added 1,5-dihydroterphenyl (dh-*m*-terp, 570 mg, kindly prepared by Dr. Abraha Habtemariam by Birch reduction of *m*-terphenyl). The reaction mixture was heated under reflux for 24 h under a nitrogen atmosphere. A brown precipitate was observed upon cooling. The solid was collected by filtration, before washing with ethanol (25 mL) and diethyl ether (5 × 25 mL). The product was obtained by Buchner filtration as a light brown amorphous solid (173 mg, 0.18 mmol, 22%). ^{1}H NMR (400 MHz, $CDCl_3$, 25°C, TMS): δ=7.11-7.49 (m, 20H; ArH), 6.16 (m, 2H; Os-ArH), 5.97 (m, 2H; Os-ArH), 5.82 (m, 2H; Os-ArH), 4.16 (m, 2H; Os-ArH).

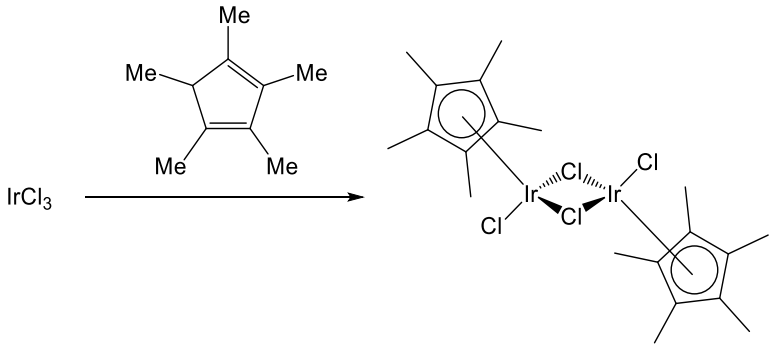

[Ir(Cp*)Cl$_2$]$_2$. This compound was synthesised following a known literature procedure.[1] Iridium trichloride trihydrate (0.5 g, 1.38 mmol) was dissolved in methanol (10 mL) that had been sonicated and de-gassed. The solution was stirred

vigorously to ensure the solid had fully dissolved. To this was then added 1,2,3,4,5-pentamethylcyclopentadiene (0.67 mL, 4.27 mmol) with stirring. The reaction vessel was placed in a CEM Discovery-SP microwave reactor for 5 min (413 K, 150 W, 250 psi) after which a precipitate of a crystalline red solid was observed. The reaction solution was cooled to ambient temperature (298 K) before washing with n-pentane (3 × 10 mL). The precipitated solid was collected and washed further with diethyl ether to yield the product as a crystalline red solid. ^{1}H NMR (300 MHz, $CDCl_3$, 25°C, TMS): δ=1.59 (s, 30H; CH_3).

2.2 Instrumentation

2.2.1 Nuclear magnetic resonance spectroscopy (NMR)

Samples were prepared in $CDCl_3$ (0.05% v/v TMS) unless stated otherwise. 5 mm NMR tubes were used to record spectra at 298 K (unless specified) on Bruker DPX-400, HD-500, or AV-600 spectrometers. Data were acquired using standard pulse sequences, and chemical shifts referenced to residual solvent(s): $CHCl_3$ (δ=7.26 ppm), C_6H_6 (δ=7.16 ppm), $(CH_3)_2SO$ (δ=2.50 ppm), 1,4-dioxane (3.71 ppm in H_2O) or $(CH_3)_2CO$ (δ=2.05 ppm). Data were processed using TOPSPIN 3.2 (Bruker UK). Experiments in aqueous solution (90% H_2O / 10% D_2O) were carried out using WATERGATE (water suppression by gradient-tailored excitation) pulse sequences for solvent suppression (zggpw5) with five pairs of symmetric pulses (W5),[3] 128 scans into 32k data points over a spectral width of 10 ppm.

2.2.2 Electronic absorption spectroscopy (UV-Vis)

Electronic absorption spectra were recorded using a Varian Cary 300 Bio scan spectrophotometer fitted with a PTP1 Peltier temperature controller. Data were recorded using quartz cuvettes (600 μL) at 298 K unless specified otherwise. Path-length of cell 1 cm, range 800-200 nm, average time 0.1 s, data interval 1 nm; scan rate 600 nm min^{-1}. Data were processed using Winlab UV software for Windows.

2.2.3 Elemental analysis

Elemental analysis (C, H, N) was carried out by Warwick Analytical Services UK on an Exeter elemental analyser CE440.

2.2.4 Mass spectrometry

Low resolution ESI-MS spectra were obtained using an Agilent 6130B ESI mass spectrometer. Samples were prepared in acetonitrile. Fragments were detected using a positive ion scan range of either *m*/*z* 400-1000 or *m*/*z* 50-500. High resolution mass spectra were obtained by Dr. Lijiang Song and Mr. Phil Aston using a Bruker UHR-Q-TOF MaXis, with a positive ion scan range of *m/z* 50-3000 (spectra rate of 1 Hz). Analysis was carried out through direct infusion (2 µL/min) with a syringe pump, with sodium formate (10 mM) calibration. Source conditions: ESI (+); end plate offset: -500 V; capillary: -3000 V; nebulizer gas (N2): 0.4 bar; dry gas (N2): 4 L/min; dry temperature: 453 K; funnel RF: 200 Vpp; multiple RF: 200Vpp; quadruple low mass: 55 *m/z*; collision energy: 5.0 eV; collision RF: 600 Vpp; ion cooler RF: 50-250 Vpp ramping; transfer time: 121 µs; pre-pulse storage time: 1 µs.

2.2.5 ATR Fourier-transform infrared (FTIR) spectroscopy

Attenuated total reflection ATR-FTIR spectra were acquired on a Bruker Alpha Platinum ATR. Range: 4000-400 cm^{-1}; Spectral resolution: 4 cm^{-1} using 16 interferograms. Data were acquired using OPUS software 7.0.

2.2.6 Gas chromatography (GC)

Gas chromatography was carried out with kind assistance from Dr Roy Hodgkinson (University of Warwick, UK) using either a Chrompac cyclodextrin-β-236M-19, 50 m x 0.25 mm x 0.25 µm, or a Chrompac-chirasil-DEX CB, 25 m x 0.25 mm x 0.25 µm, T = 383 K. The carrier gas was H_2 or He, P = 18 psi. Data were processed using Clarity Chromatography Suite for Windows.

2.2.7 X-ray crystallography

X-ray crystallographic data were acquired by Dr. Guy Clarkson (University of Warwick). A suitable crystal was selected and mounted on a glass fibre with Fromblin oil and placed on an Oxford Diffraction Gemini diffractometer with a Ruby CCD area detector at 150(2) K during data collection. Using Olex2,[4] the structure was solved with the ShelXS[5] structure solution program using Direct Methods and refined with the ShelXL[5] refinement package using Least Squares minimisation. The enantiopure complexes were synthesised from starting materials of known chirality and also gave low Flack parameter values for the structural determinations refined using BASF/TWIN in Shelx2014. Data were analysed and visualised using Mercury 3.3.

2.2.8 Inductively coupled plasma spectroscopy (ICP)

ICP techniques were used to determine trace metal concentration(s) in aqueous solutions. For osmium analysis, solutions were supplemented with thiourea (10 mM) and ascorbic acid (100 mg/L) to stabilise osmium in nitric acid solution and prevent formation of osmium tetroxide, known to have a higher nebulizing efficiency.[6] The standard addition of thiourea and ascorbic acid was not found to affect calibrations of iridium, platinum or ruthenium.

Inductively-coupled plasma optical emission spectroscopy. ICP-OES data for Os (λ = 225.585, 228.226), Ir (λ = 208.882, 237.277), Ru (λ = 240.272, 349.894) and Pt (λ = 265.945, 204.937) were obtained using a Perkin Elmer Optima 5300 DV Optical Emission Spectrophotometer. Total dissolved solids did not exceed 0.2 % w/v. Calibration standards were freshly prepared (50-700 ppb) in 3.6% v/v nitric acid and

samples diluted to within this range. The salinity of the calibration standards and calibration blanks was adjusted to match the matrix of the samples by standard addition of sodium chloride solution. Data were acquired and processed using WinLab32 V3.4.1 for Windows.

Inductively-coupled plasma mass spectrometry. ICP-MS data for ^{189}Os, ^{193}Ir, ^{101}Ru and ^{195}Pt were obtained using an ICP-MS Agilent Technologies 7500 series in no-gas mode. Data acquisition was carried out using ICP-MS TOP with an internal standard of ^{166}Er (50 ppb), and processing was carried out using Offline Data Analysis (ChemStation version B.03.05, Agilent Technologies, Inc.). Total dissolved solids did not exceed 0.1 % w/v. Calibration standards were freshly prepared (0.1-1000 ppb) in 3.6% v/v nitric acid and samples diluted to within this range.

2.2.9 Flow Cytometry

Flow cytometry data were acquired using a Becton Dickinson FACScan Flow Cytometer (School of Life Sciences, University of Warwick, UK). Voltages, amplitude gains, and compensation were set using negative and positive control experiments. Sample preparation is described for individual experiments. Data were processed using FlowJo V10 for Windows.

2.3 Methods

2.3.1 Transfer hydrogenation kinetics

Transfer hydrogenation kinetics were calculated based on previously reported methods.[7] Samples of compounds were prepared in formic acid : triethylamine azeotrope (5:2 v/v) with standard addition of 100 μL C_6D_6. Samples were placed under an inert nitrogen atmosphere at 310 K. A substrate molecule of choice was added with stirring and the mixture transferred to a 5 mm NMR tube. Proton NMR spectra were recorded every 73 s at 310 ± 0.5 K (for 1 h) using a Bruker AV-400 spectrometer. Data processing was carried out using TOPSPIN version 3.2 (Bruker UK). Experiments were performed in triplicate. Conversion was monitored by two integration regions: (the methyl protons (3H) in the reagent (δ = 2.25-2.65 ppm) and the quartet of the newly formed CH in the product (δ = 4.55-5.00 ppm). Triethylamine (2.9 ppm, quartet) did not overlap either of the integration regions.

The turnover number at any time-point (TON_t; moles of substrate turned over per mole of catalyst at time, t) , was calculated for each spectrum and percentage conversion was calculated using the formulae:

$$\text{conversion} = 100 - \left(\frac{\frac{I_{2.25-2.65}}{3}}{I_{4.55-5.00} + \frac{I_{2.25-2.65}}{3}} \times 100\% \right)$$

$$\text{TON}_t = \frac{[\text{conversion}]_t}{100} \cdot \frac{[\text{substrate}]_0}{[\text{catalyst}]} = \frac{\delta[\text{TON}]_t}{\delta t}$$

The maximum turnover frequency (TOF_{max}) was calculated using the initial rate of reaction (t = 0 h) at which the gradient of a TON vs. time plot was at a maximum.

2.3.2 Biological studies (*in vitro* cell culture)

Human cell culture experiments were carried out under the guidance of Dr. Isolda Romero-Canelón with assistance from Dr. Anthony Knight, Mrs. Ji-Inn Song, Mrs. Sukhbinder Heer and Mrs. Hannah E. Bridgewater at the School of Life Sciences and Department of Engineering, University of Warwick.[8]

A2780, SK-OV-3 and SW-626 human ovarian carcinomas, A2780cis cisplatin-resistant human ovarian carcinoma, A549 human lung carcinoma, HCT116 human colorectal carcinoma, HCT116-p21-/- *P21*-knockout colorectal carcinoma, HCT116-p53-/- *P53*-knockout colorectal carcinoma, HEPG2 human hepatocellular carcinoma, OE19 human esophageal carcinoma, MCF7 human breast adenocarcinoma, MRC5 human fetal fibroblasts, and PC3 human prostate carcinoma cells were purchased from the European Collection of Cell Cultures (ECACC). HOF human ovarian fibroblasts were purchased from ScienCell. Mycoplasma-free status was confirmed every 6 months by Public Health England. Cell culture media (RPMI-1640, DMEM, McCoy 5A), phosphate buffered saline, L-glutamine, penicillin / streptomycin, fetal bovine serum and trypsin / EDTA were purchased from PAA Laboratories and kindly prepared by technicians at the School of Life Sciences (University of Warwick, UK). RPMI-1640 media (without phenol red) and phosphate buffered saline were purchased from Lonza. Fibroblast medium was purchased from ScienCell Research Laboratories.

Cell maintenance: Defrosting

Ampoule(s) were rapidly defrosted in a water bath (310 K). Cells were transferred to falcon tubes and centrifuged (5 min, 1000 rpm, 295 K) to remove supernatant freezing medium. Pellets were re-suspended in media (5 mL) and transferred to a T25 flask.

Cell maintenance: Passaging

A2780, MRC5 and PC3 cells were grown in Roswell Park Memorial Institute medium (RPMI-1640) supplemented with 10% fetal bovine serum, 1% glutamine (2 mM) and 1% penicillin / streptomycin. A549, HEPG2 and MCF7 cells were grown in Dulbecco's Modified Eagle medium (DMEM) supplemented with 10% fetal bovine serum, 1% glutamine (2 mM) and 1% penicillin / streptomycin. HCT116 cells were grown in McCoy's Modified 5A medium supplemented with 10% fetal bovine serum, 1% glutamine (2 mM) and 1% penicillin / streptomycin. HOF cells were grown in fibroblast growth medium supplemented with 5% fetal bovine serum, 1% penicillin / streptomycin and 1% fibroblast growth factor serum.

Cells were grown as adherent monolayers in 75 cm^2 culture flasks (surface-treated, fitted with filters) at 310 K in a 5% CO_2 humidified atmosphere until 80-90% confluence was achieved.

Upon reaching 80-90% confluence, cells were washed with PBS (5 mL). 0.25% trypsin / EDTA (2 mL) was added, and the flask was placed in an incubator (310 K) for 3-5 min. Once cells were observed to be detaching from the bottom of the flask, the solution was diluted with the corresponding medium to obtain a single cell suspension. A suitable volume (typically 1:4) was transferred into a T75 (75 cm^2) cell culture flask containing fresh media and placed in an incubator (310 K).

When passaging HOF fibroblasts, trypsin / EDTA activity was quenched with foetal bovine serum (FBS: 5 ml, 5 min). The supernatant containing trypsin was removed after centrifugation (5 min, 1000 rpm, 295 K) and the pellet re-suspended in (supplemented) fibroblast growth medium. Primary cell lines (MRC5 and HOF) were not used after passage 5 due to cells entering senescence.

Sulforhodamine B (SRB) colorimetric assay

The sulforhodamine B (SRB) assay can be used to determine cell density based on the protein concentration per sample.[9] Sulforhodamine B (Figure 2.2) electrostatically binds basic amino acid residues present in viable cells under mild acidic conditions. Release under mild basic conditions is quantitative, and dye absorbance is linear with protein concentration.[9]

An alternative assay, the MTT assay (MTT = 3-(4,5)-dimethylthiazol-2-yl)-2,5-diphenyltetrazolium bromide), quantifies the number of viable cells by reducing colourless MTT into a dark blue (formazan) species, requiring metabolic processes in live cells.[9, 10] Similarly to the SRB assay, the production of formazan is linear with the number of cells.[10] Because of the metabolic dependence, the MTT assay can distinguish between live and dead cells,[10] unlike the SRB assay.[9] Reduction of MTT may however be influenced by certain reagents, and requires optimisation for some cell lines due to the metabolic dependence.[9] Conversely, the SRB assay has been found to provide better linearity and sensitivity, and is compatible with a range of cell lines, including those investigated in this thesis.[11]

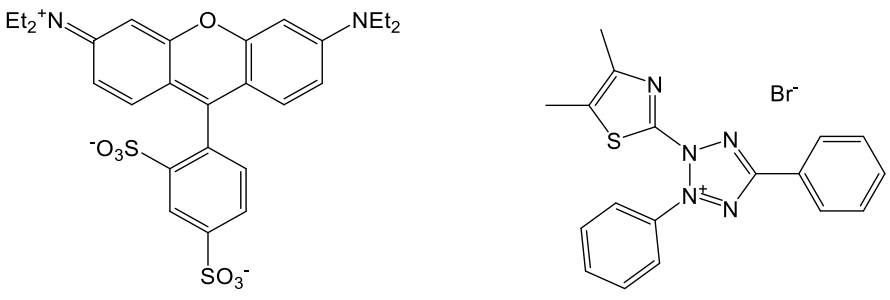

Figure 2.2. Colorimetric cell assay dyes: sulforhodamine B (left) and MTT (right).

In vitro growth inhibition assay

Cells were washed with PBS and detached using 2 mM trypsin / EDTA (2 mL) with incubation for 5 min (310 K). A single cell suspension was obtained, and counted using a haemocytometer. The suspension was diluted to seed a 96-well plate with 5000 cells per well using 150 µL (with the exception of SK-OV3 which were seeded at a density of 10'000 cells per well using 150 µL) which were left to incubate in drug-free media for 48 h (310 K). 100 µM drug stock solutions were prepared (0.5% DMSO, 95% culture medium). Serial dilutions were performed to prepare 6 drug concentrations (typically 0.01-100 µM). Solutions (200 µL) were added to the wells in triplicate, alongside positive (CDDP) and negative control samples. A drug exposure period of 24 h was allowed (310 K). Supernatants were removed, and the wells washed with PBS (100 µL). A recovery period of 72h was allowed in drug-free medium (200 µL, 310 K). Aliquots of stock solutions (*ca*. 100 µM) were analysed by ICP-OES to determine the exact metal concentration.

The SRB assay was used to determine cell viability. Cold 50% trifluoroacetic acid (TCA, 50 µL) was added to each well for 1 h (277 K). The plate was washed with slow running water and dried. 0.4% SRB dye (50 µL, prepared in 1% acetic acid) was added for 30 mins (298 K). Excess dye was removed with 1% acetic acid, and the plate was dried. 10 mM Tris base solution (200 µL) was added to each well for 1 h (298 K). Absorbance was read with a BioRad iMark microplate reader. Survival percentages were obtained relative to negative control wells. Data was plotted as survival percentage versus the logarithm of drug concentration using OriginPro 2016. IC_{50} (half-maximal inhibitory) concentrations were determined as the inflection point of the fitted sigmoidal curve. Experiments were performed as duplicates of triplicates and standard deviations were calculated.

Metal accumulation in cancer cells

Cells were grown as described previously.[8] The medium was removed, cells were washed with phosphate-buffered saline (PBS) and detached using 2 mL of trypsin / EDTA (2 mM, 310 K, 5 min). The solution was diluted using the corresponding medium and mixed to achieve a single cell suspension, and cell density determined using a plastic disposable haemocytometer. The suspension was diluted to seed 4×10^6 cells per well in a P100 petri dish (10 mL).

After 24 h of pre-incubation, solutions of the complexes (DMSO not exceeding 0.5%) and negative controls were added in triplicate to give final (equipotent) concentrations equal to the IC_{50} determined in A2780 (unless stated otherwise). 24 h drug exposure was allowed. The experiments did not include any recovery time in drug-free media stated otherwise. Cells were incubated at 310 K unless stated otherwise.

The supernatant was removed. Cells were washed with PBS and detached with trypsin-EDTA. The number of cells in each sample was determined using a haemocytometer. Cells were collected by centrifugation (5 min, 1000 rpm), re-suspended in PBS (1 mL) and transferred to glass microwave vials. After further centrifugation (5 min, 1000 rpm), the supernatant was removed by suction to obtain whole cell pellets. Freshly distilled 72% v/v nitric acid (500 µL) was added to the pellets which were digested using a CEM Discovery microwave (453 K, 3 min, 300W, 450 psi). Solutions were diluted using doubly-distilled milliQ water containing thiourea (10 mM) and ascorbic acid (100 mg/L) to achieve a final acid concentration of 3.6% v/v HNO_3 (final working volume = 10 mL). The amount of metal taken up by the cells was determined by ICP-MS. The experiments were all carried out in triplicate and the s.d. were calculated. Final results were reported as ng Os / Ir / Pt $\times 10^6$ cells.

2.4 References

1. J. Tönnemann, J. Risse, Z. Grote, R. Scopelliti and K. Severin, *Eur. J. Inorg. Chem.*, 2013, **2013**, 4558-4562.
2. J. P. C. Coverdale, C. Sanchez-Cano, G. J. Clarkson, R. Soni, M. Wills and P. J. Sadler, *Chem. Eur. J.*, 2015, **21**, 8043-8046.
3. M. Liu, X. Mao, C. Ye, H. Huang, J. K. Nicholson and J. C. Lindon, *J. Magn. Reson.*, 1998, **132**, 125-129.
4. O. V. Dolomanov, L. J. Bourhis, R. J. Gildea, J. A. K. Howard and H. Puschmann, *J. Appl. Crystallogr.*, 2009, **42**, 339-341.
5. G. Sheldrick, *Acta Crystallogr., Sect. A: Found. Crystallogr.*, 2008, **64**, 112-122.
6. C. Venzago, M. Popp, J. Kovac and A. Kunkel, *J. Anal. At. Spectrom.*, 2013, **28**, 1125-1129.
7. J. J. Soldevila-Barreda, Doctor of Philosphy, University of Warwick, 2014.
8. I. Romero-Canelón, Doctor of Philosphy, University of Warwick, 2012.
9. V. Vichai and K. Kirtikara, *Nat. Protocols*, 2006, **1**, 1112-1116.
10. T. Mosmann, *J. Immunol. Methods*, 1983, **65**, 55-63.
11. Y. P. Keepers, P. E. Pizao, G. J. Peters, J. van Ark-Otte, B. Winograd and H. M. Pinedo, *Eur. J. Cancer*, 1991, **27**, 897-900.

Chapter 3

Asymmetric catalytic osmium sulfonamide complexes

Some of the work in this chapter has been published.

J. P. C. Coverdale, C. Sanchez-Cano, G. J. Clarkson, R. Soni, M. Wills, P. J. Sadler, Easy To Synthesize, Robust Organo-osmium Asymmetric Transfer Hydrogenation Catalysts, *Chemistry – A European Journal,* 2015, **21**, 8043-8046

3. Asymmetric catalytic osmium sulfonamide complexes

3.1 Introduction

Selective hydrogenation of functional groups with control of enantioselectivity allows chemists to synthesise complex products from simple and readily available prochiral reagents; an example of which is transfer hydrogenation, which describes the catalysis of hydrogen transferral from a donor molecule to a substrate.[1-3] The importance of this chemistry was highlighted by the award of the 2001 Nobel Prize in Chemistry to Professor R. Noyori for his contributions to asymmetric reduction catalysis.[2] The first-generation Noyori catalysts were based on ruthenium coordinated to a diamine and BINAP (2,2'-bis(diphenylphosphino)-1,1'-binaphthyl) chelating ligands, achieving high conversion and enantioselectivity for the reduction of ketones.[4, 5] Analogous osmium complexes, both chiral and non-chiral variants, have since been reported for the rapid hydrogenation of carbonyls.[6]

Second generation Noyori-type ruthenium transfer hydrogenation catalysts replaced the diphosphine ligand with an η^6-coordinated arene and a chloride as the leaving ligand. The compounds are prepared by the complexation of a sulfonamide with a ruthenium-arene chlorido dimer, in the presence of a base (Figure 3.1).[1] The resulting chlorido pre-catalyst is highly stable and easy to handle, and eliminates HCl to become the active catalytic species.[7] Isoelectronic Rh(III) and Ir(III) Cp* complexes (Cp* = 1,2,3,4,5-cyclopentadienyl) have been reported and retain the high conversion and enantioselectivity of the ruthenium complex,[8, 9] however no examples of osmium analogues of the second-generation Noyori catalyst were identified in the literature prior to the investigations in this project.

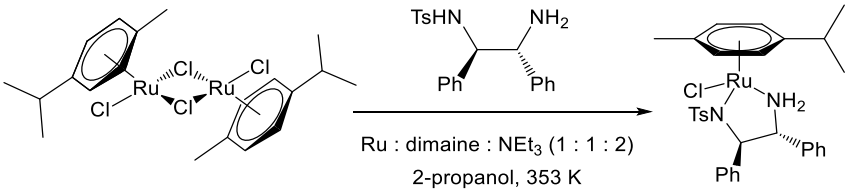

Figure 3.1. Synthesis of Noyori-type synthesis of a Ru pre-catalyst in 2-propanol (Ts = tosyl).[1]

The role of the metal in transfer hydrogenation catalysts is not purely structural. The Rh(III) TsDPEN catalyst was found to be more efficient than Ir(III) and Ru(II) analogues for the reduction of various ketones in water, achieving 99% ee even at low catalyst loading.[10]

This Chapter explores the synthesis, chemistry and catalytic properties of osmium analogues of the Noyori second-generation ruthenium bifunctional catalyst, complexes **1**-**10** (Table 3.1). Osmium-based catalysts may have previously attracted little attention due to the apparent inertness of osmium(II), as commonly observed for the *ca*. 100× slower hydrolysis of Os-Cl, compared to that of Ru-Cl.[11] However, recent examples demonstrate promise for osmium hydrogenation catalysts bearing various bidentate ligands.[12-17] As discussed in Chapter 1 (section 1.1.2), many Os catalysts achieve high turnover frequencies (TOF = 10^6 h^{-1}) for the transfer hydrogenation of carbonyls, in some cases, at greater rates than the ruthenium isoelectronic analogues.[17]

Electrostatic interactions between the arene of the catalyst and the substrate are critical in the enantioselectivity of the catalyst,[18, 19] but the effect of *p*-cymene substitution has not been widely explored for sulfonamide catalysts. The sulfonamide group is known to be important, particularly for interactions with protonated imines and amines.[20, 21] However, few examples of other sulfonamides exist beyond tosyl-diamine complexes. In addition, phenyl groups of the diamine were modified by addition of methoxy-

substituents in an effort to increase water solubility. Such modifications are evaluated for their impact on both the chemistry of the complexes, and their catalytic performance for the reduction of prochiral ketones, using chemical and computational techniques. Osmium analogues **1**-**10** are compared to Noyori-type ruthenium complex **11**, from which they are derived, to examine the effect changing the metal centre (Ru for Os) has on kinetics, stability and reactivity.

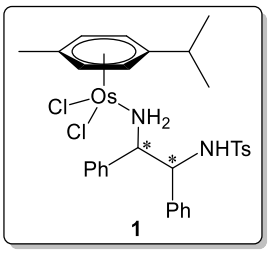

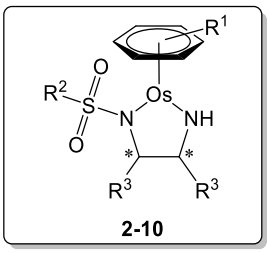

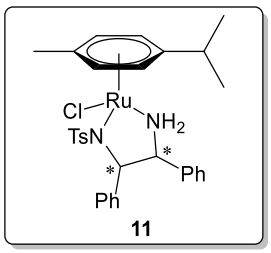

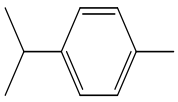

***p*-cymene (*p*-cym)**

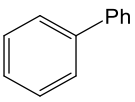

biphenyl (bip)

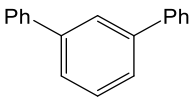

***m*-terphenyl (*m*-terp)**

Complex	Metal	η^6-arene (R^1)	R^2	R^3
1	Os	*p*-cymene	4-tolyl ((H)TsDPEN)	phenyl
2	Os	*p*-cymene	4-tolyl (TsDPEN)	phenyl
3	Os	*p*-cymene	methyl (MsDPEN)	phenyl
4	Os	*p*-cymene	4-nitrophenyl (NsDPEN)	phenyl
5	Os	*p*-cymene	4-fluorophenyl (FbDPEN)	phenyl
6	Os	*p*-cymene	phenyl (BsDPEN)	phenyl
7	Os	biphenyl	4-tolyl (TsDPEN)	phenyl
8	Os	*m*-terphenyl	4-tolyl (TsDPEN)	phenyl
9	Os	*p*-cymene	4-tolyl (TsBMEN)	4-methoxyphenyl
10	Os	biphenyl	4-tolyl (TsBMEN)	4-methoxyphenyl
11	Ru	*p*-cymene	4-tolyl ((H)TsDPEN)	phenyl

Table 3.1. Structures of complexes **1**-**11** studied in this chapter. * denotes a chiral centre.

3.2 Experimental

3.2.1 Materials

Osmium trichloride hydrate was purchased from Heraeus. Osmium(II) arene dimers $[OsCl_2(p\text{-cymene})]_2$, $[OsCl_2(\text{biphenyl})]_2$ and $[OsCl_2(m\text{-terphenyl})]_2$ were prepared following an adapted literature procedure for synthesis using a microwave reactor (Chapter 2, section 2.1.2).[22] Enantiomerically-pure enantiomers of 1,2-di(4-methoxyphenyl)ethylenediamine were purchased from Sigma Aldrich. Enantiomerically-pure enantiomers of 1,2-diphenylethylenediamine were purchased from Arran Chemical Company Ltd (Ireland). Sulfonyl chlorides were purchased from Sigma Aldrich. Potassium hydroxide, magnesium sulphate, sodium chloride and all non-dried solvents were purchased from Fischer Scientific. Deuterated solvents were purchased from Goss Scientific. Water used for biphasic reactions was purified by reverse osmosis (RO) unless specified. All other reagents and solvents were purchased from Sigma Aldrich and used as received, unless stated otherwise.

Acknowledgements

Reduced precursors (1,4-dihydro-biphenyl and 1,4-dihydro-*m*-terphenyl) were kindly provided by Miss. Khatija Bhayat, Dr. Russell Needham and Dr. Abraha Habtemariam (University of Warwick, UK). Complexes **9** and **10** (and the corresponding bis(methoxyphenyl)sulfonamide ligand) were synthesised by Miss. Yasmin Khanom (University of Warwick, UK). Both enantiomers of complex **11** were purchased from Sigma Aldrich. Methods for NMR, mass spectrometry, UV-visible spectroscopy and FT-IR spectroscopy are described in Chapter 2 (section 2.2).

3.2.2 Synthesis of diamine sulfonamide ligands

Both enantiomers of diamine ligands were individually synthesised from enantiomerically-pure starting materials, either (1*R*,2*R*)-diphenylethylenediamine / (1*S*,2*S*)-diphenylethylenediamine, or (1*R*,2*R*)-bis(4-methoxyphenyl)ethylenediamine / (1*S*,2*S*)-bis(4-methoxyphenyl)ethylenediamine (Figure 3.2).

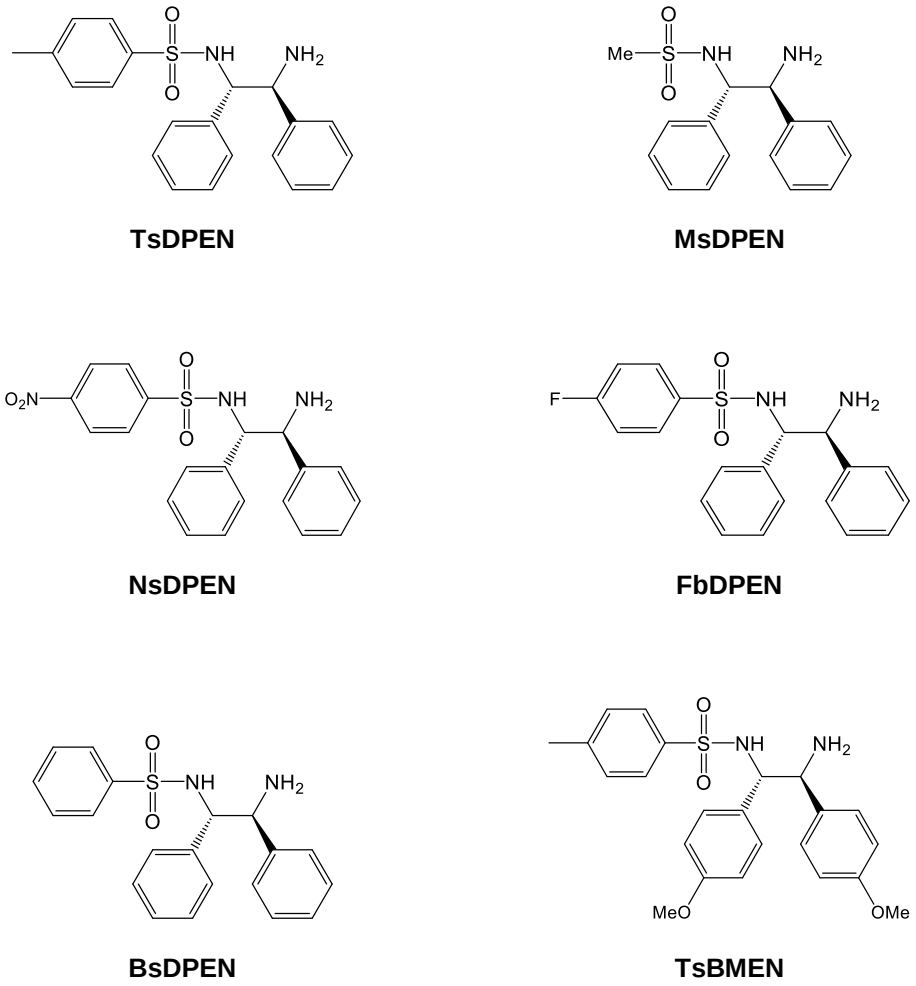

Figure 3.2. Six sulfonamide ligands synthesised from enantiomerically-pure starting materials. Only (1*R*,2*R*)-ligands shown.

***N*-(toluenesulfonyl)-1,2-diphenylethylenediamine (TsDPEN).** These ligands were purchased as enantiomerically-pure compounds, (1*R*,2*R*)-TsDPEN and (1*S*,2*S*)-TsDPEN, from Arran Chemical Company Ltd.

***N*-(Methanesulfonyl)-1,2-diphenylethylenediamine (MsDPEN).** To either (1*R*,2*R*)-diphenylethylenediamine or (1*S*,2*S*)-diphenylethylenediamine (212 mg, 1.0 mmol) and triethylamine (202 mg, 2 mmol) in ice-cold dichloromethane (3.2 mL) was added methanesulfonyl chloride (138 mg, 1.2 mmol) in dichloromethane (2.1 mL) dropwise over 6 h. The product was washed with water, dried over magnesium sulphate and concentrated *in vacuo* to afford an oil which was dissolved in toluene, obtaining a white crystalline solid. (113 mg, 0.39 mmol, 39%). ^{1}H NMR (500 MHz, $CDCl_3$, 25°C, TMS): δ=7.10-7.40 (m, 10H; ArH), 4.56 (d, ^{3}J(H,H)=5.2 Hz, 1H; C*H*NHTs), 4.30 (d, ^{3}J(H,H)=5.2 Hz, 1H; C*H*NH_2), 2.27 (s, 3H; CH_3); ^{13}C NMR (125 MHz, $CDCl_3$, 25°C, TMS) δ 128.9, 128.7, 128.6, 128.5, 127.9, 127.8, 127.6, 126.9, 126.7, 63.4, 62.6, 60.2, 41.9, 40.7; UV/Vis: λ_{max} 227 and 259 nm; HRMS (*m/z*): $[M+H]^+$ calcd. for $C_{15}H_{19}N_2O_2S$, 291.1162; found, 291.1164.

***N*-(4-Nitrobenzenesulfonyl)-1,2-diphenylethylenediamine (NsDPEN).** The compounds were obtained following the method described for the synthesis of MsDPEN, using 4-nitrobenzenesulfonyl chloride (266 mg, 1.2 mmol) in place of 4-toluenesulfonyl chloride. The product was recrystallized from toluene as a white crystalline solid. (230 mg, 0.58 mmol, 58%). ^{1}H NMR (500 MHz, $CDCl_3$, 25°C, TMS): δ=7.96 (d, ^{3}J(H,H)=8.7 Hz, 2H; ArH), 7.53 (d, ^{3}J(H,H)=8.7 Hz, 2H; ArH), 7.18-7.25 (m, 5H; ArH), 7.12-7.18 (m, 5H; ArH), 4.49 (d, ^{3}J(H,H)=4.3 Hz, 1H; C*H*NHSO_2R), 4.21 (d, ^{3}J(H,H)=4.3 Hz, 1H; C*H*NH_2); ^{13}C NMR (125 MHz, $CDCl_3$, 25°C, TMS) δ 128.7, 128.6, 128.3, 128.1, 127.9, 127.7, 127.4, 126.8, 126.3, 123.7, 63.2, 60.1; UV/Vis: λ_{max} 264 nm; HRMS (*m/z*): $[M+H]^+$ calcd. for $C_{20}H_{20}N_3O_4S$, 398.1169; found, 398.1169. Elemental analysis found (calcd. for (1*R*,2*R*)-$C_{20}H_{19}N_3O_4S$): C 60.40 (60.44), H 4.90 (4.82), N 10.41 (10.57); Elemental analysis

found (calcd. for (1*S*,2*S*)-$C_{20}H_{19}N_3O_4S$): C 60.42 (60.44), H 4.87 (4.82), N 10.45 (10.57).

***N*-(4-Fluorobenzenesulfonyl)-1,2-diphenylethylenediamine (FbDPEN).** The compounds were obtained following the method described for the synthesis of MsDPEN, using 4-fluorobenzenesulfonyl chloride (934 mg, 4.8 mmol) in place of 4-toluenesulfonyl chloride. The product was recrystallized from toluene as a white crystalline solid. (1076 mg, 2.90 mmol, 73%). ^{1}H NMR (400 MHz, $CDCl_3$, 25°C, TMS): δ=7.41 (ddd, ^3J(H,H)=5.1 Hz, ^3J(H,F)=8.7 Hz, ^4J(H,H)=5.0 Hz, 2H; ArH) 7.06-7.22 (m, 10H; ArH), 6.81 (ddd, ^3J(H,H)=9.1, ^3J(H,H)=8.6 Hz, ^4J(H,F)=5.0 Hz, 2H; ArH), 4.43 (d, ^3J(H,H)=5.1 Hz, 1H; CH), 4.18 (d, ^3J(H,H)=5.1 Hz, 1H; CH); ^{13}C NMR (125 MHz, $CDCl_3$, 25°C, TMS) δ 129.5, 129.4, 128.4, 127.7, 127.6, 127.5, 127.0, 126.5, 115.7, 115.5, 63.2, 60.4; UV/Vis: λ_{max} 235 and 260 nm; HRMS (*m/z*): $[M+H]^+$ calcd. for $C_{20}H_{20}FN_2O_2S$, 371.1224; found, 371.1230. Elemental analysis found (calcd. for (1*R*,2*R*)-$C_{20}H_{19}FN_2O_2S$): C 64.46 (64.85), H 5.02 (5.17), N 7.48 (7.56); Elemental analysis found (calcd. for (1*S*,2*S*)-$C_{20}H_{19}FN_2O_2S$): C 64.51 (64.85), H 5.24 (5.17), N 7.51 (7.56).

***N*-(Benzenesulfonyl)-1,2-diphenylethylenediamine (BsDPEN).** The compounds were obtained following the method described for the synthesis of MsDPEN, using benzenesulfonyl chloride (848 mg, 4.8 mmol) in place of 4-toluenesulfonyl chloride. The product was recrystallized from toluene as a white crystalline solid. (569 mg, 1.61 mmol, 40%). ^{1}H NMR (500 MHz, $CDCl_3$, 25°C, TMS): δ=7.43 (d, ^3J(H,H)=7.6 Hz, 2H; ArH), 7.34 (t, ^3J(H,H)=7.4 Hz, 1H; ArH), 7.05-7.22 (m, 12H; ArH), 4.44 (br. d, ^3J(H,H)=5.2 Hz, 1H; C*H*NHSO$_2$R), 4.18 (br. s, 1H; C*H*NH$_2$); ^{13}C NMR (125 MHz,

$CDCl_3$, 25°C, TMS) δ 131.9, 128.5, 128.5, 128.3, 127.7, 127.4, 127.0, 126.8, 63.2, 60.4; UV/Vis: λ_{max} 231, 233 and 260 nm; HRMS (*m/z*): $[M+H]^+$ calcd. for $C_{20}H_{21}N_2O_2S$, 353.1318; found, 353.1319. Elemental analysis found (calcd. for (1*R*,2*R*)-$C_{20}H_{20}N_2O_2S$): C 67.87 (68.16), H 5.74 (5.72), N 7.94 (7.95); Elemental analysis found (calcd. for (1*S*,2*S*)-$C_{20}H_{20}N_2O_2S$): C 67.85 (68.16), H 5.73 (5.72), N 7.93 (7.95).

***N*-(Toluenesulfonyl)-1,2-bis(4-methoxyphenyl)ethylenediamine (TsBMEN).** To a either enantiomerically-pure (1*S*,2*S*)-di(4-methoxyphenyl)-ethylenediamine or (1*R*,2*R*)-di(4-methoxyphenyl)-ethylenediamine (300 mg, 1.1 mmol) and triethylamine (230 μL, 1.7 mmol) in dichloromethane (50 mL) was added a solution of 4-toluenesulfonyl chloride (210 mg, 1.1 mmol) in dichloromethane (80 mL) dropwise over a period of 30 min. The resulting reaction mixture was washed with water (3 × 15 mL), followed by saturated brine solution, dried over magnesium sulphate, filtered and concentrated *in vacuo* to yield a transparent oil, which was titurated in diethyl ether to afford a white amorphous solid. (363 mg, 0.85 mmol, 74%). ^{1}H NMR (500 MHz, $CDCl_3$, 25°C, TMS): δ=7.32 (d, ^3J(H,H)=8.1 Hz, 2H; ArH), 7.04 (m, 2H; ArH), 6.98 (d, ^3J(H,H)=7.7 Hz, 4H; ArH), 6.67 (d, ^3J(H,H)=8.1 Hz, 4H; ArH), 4.34 (*br*. s, 1H; TsNHC*H*), 4.10 (*br*. s 1H C*H*NH_2), 3.73 (br. s, 3H; OCH_3), 3.70 (br. s, 3H; OCH_3), 2.32 (s, 3H; CH_3); ^{13}C NMR (125 MHz, $CDCl_3$, 25°C, TMS) δ 158.8, 142.4, 137.3, 129.0, 128.6, 127.0, 113.7, 113.6, 55.2, 55.1, 45.8, 21.4; UV/Vis: λ_{max} 275, 283 nm; HRMS (*m/z*): $[M+Na]^+$ calcd. for $C_{23}H_{26}N_2NaO_4S$, 449.1505; found, 449.1503. Elemental analysis found (calcd. for $C_{23}H_{26}N_2O_4S$): C 64.46 (64.77), H 6.10 (6.14), N 6.60 (6.57).

3.2.3 Synthesis of osmium sulfonamide complexes 1-10

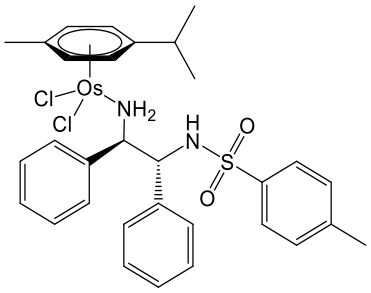

(*R*,*R*)-1

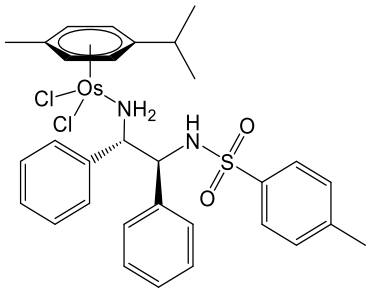

(*S*,*S*)-1

[OsCl$_2$(η^6-*p*-cymene)(TsDPEN)] (1).[23] Either (1*R*,2*R*)-(H)TsDPEN or (1*S*,2*S*)-(H)TsDPEN (50 mg, 0.14 mmol) and [Os(η^6-*p*-cymene)Cl$_2$]$_2$ (50 mg, 0.06 mmol) in dichloromethane (5 mL) were placed in a CEM Discovery-SP microwave reactor (393 K, 10 min, 150 W, 250 psi). The product was precipitated with hexane yielding a yellow solid (88 mg, 0.12 mmol, 89%). ^{1}H NMR (400 MHz, CDCl$_3$, 25°C, TMS) δ=7.41 (d, ^3J(H,H)=7.9 Hz, 2H, ArH), 7.17-7.22 (m, 2H, ArH), 7.04-7.08 (m, 2H, ArH), 6.89-6.96 (m, 3H, ArH), 6.81-6.86 (m, 3H, ArH), 6.64 (d, ^3J(H,H)=7.6, 2H, ArH), 6.38 (d, ^3J(H,H)=8.3 Hz, H, TsNH), 5.60 (d, ^3J(H,H)=5.3 Hz, 1H, ArH), 5.32-5.37 (m, 2H, ArH), 5.23 (d, ^3J(H,H)=5.3 Hz, 1H, ArH), 5.20 (d, ^3J(H,H)=11.6 Hz, 1H, NH$_2$), 4.50-4.58 (m, 1H, C*H*NH$_2$), 4.43-4.50 (m, 1H, C*H*NHTs), 4.20 (t, ^3J(H,H)=10.7 Hz, 2H, NH$_2$), 2.59 (sept., ^3J(H,H)=6.9 Hz, 1H, C*H*(CH$_3$)$_2$), 2.20 (s, 3H, CH$_3$), 2.02 (s, 3H, CH$_3$), 1.13 (d, ^3J(H,H)=6.9 Hz, 3H, CH(C*H*$_3$)$_2$), 1.08 (d, ^3J(H,H)=6.9 Hz, 3H, CH(C*H*$_3$)$_2$); ^{13}C NMR (100 MHz, CDCl$_3$, 25°C, TMS) δ 129.3, 128.9, 128.2, 127.7, 127.4, 127.2, 72.6, 71.5, 70.9, 70.8, 65.1, 63.8, 31.0, 22.6, 22.4, 21.4, 18.7; UV/Vis: λ$_{max}$ 264 and 337 nm; ν$_{max}$ 2593 and 3078 cm^{-1}; HRMS (*m/z*): [M-H]$^-$ calcd. for C$_{31}$H$_{35}$Cl$_2$N$_2$O$_2$OsS, 761.1406; found, 761.1347. Elemental analysis for **(*R*,*R*)-1**: found (calcd. C$_{31}$H$_{36}$Cl$_2$N$_2$O$_2$OsS): C 48.72 (48.87), H 4.73 (4.76), N 3.76 (3.68); Elemental analysis for **(*S*,*S*)-1**: found (calcd. C$_{31}$H$_{36}$Cl$_2$N$_2$O$_2$OsS): C 48.78 (48.87), H 4.75 (4.76), N 3.74 (3.68).

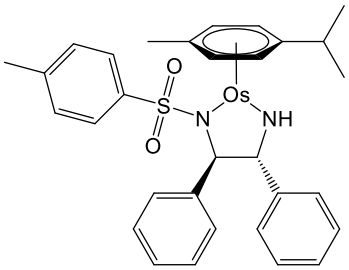

(*R*,*R*)-2

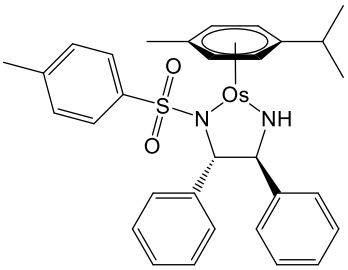

(*S*,*S*)-2

[Os(η^6-*p*-cymene)(TsDPEN)] (2).[23] Osmium *p*-cymene-chlorido dimer (51.4 mg, 0.065 mmol) and either (1*R*,2*R*)- or (1*S*,2*S*)-(H)TsDPEN (51.3 mg, 0.14 mmol) were stirred in chloroform (5 ml) in the presence of potassium hydroxide (56.1 mg, 1 mmol). A colour change from yellow to red was observed in < 1 min. After 5 min, deionized water (5 ml) was added with stirring for a further 10 min. The organic layer was concentrated *in vacuo* to yield a red solid, which was recrystallized from dichloromethane / hexane (68 mg, 0.10 mmol, 75%). ^{1}H NMR (400 MHz, $CDCl_3$, 25°C, TMS): δ = 7.41 (d, ^3J(H,H)=7.6 Hz, 2H, ArH), 7.05-7.20 (m, 10H, ArH), 6.82 (d, ^3J(H,H)=8.0 Hz, 2H, ArH), 6.80 (*br* s, 1H, NH), 5.79 (d, ^3J(H,H)=5.6 Hz, 1H, Os-ArH), 5.62 (d, ^3J(H,H)=5.6 Hz, 1H, Os-ArH), 5.52 (d, ^3J(H,H)=5.6 Hz, 1H, Os-ArH), 5.42 (d, ^3J(H,H)=5.6 Hz, 1H, Os-ArH), 4.42 (s, 1H, C*H*NH$_2$), 3.94 (d, ^3J(H,H)=4.3 Hz, 1H, TsNCH), 2.45 (sept, ^3J(H,H)=6.9 Hz, 1H, C*H*(CH$_3$)$_2$), 2.23 (s, 3H, CH$_3$), 2.22 (s, 3H, CH$_3$), 1.23 (d, ^3J(H,H)=6.9 Hz, 3H, CH(C*H*$_3$)$_2$), 1.17 (d, ^3J(H,H)=6.9 Hz, 3H, CH(C*H*$_3$)$_2$); ^{13}C NMR (100 MHz, $CDCl_3$, 25°C, TMS) δ = 127.4, 127.0, 126.8, 126.0, 125.9, 125.9, 125.4, 81.7, 76.2, 72.4, 70.7, 70.0, 66.2, 22.5, 22.4, 20.2; UV/Vis: λ_{max} 260, 410 and 478 nm; HRMS (ESI): *m/z* calculated for $C_{31}H_{35}N_2O_2OsS$ [M+H$^+$]: 691.2028. Found: 691.2031. Elemental analysis for **(*R*,*R*)-2**: found (calcd. $C_{31}H_{34}N_2O_2OsS$): C 53.66 (54.05), H 4.88 (4.97), 3.95 (4.07); Elemental analysis for **(*S*,*S*)-2**: found (calcd. for $C_{31}H_{34}N_2O_2OsS$): C 53.71 (54.05), H 4.84 (4.97), N 4.00 (4.07).

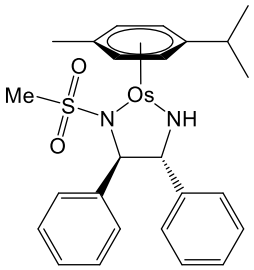

(*R*,*R*)-3

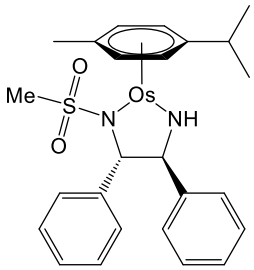

(*S*,*S*)-3

[Os(η^6-*p*-cymene)(MsDPEN)] (3). The complex was synthesised following the method described for complex **2**. Either (1*R*,2*R*)- or (1*S*,2*S*)-(H)MsDPEN (41 mg, 0.14 mmol) was reacted with osmium *p*-cymene-chlorido dimer (51.4 mg, 0.065 mmol) in the presence of potassium hydroxide (56.1 mg, 1 mmol) in chloroform and water. The product was isolated as an orange amorphous solid which was recrystallized from dichloromethane / hexane. (54 mg, 0.087 mmol, 67%). ^{1}H NMR (500 MHz, $CDCl_3$, 25°C, TMS): δ = 7.45 (d, ^3J(H,H) = 7.3 Hz, 2H, ArH), 7.00-7.40 (m, 9H, ArH), 5.87 (d, ^3J(H,H) = 5.6 Hz, 1H, Os-ArH), 5.79 (d, ^3J(H,H) = 5.6 Hz, 1H, Os-ArH), 5.75 (d, ^3J(H,H) = 5.7 Hz, 1H, Os-ArH), 5.72 (d, ^3J(H,H) = 5.7 Hz, 1H, Os-ArH), 4.34 (s, 1H, TsNCH), 3.99 (d, ^3J(H,H) = 2.8 Hz, 1H, CH), 2.68 (sept, ^3J(H,H) = 6.9 Hz, 1H, C*H*(CH_3)$_2$), 2.49 (s, 3H, CH_3), 2.37 (s, 3H, CH_3), 1.36 (d, ^3J(H,H) = 6.9 Hz, 6H, CH(C*H*$_3$)$_2$). ^{13}C NMR (125 MHz, $CDCl_3$) δ = 128.3, 128.0, 127.4, 127.1, 126.9, 126.4, 83.0, 75.9, 72.6, 72.5, 70.3, 68.5, 40.3, 32.9, 23.7, 23.5, 21.0. UV/Vis: λ_{max} 409 and 475 nm; HRMS (ESI): *m/z* calculated for $C_{25}H_{31}N_2O_2OsS$ [M+H$^+$]: 615.1714. Found: 615.1710. Elemental analysis for **(*R*,*R*)-3**: found (calcd. for $C_{25}H_{30}N_2O_2OsS$): C 49.06 (49.00), H 4.92 (4.93), N 4.66 (4.57); Elemental analysis for **(*S*,*S*)-3**: found (calcd. for $C_{25}H_{30}N_2O_2OsS$): C 48.72 (49.00), H 4.80 (4.93), N 4.62 (4.57).

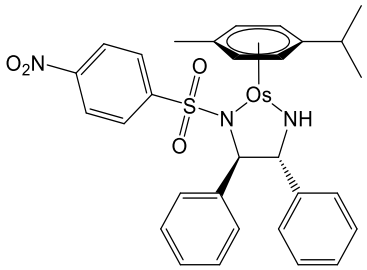

(*R*,*R*)-4

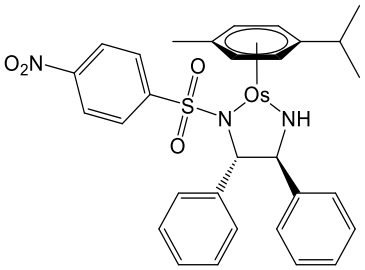

(*S*,*S*)-4

[Os(η^6-*p*-cymene)(NsDPEN)] (4). The complex was synthesised following the method described for complex **2**. Either (1*R*,2*R*)- or (1*S*,2*S*)-(H)NsDPEN (56 mg, 0.14 mmol) was reacted with osmium *p*-cymene-chlorido dimer (51.4 mg, 0.065 mmol) in the presence of potassium hydroxide (56.1 mg, 1 mmol) in chloroform and water. The product was isolated as an dark red amorphous solid which was recrystallized from dichloromethane / hexane. (57 mg, 0.079 mmol, 70%). ^{1}H NMR (500 MHz, $CDCl_3$, 25°C, TMS): δ = 7.86 (d, ^3J(H,H) = 8.9 Hz, 2H, ArH), 7.45 (d, ^3J(H,H) = 8.9 Hz, 2H, ArH), 7.00-7.25 (m, 11H, ArH), 5.95 (d, ^3J(H,H) = 5.6 Hz, 1H, Os-ArH), 5.80 (d, ^3J(H,H) = 5.6 Hz, 1H, Os-ArH), 5.74 (d, ^3J(H,H) = 5.5 Hz, 1H, Os-ArH), 5.68 (d, ^3J(H,H) = 5.5 Hz, 1H, Os-ArH), 4.37 (s, 1H, TsNCH), 4.02 (d, ^3J(H,H) = 4.2 Hz, 1H, CH), 2.61 (sept, ^3J(H,H) = 6.9 Hz, 1H, C*H*(CH_3)$_2$), 2.39 (s, 3H, CH_3), 1.35 (d, ^3J(H,H) = 6.9 Hz, 3H, CH(C*H*$_3$)$_2$), 1.28 (d, ^3J(H,H) = 6.9 Hz, 3H, CH(C*H*$_3$)$_2$). ^{13}C NMR (125 MHz, $CDCl_3$): δ = 128.1, 127.9, 127.4, 127.3, 126.9, 126.8, 126.3, 126.2, 123.1, 82.5, 73.3, 72.0, 71.1, 67.4, 32.9, 24.1, 23.5, 21.0; UV/Vis: λ_{max} 263 and 409 nm; HRMS (ESI): *m/z* calculated for $C_{30}H_{32}N_3O_4OsS$ [M+H$^+$]: 722.1722. Found: 722.1716. Elemental analysis for **(*R*,*R*)-4**: found (calcd. for $C_{30}H_{31}N_3O_4OsS$): C 49.69 (50.05), H 4.47 (4.34), N 5.58 (5.84); Elemental analysis for **(*S*,*S*)-4**: found (calcd. for $C_{30}H_{31}N_3O_4OsS$): C 50.02 (50.05), H 4.22 (4.37), N 5.79 (5.84).

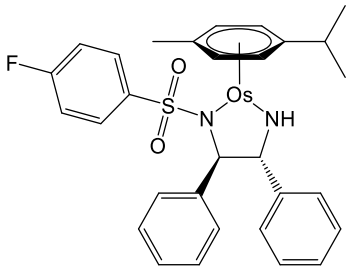

(*R*,*R*)-5

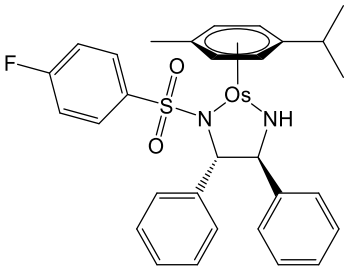

(*S*,*S*)-5

[Os(η^6-*p*-cymene)(FbDPEN)] (5). This complex was synthesised as reported previously. Following the method described for complex **2**, (1*R*,2*R*)- or (1*S*,2*S*)-(H)FbDPEN (52 mg, 0.14 mmol) was reacted with osmium *p*-cymene-chlorido dimer (51.4 mg, 0.065 mmol) in the presence of potassium hydroxide (56.1 mg, 1 mmol) in chloroform and water. The product was isolated as an orange amorphous solid which was recrystallized from dichloromethane / hexane. (50 mg, 0.072 mmol, 52%). ^{1}H NMR (500 MHz, $CDCl_3$, 25°C, TMS): δ = 7.46 (d, ^3J(H,H) = 7.5Hz, 2H, ArH), 7.29-7.34 (m, 2H, ArH), 6.90-7.26 (m, 9H, ArH), 6.75 (m, 2H, ArH), 5.90 (d, ^3J(H,H) = 5.6 Hz, 1H, Os-ArH), 5.73 (d, ^3J(H,H) = 5.6 Hz, 1H, Os-ArH), 5.64 (d, ^3J(H,H) = 5.6 Hz, 1H, Os-ArH), 5.55 (d, ^3J(H,H) = 5.6 Hz, 1H, Os-ArH), 4.47 (s, 1H, TsNCH), 4.03 (d, ^3J(H,H) = 3.6 Hz, 1H, CH), 2.55 (sept, ^3J(H,H) = 6.9 Hz, 1H, C*H*(CH_3)$_2$), 2.32 (s, 3H, CH_3), 1.32 (d, ^3J(H,H) = 6.9 Hz, 3H, CH(C*H*$_3$)$_2$), 1.25 (d, ^3J(H,H) = 6.9 Hz, 3H, CH(C*H*$_3$)$_2$). ^{13}C NMR (125 MHz, $CDCl_3$): δ = 129.2, 129.1, 128.1, 127.9, 127.2, 126.9, 126.6, 126.4, 114.8, 114.6, 82.6, 76.6, 73.5, 72.0, 71.0, 67.3, 32.8, 23.6, 23.4, 21.0. UV/Vis: λ_{max} 408 and 474 nm; HRMS (ESI): *m/z* calculated for $C_{30}H_{32}FN_2O_2OsS$ [M+H$^+$]: 695.1777. Found: 695.1780. Elemental analysis for **(*R*,*R*)-5**: found (calcd. for $C_{30}H_{31}FN_2O_2OsS$): C 51.85 (52.00), H 4.46 (4.51), N 4.09 (4.04); Elemental analysis for **(*S*,*S*)-5**: found (calcd. for $C_{30}H_{31}FN_2O_2OsS$): C 51.70 (52.00), H 4.43 (4.51), N 4.04 (4.04).

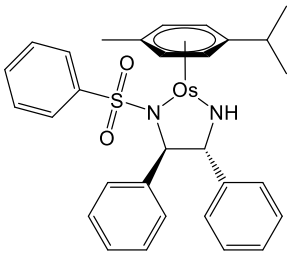

(*R*,*R*)-6

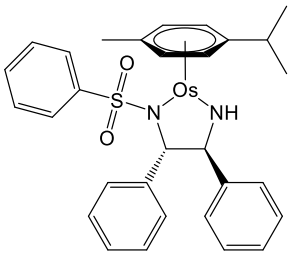

(*S*,*S*)-6

[Os(η^6-*p*-cymene)(BsDPEN)] (6). This complex was synthesised as reported previously. Following the method described for complex **2**, (1*R*,2*R*)- or (1*S*,2*S*)-(H)BsDPEN (49 mg, 0.14 mmol) was reacted with osmium *p*-cymene-chlorido dimer (51.4 mg, 0.065 mmol) in the presence of potassium hydroxide (56.1 mg, 1 mmol) in chloroform and water. The product was isolated as an orange amorphous solid which was recrystallized from dichloromethane / hexane. (44 mg, 0.065 mmol, 46%). ^{1}H NMR (500 MHz, $CDCl_3$, 25°C, TMS): δ = 7.48 (d, ^3J(H,H) = 7.5 Hz, 2H, ArH), 7.36 (m, 2H, ArH), 6.90-7.30 (m, 12H, ArH), 5.87 (d, ^3J(H,H) = 5.6 Hz, 1H, Os-ArH), 5.70 (d, ^3J(H,H) = 5.6 Hz, 1H, Os-ArH), 5.60 (d, ^3J(H,H) = 5.6 Hz, 1H, Os-ArH), 5.48 (d, ^3J(H,H) = 5.6 Hz, 1H, Os-ArH), 4.55 (s, 1H, TsNCH), 4.05 (d, ^3J(H,H) = 4.0 Hz, 1H, CH) 2.50 (sept, ^3J(H,H) = 6.9 Hz, 1H, C*H*(CH_3)$_2$), 2.27 (s, 3H, CH_3), 1.30 (d, ^3J(H,H) = 6.9 Hz, 3H, CH(C*H*$_3$)$_2$), 1.22 (d, ^3J(H,H) = 6.9 Hz, 3H, CH(C*H*$_3$)$_2$). ^{13}C NMR (125 MHz, $CDCl_3$): δ = 130.4, 128.1, 127.8, 127.2, 126.9, 126.5, 82.8, 73.6, 71.9, 70.9, 67.3, 32.7, 23.6, 23.4, 20.6. UV/Vis: λ_{max} 259, 409 and 475 nm; HRMS (ESI): *m/z* calculated for $C_{30}H_{33}N_2O_2OsS$ [M+H$^+$]: 677.1871. Found: 677.1876. Elemental analysis for **(*R*,*R*)-6**: found (calcd. for $C_{30}H_{32}N_2O_2OsS$): C 53.63 (53.39), H 4.72 (4.78), N 4.14 (4.15); Elemental analysis for **(*S*,*S*)-6**: found (calcd. for $C_{30}H_{32}N_2O_2OsS$): C 53.46 (53.39), H 4.75 (4.78), N 4.16 (4.15).

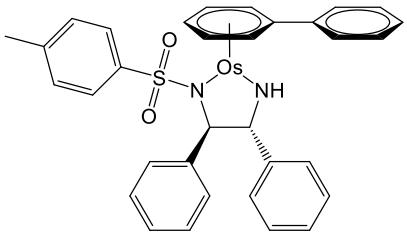

(*R*,*R*)-7

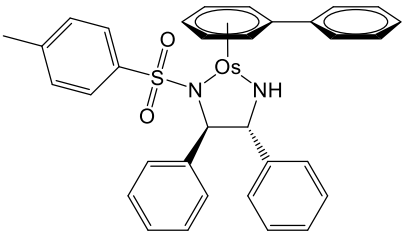

(*S*,*S*)-7

[Os(η^6-biphenyl)(TsDPEN)] (7). Osmium biphenyl dimer [Os(η^6-biphenyl)Cl_2]$_2$ (67 mg, 0.081 mmol) and (1*R*,2*R*)- or (1*S*,2*S*)-TsDPEN (55 mg, 0.15 mmol) were stirred in dichloromethane (2.5 mL) in a microwave vial, then placed in a CEM Discovery-SP microwave reactor for 10 min (393K, 150 W, 250 psi). The yellow-orange solution was filtered to remove any remaining osmium dimer, and the resulting solution was combined with freshly ground potassium hydroxide (56.1 mg, 1 mmol). Vigorous stirring was continued for 30 min until a color change from yellow to red was observed. Water (5 mL) was then added with stirring for a further 15 min. The aqueous layer was extracted with dichloromethane (3 x 5 mL) and concentrated *in vacuo* to yield a red amorphous solid which was recrystallized from dichloromethane / hexane (62 mg, 0.09 mmol, 59%). ^{1}H NMR (500 MHz, $CDCl_3$, 25°C, TMS): δ = 7.50-6.85 (m, 19H, ArH), 6.25-5.95 (m, 4H, Os-ArH), 4.45 (s, 1H, CH), 3.95 (d, ^3J(H,H) = 3.8 Hz, 1H, C*H*NH), 2.30 (s, 3H, CH_3). ^{13}C NMR (125 MHz, $CDCl_3$): δ = 146.3, 144.1, 141.2, 140.8, 137.7, 129.2, 128.9, 128.6, 128.2, 128.0, 127.2, 127.0, 126.9, 126.6, 126.5, 83.3, 73.7, 73.3, 73.1, 70.9, 70.5, 68.3, 21.4. UV/Vis: λ_{max} 358, 416 and 486 nm; HRMS (ESI): *m/z* calculated for $C_{33}H_{31}N_2O_2OsS$ [M+H$^+$]: 711.1715. Found: 711.1712. Elemental analysis for **(*R*,*R*)-7**: found (calcd. for $C_{33}H_{30}N_2O_2OsS$): C 55.62 (55.91), H 4.11 (4.27), N 3.88 (3.95); Elemental analysis for **(*S*,*S*)-7**: found (calcd. for $C_{33}H_{30}N_2O_2OsS$): C 55.60 (55.91), H 4.08 (4.27), N 4.00 (3.95).

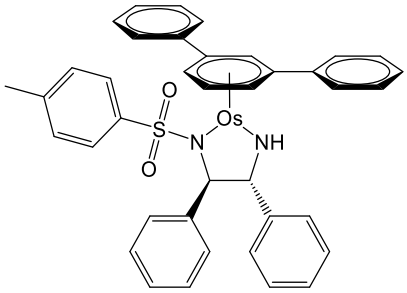

(*R*,*R*)-8

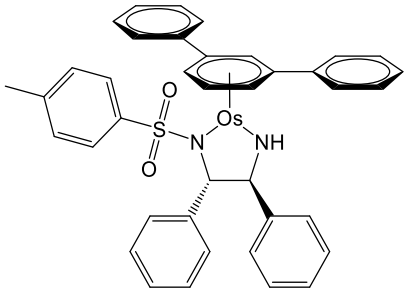

(*S*,*S*)-8

[Os(η^6-*m*-terp)(TsDPEN)] (8). Osmium *m*-terphenyl dimer [Os(η^6-*m*-terphenyl)Cl_2]$_2$ (40 mg, 0.04 mmol) and (1*R*,2*R*)- or (1*S*,2*S*)-TsDPEN (55 mg, 0.15 mmol) were stirred in dichloromethane (2.5 mL) in a microwave vial, then placed in a CEM Discovery-SP microwave reactor for 10 min (393K, 150 W, 250 psi). The resulting solution was combined with freshly ground potassium hydroxide (56.1 mg, 1 mmol). Vigorous stirring was continued for 30 min until a color change from yellow to red was observed. Water was added with stirring for a further 15 min. The aqueous layer was extracted with dichloromethane (3 x 5 mL) and concentrated *in vacuo* to yield an orange amorphous solid which was recrystallized from dichloromethane / hexane (28 mg, 0.036 mmol, 43%). ^{1}H NMR (400 MHz, $CDCl_3$, 25°C, TMS): δ = 7.80-7.74 (m, 2H, ArH), 7.57-7.51 (m, 2H, ArH), 7.45-7.36 (m, 6H, ArH), 7.33-7.28 (m, 2H, ArH), 7.19-7.03 (m, 8H, ArH), 7.00-6.94 (m, 2H, ArH), 6.89 (br. d, 1H, NH), 6.80-6.75 (m, 2H, ArH), 6.70 (d, ^3J(H,H) = 5.7 Hz, 1H, ArH), 6.60 (s, 1H, ArH), 6.46 (d, ^3J(H,H) = 5.5 Hz, 1H, ArH), 6.30 (t, ^3J(H,H) = 5.7 Hz, 1H, ArH), 4.41 (s, 1H, C*H*NTs), 3.84 (d, ^3J(H,H) = 4.3 Hz, 1H, C*H*NH), 2.28 (s, 3H, CH_3). ^{13}C NMR (100 MHz, $CDCl_3$): δ = 129.2, 129.0, 128.8, 128.7, 128.6, 128.4, 128.3, 128.0, 127.8, 127.3, 126.9, 126.7, 126.3, 83.2, 74.6, 73.9, 68.9, 66.7. UV/Vis: λ_{max} 419 and 490 nm; HRMS (ESI): *m/z* calculated for $C_{39}H_{35}N_2O_2OsS$ [M+H$^+$]: 787.2029. Found: 787.2033.

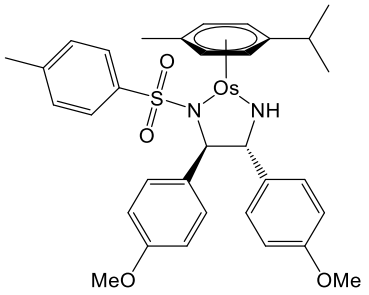

(*R*,*R*)-9

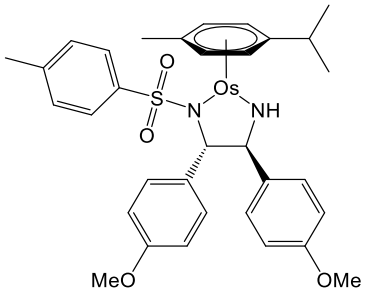

(*S*,*S*)-9

[Os(η^6-*p*-cymene)(TsBMEN)] (9). Complex **9** was synthesised by Miss. Yasmin Khanom. Following the method described for **2**, osmium *p*-cymene-chlorido dimer (44.1 mg, 0.056 mmol) was reacted with (1*R*,2*R*)- or (1*S*,2*S*)-(H)TsBMEN (50.0 mg, 0.17 mmol). After concentration *in vacuo*, the red oil was precipitated with hexane yielding an orange solid, then recrystallized from dichloromethane / hexane (9.0 mg, 0.01 mmol, 21%). ^{1}H NMR (500 MHz, $CDCl_3$, 25°C, TMS): δ=7.37 (d, ^3J(H,H) = 8.4 Hz, 2H, ArH), 7.26 (d, ^3J(H,H) = 7.7 Hz, 2H, ArH), 7.03 (d, ^3J(H,H) = 8.4 Hz, 2H, ArH), 6.93 (d, ^3J(H,H) = 7.7 Hz, 2H, ArH), 6.77 (d, ^3J(H,H) = 8.4 Hz, 2H, ArH), 6.70 (d, ^3J(H,H) = 8.4 Hz, 2H, ArH), 6.61-6.42 (m, 1H, NH), 5.83 (d, ^3J(H,H) = 5.4 Hz, 1H, ArH), 5.65 (d, ^3J(H,H) = 5.4 Hz, 1H, ArH), 5.60 (d, ^3J(H,H) = 5.4 Hz, 1H, ArH), 5.49 (d, ^3J(H,H) = 5.4 Hz, 1H, ArH), 4.37 (s, 1H; NHC*H*), 3.91 (d, ^3J(H,H) = 3.6 Hz, 1H, TsNC*H*), 3.80 (s, 3H; OCH_3), 3.78 (s, 3H; OCH_3), 2.51(sept, 1H; CH), 2.32 (*br.* s, 3H; CH_3), 2.30 (*br.* s, 3H; CH_3), 1.29 (d, ^3J(H,H) = 6.8 Hz, 3H, CH_3), 1.24 (d, ^3J(H,H) = 6.8 Hz, 3H, CH_3); ^{13}C NMR (125 MHz, $CDCl_3$, 25°C, TMS) δ 141.5, 140.6, 138.7, 136.7, 128.4, 128.0, 127.4, 126.9, 113.2, 91.0, 82.0, 82.4, 80.2, 72.7, 71.6, 70.8, 67.2, 55.3, 32.7, 23.5, 21.3, 20.7; UV/Vis: λ_{max} 275, 410, 477 nm; HRMS (*m/z*): $[M+H]^+$ calcd. for $C_{33}H_{39}N_2O_4OsS$, 751.2240; found, 751.2243. Elemental analysis for **(*R*,*R*)-9**: found (calcd. for $C_{33}H_{38}N_2O_4OsS$): C 53.39 (52.92), H 5.12 (5.11), N 3.89 (3.74).

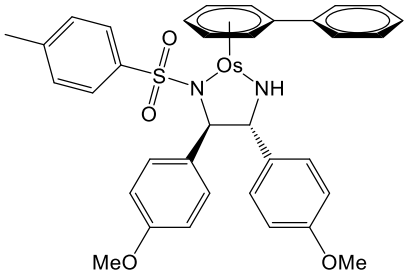

(*R*,*R*)-10

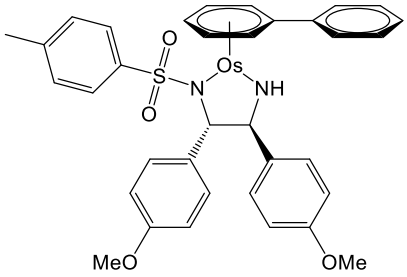

(*S*,*S*)-10

[Os(η^6-biphenyl)(TsBMEN)] (10). Complex **10** was synthesised and characterised by Miss. Yasmin Khanom. Following the method described for **2**, osmium *p*-cymene-chlorido dimer (48.1 mg, 0.058 mmol) was reacted with either (1*R*,2*R*)- or (1*S*,2*S*)-(H)TsBMEN (50 mg, 0.17 mmol). The purple oil was precipitated with hexane yielding an amorphous purple solid, which was recrystallized from dichloromethane / hexane (22 mg, 0.03 mmol, 50%). ^{1}H NMR (500 MHz, $CDCl_3$, 25°C, TMS): δ=7.40-7.49 (m, 2H, ArH), 7.28-7.35 (m, 3H, ArH), 7.24 (m, 1H, ArH), 7.19 (m, 1H, ArH), 7.17 (d, ^3J(H,H) = 8.1 Hz, 2H, ArH), 7.05 (*br*. s, 1H, NH), 6.86 (d, ^3J(H,H) = 8.3 Hz, 2H, ArH), 6.81 (d, ^3J(H,H) = 7.8 Hz, 2H, ArH), 6.63 (d, ^3J(H,H) = 8.3 Hz, 2H, ArH), 6.60 (d, ^3J(H,H) = 8.3 Hz, 2H, ArH), 6.18 (d, ^3J(H,H) = 5.3 Hz, 1H, ArH), 6.12 (d, ^3J(H,H) = 5.3 Hz, 1H, ArH), 6.08 (d, ^3J(H,H) = 5.3 Hz, 1H, ArH), 5.97 (d, ^3J(H,H) = 5.3 Hz, 1H, ArH), 5.91 (d, ^3J(H,H) = 5.3 Hz, 1H, ArH), 4.25 (s, 1H, CH), 3.75 (d, ^3J(H,H) = 3.8 Hz, 1H, CH), 3.71 (s, 3H, OCH_3), 3.68 (s, 3H, OCH_3), 2.24 (s, 3H, CH_3); ^{13}C NMR (125 MHz, $CDCl_3$, 25°C, TMS) δ 157.8, 157.2, 140.1, 139.6, 137.4, 136.6, 135.0, 128.0, 127.7, 127.4, 126.9, 126.4, 112.3, 81.8, 71.9, 69.7, 69.5, 67.2, 54.3, 20.3; UV/Vis: λ_{max} 275, 415, 486 nm; HRMS (*m/z*): $[M+Na]^+$ calcd. for $C_{35}H_{34}NaN_2O_4OsS$, 771.1929; found, 771.1920. Elemental analysis for **(*R*,*R*)-10**: found (calcd. for $C_{35}H_{34}N_2O_4OsS$): C 54.67 (54.67), H 4.74 (4.46), N 3.89 (3.64).

Os-H hydride formation.[23] **(*R*,*R*)-1** was titrated with triethylamine (4.0 mol equiv.) and formic acid (2 μL), allowing the observation of osmium hydride resonances. ^{1}H-NMR (600 MHz, C_6D_6, 298 K) δ = -5.89 (s, 1H; Os-H), -6.04 (s, 1H; Os-H).

3.2.4 X-ray crystallography

Single crystals of **(*R*,*R*)-2**, and **(*R*,*R*)-7·2CHCl$_3$** were grown from $CHCl_3$ / hexane. Crystallographic data were acquired and processed by Dr. Guy Clarkson (University of Warwick) as described in Chapter 2 (section 2.2.7).[24, 25]

3.2.5 Catalytic reactions

Studies were carried out with kind assistance from Dr. Roy Hodgkinson and Dr. Ivan Prokes (University of Warwick, UK). Transfer hydrogenation reactions using complexes **9** and **10** were carried out by Miss. Yasmin Khanom (University of Warwick, UK).

Racemic reduction of ketones with NaBH$_4$.[23] To an ice-cold solution of sodium borohydride (100 mg, 2.53 mmol, 2 mol equiv of H^-) in ethanol (1.5 mL) was added a prochiral ketone (5.14 mmol) dropwise under an atmosphere of nitrogen over 1 h, then allowed to warm to ambient temperature overnight. A white solid was precipitated by addition of HCl (3 M, 0.5 mL) which was extracted with diethyl ether (5 mL) and washed with water (5 mL). The organic layer was separated, dried over magnesium sulphate, and concentrated *in vacuo* yielding a colourless liquid. The product was characterised by ESI-MS and ^{1}H-NMR, and data obtained matched those previously reported.

Asymmetric reduction of ketones (S/C = 200).[23] 5:2 v/v formic acid / triethylamine azeotrope (500 μL) was added to a nitrogen-purged flask containing the catalyst (5 μmol, 1 mol equiv). A prochiral ketone was injected (1 mmol, 200 mol equiv) and stirred for 24 h. Aliquots of reaction solution were placed into 1 mL EtOAc and 1 mL $NaHCO_3$ and filtered through a plug of silica. Conversion and *ee* were analysed by GC-FID (Chrompac cyclodextrin-β-236M-19, 50 m x 0.25 mm x 0.25 μm, P = 15 psi, gas H_2; temperature varied for substrates) using Clarity Chromatography Suite.

Transfer hydrogenation kinetics. Catalyst **2-11** (5 μmol, 1 mol equiv) was dissolved in d^6-benzene (100 μL) and formic acid / triethylamine azeotrope (5:2, 500 μL) under a nitrogen atmosphere for 30 min (310 K). Acetophenone (1 mmol, 200 mol equiv) was injected and the mixture transferred to an NMR tube. Final solution concentrations: substrate 1.67 M; Os catalyst 8.33 mmol. Spectra were recorded in triplicate every 73 s at 310.0 ± 0.5 K for 1 h using a Bruker AV-400 spectrometer (Figure 3.3). Data processing is described in Chapter 2 (section 2.3.1).

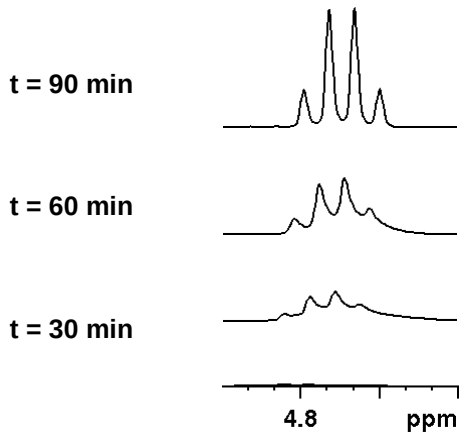

Figure 3.3. Reduction of acetophenone using **(*R*,*R*)-2** in formic acid / triethylamine, forming 1-phenylethanol (1H, quartet, 4.77 ppm) observed by time-dependent ^{1}H-NMR (400 MHz, 310 K, C_6D_6).

3.2.6 Density Functional Theory (DFT) calculations

Density functional theory (DFT) calculations were carried out using Gaussian 03W[26] with assistance from Dr. Adam Millett and Robbin Vernooij (University of Warwick).[27]

Gas phase geometry optimization was carried out using the hybrid Perdew-Burke-Ernzerhof functional (PBE0)[28] which is a combination of DFT (75%) and Hartree-Fock (25%) methods. The Lanl2DZ basis set including effective core potential was used for Os and 6-31+G** basis set for all other atoms.[29, 30] The calculations converged to optimized geometries by allowing all parameters to relax and they correspond to true energy minima, as revealed by the lack of imaginary values in the vibrational mode calculations. Structures were optimized using the x–ray crystallographic data as a starting guess and modifications made accordingly using GaussView 3.0.[31] Electrostatic potential surfaces (EPS) were mapped onto total electron density (isovalue = 0.04), represented with a colour scale from red (-0.025 au) to blue (0.250 au).

3.3 Results

3.3.1 Synthesis and characterisation of novel osmium(II) catalysts

The low-temperature reaction of a sulfonyl chloride with a chiral diamine, either (*R*,*R*) or (*S*,*S*)-configured, successfully yielded the mono-substituted sulfonamides (Figure 3.4a), which were readily recrystallized from toluene. Noyori-type ruthenium chlorido complexes are readily prepared by combining a metal-arene dimer $[RuCl_2(\eta^6\text{-arene})]_2$ and chiral sulfonamide in 2-propanol with triethylamine,[1] however the poor solubility of osmium-arene dimers in isopropanol meant that an alternative strategy was required.[23] We looked to previous methods used to isolate the active Ru catalyst, using a biphasic reaction with dichloromethane and water.[7]

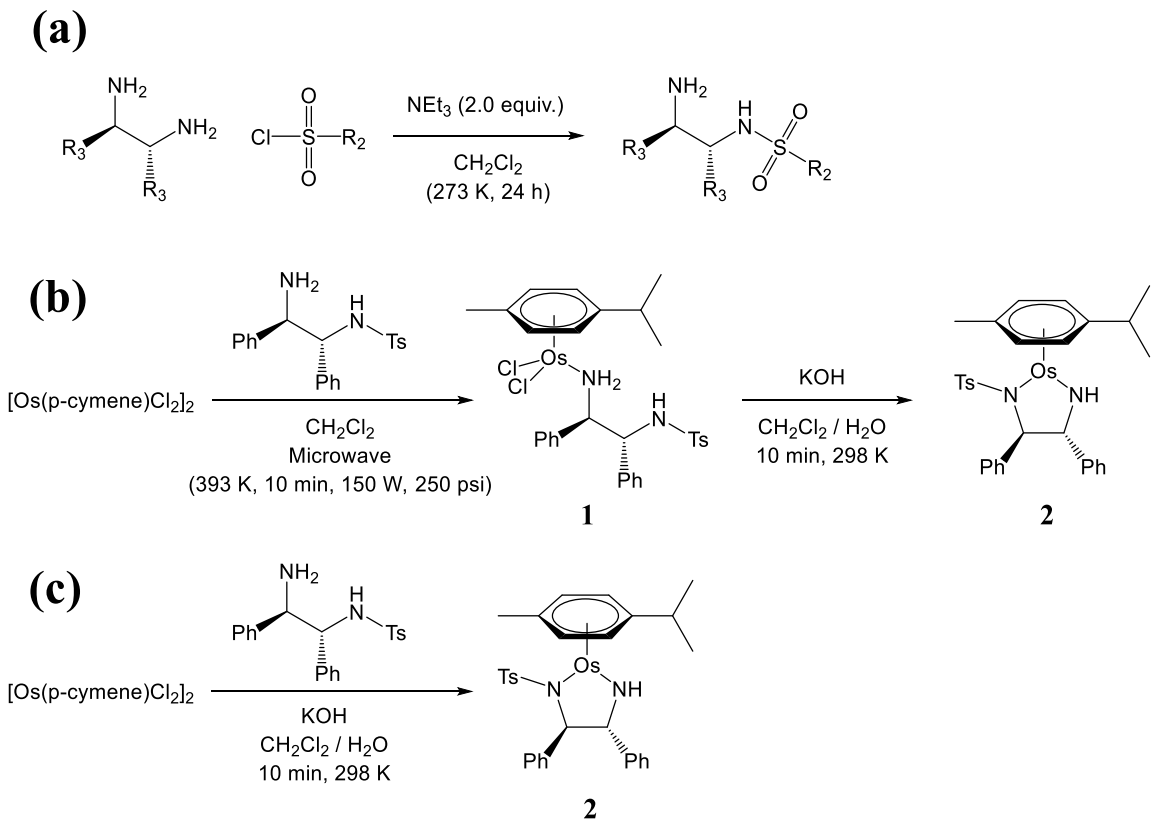

Figure 3.4. (a) General synthesis of sulfonamide ligands from the corresponding sulfonyl chloride, shown for (*R*,*R*)-diamine; (b) Synthesis of osmium 16-electron catalyst **2** via complex **1**, which was isolated and fully characterised. Scheme (b) applies for the synthesis of complexes **7**-**8**, and **10**;[23] (c) One-step synthesis of Os complex **2**. Scheme (c) applies for the synthesis of complexes **2**-**6**, and **9**.

Without addition of base, pale yellow 18-electron di-chlorido complexes were obtained (e.g. complex **1**, Figure 3.4b) which were readily synthesised using a microwave reactor. Upon treatment of **1** with a base, a red 16-electon amido complex **2** was obtained. analogous to the active ruthenium catalyst.[7, 23] Alternatively, direct reaction of the osmium *p*-cymene dimer with either enantiomer of the sulfonamide and a base at room temperature provided a one-step alternative synthetic strategy to obtain catalysts **2**-**6** and **9** (Figure 3.4c).[23] The poor solubility of the osmium biphenyl and terphenyl dimers in dichloromethane at room temperature meant that direct isolation of **7**, **8** or **10** at room temperature was not possible, so these complexes were synthesised by method (b). In each case, both enantiomers of the 16-electron osmium complexes (**2**-**10**) were individually synthesised by reacting the osmium dimer with either an (*R*,*R*) or (*S*,*S*)-ligand to obtain enantiomerically-pure complexes.

Treatment of **(*R*,*R*)-1** with triethylamine and formic acid allowed for observation of osmium hydride complex [OsH(*p*-cymene)(TsDPEN)] by ^{1}H-NMR. The hydride was detected as two singlets, δ = -5.89 ppm and -6.04 ppm, suggesting formation of two diastereomers, with ^{187}Os satellites ($^{1}J(^{187}\text{Os},^{1}\text{H})$ = 44 Hz). The ratio between the singlets changed over 30 min, from 3:1 (left), to 1.2:1 (right) shown in Figure 3.5.[23]

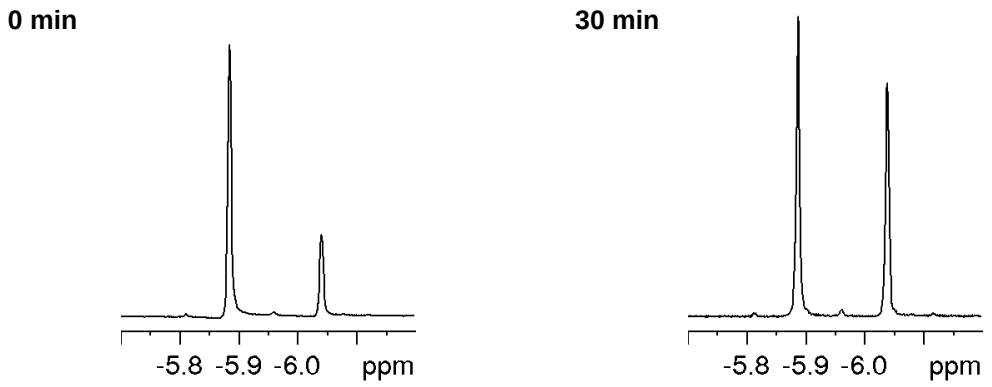

Figure 3.5. ^{1}H-NMR spectrum (600 MHz, C_6D_6, 298 K) of **(*R*,*R*)-1** treated with formic acid / triethylamine showing the peaks for Os-H species with ^{187}Os satellites (1.96% abundance).[23]

3.3.2 X-ray crystallography

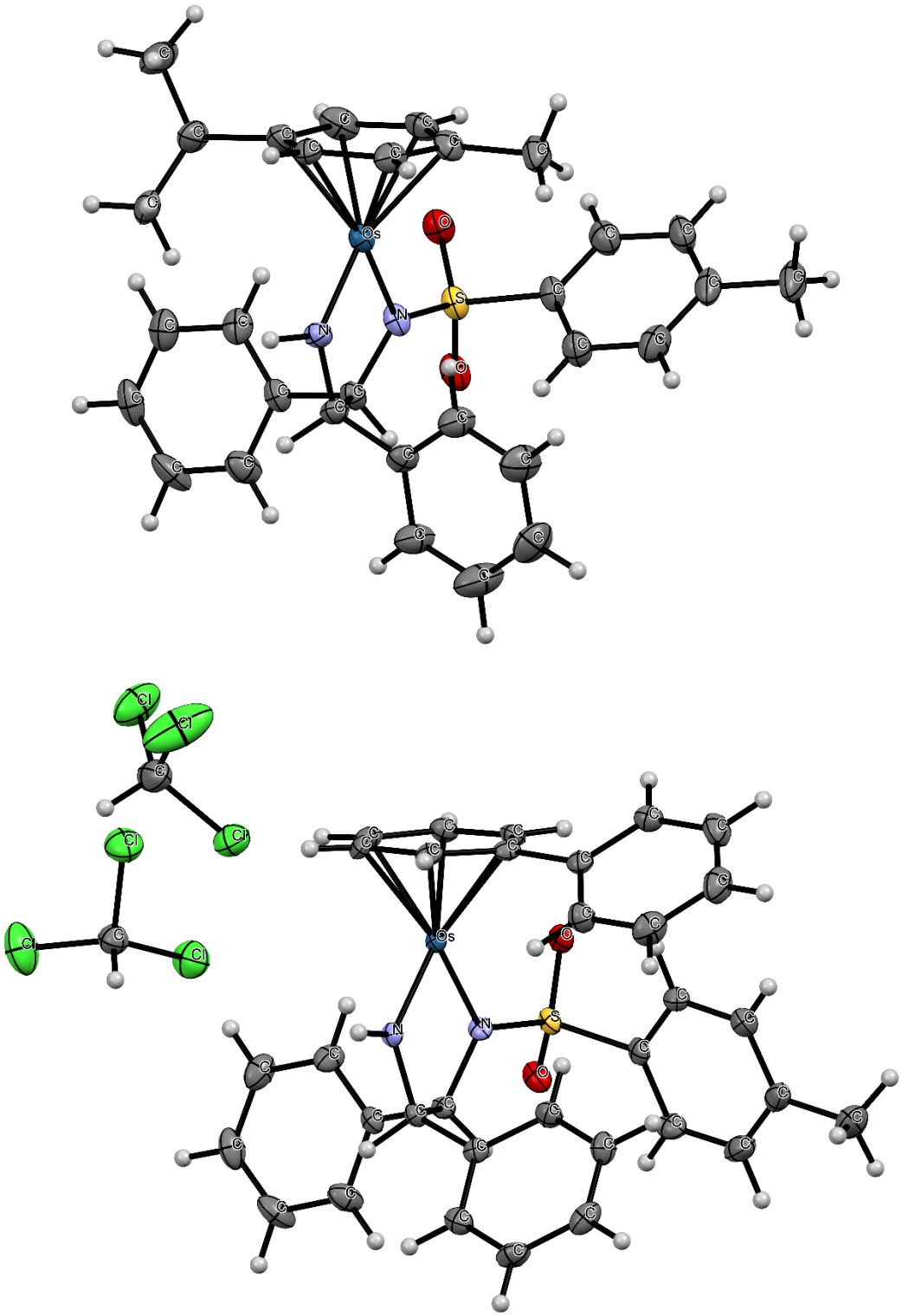

Figure 3.6. ORTEP diagrams of *p*-cymene complex **(*R*,*R*)-2** (above) and biphenyl complex **(*R*,*R*)-7** (below). Thermal ellipsoids shown at 50% probability level, coloured and labelled by element. See appendix Tables A1-A2 for Cartesian atom coordinates.[23]

Table 3.2. X-ray crystallographic data for *p*-cymene **(*R*,*R*)-2** and biphenyl **(*R*,*R*)-7** complexes.[23]

	(*R*,*R*)-2	**(*R*,*R*)-7 • 2CHCl$_3$**
Crystal character	red block	red rod
Empirical formula	$C_{31}H_{34}N_2O_2OsS$	$C_{33}H_{30}N_2O_2OsS \bullet 2CHCl_3$
MW / gmol^{-1}	688.86	947.59
Temperature / K	150(2)	150(2)
Crystal system	orthorhombic	orthorhombic
Space group	$P2_12_12_1$	$P2_12_12_1$
***a* (Å)**	10.6100(3)	7.95564(14)
***b* (Å)**	13.8464(3)	16.3879(3)
***c* (Å)**	18.9830(5)	26.8668(5)
***α* / °**	90	90
***β* / °**	90	90
***γ* / °**	90	90
Volume / Å^3	2788.79(11)	3502.80(11)
Z	4	4
μ / mm^{-1}	4.678 mm^{-1}	4.194
F (000)	1368.0	1864.0
Crystal size / mm^3	0.16 × 0.10 × 0.10	0.35 × 0.01 × 0.01
Reflections measured	33345	49980
Independent reflections	8053	10869
R_1 [I>2σ(I)]	0.0333	0.0333
wR_2	0.0927	0.0574
ρ_{calc} / gcm^{-3}	1.641	1.797
Radiation	Mo Kα (λ = 0.71073)	Mo Kα (λ = 0.71073)
Flack parameter	-0.023(5)	-0.012(4)
2Θ range for collection / °	4.836 to 61.698	5.2 to 63.1
Goodness-of-fit on F^2	1.162	1.020
CCDC number	1035611	1507733

Single crystals of both enantiomers of **2** and **7** suitable for x-ray diffraction were obtained from a saturated solution of the complex in dichloromethane with addition of *n*-hexane at 253 K (see appendix Tables A1-A2 for Cartesian atom coordinates).

3.3.3 Storage stability of osmium sulfonamide complexes

Storage of the solid catalyst in atmospheric air at 298 K was studied by ^{1}H-NMR (400 MHz, $CDCl_3$). No evidence of ligand release was identified after three months.[23] After twelve months, the formation of a new septet (2.87 ppm) was apparent, corresponding to release of *p*-cymene (Figure 3.7).

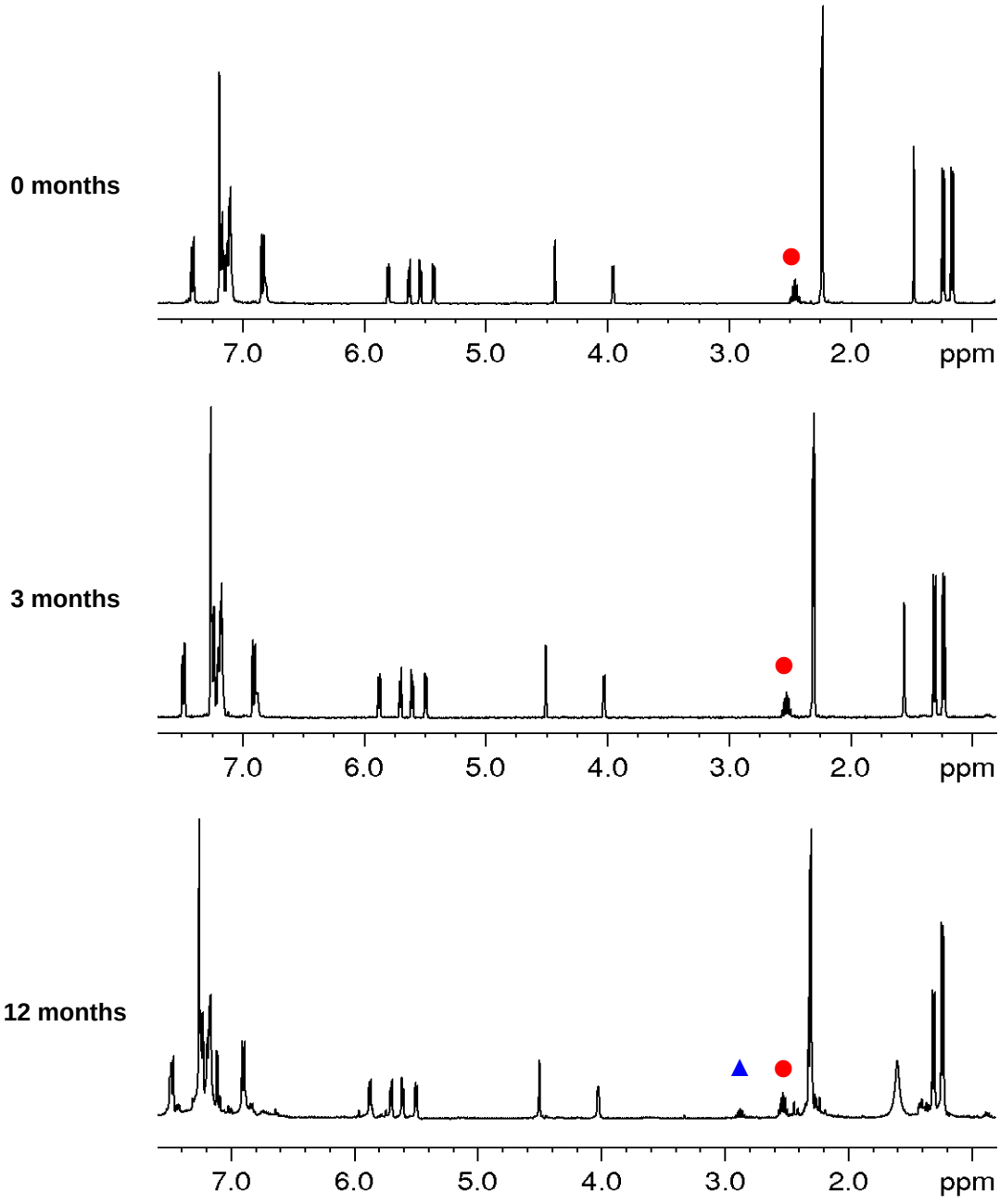

Figure 3.7. ^{1}H-NMR (400 MHz, $CDCl_3$, TMS, 298 K) of complex **(*S*,*S*)-2** stored under ambient conditions (298 K, atmospheric air): (a) day of synthesis; (b) three months; (c) twelve months. ● *p*-cymene ArC*H*$(CH_3)_2$ (coordinated ligand); ▲ *p*-cymene ArC*H*$(CH_3)_2$ (uncoordinated ligand).

3.3.4 Solution stability of osmium sulfonamide complexes

Aqueous stabilities were investigated in phosphate-buffered saline by UV-visible spectroscopy over a 24 h period at 310 K. Though previous studies use water/methanol solutions to probe the aqueous chemistry of half-sandwich piano stool compounds,[32] the possibility of methanol acting as a hydride donor (becoming itself reduced to formaldehyde) means that an alternative solubilising agent was required. In accordance with biological experiments carried out later in this thesis, dimethylsulfoxide (DMSO, 5 % v/v) was used. All osmium complexes displayed surprisingly high stability in phosphate buffered saline (137 mM NaCl, 5 % DMSO, 310 K) with no change observed in the absorbance profile (Figure 3.8 – representative example for parent osmium tosyl complex **2**). Though solubility in PBS was poor, arene extension in complexes **7**-**8** did not affect the aqueous stability. Similarly, neither sulfonamide variation in complexes **3**-**6**, nor methoxy substitution to the phenyl groups at the chiral centres in complexes **9**-**10**, affected stability in phosphate-buffered saline (137 mM NaCl, 5 % DMSO, 310 K)

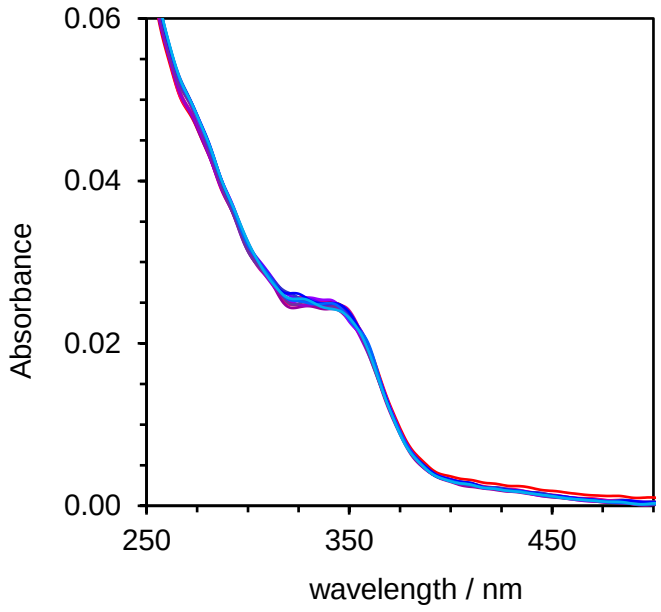

Figure 3.8. Representative example (complex **(*S*,*S*)-2**) of UV-visible spectroscopy stability study in phosphate-buffered saline containing 5% v/v DMSO (24 h, 310 K) recorded every 1 h.

Though dimethylsulfoxide (DMSO) is commonly used to aid dissolution of hydrophobic complexes in aqueous solution, DMSO can act as a ligand, either through sulphur or oxygen coordination, and so it is important to investigate whether any interaction between the complex and solvent occurs. This was examined using ^{1}H-NMR spectroscopy over a 24 h period (Figure 3.9), after incubation at 310 K. The spectra were unchanged for all complexes after 24 h, suggesting that the osmium complexes are either highly stable in DMSO and do not form solvent adducts, or adducts form very fast quickly.

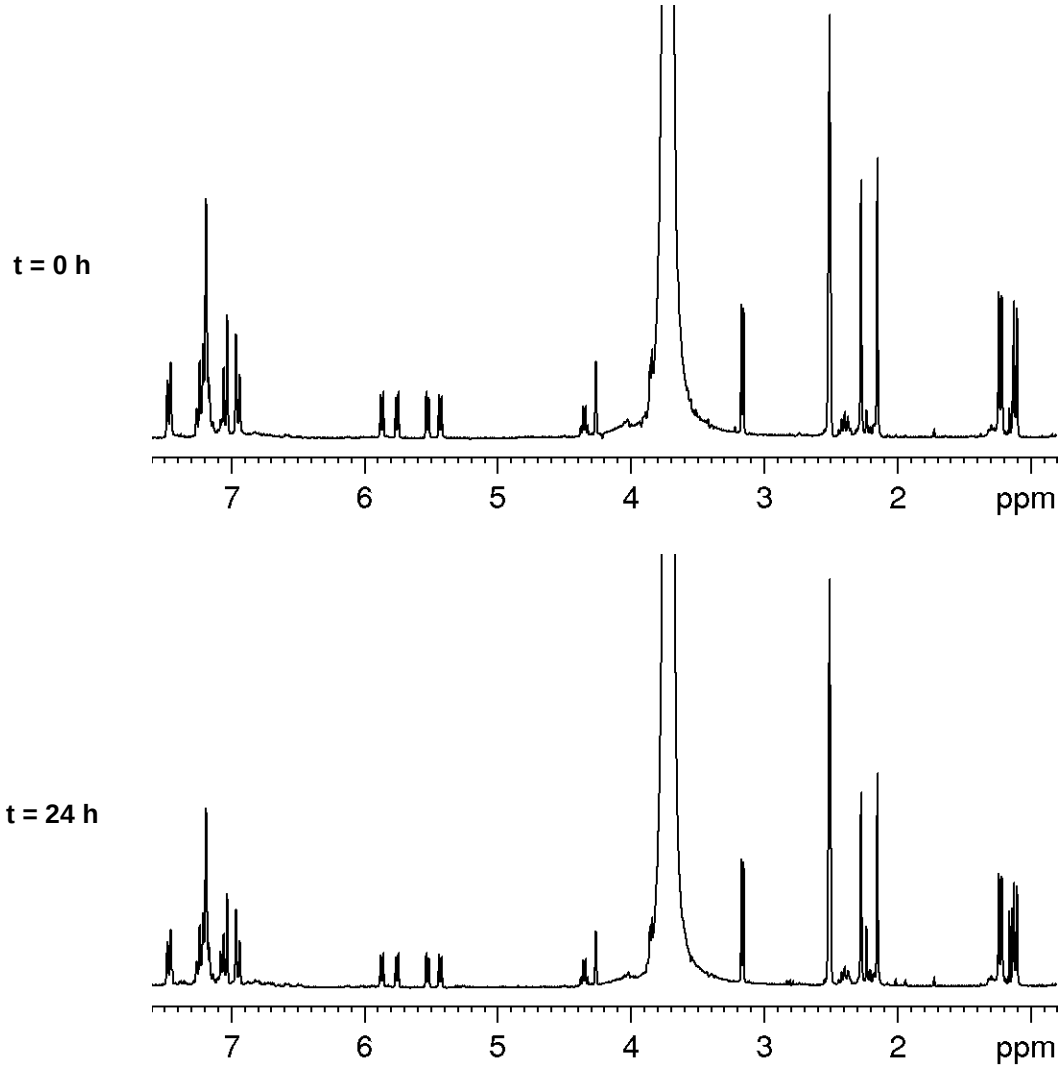

Figure 3.9. ^{1}H-NMR spectroscopy stability study in d^{6}-DMSO (24 h, 310 K). Representative example shown for complex **(*S*,*S*)-2**.

The active catalysts are rapidly synthesised using a biphasic solvent system of dichloromethane (containing the metal arene dimer and ligand) and water (containing a base, typically potassium hydroxide), Figure 3.4. An inert atmosphere was not necessary during synthesis. Controlled deprotonation of intermediate **1** can occur, the organic layer isolated (base removed with aqueous extractions), and the compound slowly precipitated from dichloromethane on addition of a suitable hydrocarbon solvent (*n*-hexane) to yield **2** as a red solid.[23] Substitution of the sulfonamide, arene and phenyl groups at the chiral centres was not found to affect the stability of the active 16-electron catalyst, and so an analogous method may be utilised to obtain complexes **3**-**10**, using the corresponding diamine ligand and osmium arene chlorido dimer.

The active 16-electron osmium complexes proved highly stable under storage in both atmospheric air and aqueous solution. The aqueous reactivity of Os(II) complexes has previously been shown to be highly dependent on the chelating ligand(s), as while the rate of hydrolysis of [Os(arene)(acac)Cl] was too fast to observe by NMR (298 K), the hydrolysis of $[Os(arene)Cl(ethylenediamine)]^+$ is ca. 40× slower than the isoelectronic ruthenium analogue.[33] Third-row transition metal ions are typically more kinetically inert than second-row ions, which likely discouraged investigation of the osmium TsDPEN analogues. This work demonstrates that the osmium 16-electron catalysts are kinetically inert, and stable upon storage and in solution.

3.3.5 Asymmetric transfer hydrogenation

Reduction of acetophenone, a widely used prochiral ATH substrate, was studied using formic acid as a hydride donor in the presence of a base (triethylamine), catalysed by complexes **1-11**. Conversion and enantioselectivity were determined using chiral gas chromatography,[23] and maximum turnover frequencies (TOF_{max}) were determined by ^{1}H-NMR (Table 3.4). All complexes achieved >92% conversion and higher TOF_{max} than Ru catalyst **11** under identical conditions.

Table 3.4. Reduction of acetophenone using formic acid catalysed by **2**-**10** or Ru analogue **11**.[23]

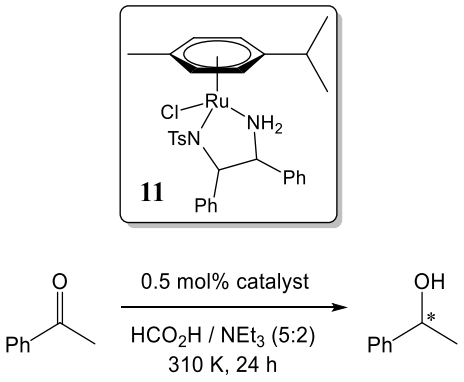

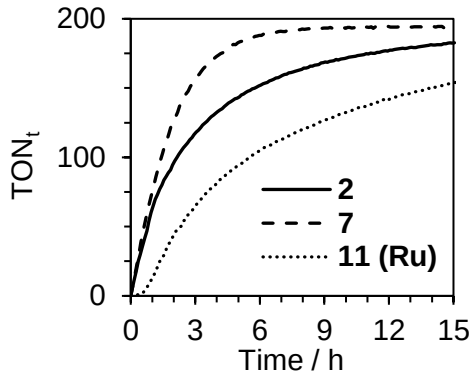

Catalyst	S/C [a]	Temp. / K	conv. [b]	ee (%) [b]	config. [b]	TOF / h^{-1} [c]
(*R*,*R*)-2	200	310	99	99	(*R*)	63.6 ± 0.6
(*S*,*S*)-2	200	310	99	99	(*S*)	63.9 ± 0.3
(*S*,*S*)-3	200	310	99	96	(*S*)	58 ± 2
(*S*,*S*)-4	200	310	99	95	(*S*)	61 ± 2
(*S*,*S*)-5	200	310	99	96	(*S*)	40 ± 2
(*S*,*S*)-6	200	310	92	97	(*S*)	58 ± 1
(*R*,*R*)-7	200	310	98	92	(*R*)	78.2 ± 0.4
(*S*,*S*)-7	200	310	99	95	(*S*)	78 ± 1
(*S*,*S*)-8	200	310	99	99	(*S*)	43 ± 2
(*R*,*R*)-9	200	310	98	99	(*R*)	35 ± 1
(*R*,*R*)-10	200	310	99	99	(*R*)	61.4 ± 0.6
(*S*,*S*)-11	200	310	99	99	(*S*)	23 ± 1

[a] Substrate / catalyst ratio. [b] Determined by chiral GC. [c] Maximum turnover frequency (initial linear reaction rate) determined by ^{1}H-NMR.

Catalyst **1** was screened for the reduction of alpha- and *para*-substituted acetophenone derivatives (Table 3.5), for comparison with ruthenium complex **11**. The osmium complexes maintained high enantioselectivity but conversion was decreased for reduction of propiophenone (Y = Et) and 4'-methoxyacetophenone (X = OMe).[23] **1** and **2** were also investigated after 2 months storage in atmospheric conditions and retained high conversion and enantioselectivity (Table 3.6).[23]

Table 3.5. Reduction of acetophenone-derived ketones by pre-catalyst **1**, compared to the Noyori second-generation ruthenium(II) analogue, **11**.[23]

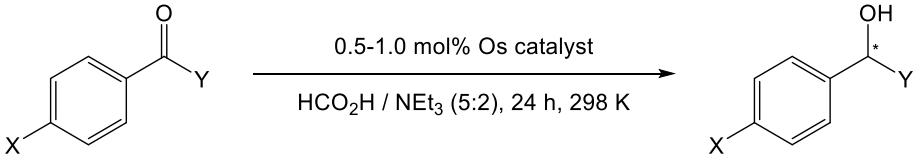

Ketone	Catalyst	S/C	conv.[a]	ee (%)[a]	config.[a]
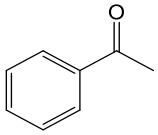	**(*R*,*R*)-1**	100	99	98	(*R*)
	(*S*,*S*)-1	100	99	98	(*S*)
	(*S*,*S*)-11	200	99	99	(*S*)
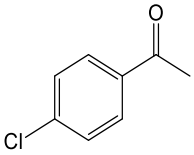	**(*R*,*R*)-1**	100	98	96	(*R*)
	(*S*,*S*)-1	100	97	94	(*S*)
	(*S*,*S*)-11	200	99	95	(*S*)
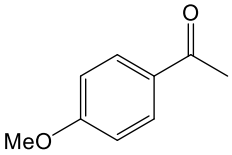	**(*R*,*R*)-1**	100	67	N.D.[b]	(*R*)
	(*S*,*S*)-1	100	70	99	(*S*)
	(*S*,*S*)-11	200	99	97	(*S*)
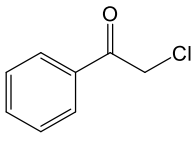	**(*R*,*R*)-1**	100	97	94	(*S*)
	(*S*,*S*)-1	100	92	84	(*R*)
	(*S*,*S*)-11	1000	36[c]	91[c]	(*R*)
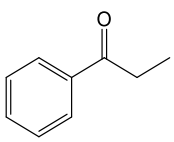	**(*R*,*R*)-1**	100	56	96	(*R*)
	(*S*,*S*)-1	100	54	95	(*S*)
	(*S*,*S*)-11	200	96	97	(*S*)

[a] Determined by chiral GC. [b] e.e. undetermined for the reduction of α-chloroacetophenone ($R_2 = CH_2Cl$) due to poor separation of enantiomers. [c] Reduction of propiophenone (Y = Et) with Ru^{II} catalyst was conducted in 1.0 M EtOAc with S/C = 1000

Table 3.6. Reduction of acetophenone by formic acid catalysed by Os (pre)catalysts **1** and **2**. Conversion and enantiomeric excess remain high after several months of storage under ambient conditions.[23]

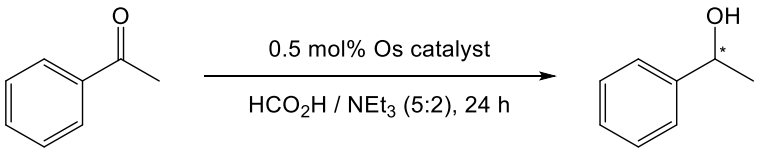

Catalyst	Storage	S/C	Temp. / K	conv.[a]	ee (%)[a]
(*R*,*R*)-1	2 months	200	310	99	98
(*R*,*R*)-2	2 months	200	310	95	98

[a] Determined by chiral GC.

3.3.6 Density Functional Theory (DFT)

Density functional theory was used to examine the effect of sulfonamide substitution on key bonds involved in the Noyori-type catalytic mechanism, and visualisation of the distribution of charge density across the molecule. Calculations were carried out at the PBE0/Lanl2DZ/6-31+G** level.[29] Only (*R*,*R*)-complexes were assessed by DFT. The input guesses for the geometry optimisations were based on the crystal structures of **(*R*,*R*)-2** and **(*R*,*R*)-7** and modified accordingly. The obtained ground state geometries of the complexes **2-10** were compared to the crystal structures. Calculated Cartesian coordinates are listed in Appendix Tables A3-A11.

Calculated bond lengths were found to correlate well with crystallographic data, and selected bond lengths are shown in Table 3.7. No significant trends were observed between the compounds with regards to the selected bond lengths.

Electrostatic potential surfaces were obtained by mapping electrostatic potential onto the total electron density surface for Os(II) sulfonamide complexes **2-10.** The calculated surfaces provide an indication of charge distribution on the overall

complex, and were used to identify sites at which electrostatic interactions with a substrate molecule may occur (such as the highly polarised sulfonamide). Furthermore, the EPS surfaces could be used to assess the effect of different substitutions on the electrostatics within the series of complexes (Figure 3.10). Substitution at the sulfonamide group results in localised charge effects only, clearly identifiable for **4** (R = nitrophenyl) and **5** (R = fluorophenyl). No significant charge effect is observed at the metal centre, *p*-cymene ring (in the case of **2**-**6**) nor at the nitrogen atoms of the diamine, which are considered essential for transfer hydrogenation by M-TsDPEN complexes.[34] Methoxy-substituents in **9** and **10** cause the chiral aromatic groups to become slightly more negatively charged due to electron-donation from OMe into the π system from the oxygen lone pair. This donation strengthens the C-O bond, observed by the shorter bond length (1.36 Å), compared to a typical C-O (1.43 Å).

Table 3.7. Calculated (DFT) bond lengths of **2**-**10** compare well to x-ray crystallographic data. Data were calculated at the PBE0/Lanl2DZ/6-31+G** level.[29]

	Os-N(H)	**Os-N**(S)	**C-N**(S)	**C-N**(H)	**C-C**	**S-N**(S)
2 (XRD) [a]	1.916	2.046	1.447	1.469	1.557	1.611
2	1.917	2.017	1.465	1.450	1.541	1.646
3	1.914	2.021	1.464	1.451	1.542	1.646
4	1.916	2.024	1.468	1.451	1.540	1.636
5	1.916	2.021	1.466	1.450	1.540	1.644
6	1.917	2.020	1.456	1.450	1.541	1.644
7 (XRD) [a]	1.902	2.066	1.477	1.465	1.546	1.59]
7	1.908	2.024	1.467	1.454	1.546	1.649
8	1.903	2.023	1.472	1.454	1.542	1.655
9	1.915	2.018	1.466	1.451	1.541	1.644
10	1.905	2.025	1.467	1.455	1.547	1.647
11 (XRD) [a]	1.897	2.065	1.472	1.454	1.551	1.592

[a] From published crystallographic data.[7, 23]

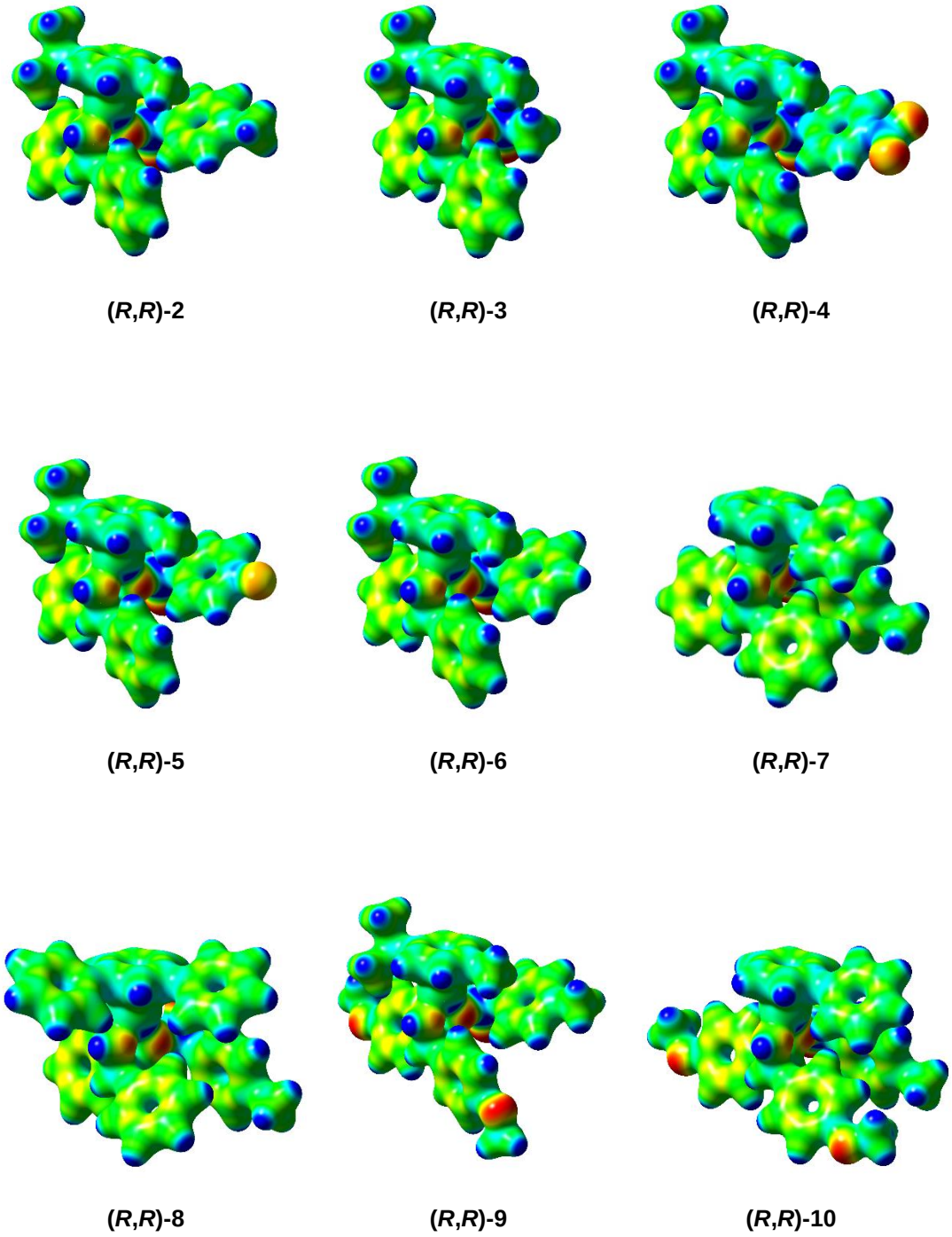

Figure 3.10. Electrostatic potential surfaces for osmium sulfonamide complexes **2**-**10** (calculated at the PBE0/Lanl2DZ/6-31+G** level) mapped onto total electron density. Isovalue = 0.04. (*R*,*R*)-configured catalysts only. Surface mapping colours range from red (-0.025 au) to blue (+0.250 au). Calculated Cartesian atom coordinates are fully listed in appendix Tables A3-A11.

3.4 Discussion

3.4.1 Structure elucidation of a novel osmium(II) pre-catalyst

It was anticipated that Os complexes synthesised in the absence of base would differ structurally from the analogous Ru species containing a bidentate diamine.[7] Elemental analysis suggested that complex **1** contained the diamine coordinated only by the terminal amine, while two chlorido ligands remained complexed to the metal centre. By infrared (FT-IR) spectroscopy, the TsN-H bond stretch (2859 cm^{-1}) remains unchanged between **1** and the free ligand, whilst terminal amine N-H stretches were shifted from 3344 and 3281 cm^{-1} to 3078 and 2953 cm^{-1} upon coordination. Dichlorido **1** was also identified by high resolution mass spectrometry ($[M-H]^-$ calculated for $C_{31}H_{35}Cl_2N_2O_2OsS$, 761.1406; found, 761.1347).[23]

3.4.2 X-ray crystallography

The crystal structures of **2** and **7** were determined to have a Flack parameter greater than 2σ from zero however this is within an acceptable range for complexes synthesised from compounds of known chirality.[23, 35] The osmium(II) structures are remarkably similar to the known 16-electron Ru(II) analogue (CCDC 686925).[7] Catalyst **7** was isolated as a single crystal co-crystallised with two molecules of dichloromethane (Figure 3.6). The N-H bond in the osmium biphenyl compound is found to resemble closely that of the Noyori complex N-H (0.88 Å). In the case of both enantiomers of *p*-cymene complexes **2**, a single hydrogen bond is observed in the solid state between the NH proton and sulfonamide oxygen (2.11 Å), however complexes **7** (biphenyl complexes) do not display such hydrogen bonding. In addition, no π-π stacking < 4 Å was observed in any of the structures.

3.4.3 Transfer hydrogenation catalysis

Formic acid was utilised as a sacrificial source of hydride. Unlike reversible hydride donation by alcohols such as isopropanol,[1, 36] formic acid provides an effectively irreversible solution due to the evolution of carbon dioxide.[37] Treatment of **1** with formic acid allowed for the observation of an osmium hydride intermediate by ^{1}H-NMR, observed as two singlets (-5.89 and -6.04 ppm) corresponding to the two hydride complex diastereomers (Figure 3.11). ^{187}Os (I = ½, 1.6% natural abundance) satellites were also observed, with a coupling constant ($^{1}J(^{187}\text{Os},^{1}\text{H})$ = 44 Hz) similar to other reported osmium hydrides (14.4-38.1 Hz).[38] Over 30 min, the ratio between the hydride resonances decreased, from 3:1 to 1.2:1. Though both hydrides form, enantioselectivity of ketone reduction likely results from either (a) greater rate of reactivity of one hydride isomer, as suggested for the analogous ruthenium hydride;[39, 40] or (b) thermodynamically favourable interaction between a specific hydride enantiomer and the ketone.[23]

The traditionally-accepted mechanism of enantioselectivity by Noyori-type catalysts involves a combination of steric effects (involving the phenyl groups at the chiral centres of the diamine, Figure 3.11) and electrostatic interaction between the catalyst arene and the aromatic group of the substrate, occurring via a concerted outer-sphere transition state.[2, 41] However, recent studies suggest that a step-wise mechanism involving the solvent may more accurately describe face-specific hydrogen transfer.

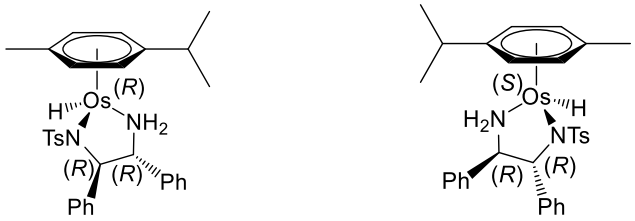

Figure 3.11. The osmium hydride [OsH(arene)(diamine)].forms as a mixture of diastereomers.

Catalytic activity of osmium sulfonamide complexes

Tosyl-DPEN complexes (**2**, **7**, **8-10**) achieved remarkably high enantioselectivity and conversions (> 99% *ee*).[23] Similarly to the parent ruthenium analogue **11**, (*R*,*R*)-configured catalysts afforded the corresponding (R)-alcohol, and (S) catalysts afforded the (*S*)-alcohol, respectively.[19, 37] No statistically-significant difference in activity was observed between enantiomers of **2** or **7**. Sulfonamide substitution (**3-6**) led to a reduction in enantioselectivity, however the complexes still achieved high conversion in 24 h. Reported studies have suggested that the disfavoured transition state may be destabilised by an unfavourable interaction with the sulfonyl of the ligand.[19, 42, 43] The addition of methoxy-substituents on complexes **9-10** did not have an effect on the enantioselectivity of the catalyst.

All osmium catalysts investigated displayed hydrogenation rates (TOF) greater than that of parent Ru catalyst **9** under identical conditions ($23 \pm 1\ h^{-1}$), even after allowing the ruthenium active catalyst to form *in situ*. The highest turnover frequency was achieved by the biphenyl catalyst **7** ($78.2 \pm 0.4\ h^{-1}$). Both sulfonamide substitution and methoxy substitution were found to reduce significantly the TOF relative to the tosyl compound **2** (63.9 ± 0.3). The fluorine atom of complex **5** may have led to a hindrance of reaction rate by forming a hydrogen bond with another catalyst molecule (Figure 3.12) however this is difficult to prove experimentally.

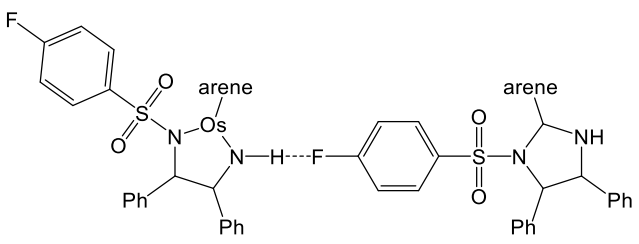

Figure 3.12. Suggested intermolecular hydrogen bonding between molecules of **5**.

Dichlorido osmium complex **1** is also able to act as a catalyst for ATH reactions (Table 3.4). Upon treatment with a base, osmium complex **2** forms *in situ*.[23] The high stability of osmium catalyst **2** allows for it to be prepared and used directly, and hence the catalysed reaction occurs immediately without a lag phase. This is unlike the reaction profile of Ru complex **11**, which requires chloride dissociation before catalysis is initiated (Figure 3.13). Whilst the ruthenium 16-electron active catalyst has been isolated and fully characterised, it is not sufficiently stable to warrant use over the Ru(II) chlorido pre-catalyst.

Reduction of acetophenone-derived ketones using complex **1** exhibited similar behaviour for Ru and Os catalysts. In both cases, conversion is decreased for ketones bearing electron-donating substituents (e.g. MeO) while ketones containing electron withdrawing groups maintain high conversion but exhibit decreased enantiomeric excess. The resulting enantioselectivity therefore results from a combination of both steric and electronic effects in the substrate.

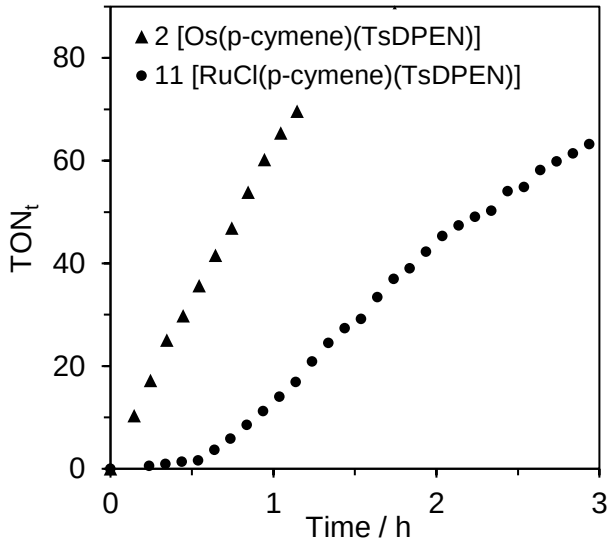

Figure 3.13. Ru catalyst **11** (●) must first dissociate chloride, observed as a lag-phase in the first hour of reduction. Os catalyst **2** (▲) exhibits instantaneous rate linearity.

Based on experimental data, the postulated mechanism of transfer hydrogenation is summarised in Figure 3.14. Pre-catalyst **1** eliminates chloride ligands to form active catalyst **2**. Hydride is then transferred to **2** from formic acid, yielding an intermediate hydride complex as a mixture of diastereomers. Favourable CH-π interactions between a prochiral ketone substrate and the catalyst orientate the transition state to favour reduction of the carbonyl on a specific face, controlled by steric interactions with the chiral diamine of the catalyst. After transfer, the 16-electron catalyst is regenerated.

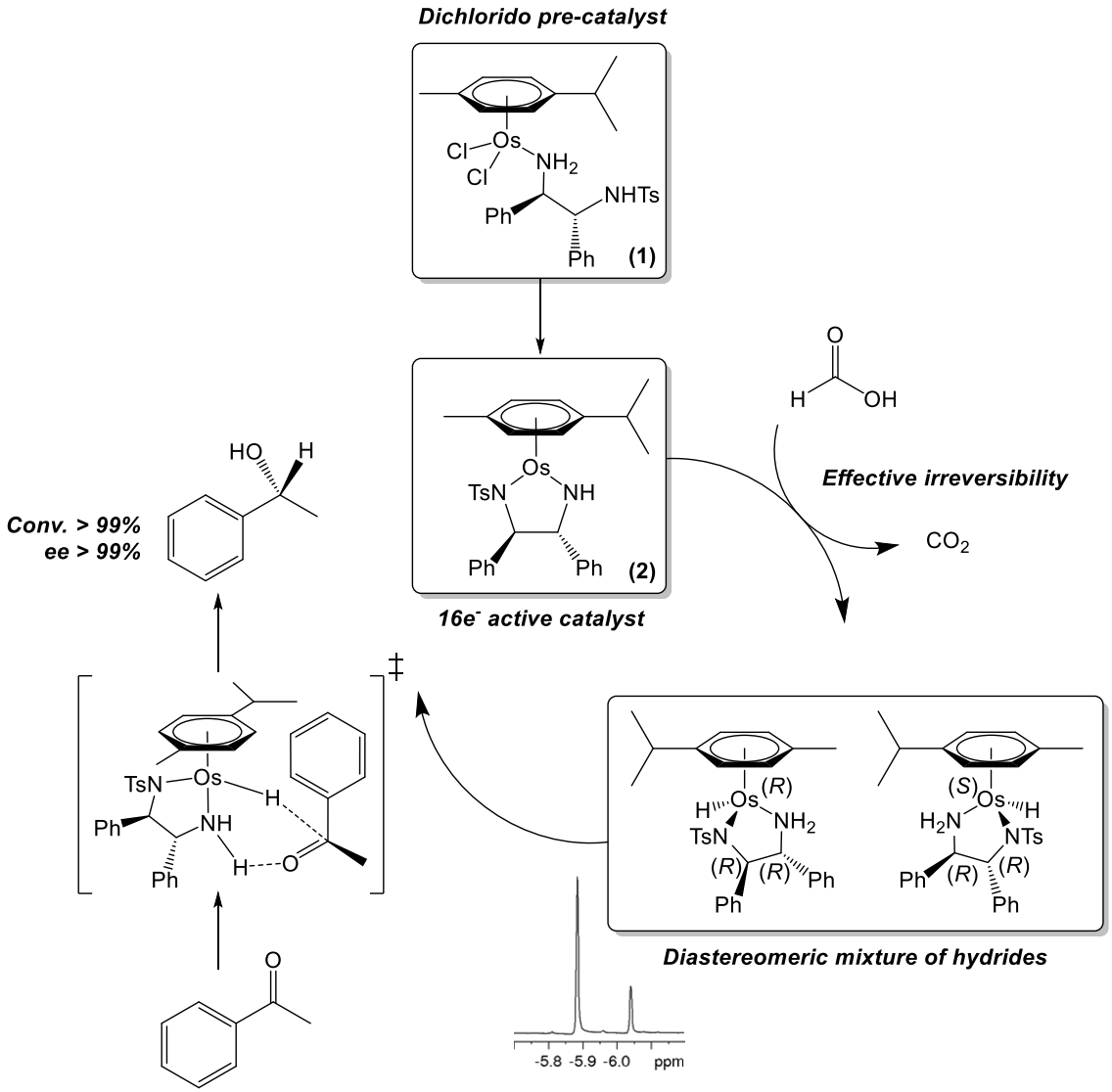

Figure 3.14. Proposed mechanism of transfer hydrogenation by Os sulfonamide complexes **1** and **2**.

3.4.4 Density Functional Theory (DFT)

To better understand and compare the catalytic performance of the osmium complexes, we looked to theoretical methods. In particular, Density Functional Theory (DFT) is a valuable tool for an N-body system, where solving the Schrödinger equation would be computationally impossible. Instead, DFT provides an approximation of the solution, using the electron density. Mixed basis sets (Lanl2DZ/6-31+G**) are frequently used to simulate organometallic complexes.[44] The metal centre was approximated by using Los Alamos National Laboratory basis set with an effective core potential (ECP; Lanl2DZ)[29] and all other atoms by the Pople basis set, (6-31+G**).

DFT calculations for complexes **2**-**10** show high similarity between all systems, in agreement with high conversions and enantioselectivities observed in catalytic studies. The more positive electrostatic potentials of *p*-cymene and biphenyl (compared to the phenyl groups) are due to the donation of electrons from aromatic π orbitals to form σ and π-bonds with metal-based orbitals. The metal is also capable of δ-backbonding interactions with aromatic molecular orbitals. Activating groups such as OMe in complexes **9** and **10** give rise to localised charge effects, with some donation of electron density into the corresponding aromatic rings. Little effect, however, is observed at the metal centre. This is mostly likely due to the distance of the substitution site from the inner coordination sphere. This could explain why **9**-**10** retain the high activity and enantioselectivity of parent compounds **2** and **7**, respectively. The low TOF for acetophenone reduction using catalyst **5** may be due to the presence of intermolecular hydrogen bonding via fluorine, observed as a charge localisation at the point of substitution. However, this is difficult to prove experimentally as well as computationally and goes beyond the scope of this thesis.

3.5 Conclusions

Coordinatively-unsaturated 16-electron osmium sulfonamide complexes can be prepared from their corresponding metal-arene dimer and diamine ligand in the presence of a base, in under an hour. Structural modifications are readily introduced, by substitution of various groups at the sulfonamide or chiral phenyl groups, or by arene chain extension. Though coordinatively-unsaturated, complexes **2**-**10** were found to be highly stable in both air and in both PBS and DMSO solutions. Crystallographic data were obtained for *p*-cymene (**2**) and biphenyl (**7**) complexes, and were found to be similar to the Ru catalyst to which they are related (Table 3.7).

Upon treatment of complex **1** with formic acid as a hydride source, an osmium-hydride intermediate was observed by ^{1}H-NMR, evidence for the postulated transfer hydrogenation mechanism. All osmium catalysts exhibited higher turnover frequencies for the reduction of acetophenone than the ruthenium sulphonamide **11**, under identical conditions. The osmium catalysts demonstrated good tolerance of electron donating and withdrawing substituents on acetophenone-derived ketone substrates, maintaining high conversion and enantioselectivity. The structure of a novel dichlorido osmium complex (**1**) was elucidated, which was shown to be equally as useful as a catalyst as the 16-electron active catalyst. DFT calculations highlight the similarity between the Os series, and that substitution on complexes **3**-**6** and **9**-**10** appears to only cause localised effects.

The complexes would benefit from future investigation into scope of the catalytic reactions; including more challenging substrates (such as imines and aliphatic ketones) or exploration of tolerance towards forcing reaction conditions (i.e. increased temperature, lower catalyst loading). Overall, Os sulfonamide complexes offer a viable and useful alternative to existing Ru catalysts in ATH reactions.

3.6 References

1. S. Hashiguchi, A. Fujii, J. Takehara, T. Ikariya and R. Noyori, *J. Am. Chem. Soc.*, 1995, **117**, 7562-7563.
2. R. Noyori, M. Yamakawa and S. Hashiguchi, *J. Org. Chem.*, 2001, **66**, 7931-7944.
3. C. Wang, X. Wu and J. Xiao, *Chem. Asian J.*, 2008, **3**, 1750-1770.
4. T. Ohkuma, *Proc. Jpn. Acad. Ser. B Phys. Biol. Sci.*, 2010, **86**, 202-219.
5. C. A. Sandoval, T. Ohkuma, K. Muñiz and R. Noyori, *J. Am. Chem. Soc.*, 2003, **125**, 13490-13503.
6. W. Baratta, C. Barbato, S. Magnolia, K. Siega and P. Rigo, *Chem. Eur. J.*, 2010, **16**, 3201-3206.
7. K.-J. Haack, S. Hashiguchi, A. Fujii, T. Ikariya and R. Noyori, *Angew. Chem., Int. Ed.*. 1997, **36**, 285-288.
8. K. Mashima, T. Abe and K. Tani, *Chem. Lett.*, 1998, **27**, 1201-1202.
9. K. Murata, T. Ikariya and R. Noyori, *J. Org. Chem.*, 1999, **64**, 2186-2187.
10. X. Wu, X. Li, A. Zanotti-Gerosa, A. Pettman, J. Liu, A. J. Mills and J. Xiao, *Chem. Eur. J.*, 2008, **14**, 2209-2222.
11. M. Hanif, A. A. Nazarov, C. G. Hartinger, W. Kandioller, M. A. Jakupec, V. B. Arion, P. J. Dyson and B. K. Keppler, *Dalton Trans.*, 2010, **39**, 7345-7352.
12. D. Carmona, F. J. Lahoz, P. García-Orduña, L. A. Oro, M. P. Lamata and F. Viguri, *Organometallics*, 2012, **31**, 3333-3345.
13. A. Acosta-Ramirez, M. Bertoli, D. G. Gusev and M. Schlaf, *Green Chem.*, 2012, **14**, 1178-1188.

14. W. Baratta, M. Ballico, A. Del Zotto, K. Siega, S. Magnolia and P. Rigo, *Chem. Eur. J.*, 2008, **14**, 2557-2563.

15. W. Baratta, F. Benedetti, A. Del Zotto, L. Fanfoni, F. Felluga, S. Magnolia, E. Putignano and P. Rigo, *Organometallics*, 2010, **29**, 3563-3570.

16. R. Castarlenas, M. A. Esteruelas and E. Oñate, *Organometallics*, 2008, **27**, 3240-3247.

17. G. Chelucci, S. Baldino and W. Baratta, *Acc. Chem. Res.*, 2015, **48**, 363-379.

18. D. A. Alonso, P. Brandt, S. J. M. Nordin and P. G. Andersson, *J. Am. Chem. Soc.*, 1999, **121**, 9580-9588.

19. P. A. Dub and J. C. Gordon, *Dalton Trans.*, 2016, **45**, 6756-6781.

20. J. Václavík, P. Šot, J. Pecháček, B. Vilhanová, O. Matuška, M. Kuzma and P. Kačer, *Molecules*, 2014, **19**, 6987-7007.

21. J. Václavík, P. Šot, B. Vilhanová, J. Pecháček, M. Kuzma and P. Kačer, *Molecules*, 2013, **18**, 6804-6828.

22. J. Tönnemann, J. Risse, Z. Grote, R. Scopelliti and K. Severin, *Eur. J. Inorg. Chem.*, 2013, **2013**, 4558-4562.

23. J. P. C. Coverdale, C. Sanchez-Cano, G. J. Clarkson, R. Soni, M. Wills and P. J. Sadler, *Chem. Eur. J.*, 2015, **21**, 8043-8046.

24. O. V. Dolomanov, L. J. Bourhis, R. J. Gildea, J. A. K. Howard and H. Puschmann, *J. Appl. Crystallogr.*, 2009, **42**, 339-341.

25. G. Sheldrick, *Acta Crystallogr., Sect. A: Found. Crystallogr.*, 2008, **64**, 112-122.

26. M. J. Frisch, G. W. Trucks, H. B. Schlegel, G. E. Scuseria, M. A. Robb, J. R. Cheeseman, J. A. Montgomery Jr., T. Vreven, K. N. Kudin, J. C. Burant, J. M. Millam, S. S. Iyengar, J. Tomasi, V. Barone, B. Mennucci, M. Cossi, G.

Scalmani, N. Rega, G. A. Petersson, H. Nakatsuji, M. Hada, M. Ehara, K. Toyota, R. Fukuda, J. Hasegawa, M. Ishida, T. Nakajima, Y. Honda, O. Kitao, H. Nakai, M. Klene, X. Li, J. E. Knox, H. P. Hratchian, J. B. Cross, V. Bakken, C. Adamo, J. Jaramillo, R. Gomperts, R. E. Stratmann, O. Yazyev, A. J. Austin, R. Cammi, C. Pomelli, J. W. Ochterski, P. Y. Ayala, K. Morokuma, G. A. Voth, P. Salvador, J. J. Dannenberg, V. G. Zakrzewski, S. Dapprich, A. D. Daniels, M. C. Strain, O. Farkas, D. K. Malick, A. D. Rabuck, K. Raghavachari, J. B. Foresman, J. V. Ortiz, Q. Cui, A. G. Baboul, S. Clifford, J. Cioslowski, B. B. Stefanov, G. Liu, A. Liashenko, P. Piskorz, I. Komaromi, R. L. Martin, D. J. Fox, T. Keith, M. A. Al-Laham, C. Y. Peng, A. Nanayakkara, M. Challacombe, P. M. W. Gill, B. Johnson, W. Chen, M. W. Wong, C. Gonzalez and J. A. Pople, *Gaussian, Inc.*, 2004.

27. A. J. Millett, A. Habtemariam, I. Romero-Canelón, G. J. Clarkson and P. J. Sadler, *Organometallics*, 2015, **34**, 2683-2694.
28. C. Adamo and V. Barone, *J. Chem. Phys.*, 1999, **110**, 6158-6170.
29. W. R. Wadt and P. J. Hay, *J. Chem. Phys.*, 1985, **82**, 284-298.
30. A. D. McLean and G. S. Chandler, *J. Chem. Phys.*, 1980, **72**, 5639-5648.
31. R. Dennington, T. A. Keith and J. M. Millam, *Semichem Inc.*, 2003.
32. S. J. Dougan, A. Habtemariam, S. E. McHale, S. Parsons and P. J. Sadler, *Proc. Natl. Acad. Sci. U. S. A.*, 2008, **105**, 11628-11633.
33. A. Bonetti, R. Leone, F. M. Muggia and S. B. Howell, *Platinum and Other Heavy Metal Compounds in Cancer Chemotherapy*, Humana (Springer), New York, 2009.
34. R. Soni, F. K. Cheung, G. C. Clarkson, J. E. D. Martins, M. A. Graham and M. Wills, *Org. Biomol. Chem.*, 2011, **9**, 3290-3294.

35. H. D. Flack and G. Bernardinelli, *Chirality*, 2008, **20**, 681-690.

36. R. Noyori and S. Hashiguchi, *Acc. Chem. Res.*, 1997, **30**, 97-102.

37. A. Fujii, S. Hashiguchi, N. Uematsu, T. Ikariya and R. Noyori, *J. Am. Chem. Soc.*, 1996, **118**, 2521-2522.

38. E. C. Constable, B. F. G. Johnson, J. Lewis, G. N. Pain and M. J. Taylor, *J. Chem. Soc. Chem. Commun.*, 1982, DOI: 10.1039/C39820000754, 754-756.

39. R. Hodgkinson, V. Jurčík, A. Zanotti-Gerosa, H. G. Nedden, A. Blackaby, G. J. Clarkson and M. Wills, *Organometallics*, 2014, **33**, 5517-5524.

40. N. A. Strotman, C. A. Baxter, K. M. J. Brands, E. Cleator, S. W. Krska, R. A. Reamer, D. J. Wallace and T. J. Wright, *J. Am. Chem. Soc.*, 2011, **133**, 8362-8371.

41. P. Brandt, P. Roth and P. G. Andersson, *J. Org. Chem.*, 2004, **69**, 4885-4890.

42. P. A. Dub and T. Ikariya, *J. Am. Chem. Soc.*, 2013, **135**, 2604-2619.

43. J. W. Handgraaf and E. J. Meijer, *J. Am. Chem. Soc.*, 2007, **129**, 3099-3103.

44. Y. Yang, M. N. Weaver and K. M. Merz, *J. Chem. Phys. A*, 2009, **113**, 9843-9851.

Chapter 4

Contrasting biological activities of Os(II) / Ir(III) sulfonamide complexes

4. Contrasting biological activities of Os(II) / Ir(III) sulfonamide complexes

4.1 Introduction

Research into metal-based anticancer agents was stimulated by the discovery of the platinum complex *cis*-[$PtCl_2(NH_3)_2$] in the 1960s. While the commonly accepted mechanism of action of platinum complexes is DNA binding leading to apoptotic cell death,[1] this approach does not allow discrimination between cancer cells and healthy proliferating tissues. In addition to increasing tumour selectivity, novel organometallic compounds that exhibit a unique, or multiple mechanism(s) of action may circumvent inherent or acquired drug resistance. This is of great importance when considering the high incidence of cisplatin-resistant tumours, because platinum-based drugs are currently used in over half of all chemotherapy regimens.[2]

Organometallic compounds of ruthenium have been explored and reviewed extensively,[3-6] and a ruthenium indazole complex (NKP-1339: sodium trans-[tetrachloridobis(1*H*-indazole)ruthenate(III)]) has entered a phase II clinical trial for the treatment of solid cancers.[7] While complexes of Os(II), Ir(III) and Rh(III) have shown promise as alternatives to platinum-based therapies, achieving high potency against cancer cells while circumventing cross-resistance, none have yet reached clinical application.[8-13] These organometallic complexes are commonly multi-targeted, and one mechanism of action involved is the induction of reactive oxygen species (ROS) in cells.[14-17] For example, the highly potent Os(II) complex [Os(*p*-cymene)(4-(2-pyridylazo)-*N*,*N*-dimethylaniline)I]PF_6 was shown to disrupt cellular metabolism by generation of ROS while also inducing apoptotic cell death.[18]

This chapter compares the novel Os(II) sulfonamide complexes explored in Chapter 3 (section 3.3.1, page 78) to structurally-similar Ir(III) compounds to evaluate the role of the catalytic metal centre on the biological properties (Figure 4.1). Since the compounds are able to catalyse transfer hydrogenation reactions, the catalytic oxidation of NADH (an important cellular hydride source) to NAD^+ is investigated. The consequences of altering the NADH/NAD^+ ratio are explored by detecting oxidative stress in cells. This chapter also evaluates the efficacy of sulfonamide complexes as anti-cancer agents, describes the time, temperature and concentration dependence of drug accumulation by A2780 cells, and explores metal compartmentalisation. Metallodrugs prove advantageous for such studies, since trace levels of the xenobiotic metal may be detected using various techniques, including ICP-MS (atomic mass), ICP-OES (atomic emission spectra) and x-ray fluorescence.[19]

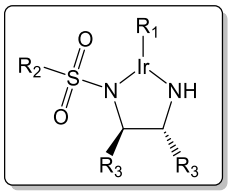

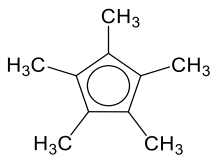

Cp*

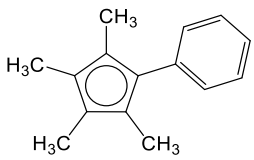

Cp^{xPh}

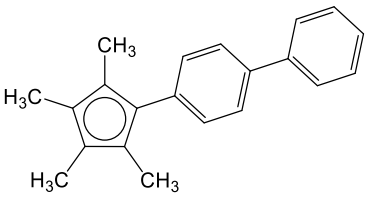

Cp^{xBip}

Complex	Metal	η^5-arene (R_1)	R_2	R_3
12	Ir	Cp*	4-tolyl (TsDPEN)	phenyl
13	Ir	Cp^{xPh}	4-tolyl (TsDPEN)	phenyl
14	Ir	Cp^{xBip}	4-tolyl (TsDPEN)	phenyl
15	Ir	Cp*	4-tolyl (TsBMEN)	4-methoxyphenyl
16	Ir	Cp^{xPh}	4-tolyl (TsBMEN)	4-methoxyphenyl
17	Ir	Cp^{xBip}	4-tolyl (TsBMEN)	4-methoxyphenyl

Figure 4.1. Iridium complexes **12-17** introduced in this chapter.

4.2 Experimental

4.2.1 Materials

Precursor iridium dimer $[IrCl_2(Cp^*)]_2$ was synthesised as described in Chapter 2 (Section 2.1.2). TsDPEN was purchased as an optically pure compound from Arran Chemical Company (Ireland). DPEN and BMEN were purchased as optically pure compounds from Sigma Aldrich (UK). Potassium hydroxide, magnesium sulphate, sodium chloride (TraceSELECT, ≥99%) and all non-dried solvents were purchased from Fischer Scientific. L-ascorbic acid (≥99%), c*is*-diaminedichloroplatinum(II) (CDDP, cisplatin, ≥99%), DMSO (> 99%, molecular biology grade), 1-octanol (anhydrous, ≥99%), thiourea (≥99%) and (±)-verapamil hydrochloride (≥99%) were purchased from Sigma Aldrich and used as received. Deuterated solvents were purchased from Goss Scientific. Water used for biphasic reactions was purified by reverse osmosis (RO) unless specified. Ultrapure grade nitric acid (72% v/v) was freshly distilled before use. All other reagents and solvents were purchased from Sigma Aldrich and used as received, unless stated otherwise.

The FractionPREP kit for cellular fractionation was purchased from BioVision, and stored at 253 K before use. The ROS / Superoxide detection kit was purchased from Sigma Aldrich and stored at 253 K before use.

Iridium arene chlorido dimer complexes $[IrCl_2(Cp^{xPh})]_2$ and $[IrCl_2(Cp^{xBip})]_2$ were kindly provided by Dr. Abraha Habtemariam (University of Warwick, UK). 4-Methoxyphenyl-substituted complexes **15-17** were synthesised and fully characterised by Miss Yasmin Khanom (University of Warwick, UK).

4.2.2 Synthesis of iridium sulfonamide complexes 12-17

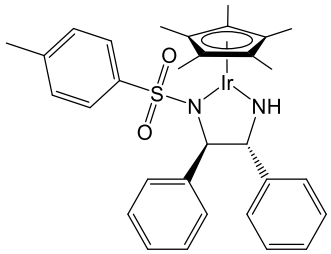

(*R*,*R*)-12

[Ir(Cp*)((1*R*,2*R*)-TsDPEN)] (12). The synthesis of **12** has been previously reported.[20] $[Ir(Cp^*)Cl_2]_2$ (120 mg, 0.15 mmol) and (1*R*,2*R*)-(H)TsDPEN (110.6 mg, 0.30 mmol) were stirred in chloroform (10 mL) with freshly ground KOH (168 mg, 3 mmol). A colour change from orange to purple was observed < 1 min. After 5 min, water (10 mL) was added with stirring for a further 10 min. The organic layer was removed and concentrated *in vacuo* to yield a purple oil, which was dissolved in the minimum amount of DCM, followed by precipitation with *n*-pentane. The product was collected as a purple crystalline solid. (144 mg, 0.21 mmol, 69%). ^{1}H NMR (400 MHz, $CDCl_3$, 25°C, TMS): δ=7.55 (d, ^3J(H,H)=7.4 Hz, 2H), 7.06-7.36 (m, 10H), 6.79 (d, ^3J(H,H)=8.0 Hz, 2H), 5.34 (s, 1H; CHNTs), 4.15 (*br*. d, 1H; C*H*NH), 2.24 (s, 3H; CH_3), 1.92 (s, 15H; Cp*); ^{13}C NMR (100 MHz, $CDCl_3$, 25°C, TMS) δ 128.2, 127.8, 127.6, 126.9, 126.6, 126.5, 126.2, 85.2, 80.3, 74.1, 10.2; UV/Vis: λ_{max} 429 and 536 nm; HRMS (*m/z*): $[M+H]^+$ calcd. for $C_{31}H_{36}IrN_2O_2S$, 693.2121; found, 693.2118; analysis (calcd. for $C_{31}H_{35}IrN_2O_2S$, found): C (53.81, 53.80), H (5.10, 5.09), N (4.05, 4.02).

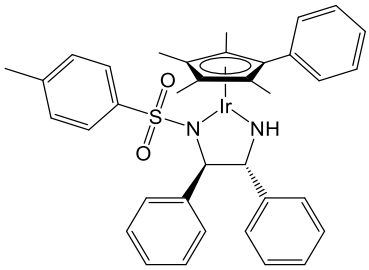

(*R*,*R*)-13

[Ir(Cp^{xPh})((1*R*,2*R*)-TsDPEN)] (13). This complex was obtained following the method described for complex **12** using dimer **[Ir(Cp^{xPh})Cl$_2$]$_2$** (50.3 mg, 0.055 mmol) and (1*R*,2*R*)-(H)TsDPEN (40 mg, 0.11 mmol). The product was isolated as a dark purple amorphous solid. (50 mg, 0.066 mmol, 61%).^{1}H NMR (500 MHz, $CDCl_3$, 25°C, TMS): δ=7.58 (d, ^3J(H,H)=7.5 Hz, 2H), 7.08-7.53 (m, 15H), 6.79 (d, ^3J(H,H)=8.0 Hz, 2H), 5.67 (br. d, ^3J(H,H)=4.0 Hz, 1H; NH), 4.42 (s, 1H; CHNTs), 4.20 (d, ^3J(H,H)=4.0 Hz, 1H; C*H*NH), 2.25 (s, 3H; CH_3), 2.07 (s, 3H; Cp*), 2.02 (s, 3H; Cp*), 1.89 (s, 3H; Cp*), 1.88 (s, 3H; Cp*); ^{13}C NMR (125 MHz, $CDCl_3$, 25°C, TMS) δ 146.7, 146.5, 141.1, 140.1, 131.5, 130.9, 128.6, 128.2, 127.9, 127.7, 126.9, 126.7, 126.6, 126.3, 89.8, 88.0, 87.5, 84.8, 83.8, 80.5, 74.2, 21.2, 10.7, 10.6, 10.5, 10.3; UV/Vis: λ_{max} 432 and 547 nm; HRMS (*m/z*): $[M+H]^+$ calcd. for $C_{36}H_{38}IrN_2O_2S$, 755.2278; found, 755.2268; analysis (calcd. for $C_{36}H_{37}IrN_2O_2S$, found): C (57.35, 56.94), H (4.95, 4.96), N (3.72, 3.70).

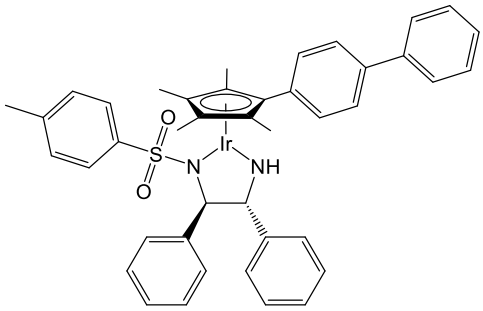

(*R*,*R*)-14

[Ir(Cp^{xBip})((1*R*,2*R*)-(TsDPEN)] (14). This complex was obtained following the method described for complex **12** using dimer **[Ir(Cp^{xBip})Cl$_2$]$_2$** (58.6 mg, 0.055 mmol) and (1*R*,2*R*)-(H)TsDPEN (40 mg, 0.11 mmol). The product was isolated as a dark purple crystalline solid. (33 mg, 0.040 mmol, 37%). ^{1}H NMR (500 MHz, $CDCl_3$, 25°C, TMS): δ= 7.52-7.64 (m, 8H), 7.44-7.50 (m, 2H), 7.35-7.42 (m, 1H), 7.07-7.30 (m, 10H), 6.80 (d, ^3J(H,H)=8.0 Hz, 2H; ArH), 5.67 (d, ^3J(H,H)=4.0 Hz, 1H; NH), 4.43 (s, 1H; CHTs), 4.22 (d, ^3J(H,H)=4.0 Hz, 1H; C*H*NH), 2.25 (s, 3H; CH_3), 2.09 (s, 3H; Cp*), 2.03 (s, 3H; Cp*), 1.94 (s, 3H; Cp*), 1.93 (s, 3H; Cp*); ^{13}C NMR (125 MHz, $CDCl_3$, 25°C, TMS) δ 146.7, 146.5, 141.1, 141.0, 140.4, 140.1, 131.3, 128.9, 128.6, 127.9, 127.7, 127.6, 127.3, 127.1, 127.1, 127.0, 126.7, 126.6, 126.3, 89.4, 88.1, 87.6, 84.8, 83.9, 80.6, 74.2, 21.25, 10.8, 10.6, 10.5, 10.3; UV/Vis: λ_{max} 430 and 547 nm; HRMS (*m/z*): $[M+H]^+$ calcd. for $C_{42}H_{42}IrN_2O_2S$, 831.2592; found, 831.2599; analysis (calcd. for $C_{42}H_{41}IrN_2O_2S$, found): C (60.77, 61.21), H (4.98, 5.07), N (3.37, 3.34).

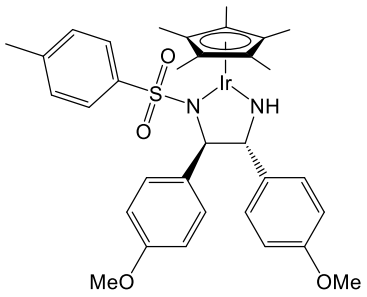

(*R*,*R*)-15

[Ir(Cp*)((1*R*,2*R*)-TsBMEN)] (15). Complex **(*R*,*R*)-15** was synthesised by Miss Yasmin Khanom. This complex was obtained following the method described for complex **12** using dimer **[Ir(Cp*)Cl$_2$]$_2$** (46.7 mg, 0.058 mmol) and (1*R*,2*R*)-(H)TsBMEN (50 mg, 0.17 mmol). The product was isolated as a dark purple amorphous solid. (37.5 mg, 0.049 mmol, 86%).^{1}H NMR (500 MHz, $CDCl_3$, 25°C, TMS): δ=7.44 (d, ^3J(H,H)=8.4 Hz, 2H; ArH), 7.25 (d, ^3J(H,H)=8.2 Hz, 2H; ArH), 7.04 (d, ^3J(H,H)=8.5 Hz, 2H; ArH), 6.82 (d, ^3J(H,H)=8.0 Hz, 2H; ArH), 6.79 (d, ^3J(H,H)=8.5 Hz, 2H; ArH), 6.65 (d, ^3J(H,H)=8.6 Hz, 2H; ArH), 5.36 (*br*. s, 1H; NH), 4.18 (s, 1H; TsNC*H*), 4.05 (s, 1H; C*H*NH), 3.78 (s, 3H; OCH_3), 3.78 (s, 3H; OCH_3), 2.26 (s, 3H; CH_3), 1.91 (s, 15H; CH_3); ^{13}C NMR (125 MHz, $CDCl_3$, 25°C, TMS) δ 158.5, 158.1, 140.9, 138.9, 138.7, 128.2, 127.1, 126.7, 113.1, 85.1, 79.8, 73.4, 55.3, 21.2, 10.2; UV/Vis: λ_{max} 285, 430, 538 nm; HRMS (*m/z*): $[M+H]^+$ calcd. for $C_{33}H_{40}IrN_2O_4S$, 753.2333; found, 753.2336; analysis (calcd. for $C_{33}H_{39}IrN_2O_4S$, found): C (52.71, 53.03), H (5.23, 5.43), N (3.73, 3.65).

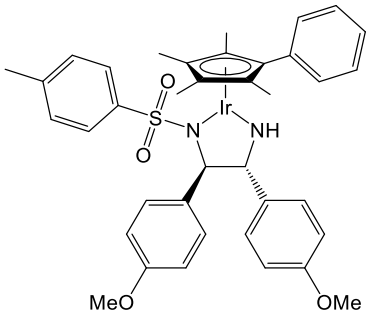

(*R*,*R*)-16

[Ir(Cp^{xPh})((1*R*,2*R*)-TsBMEN)] (16). Complex **(*R*,*R*)-16** was synthesised by Miss Yasmin Khanom. This complex was obtained following the method described for complex **12** using dimer **[Ir(Cp^{xPh})Cl$_2$]$_2$** (53.9 mg, 0.058 mmol) and (1*R*,2*R*)-(H)TsBMEN (50 mg, 0.17 mmol). The product was isolated as a dark purple amorphous solid. (35.5 mg, 0.044 mmol, 75%).^{1}H NMR (500 MHz, $CDCl_3$, 25°C, TMS): δ=7.51 (d, ^3J(H,H)=6.9 Hz, 2H; ArH), 7.47 (d, ^3J(H,H)=8.5 Hz, 2H; ArH), 7.39 (*br*. s, 1H; NH), 7.32-7.38 (m, 3H; ArH), 7.28 (d, ^3J(H,H)=8.2 Hz, 2H; ArH), 7.05 (d, ^3J(H,H)=8.5 Hz, 2H; ArH), 6.82 (d, ^3J(H,H)=7.9 Hz, 2H; ArH), 6.77 (d, ^3J(H,H)=8.5 Hz, 2H; ArH), 6.65 (d, ^3J(H,H)=8.5 Hz, 2H; ArH), 4.30 (s, 1H; C*H*NTs), 4.10 (s, 1H; C*H*NH), 3.79 (s, 3H; OCH_3), 3.78 (s, 3H; OCH_3), 2.26 (s, 3H; CH_3), 2.07 (s, 3H; CH_3), 2.02 (s, 3H; CH_3), 1.89 (s, 3H; CH_3), 1.88 (s, 3H; CH_3); ^{13}C NMR (125 MHz, $CDCl_3$, 25°C, TMS) δ 158.6, 158.2, 141.2, 140.0, 138.8, 131.5, 130.9, 128.6, 128.2, 127.9, 127.2, 126.7, 113.1, 89.8, 87.9, 87.5, 84.6, 84.0, 80.0, 73.5, 55.3, 21.2, 10.7, 10.6, 10.5, 10.4; UV/Vis: λ_{max} 278, 433, 549 nm; HRMS (*m/z*): $[M+H]^+$ calcd. for $C_{38}H_{42}IrN_2O_4S$, 815.2490; found, 815.2485; analysis (calcd. for $C_{38}H_{41}IrN_2O_4S$, found): C (56.07, 55.98), H (5.08, 5.31), N (3.44, 3.31).

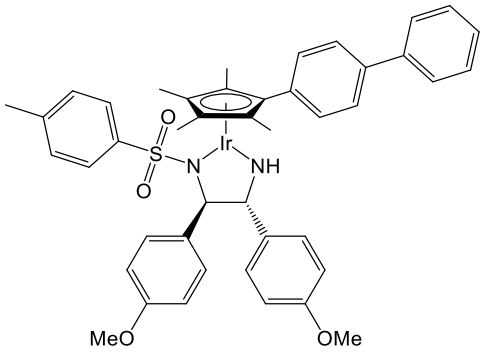

(*R*,*R*)-17

[Ir(Cp^{xBip})((1*R*,2*R*)-TsBMEN)] (17). Complex **(*R*,*R*)-17** was synthesised by Miss Yasmin Khanom. This complex was obtained following the method described for complex **12** using dimer **[Ir(Cp^{xPh})Cl$_2$]$_2$** (62.2 mg, 0.058 mmol) and (1*R*,2*R*)-(H)TsBMEN (50 mg, 0.17 mmol). The product was isolated as a dark purple amorphous solid. (30.7 mg, 0.034 mmol, 60%).^{1}H NMR (500 MHz, $CDCl_3$, 25°C, TMS): δ=7.61 (d, ^3J(H,H)=7.5 Hz, 2H; ArH), 7.57 (d, ^3J(H,H)=5.1 Hz, 2H; ArH), 7.44-7.51 (m, 4H; ArH), 7.39 (m, 2H; ArH), 7.30 (d, ^3J(H,H)=8.0 Hz, 2H; ArH), 7.16 (d, ^3J(H,H)=8.5 Hz, 1H; ArH), 7.07 (d, ^3J(H,H)=8.4 Hz, 2H; ArH), 6.96-7.04 (*br*. s, 1H; NH), 6.84 (d, ^3J(H,H)=8.0 Hz, 2H; ArH), 6.79 (d, ^3J(H,H)=8.5 Hz, 2H; ArH), 6.66 (d, ^3J(H,H)=8.5 Hz, 2H; ArH), 4.31 (s, 1H; C*H*NTs), 4.11 (s, 1H; C*H*NH), 3.79 (s, 3H; OCH_3), 3.78 (s, 3H; OCH_3), 2.27 (s, 3H; CH_3), 2.09 (s, 3H; CH_3), 2.04 (s, 3H; CH_3), 1.94 (s, 3H; CH_3), 1.93 (s, 3H; CH_3); ^{13}C NMR (125 MHz, $CDCl_3$, 25°C, TMS) δ 158.6, 158.2, 141.2, 141.0 140.4, 140.1, 138.8, 131.3, 128.9, 128.2, 127.9, 127.7, 127.3, 1271, 126.7, 113.6, 113.2, 113.1, 89.2, 88.0, 87.6, 84.7, 84.0, 80.0, 73.5, 61.2, 55.3, 21.2, 10.9, 10.7, 10.5, 10.4; UV/Vis: λ_{max} 263, 431, 548 nm; HRMS (*m/z*): $[M+H]^+$ calcd. for $C_{44}H_{46}IrN_2O_4S$, 891.2803; found, 891.2800.

4.2.3 Conversion of NADH to NAD^+

The conversion of nicotinamide adenine dinucleotide (1,4-NADH) to its oxidised form (NAD^+) under biologically-relevant conditions (phosphate buffered saline, DMSO < 1.0% v/v, pH = 7.4) was determined using either catalyst **2** [Os(*p*-cymene)(TsDPEN)] or **12** [Ir(Cp*)(TsDPEN)], monitored using UV-visible spectroscopy. Stock solutions of **2** or **12** (*ca*. 100 μM) were prepared in 5% v/v DMSO / 95% v/v phosphate-buffered saline (PBS, pH 7.4). A separate stock solution of 1,4-NADH was prepared in PBS (*ca.* 5 mM). Solutions were diluted to achieve final working concentrations: metal complex, 10 μM; NADH, 124 μM ($A_{340\ nm}$ = 0.77). Spectra (800-200 nm, scan rate: 600 nm min^{-1}) were acquired every 1 h over a 24 h period (298 K). The final DMSO concentration in the working solution did not exceed 1.0 % v/v.

The oxidation of 1,4-NADH to NAD^+ was determined by recording the absorbance at 340 nm ($\varepsilon_{(NADH)}$ = 6.22 cm^{-1} mM^{-1}). Absorbance data were plotted as a function of time. Additionally, a plot of ln(absorbance) as a function of time was constructed to demonstrate that the reaction rate was first order with respect to NADH. The turnover number after 24 h incubation (TON, 24 h) and maximum observed turnover frequency (TOF_{max} / h^{-1}) were determined after quantification of the metal stock solution concentration using ICP-OES.

4.2.4 Octanol-water partition coefficients (Log P)

Octanol / water partition coefficients for complexes **2-17** were determined using the shake-flask method.[21] 1-Octanol saturated water (OSW) and water saturated 1-octanol (WSO) were prepared by stirring equal quantities of each solvent overnight (*ca*. 200 mL), and allowing 24 h before separation of the two phases. Saturated aqueous solutions of each complex were prepared using octanol-saturated water. The saturated solutions were filtered, then shaken with equal volumes of water saturated octanol (2 mL + 2 mL) for 24 h using an IKA Vibrax VXC basic shaker (1000 g/min). The experiment was conducted at ambient temperature (~293 K).

The osmium / iridium concentration of the aqueous layer was determined by ICP-MS before and after shaking. Analysis was conducted immediately after solution preparation or equilibration time in all cases. Serial dilutions were performed using dilute nitric acid (3.6% v/v) containing thiourea (10 mM) and ascorbic acid (100 mg/L) to stabilise osmium in nitric acid solution, using dilution factors *i* and *j*, for t = 0 h and t = 24 h samples, resepectively.[22] ICP-MS analysis for ^{189}Os and ^{193}Ir was performed as described in Chapter 2 (section 2.2.8, page 47, calibration range: 0.1-1000 ppb) using an internal standard (50 ppb ^{166}Er). Log P values and calculated standard deviations were determined as duplicates of triplicates as part of two independent experiments using separately-prepared sample batches (Formula 4.1).

$$\text{Log P} = \left(\frac{[\text{M}]_{\text{octanol}}}{[\text{M}]_{\text{aqueous}}}\right)$$

$$\text{Log P} = \left(\frac{i[\text{M}]_{\text{aqueous (t = 0 h)}} - j[\text{M}]_{\text{aqueous (t = 24 h)}}}{j[\text{M}]_{\text{aqueous (t = 24 h)}}}\right)$$

Formula 4.1. Determination of partition coefficient (Log P) using metal concentrations in the aqueous layer determined by ICP-MS, where *i* and *j* are the corresponding ICP dilution factors.

4.2.5 Biological studies

Cell maintenance, *in vitro* growth inhibition assays and cellular metal accumulation experiments undertaken at the University of Warwick were carried out with assistance from Dr Isolda Romero-Canelón, Mrs Hannah E Bridgewater, Mrs Ji Inn Song and Mrs Sukhbinder Heer (University of Warwick, UK). The relevant methods are described in Chapter 2 (section 2.3.2, page 57).

Maintenance of A2780cis (cisplatin-resistant ovarian cancer cells). Approximately every 10 passages, cells were exposed to cisplatin (10 μM; *ca*. 10× IC_{50} of CDDP in A2780 cancer cells) for 24 h, washed with PBS and supplied with drug-free media.

Cellular accumulation studies. Cell accumulation experiments were carried out as described in Chapter 2 (section 2.3,2, page 54). Variations on the cellular accumulation protocol are described:

(1) *Concentration dependence***.** Experiments were carried out using 4 metal concentrations (0.25, 0.50, 1.00, 1.50 × IC_{50} concentration) and 24 h drug exposure. No recovery time. Incubation at 310 K;

(2) *Time dependence***.** Experiments were carried out with 3 h, 6 h, and 24 h drug exposure. No recovery time. Cells were incubated at 310 K;

(3) *Temperature dependence***.** Experiments were carried out at 277 K and 310 K using IC_{50} concentrations of the complexes with 24 h drug exposure. No recovery time;

(4) *P-gp involvement in metal efflux.* Experiments were carried out using IC_{50} concentrations. The drug was removed after 24 h, cells were washed with PBS, and either fresh media, or media containing a known P-gp inhibitor (verapamil: 20 μM), was added. Cells were incubated at 310 K and collected after 24 h, 48 or 72 h recovery.

Metal distribution in cancer cells. Cell pellets were obtained in triplicate as described for cellular metal accumulation using 1× IC_{50} equipotent concentrations (section 2.3.2, page 54), and fractioned using the Fraction PREP kit (BioVision). The fractions (cytosolic, membrane, nucleic, cytoskeletal) were digested in concentrated 72% v/v nitric acid (200 μL, 343 K, 24 h) then diluted with milliQ water containing thiourea and ascorbic acid to stabilise Os in nitric acid, achieving 3.6% v/v final working acid concentration. Metal concentrations (Os / Ir) were determined by ICP-MS in triplicate (section 2.2.8, page 48), and normalised to cell count in order to report % distributions and standard deviations.

Reactive oxygen species (ROS) determination. ROS and superoxide were detected in A2780 cancer cells using the ROS / Superoxide detection kit (Enzo Life Sciences). A 6-well plate was seeded with 1.5×10^6 A2780 cells per well, and incubated for 24 h (310 K). Cells were exposed to complex **2** or **12** (1.0 × IC_{50}) for 24 h. Cells were washed, pellets collected by centrifugation (1000 rpm, 5 min, 277 K), then re-suspended in PBS (500 μL) and stained with green and orange fluorescent reagents (2 μL). Positive control samples were treated with pyocyanin (5 μL, 30 min) and stained either green, orange, or were dual-stained (for compensation purposes). Data were

collected using a Becton Dickson FACScan Flow Cytometer (FL1 for total ROS, Ex/Em: 490/525 nm; FL2 for superoxide, Ex/Em: 550/620 nm) and were processed using FlowJo V10 for Windows.

Redox modulation by co-administration of L-BSO. Antiproliferative activities were determined as described in Chapter 2 (section 2.3.2, page 60) with the following modification: Complex **2** or **12** was co-administered to A2780 cells with a non-toxic concentration of L-BSO (5 μM), added independently, but within 5 min of each other.

4.3 Results

4.3.1 Synthesis of Ir(III) sulfonamide complexes

For comparison to Os transfer hydrogenation catalysts **2-10**, introduced in Chapter 3 (section 3.3.1, page 78), a series of structurally similar Ir(III) complexes was synthesised. Complex **12** [Ir(Cp*)(TsDPEN)] has previously been reported as a catalytic intermediate,[20] however its biological activity, at the time of writing, had not been explored. The 16-electron extended arene (**13-14**) and methoxy-substituted (**15-17**) series were synthesised by the same method described for Os complexes, rapidly forming a purple solution upon addition of base to a solution of the chiral diamine ligand and metal dimer $[Ir(Cp^x)Cl_2]_2$ in dichloromethane (Figure 4.2). The products were recrystallised from dichloromethane / hexane, yielding stable purple solids.

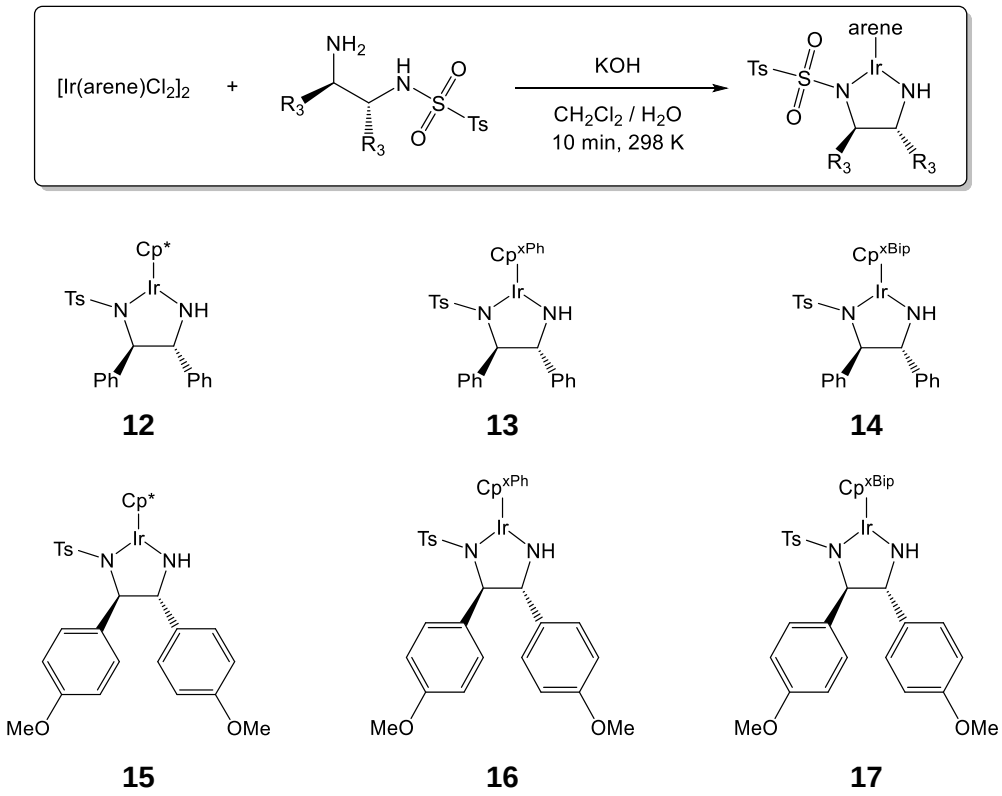

Figure 4.2. Synthesis of iridium(III) complexes **12-17** using the method described in Chapter 3.

Solution stability of Ir(III) sulfonamide complexes in PBS and DMSO

Complexes **12-17** were investigated for their stability in phosphate-buffered saline (containing < 5% v/v DMSO to solubilise the complexes) by UV-visible spectroscopy, and stability in d^6-DMSO by ^{1}H-NMR, as first described in Chapter 3 (section 3.3.4, page 85). After incubation at 310 K for 24 h, no changes were observed in UV-visible spectra, and no new peaks (or shifted peaks) were observed by ^{1}H-NMR (Figure 4.3), suggesting that the Ir(III) complexes are highly stable and comparable to their Os(II) counterparts. Though it is possible that chemical modification in solution may occur on a timescale that is more rapid than the time taken to acquire the first spectrum, the chemical species identified in the first spectrum acquired (after *ca*. 10 min for UV-visible, or 20 min for ^{1}H-NMR) remained unchanged for the 24 h period investigated and does not undergo (further) structural modification in either solvent.

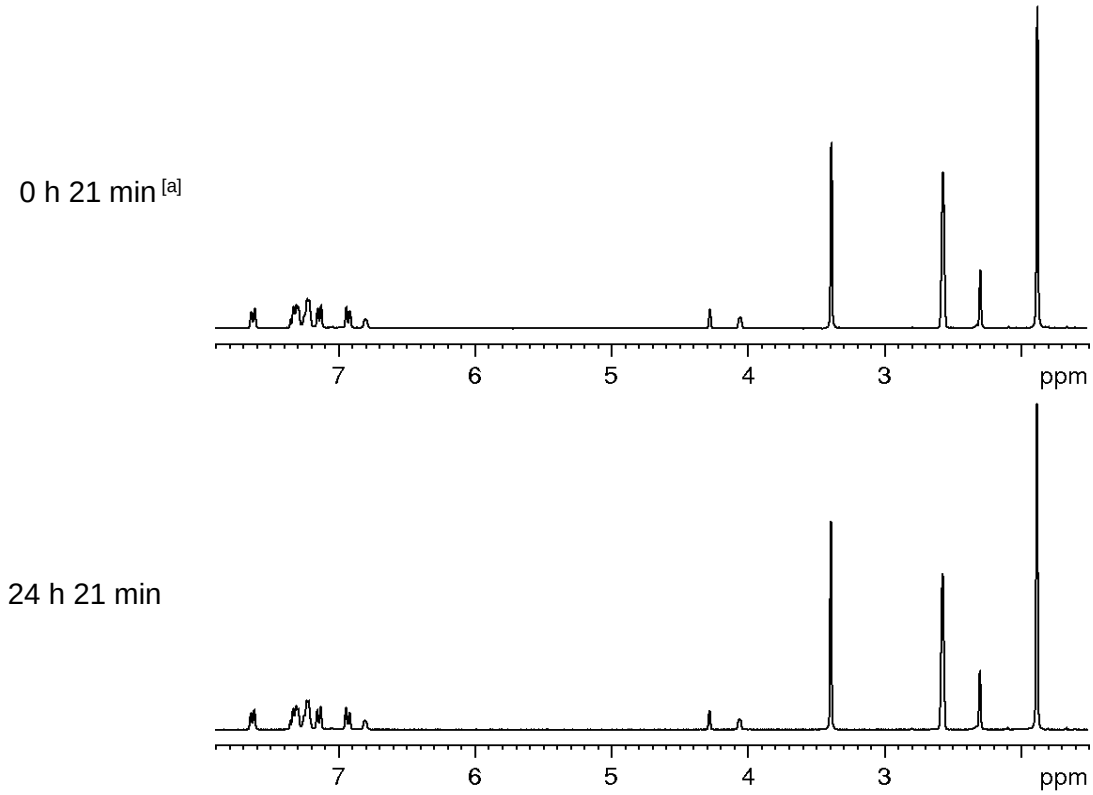

Figure 4.3. Representative ^{1}H-NMR (d^6-DMSO, 24 h, 310 K) shown for complex **12**. Complexes **13-17** are also highly stable in DMSO. [a] Time delay: lock, shim, temperature, average point of acquisition.

4.3.2 Conversion of NADH to NAD^+

The co-factor 1,4-NADH is an important hydride source in cells. The conversion (oxidation) of 1,4-NADH to NAD^+ by **2** (Os) or **12** (Ir) was monitored using UV-visible spectroscopy for 24 h at 298 K (124 μM NADH, ~10 μM complex). Conversion was determined from the absorbance at 340 nm, corresponding to 1,4-NADH. Turnover number (per mol of catalyst in 24 h) and maximum turnover frequency (TOF / h^{-1}) were calculated. Both Os and Ir complexes show activity for the oxidation of 1,4-NADH to NAD^+ (Figure 4.4). The initial rate was greater for Ir catalyst **12** (TOF = 0.3 h^{-1}) compared to Os catalyst **2** (TOF = 0.12 h^{-1}). However, the rate of oxidation of 1,4-NADH catalysed by Ir complex **12** decreased after ca. 6 h, resulting in an equal turnover number of *ca.* 3 equivalents of 1,4-NADH per mole of substrate in 24 h.

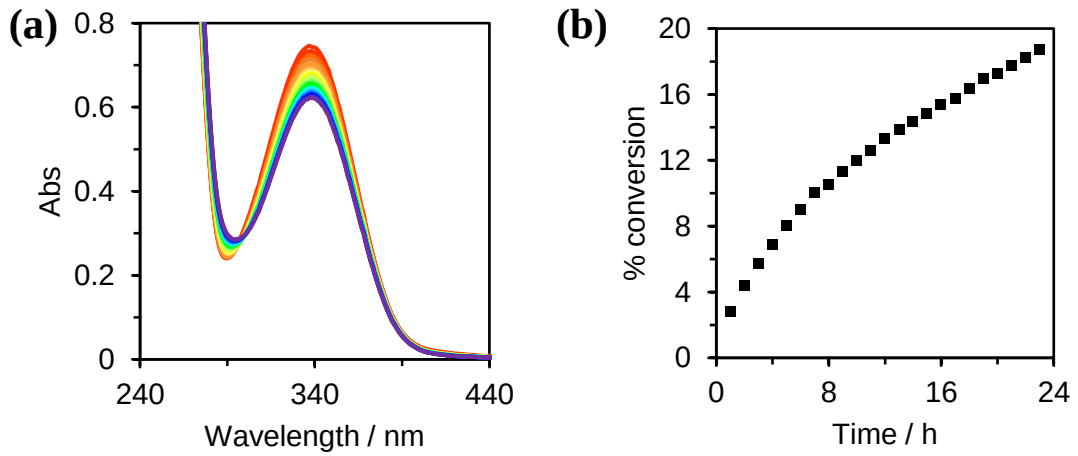

	Complex	TON (24 h)	TOF_{max} / h^{-1}
2	[Os(*p*-cymene)(TsDPEN)]	2.99	0.12
12	[Ir(Cp*)(TsDPEN)]	2.92	0.30

Figure 4.4. Conversion of 1,4-NADH to NAD^+ in PBS (pH 7.4) using either complex **2** or **12** (~10 μM) over 24 h at 298 K (<1% v/v DMSO). (a) Representative UV-visible spectrum for oxidation of 1,4-NADH (124 μM) by **12**, showing decrease in absorption at 340 nm; (b) Representative plot of conversion as a function of time for oxidation by **12**.

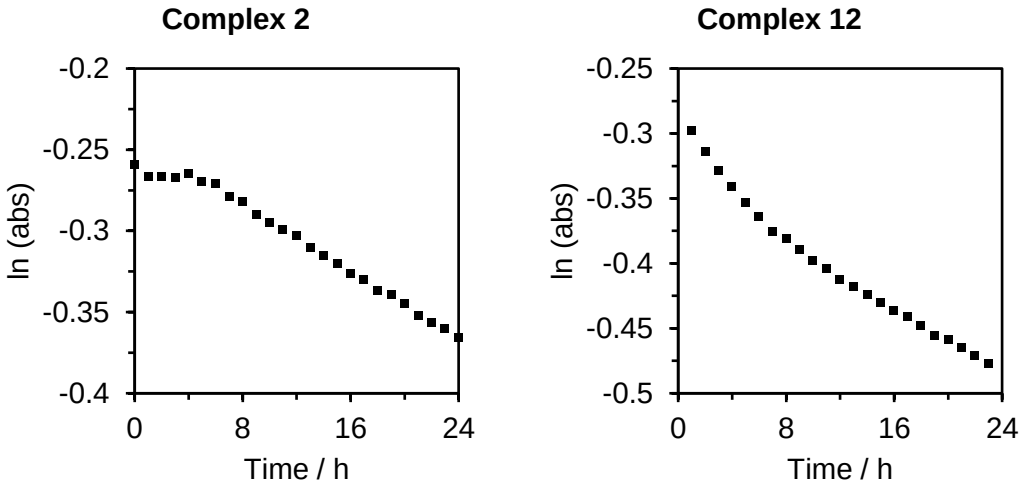

Figure 4.5. First-order kinetics plot of ln(absorance) at 340 nm as a function of time for the oxidation of 1,4-NADH to NAD^+ by complex **2** (Os) or **12** (Ir). Oxidation by Os(II) catalyst **2** shows typical first-order kinetics, however oxidation by catalyst **12** shows non-first order kinetics for the first 6 h of the reaction, after which time first-order kinetics are observed.

First order kinetic plots (ln abs plotted as a function of time) yielded a linear plot for Os complex **2**, confirming the first-order kinetics with respect to 1,4-NADH (Figure 4.5). The rate constant, *k*, for oxidation by Os complex **2** was 7.8×10^{-5} min^{-1}, an order of magnitude less than the rate constant determined for NADH oxidation by other organometallic complexes (4.03×10^{-4} min^{-1} for oxidation by Ir(III) 2-phenylpyridine complexes). The same first order kinetic plot for the reaction catalyst by Ir complex **12** was not linear until after *ca*. 6 h, and non-first order kinetics were observed in the first hours of oxidation. In this case, a second-order kinetic plot (abs^{-1} as a function of time) also did not produce a linear relationship, however the same unusual kinetic profile seen here with complex **12** (which reverts to first-order kinetics after 6 h) has also been observed with other Ir(III) complexes.[8] To investigate the hypothesised transfer hydrogenation mechanism, the detection of metal hydride resonances were attempted using ^{1}H-NMR however solution concentrations were not sufficient to facilitate observation.

4.3.3 Partition coefficient determination (Log P)

A detailed understanding of the cellular internalisation of candidate drug molecules is necessary to help explain biological interactions. A crucial step in this process is passage across the cell membrane. While large macromolecules are accumulated via endocytosis, smaller molecules may cross the membrane by either passive diffusion, or energy-dependent pathways, depending on their molecular weight, hydrophobicity and charge.[23] The octanol / water partition coefficient (Log P) describes the comparative hydrophobicity between compounds, whereby more polar (and commonly, charged) substances exhibit a more negative Log P, and more hydrophobic complexes have a more positive Log P. A partition coefficient of 0.0 indicates no preference for either the aqueous or organic phases.

Partition coefficients were determined for complexes **2-17** using the shake-flask method (Table 4.1).[24] All Log P values determined for both osmium and iridium complexes were positive, consistent with the low water solubility of the compounds, and ranged from Log P = 0.03-2.3 (Table 1). As anticipated, the more hydrophobic complexes with extended arene rings exhibited higher partition coefficients. All complexes investigated were assumed to be highly stable in water based on evidence from ^{1}H-NMR and UV-visible spectroscopic studies (see 4.3.1 for Ir complexes, Chapter 3 section 3.3.1, page 78 for Os complexes) in which no changes in spectra were observed over 24 h. The partition co-efficient for both enantiomers of osmium complexes **2**, **7** and **8** were studied independently, and found to not be statistically different. The most hydrophilic complex was [Ir(Cp*)(TsBMEN)] complex **15** (0.03 ± 0.04) demonstrating that methoxy-substitution increased water solubility, and the most hydrophobic complex was [Os(*m*-terphenyl)(TsDPEN)] complex **8** (2.3 ± 0.2). All partition coefficients were positive, indicative of preference for the octanol phase.

4.3.4 Antiproliferative activity and total cellular metal accumulation

The antiproliferative activities (half-maximal growth inhibitory concentrations, IC_{50}) of sulfonamide complexes **2**-**17** were determined in A2780 human ovarian cancer cells, using 24 h drug exposure and 72 h recovery time in drug-free medium. Final concentrations used in dose-response sigmoidal curves were corrected by ICP-OES analysis of stock solutions for Ru, Os, Pt and Ir concentrations. Both Ru(II) complex **11** and Ir complex **12** have been studied for the transfer hydrogenation of ketones and imines by Noyori and co-workers,[25-28] but their biological activities, to the best of my knowledge, have not been investigated.

Antiproliferative activities towards A2780 ovarian cancer cells

Across the series of complexes studied, antiproliferative activities towards A2780 cancer cells span over an order of magnitude, ranging from highly potent in the case of [Ir(Cp^{xBip})(TsDPEN)] **17** (0.7 ± 0.1 μM, comparable in activity to cisplatin) to only moderately active for [Os(*p*-cymene)(MsDPEN)] **3** (30 ± 2 μM). For both osmium and iridium complexes, lower IC_{50} values were determined for complexes with extended arenes: Os: **8** (*m*-terphenyl) > **7** (biphenyl) > **2** (*p*-cymene); Ir: **14** (Cp^{xBip}) > **13** (Cp^{xPh}) > **12** (Cp*). While Os complexes were typically more active than their Ir counterparts (**2**>**12**, **7**>**13**, **8**>**14**), methoxy-substitution in iridium complexes **15**-**17** greatly enhanced antiproliferative activities by up to 24× for [Ir(Cp^{xBip})(TsBMEN)] **17** compared to [Ir(Cp^{xBip})(TsDPEN)] **14**, achieving IC_{50} = 0.7 μM (**17**) compared to IC_{50} = 17 μM (**14**). In contrast, the antiproliferative activities of methoxy-substituted osmium complexes differed little from the respective un-substituted compounds, achieving only 1.5× potency increase (10 μM and 15.5 μM) in the case of Os complex **9** (methoxyphenyl) compared to **2** (phenyl), respectively.

Metal accumulation in A2780 ovarian cancer cells

Metal accumulation was compared at equipotent doses (1 × IC_{50}) after 24 h drug exposure with no recovery period (Table 4.1). Intracellular metal concentrations were determined by ICP-MS in no-gas mode, after digestion in nitric acid (72% v/v) followed by subsequent dilution to working acid concentration (3.6% v/v).

Cellular metal accumulations in A2780 cancer cells spanned almost an order of magnitude between the various sulfonamide complexes (8 to 89 ng Ir × 10^6 cells, and 4.8 to 32 ng Os × 10^6 cells). Metal accumulations were typically higher for iridium complexes, with the highest metal accumulation observed for iridium Cp* TsDPEN complex **14** (89 ± 4 ng Ir × 10^6 cells). In contrast, the lowest accumulation was for osmium *p*-cymene MsDPEN complex **3** (4.8 ± 0.8 ng Os × 10^6 cells), and the highest Os accumulation for complex **2** (32 ± 3 ng Os × 10^6 cells). The internalisation of the anticancer complex cisplatin was particularly low in comparison to the sulfonamide series (0.51 ± 0.07 ng Pt × 10^6 cells), likely due to the negative partition coefficient (corresponding to a lower lipophilicity). No correlation was observed between total metal accumulation and antiproliferative activity in A2780 cancer cells. For example, while the antiproliferative activities (IC_{50}) of **2** and **6** are similar (15.5 and 13.5 μM, respectively), Os accumulation in cells treated with **6** was ~5× lower than those treated with **2** (5.8 and 30 ng Os × 10^6 cells, respectively). While antiproliferative activities were found to increase with arene chain extension for Os (**2** < **7** < **8**) and Ir (**12** < **13** < **14**) complexes, neither the accumulation of Os (**7** < **2** = **8**) or Ir (**13** < **12** < **14**) followed the same trend. The absence of correlation between accumulation and IC_{50} has been observed previously for Pt complexes,[29] however the correlation was identified for similar Ir complexes.[30] It is therefore apparent that the *in vitro* biological activities or extent of metal accumulation cannot be readily predicted.

Table 4.1. Octanol / water partition coefficients (Log P), antiproliferative activities (IC_{50} / μM) and cellular metal accumulations (ng Os / Ir / Pt × 10^6 cells) determined for complexes **2**-**17** in A2780 human ovarian cancer cells, compared to the anticancer drug, cisplatin *cis*-$[PtCl_2(NH_3)_2]$.

	Complex	Log P $_{(oct / water)}$	IC_{50} / μM [a]	ng Os / Ir / Pt × 10^6 cells [b]
(*R*,*R*)-2	[Os(*p*-cymene)(TsDPEN)]	1.45 ± 0.02	15.5 ± 0.5	30 ± 2
(*S*,*S*)-2	[Os(*p*-cymene)(TsDPEN)]	1.45 ± 0.07	15.2 ± 0.5	32 ± 3
(*R*,*R*)-3	[Os(*p*-cymene)(MsDPEN)]	0.18 ± 0.04	30 ± 2	4.8 ± 0.8
(*S*,*S*)-3	[Os(*p*-cymene)(MsDPEN)]	-	29.9 ± 0.5	-
(*R*,*R*)-4	[Os(*p*-cymene)(NsDPEN)]	0.709 ± 0.008	19.9 ± 0.5	8.1 ± 0.3
(*S*,*S*)-4	[Os(*p*-cymene)(NsDPEN)]	-	19.4 ± 0.9	-
(*R*,*R*)-5	[Os(*p*-cymene)(FbDPEN)]	0.28 ± 0.03	17 ± 1	10 ± 2
(*S*,*S*)-5	[Os(*p*-cymene)(FbDPEN)]	-	17 ± 1	-
(*R*,*R*)-6	[Os(*p*-cymene)(BsDPEN)]	0.85 ± 0.02	13.5 ± 0.9	5.8 ± 0.7
(*S*,*S*)-6	[Os(*p*-cymene)(BsDPEN)]	-	14 ± 2	-
(*R*,*R*)-7	[Os(biphenyl)(TsDPEN)]	1.91 ± 0.04	6.5 ± 0.3	13 ± 1
(*S*,*S*)-7	[Os(biphenyl)(TsDPEN)]	1.85 ± 0.01	6.3 ± 0.1	13.3 ± 0.4
(*R*,*R*)-8	[Os(*m*-terphenyl)(TsDPEN)]	2.28 ± 0.10	4.4 ± 0.3	31.9 ± 0.4
(*S*,*S*)-8	[Os(*m*-terphenyl)(TsDPEN)]	2.3 ± 0.2	4.50 ± 0.07	-
(*R*,*R*)-9	[Os(*p*-cymene)(TsBMEN)]	0.24 ± 0.08	10 ± 1	6.6 ± 0.2
(*R*,*R*)-10	[Os(*p*-cymene)(TsBMEN)]	0.59 ± 0.05	9 ± 1	11.8 ± 0.1
(*R*,*R*)-11	[RuCl(*p*-cymene)(TsDPEN)]	-	8.2 ± 0.7	-
(*S*,*S*)-11	[RuCl(*p*-cymene)(TsDPEN)]	-	9 ± 1	-
(*R*,*R*)-12	[Ir(Cp*)(TsDPEN)]	0.86 ± 0.02	20.9 ± 0.7	52 ± 1
(*R*,*R*)-13	[Ir(Cp^{xPh})(TsDPEN)]	1.41 ± 0.02	14 ± 2	41.7 ± 0.7
(*R*,*R*)-14	[Ir(Cp^{xBip})(TsDPEN)]	2.24 ± 0.02	10.2 ± 0.6	89 ± 4
(*R*,*R*)-15	[Ir(Cp*)(TsBMEN)]	0.03 ± 0.04	17 ± 1	8 ± 1
(*R*,*R*)-16	[Ir(Cp^{xPh})(TsBMEN)]	0.32 ± 0.02	8.0 ± 0.8	13 ± 1
(*R*,*R*)-17	[Ir(Cp^{xBip})(TsBMEN)]	0.62 ± 0.03	0.7 ± 0.1	5.3 ± 0.2
Cisplatin	$[PtCl_2(NH_3)_2]$	-2.21 ± 0.06 [c]	1.20 ± 0.03	0.51 ± 0.07

[a]Antiproliferative activities determined using 24 h drug exposure + 72 h recovery time in drug-free medium. [b] Metal accumulation (investigated for (*R*,*R*)-configured complexes only) using equipotent concentrations (1.0 × IC_{50}) for 24 h with no recovery time. [c] Literature value for the partition coefficient (octanol/water) of cisplatin.[31]

Multi-cell line antiproliferative activity screening

Tosyl-DPEN complexes of Os **2**, **7**, **8** and Ir complexes **12**-**14** were further assessed for antiproliferative activity in other human cancer cell lines from different tissue origins: A2780cis (cisplatin-resistant A2780), A549 (lung), HCT116 (colon), OE19 (oesophageal), MCF7 (breast), PC3 (prostate), SK-OV-3 (ovarian) and SW626 (ovarian) cancer cells; as well as two non-cancerous primary cell lines: MRC5 (non-cancerous lung fibroblasts) and HOF (non-cancerous ovarian fibroblasts). The complexes achieved high potency against A2780, PC3 and MCF7 cancer cells; particularly complex **14** (3.7 ± 0.7 μM against MCF7 cells).

Antiproliferative activities typically increased with arene chain extension (*p*-cymene < biphenyl < terphenyl for Os; Cp* < Cp^{xPh} < Cp^{xBip} for Ir) in A2780, HEPG2, HOF, MCF7, MRC5 and OE19, however this trend was not observed for A549 or HCT116 cells. Interestingly, arene extension did not significantly affect the activities of osmium complexes **2**, **7** and **8** in PC3, however the trend was still apparent for iridium complexes **12**-**14**. Overall, complexes of iridium were typically less active than their osmium counterparts. Both osmium and iridium complexes were only moderately active (or inactive in the concentration range investigated) in HCT116 colon and OE19 oesophageal cells (Table 4.2). Compared to the parental cell line (HCT116), all sulfonamide complexes exhibited significantly decreased activities in *p21*- and *p53*-knockout cells (HCT116-*p21*-/- and HCT116-*p53*-/- respectively), suggesting that the mechanism of action is likely to be dependent on *p21* and/or *p53*.

The ratio between IC_{50} concentrations in non-cancerous fibroblasts (HOF and MRC5) compared to cancer cells (A2780 and A549, respectively) provides an indication of drug selectivity. Here, a distinct difference was observed depending on the nature of the metal. Os complexes **7**-**8** exhibited the greatest selectivity for ovarian cancer cells

compared to normal ovarian fibroblasts (6.7× and 5.5× respectively), with greater selectivity achieved with arene extension (**2** < **7** ~ **8**). In contrast, Ir complexes **12-14** showed significantly less selectivity (0.9-1.5×) which differed little upon arene extension. Upon comparison of cancerous lung cells (A549) with non-cancerous lung fibroblasts (MRC5), selectivity ratios were lower than those determined using ovarian cells (up to 3× for complex **8**), suggesting that the complexes may offer selective targeting and could be useful for the treatment of cancers of specific tissues.

Activities of the sulfonamide complexes in a laboratory-induced cisplatin-resistant cell line (A2780cis) appeared to be highly dependent on the nature of the metal centre. Activities of the osmium complexes, in particular osmium biphenyl complex **7** (IC_{50} = 25.9 μM in A2780cis compared to 6.5 μM in cisplatin-sensitive A2780), were particularly decreased in cisplatin-resistant cells. However, unlike the Os sulfonamide series, the decrease in potency was less pronounced for iridium complexes **12-14** (arene = Cp*, Cp^{xPh}, Cp^{xBip}) against cisplatin-resistant cells (17, 18 and 6.3 μM) compared to cisplatin-sensitive cells (20.9, 14 and 10.2 μM). Antiproliferative activities were also determined in SK-OV-3 and SW626 ovarian cancer cells which are both also insensitive to cisplatin, but were directly derived from a patient, and not laboratory-induced. Compared to platinum-sensitive A2780 ovarian cancer cells, SK-OV-3 cells were found to be particularly insensitive to cisplatin (IC_{50} 16.8 ± 0.8 μM compared to 1.2 ± 0.3 μM in A2780 cells). Similarly, both osmium and iridium sulfonamide complexes exhibited lower antiproliferative activities against both SK-OV-3 (IC_{50} range: 32-64 μM) and SW626 (IC_{50} range: 26.0-48.8 μM) cell lines, consistent with observations of cross-resistance determined in A2780cis. These data suggest that mechanisms of resistance (increased efflux, reduced metal accumulation, in-cell deactivation by GSH) may be maintained in the sulfonamide series.[32]

Table 4.2. Antiproliferative activities determined for Os complexes **2**, **7**, **8** and Ir complexes **12**-**14** against fourteen human cell lines, compared to Pt complex cisplatin (**CDDP**).

		IC$_{50}$ concentrations / μM						
Complex		**CDDP**	**2**	**7**	**8**	**12**	**13**	**14**
Metal		Pt	Os	Os	Os	Ir	Ir	Ir
Arene		-	*p*-cym	bip	*m*-terp	Cp*	Cp^{xPh}	Cp^{xBip}
A2780	Ovarian	1.2 ± 0.3	15.5 ± 0.5	6.5 ± 0.3	4.4 ± 0.3	20.9 ± 0.7	14 ± 2	10.2 ± 0.6
A2780cis	Pt-resistant ovarian	13.4 ± 0.3	21.6 ± 0.2	25.9 ± 0.7	10.4 ± 0.5	17 ± 2	18 ± 1	6.3 ± 0.8
A549	Lung	3.2 ± 0.1	21.1 ± 0.3	22.4 ± 0.7	25.5 ± 0.3	38 ± 2	25.2 ± 0.3	17 ± 3
HCT116	Colon	5.2 ± 0.3	37 ± 1	26.1 ± 0.3	41.2 ± 0.7	40.3 ± 0.7	58.2 ± 0.9	15.0 ± 0.1
HCT116-p21-/-	Colon (*p21* knock-out)	9.2 ± 0.5	106 ± 2	90 ± 1	N.D.	62.4 ± 0.3	75 ± 1	64 ± 1
HCT116-p53-/-	Colon (*p53* knock-out)	36.7 ± 0.3	62 ± 3	40 ± 6	N.D.	63 ± 2	55 ± 2	40.3 ± 0.7
HEPG2	Liver	5.7 ± 0.9	29 ± 2	14.6 ± 0.2	N.D.	23.5 ± 0.8	8.3 ± 0.8	3.6 ± 0.7
HOF	Ovarian fibroblast	10.2 ± 0.7	29.9 ± 0.5	44 ± 1	24.3 ± 0.4	19.0 ± 0.1	26.8 ± 0.6	15.0 ± 0.7
MCF7	Breast	6.6 ± 0.4	10.9 ± 0.7	7.8 ± 0.3	N.D.	14.6 ± 0.2	8.4 ± 1.0	3.7 ± 0.7
MRC5	Lung fibroblast	12.8 ± 0.5	21.4 ± 0.7	15.1 ± 0.5	9.7 ± 0.2	17.3 ± 0.4	11.9 ± 0.9	5.9 ± 0.2
OE19	Oesophageal	8.7 ± 1	> 50	30.0 ± 0.2	20.9 ± 0.9	> 50 [c]	33.2 ± 0.5	12.9 ± 0.3
PC3	Prostate	4.1 ± 0.5	12.0 ± 0.3	9.9 ± 0.2	13.6 ± 0.2	35.1 ± 0.6	18.8 ± 0.2	12.2 ± 1.0
SK-OV-3	Pt-resistant ovarian	16.8 ± 0.8	41.8 ± 0.1	64 ± 5	N.D.	55.7 ± 0.7	42 ± 3	34 ± 2
SW-626	Ovarian	15.7 ± 0.8	26.0 ± 0.4	36.7 ± 0.6	N.D.	48.8 ± 0.2	37.8 ± 0.9	27 ± 1

24 h drug exposure + 72 h recovery in drug-free medium. N.D. = not determined.

4.3.5 Metallodrug accumulation in cancer cells

Further cellular metal accumulations were determined in seven cancer cell lines using parental osmium(II) and iridium(III) tosyl complexes **2** [Os(*p*-cymene)(TsDPEN] and **12** [Ir(Cp*)(TsDPEN], in order to determine whether the apparent selectivity (higher antiproliferative activity) for particular tumour types arises from a greater influx of metal into the cell (Figure 4.6).

Greater antiproliferative activity was clearly observed in cell lines that exhibited increased cellular metal accumulation. The correlation was observed for both osmium complex **2** and iridium complex **12** (Figure 4.6). For both complexes, accumulation was greatest in MCF7 breast cancer cells (33 ng Os × 10^6 cells and 74 ng Ir × 10^6 cells, respectively) and lowest in OE19 oesophageal cancer cells (2.23 ng Os × 10^6 cells and 6.2 ng Ir × 10^6 cells, respectively). Accumulation of iridium complex **12** was typically 2-3-fold greater than the accumulation of osmium complex **2**, except for metal accumulation in PC3 cancer cells, where accumulation of both complexes was statistically equal (32 ± 2 and 31 ± 1 ng metal × 10^6 cells for complexes **2** and **12**, respectively). Metal accumulations could not be determined in primary cell lines (MRC5 and HOF) due to the large number of cells required (4 × 10^6 cells seeded on day 1). The passage number required to grow this quantity of cells would result in the cells entering replicative senescence or differentiation.

Metal accumulations were also determined in cisplatin-resistant A2780 cancer cells (A2780cis), and were significantly decreased by approximately one third of the metal accumulation, relative to the cisplatin-sensitive cell line (A2780) for both osmium complex **2** and iridium complex **12**. Osmium complex **2**: 9.5 ng Os × 10^6 cells compared to 30 ng Os × 10^6 cells. Iridium complex **12**: 16.5 ng Ir × 10^6 cells compared to 52 ng Ir × 10^6 cells (Figure 4.6).

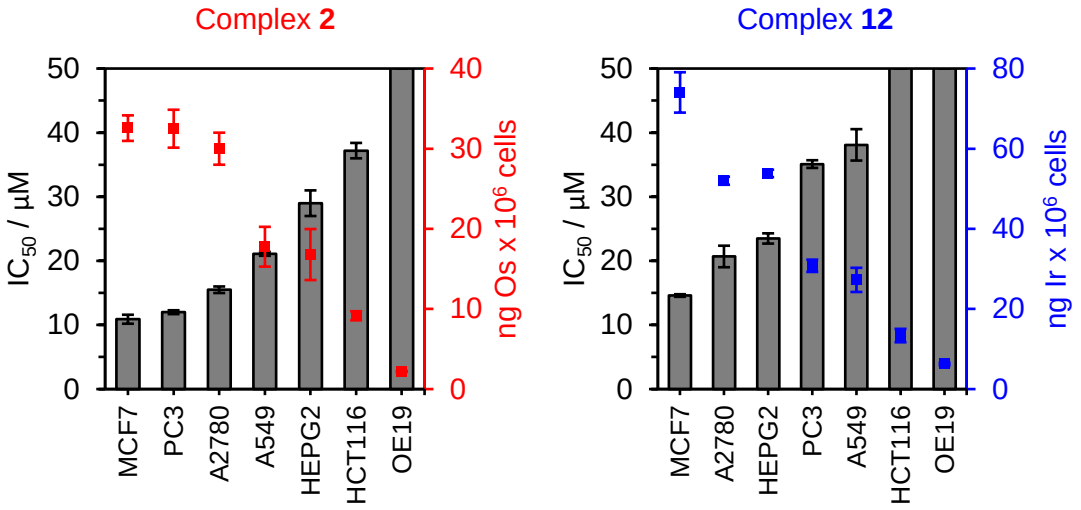

		ng Os / Ir × 10^6 cells	
		[Os(*p*-cymene)(TsDPEN)] **2**	[Ir(Cp*)(TsDPEN)] **12**
A2780	Ovarian	30 ± 2	52 ± 1
A2780cis	Ovarian [a]	9.5 ± 0.7	16.5 ± 0.5
A549	Lung	18 ± 2	27 ± 3
HCT116	Colon	9.1 ± 0.6	13 ± 2
HEPG2	Liver	17 ± 3	53.8 ± 0.9
MCF7	Breast	33 ± 2	74 ± 5
OE19	Oesophageal	2.23 ± 0.05	6.2 ± 0.3
PC3	Prostate	32 ± 2	31 ± 2

[a] Cisplatin-resistant ovarian cancer cells derived from parental cell line, A2780.

Figure 4.6. Total metal accumulation (ng Os / Ir per million cells) in eight cancer cell lines, exposed to equipotent concentrations of complexes **2** (●) or **12** (●) for 24 h with no recovery time.

Further detailed cellular accumulation studies were carried out in A2780 ovarian cancer cells using complexes **2** [Os(*p*-cymene)(TsDPEN)] and **12** [Ir(Cp*)(TsDPEN)]. The concentration, time and temperature-dependence of drug accumulation were explored, as well as the role of metal efflux in the total accumulation of the compounds over 24 h drug exposure (and with up to 72 h recovery time, in the same way antiproliferative activities were determined) to better understand how the accumulation profiles differ between Os and Ir complexes.

Concentration-dependent metal accumulation

The concentration-dependence of metal accumulation was investigated in A2780 ovarian cancer cells treated using four different concentrations of either osmium complex **2** or iridium complex **12** (0.25, 0.5, 1.0, 1.5 × IC_{50}), administered for 24 h at 310 K with no recovery time (Figure 4.7).

As observed in equipotent-concentration (1× IC_{50}) experiments, the accumulation of iridium complex **12** was found to be significantly greater (*ca.* 1.6×) than the accumulation of osmium complex **2**. Nonetheless, the extent of cellular metal accumulation in cells treated with either complex **2** or **12** was linearly dependent with respect to the concentration of the drug in solution.

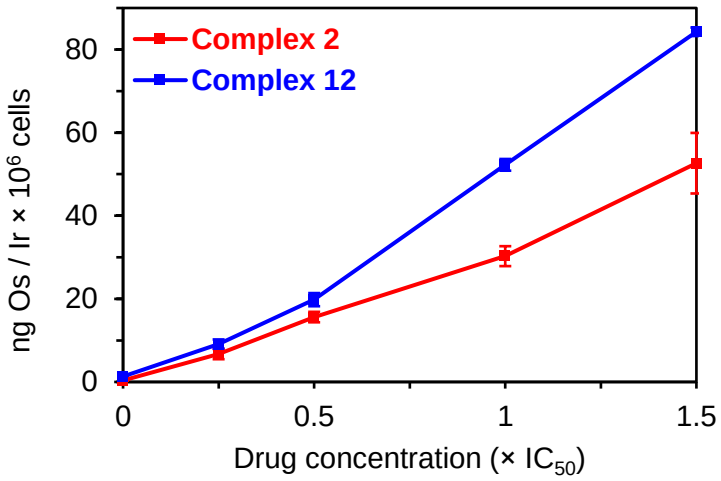

		Cellular accumulation (ng Os / Ir × 10^6 cells)			
	Complex	0.25 × IC_{50}	0.5 × IC_{50}	1.0 × IC_{50}	1.5 × IC_{50}
2	[Os(*p*-cymene)(TsDPEN)]	7 ± 1	16 ± 1	30 ± 2	53 ± 7
12	[Ir(Cp*)(TsDPEN)]	9 ± 1	20 ± 2	52 ± 1	84 ± 1

Figure 4.7. Concentration-dependent accumulation of complexes **2** (●) and **12** (●) in A2780 cells: 0.25, 0.5, 1, 1.5 × IC_{50}. (310 K, 24 drug exposure, no recovery period).

Time-dependent metal accumulation

Metal accumulation in A2780 cancer cells treated with either complex **2** or **12** was investigated in after 3, 6, 18 and 24 h drug exposure in an equipotent manner (fixed concentration equal to IC_{50} in A2780) at 310 K. After 24 h, the drug solution was removed. Cells were washed with PBS and allowed to recover in drug-free culture medium for 24 h (indicated by black line in Figure 4.8). Internalisation of iridium complex **12** was both greater and more rapid (maximum accumulation at 3 h, 53 ng Ir × 10^6 cells) than for osmium complex **2** (maximum accumulation of 42 ng Os × 10^6 cells after 6 h exposure, compared with accumulation at 3 h, p=0.03), suggesting that accumulation of Os / Ir may be associated with different transport mechanisms.

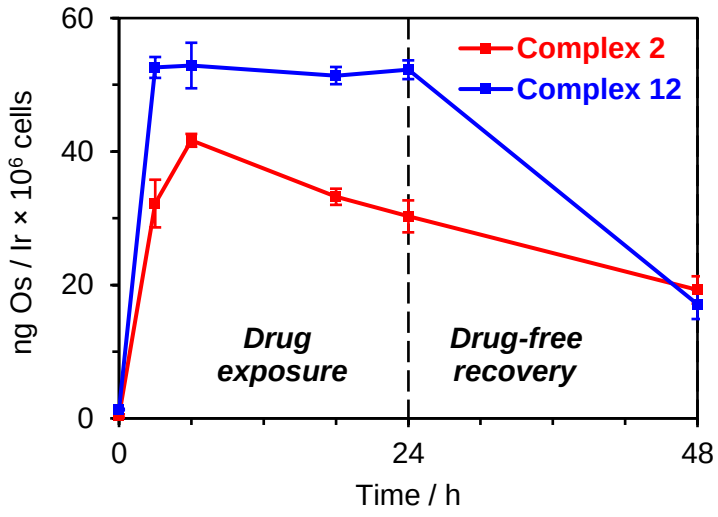

		Cellular accumulation (ng Os / Ir × 10^6 cells)				
	Complex	3 h	6 h	18 h	24 h	48 h
2	[Os(*p*-cymene)(TsDPEN)]	32 ± 4	42 ± 1	33 ± 1	30 ± 2	19 ± 2
12	[Ir(Cp*)(TsDPEN)]	53 ± 2	53 ± 3	51 ± 1	52 ± 1	17 ± 2

Figure 4.8. Time-dependent accumulation (24 h drug exposure and 24 h recovery in drug-free cell culture medium) of complexes **2** (●) and **12** (●) in A2780 cells: 3, 6, 18, 24 h drug exposure (310 K, no recovery period, 1 × IC_{50}) and with 24 h recovery time in drug-free medium. Drug removal time shown in black (24 h).

Interestingly, the greater internalisation of **12** goes against the frequently identified link between the higher internalisation of more hydrophobic complexes,[8, 29] since experimentally-determined hydrophobicities (Log P) (**Os-2** = 1.45 ± 0.02, **Ir-12** = 0.86 ± 0.02) show **2** to be more hydrophobic than **12**. These data suggest that the metal centre, rather than discrepancy between *p*-cymene and Cp* (reflected in the hydrophobicities of the complexes) appears to influence the accumulation of metal. Rapid accumulation of iridium complexes has been previously reported in many cases, achieving up to 80% of total iridium accumulation in the first hour of exposure.[33]

Os(II) and Ir(III) efflux profiles were significantly different. The amount of Os in cells treated with complex **2** accumulated decreased linearly after reaching a maximum at 6 h. No significant change in Ir accumulation in cells treated with complex **12** was observed between 3 h until drug removal after 24 h (Figure 4.8). After removal of the drug supernatant media at 24 h, cells were washed with PBS and allowed to recover in drug-free culture medium. Upon comparison of the amount of Os / Ir (ng metal × 10^6 cells) in cells after 24 h recovery with the levels of accumulation after 24 h drug exposure, a rapid efflux of iridium was identified, with only *ca*. 32% of the Ir accumulation remaining after 24 h recovery. In contrast, *ca*. 63% of the internalised Os remained inside cells after 24 h recovery in drug-free culture medium. This variance in the accumulation of osmium / iridium provides useful information in the design of structurally-similar metallodrugs. The rapid accumulation and efflux profile of iridium complex **12** may facilitate a highly-controlled exposure time in cells, minimising drug clearance times (pharmacological half-life), whereas the gradual slow detoxification of Os complex **2** may be better suited for a catalytic metallodrug, that itself possesses only moderate activity, but could be activated *in vitro* in order to target cancer cells.

Temperature-dependent metal accumulation

A2780 cancer cells were treated with equipotent concentrations (1× IC_{50}) of either Os complex **2** or Ir complex **12** over a period of six hours under two different incubation temperatures (277 K and 310 K) as part of two independent experiments (each carried out in triplicate), to explore the contribution of passive / active mechanisms in the accumulation of metal into the cell. The Os accumulation at 277 K in cells treated with complex **2** was found to be significantly decreased (p = 0.0013) at both 3 h (*ca.* 10% of the Os accumulation at 310K) and 6 h (*ca*. 25% of the Os accumulation at 310 K).

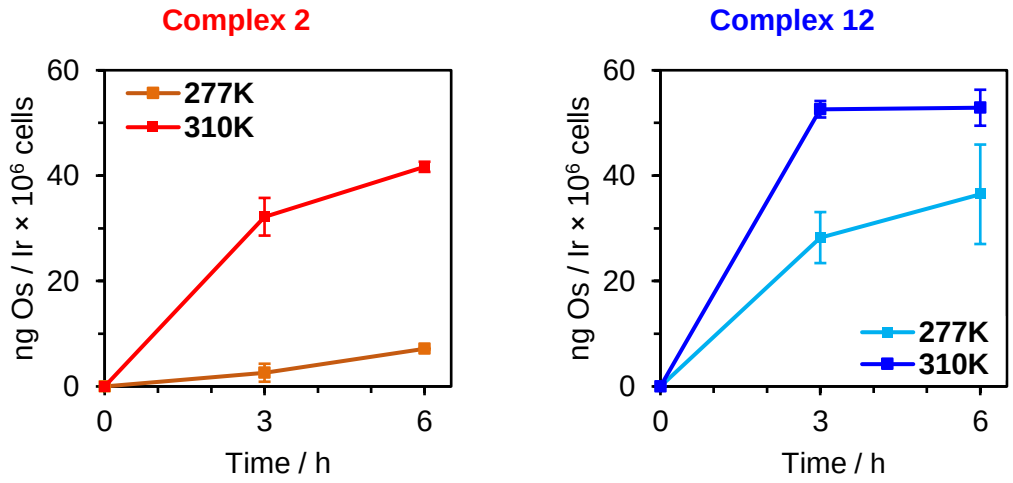

		Metal accumulation (ng Os / Ir × 10^6 cells)		
	Complex	Temp. / K	3 h	6 h
2	[Os(*p*-cymene)(TsDPEN)]	277	3 ± 2	10.2 ± 0.1
2	[Os(*p*-cymene)(TsDPEN)]	310	32 ± 4	42 ± 1
12	[Ir(Cp*)(TsDPEN)]	277	26 ± 3	36 ± 9
12	[Ir(Cp*)(TsDPEN)]	310	53 ± 2	53 ± 3

Figure 4.9. Cellular accumulation of complexes **2** (● 277 K, ● 310 K) and **12** (● 277 K, ● 310 K) in A2780 cancer cells at two incubation temperatures for 0, 3, 6 h drug exposure (1.0 × IC_{50} concentration).

The accumulation of iridium in cells treated with complex **12** was also affected by temperature (p = 0.0069) with *ca*. 49% of the Ir accumulation determined at 310K after 3 h, and 68% of the accumulation determined at 310K after 6 h. In contrast to the accumulation of Os in cells treated with complex **2**, the decrease in iridium accumulation at lower temperature was markedly less dramatic (Figure 4.9). The low accumulation of osmium at 277 K suggests that the accumulation may be largely active (energy-dependent) in nature, in contrast to complex **12**, whose Ir accumulation may be contributed to by both active (energy-dependent) and passive (energy-independent) mechanisms.

Metal efflux and evolvement of the P-gp efflux pump in ovarian cancer cells

A2780 cancer cells treated with complex **2** or **12** were also incubated with a known efflux pump (P-glycoprotein) inhibitor, verapamil (20 μM), for 72 h recovery period after 24 h drug exposure at 1.0 × IC_{50} equipotent concentrations, with cells collected and analysed after 0, 24, 48 and 72 h recovery time in either the presence and absence of verapamil.

Verapamil was found to significantly affect the efflux of both Os (complex **2**) and Ir (complex 1**2**) from treated cells ($P < 0.05$, Figure 4.10) however the effect was more apparent ($P < 0.05$) at an earlier time for Os complex **2** (24 h) compared to Ir complex **12** (48 h). The efflux of metal from treated cells was statistically the same after 72 h, regardless of verapamil concentration, suggesting that either the efficacy of verapamil is short-lived, or that a plateau in drug efflux was reached.

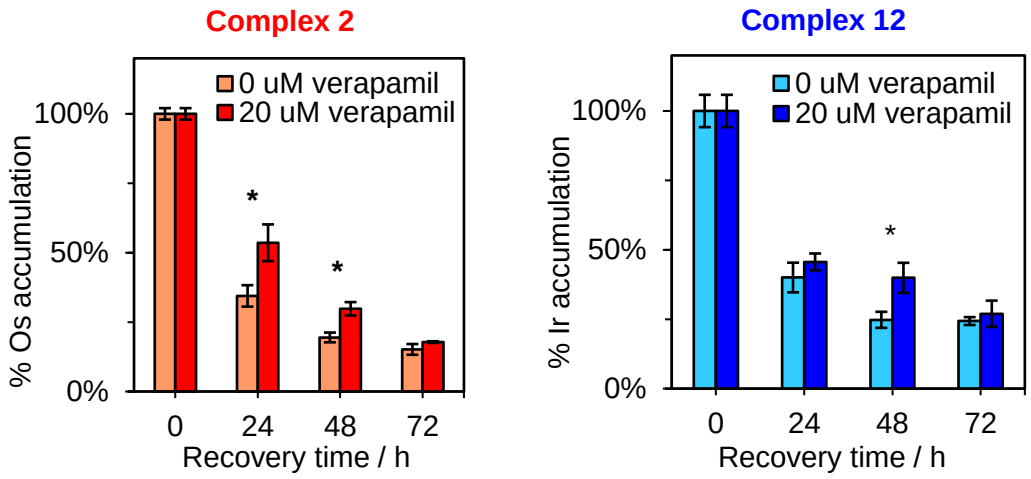

			% accumulation (recovery time)			
	Cell line	Verapamil / μM	0 h	24 h	48 h	72 h
2	A2780	0	100 ± 2	34 ± 4	19 ± 2	15 ± 2
2	A2780	20	100 ± 2	54 ± 7	30 ± 2	17.8 ± 0.3
12	A2780	0	100 ± 6	40 ± 5	25 ± 3	24 ± 1
12	A2780	20	100 ± 6	46 ± 3	40 ± 5	27 ± 5

Figure 4.10. Percentage metal efflux (normalised) of complexes **2** (●) and **12** (●) from Pt-sensitive A2780 cancer cells and Pt-resistant A2780cis cancer cells in: (a) drug free medium; (b) the presence of verapamil (20 μM) – a known PgP inhibitor. Verapamil significantly inhibits the efflux of Os and Ir from A2780 cancer cells (* P<0.05). Statistics calculated using a two-tailed t-test assuming unequal variances (Welch's t-test).

4.3.6 Cellular metal distribution in cancer cells

The distribution of Os or Ir inside A2780 cancer cells was investigated using the BioVision Fraction PREP kit (Figure 4.11). Four fractions were isolated: cytosolic (soluble cytoplasmic proteins), membrane (soluble membrane proteins and organelles), nucleic (soluble nuclear membranes and proteins) and the cytoskeletal (insoluble proteins). Metal distribution was found to differ significantly between Os and Ir complexes. Membrane localisation was significantly lower for Ir complex **12** than Os complex **2** (p < 0.01), while a lower metal percentage distribution was determined for the cytoplasmic fraction for Os complex **2** than Ir complex **12** (p < 0.05). Nuclear and cytoskeletal accumulations were low for both metal complexes.

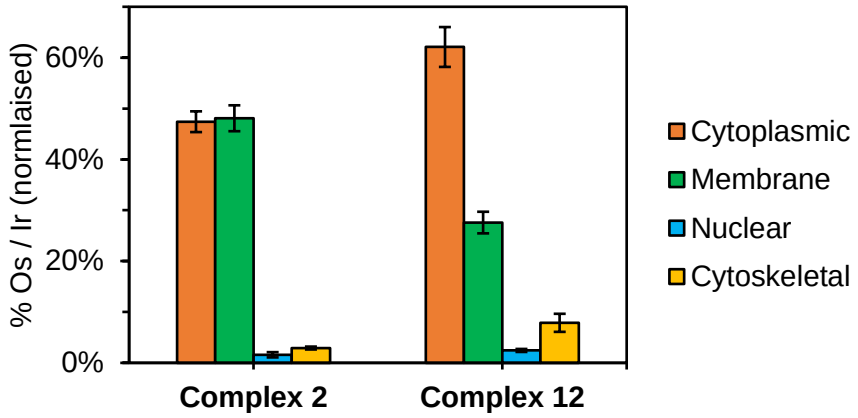

	Normalised population %			
	Cytosol	**Membrane**	**Nucleus**	**Cytoskeleton**
2	47 ± 2	48 ± 3	1.6 ± 0.5	2.9 ± 0.3
12	63 ± 7	26 ± 2	2.3 ± 0.3	8.5 ± 0.5

Figure 4.11. Cellular Os / Ir distribution in A2780 cancer cells exposed to complexes **2** and **12** (1.0 × IC_{50}) for 24 h without recovery time. * P<0.05, ** P<0.01. Four fractions: cytosolic (soluble cytoplasmic proteins; ●), membrane (soluble membrane proteins and organelles; ●), nucleic (soluble nuclear membranes and proteins; ●) and the cytoskeletal (insoluble proteins; ●).

4.3.7 Generation of reactive oxygen species (ROS) and superoxide

The generation of reactive oxygen species (ROS; hydrogen peroxide, hydroxyl-radicals, singlet oxygen, and superoxide) by complexes **2** and **12** (1 × IC_{50}) was investigated in A2780 cancer cells and HOF ovarian fibroblasts by flow cytometry using a ROS/superoxide detection kit (Enzo Life Sciences). Levels of ROS were determined after 24 h drug exposure without recovery time (since reactive oxygen species are short-lived). Both complexes of osmium and iridium produced large bursts of ROS and superoxide (Q2) in A2780 cancer cells after 24 h drug exposure (96 ± 1 % and 96 ± 2 % for **2** and **12**, respectively; Figure 4.12), which was statistically similar for both **2** (Os *p*-cymene) and **12** (Ir Cp*). The detection of ROS/superoxide by complex **2** was further explored using ovarian fibroblasts (HOF, non-cancerous cells), and the generation of superoxide was remarkably reduced in non-cancerous cells.

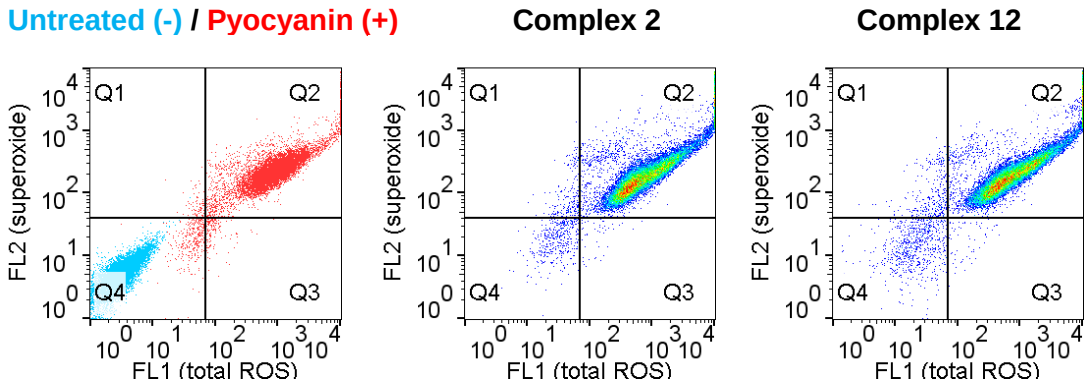

	% Population ± SD			
Complex	Q1 [a]	Q2 [b]	Q3 [c]	Q4 [d]
2	1.2 ± 0.2	96 ± 1	0.3 ± 0.1	2.4 ± 0.9
12	1.4 ± 0.2	96 ± 2	0.22 ± 0.08	2 ± 1
Untreated	0.05 ± 0.05	0.01 ± 0.02	0.00 ± 0.00	99.93 ± 0.06
Pyocyanin	1.01 ± 0.08	94.4 ± 0.4	1.23 ± 0.01	3.4 ± 0.2

Figure 4.12. Flow cytometry data for complexes **2** and **12** in A2780 cancer cells. ROS and superoxide are generated after 24 h drug exposure with no recovery time. Positive control = pyocyanin. [a] Q1: FL1-FL2+ (superoxide), [b] Q2: FL1+FL2+ (superoxide and oxidative stress), [c] Q3: FL1+FL2- (oxidative stress), [d] Q4: FL1-FL2- (no superoxide or oxidative stress).

The Q2 population (FL1+ / FL2+ for superoxide and total reactive oxygen species) decreased from 96% in A2780 cancer cells (Figure 4.12) to 38% in HOF fibroblasts (Table 4.3) suggesting a lower amount of total ROS in the non-cancerous cells, however the Q3 population (total ROS) was increased from 0.3% in A2780 cancer cells to 45.4% in HOF fibroblasts treated with **2**.

Table 4.3. Flow cytometry data for complex **2** in HOF ovarian fibroblasts. ROS and superoxide are generated after 24 h drug exposure with no recovery time. Positive control = pyocyanin [a] Q1: FL1-FL2+ (superoxide), [b] Q2: FL1+FL2+ (superoxide and oxidative stress), [c] Q3: FL1+FL2- (oxidative stress), [d] Q4: FL1-FL2- (no superoxide or oxidative stress).

	% Population ± SD			
Complex	Q1 [a]	Q2 [b]	Q3 [c]	Q4 [d]
2	9.1 ± 0.8	38 ± 1	45.4 ± 0.7	7.3 ± 0.5
Untreated	17 ± 2	0.2 ± 0.2	0.4 ± 0.2	83 ± 2
Pyocyanin	8 ± 2	90 ± 2	1.2 ± 0.2	1.2 ± 0.5

4.3.8 Combination with L-buthionine sulfoximine

The redox chemistry of osmium complex **2** was further explored by determining the IC_{50} concentration in the presence of a non-toxic concentration (5 μM) of L-buthionine sulfoximine (L-BSO), an inhibitor of γ-glutamylcysteine synthetase, an enzyme essential to the synthesis of the antioxidant molecule, glutathione (GSH). L-BSO was administered to cells independently of the osmium complex, but within 5 minutes of exposure to **2** or **12**.

The activity of complex **2** was significantly increased at the 95% confidence level, suggesting that GSH depletion and enhanced redox sensitivity increased the potency of the Os complex. The IC_{50} concentration decreased by *ca*. 36% in the presence of 5 μM L-BSO, from 15.74 ± 0.07 μM to 10.0 ± 0.7 μM (Table 4.4). Conversely, the anticancer activity of complex **12** was unaffected by the presence of 5 μM L-BSO (20.9 ± 0.7 μM compared to 21.7 ± 0.9 μM; $P = 0.3112$). These data suggest that GSH may a play a role in the detoxification of osmium complex **2** inside the cell, but is unlikely to affect the potency of iridium complex **12**. Alternatively, ROS generation by iridium complex **12** may be so great that the concentration of intracellular GSH is not adequate to sequester the effect. If so, inhibition of GSH synthesis by administration of L-BSO would not significantly improve the activity of **12**.

Table 4.4. Modulation of the antiproliferative activity of complex **2** or **12** by co-administration of a non-toxic concentration of L-BSO (5 μM), in A2780 cancer cells (24 h drug exposure, 72 h recovery time in drug-free medium).

		L-buthionine sulfoximine		
	Complex	0 μM	5 μM	*t*-test [a]
2	[Os(*p*-cymene)(TsDPEN)]	15.74 ± 0.07	10.0 ± 0.7 *	$P = 0.0050$
12	[Ir(Cp*)(TsDPEN)]	20.9 ± 0.7	21.7 ± 0.9	$P = 0.3112$

[a] Two-tailed *t*-test with unequal variances (Welch's *t*-test). * $P<0.05$

4.4 Discussion

4.4.1 Synthesis and stability of Ir(III) sulfonamide complexes

Though the synthesis of [Ir(Cp*)(TsDPEN)] **12** has been previously described,[20] the biological activities of **12**, extended arene complexes **13**-**14**, and methoxy-substituted complexes **15**-**17** have not been explored. The purple 16-electron active complexes (Figure 4.2) were all readily isolated by the same method described for Os complexes **2**-**10** (Chapter 3, section 3.3.1, page 78), and were readily recrystallised from dichloromethane / *n*-hexane. Examples of stable coordinatively-unsaturated Ir(III) 16-electron N,O-phosphoramidate and hydride-pincer complexes are known,[34, 35] and similarly the Ir(III) complexes described here were also stable.

Ir(III) complexes **12**-**17** all display high stabilities in phosphate-buffered saline solution in the presence of DMSO. Changes in UV-visible or ^{1}H-NMR spectra were not observed over a 24 h period (Figure 4.3), suggesting that it is unlikely that aqua, DMSO, or chloro- adducts form, unless the formation is immediate, and the formation cannot be detected before the acquisition of the first spectra. While iridium phenylpyridine complexes are known to form aqua adducts in solution,[33] the apparent inertness of coordinatively-unsaturated iridium sulfonamide complexes was also observed for the osmium series in Chapter 3 (section 3.3.4, page 85). Both extension of the aromatic unit, and introduction of methoxy-substituents onto the chiral pendant phenyl groups of the diamine, were found not to affect the aqueous stability. Methoxy groups have been shown to increase the *in vivo* half-lives of sulfonamides.[36] This substitution noticeably improved the aqueous solubility of **15**-**17**, reflected in the lower partition coefficients determined by the shake-flask method (**12**-**14**: 0.86, 1.41, and 2.24; **15**-**17**: 0.03, 0.32, and 0.62 respectively).

4.4.2 Hydrophobicity, metal accumulation and anticancer activity

In the design of novel anticancer metal complexes, a trade-off between hydrophobicity (greater cellular accumulation) and hydrophilicity (solubility in blood plasma to reach cells) is required. Octanol / water partition coefficients (Log P) are commonly used to model the distribution of molecules across lipid membranes, such as those present in cells. Compounds with greater partition coefficients (more hydrophobic) are anticipated to readily diffuse from the aqueous phase into the organic (octanol phase), whereas those with lower (or negative) partition coefficients.

Both osmium and iridium complexes were found to have high-to-moderate activity in A2780 cancer cells (Table 4.1) with IC_{50} values ranging from 0.7 μM (complex **17**) to 30 μM (complex **3**). Osmium complexes typically exhibited higher antiproliferative activities (15.5, 6.5, 4.4 μM for Os complexes **2** (*p*-cymene), **7** (biphenyl), **8** (*m*-terphenyl) compared to 20.9, 14, 10.2 μM for Ir complexes **12-14**), despite generally lower cellular metal accumulation (30, 13, 31.9 ng Os × 10^6 cells for complexes **2**, **7**, **8** compared to 52, 41.7, 89 ng Ir × 10^6 cells for complexes **12-14**). This suggests that the efficiency of the osmium(II) complexes inside cells may be higher than analogous iridium(III) complexes, which may relate to the lower oxidation state of Os(II), rendering the complex less prone to attack by nucleophiles present inside the cell (such as glutathione, and negatively charged amino acids such as cysteine and serine).

Arene ring extension is clearly shown to increase hydrophobicity for both the Os (**3** > **2** > **1**) and Ir (**6** > **5** > **4**) DPEN series as well as the BMEN Os (**10** > **9**) and Ir (**17** > **16** > **15**) series, which in turn correlates with antiproliferative activity against cancer cells (Figure 4.13). The low hydrophobicity of methanesulfonyl complex **3** (Log P = 0.18) may explain its lower antiproliferative activity (30 μM) compared to the rest of the Os sulfonamide complexes. The same trend between Log P and IC_{50} is commonly

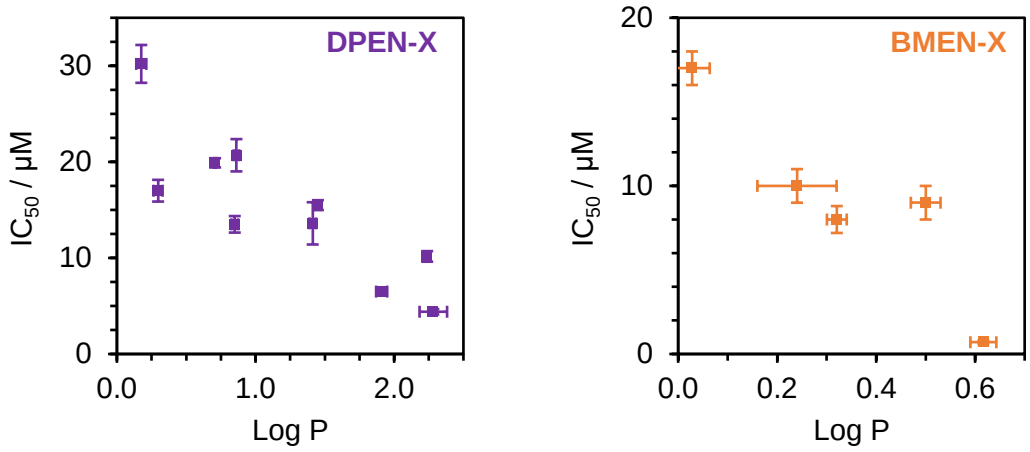

Figure 4.13. Correlation between antiproliferative activity (IC_{50} in A2780) and octanol / water partition coefficient (Log P) for both diphenylethylenediamine (DPEN) and bis(4-methoxyphenyl)-ethylenediamine (BMEN) complexes. R^2 = 0.74 (DPEN), 0.84 (BMEN).

identified for similar late-transition metal compounds,[37-39] and we now show that this trend is also observed for the sulfonamide complexes. Interestingly, while methoxy-substituted compounds **9**-**10** and **15**-**17** had lower hydrophobicity than their DPEN counterparts (achieving greater water solubility), the BMEN complexes were generally more active against A2780 cancer cells (Table 4.1 and Figure 4.13), which was particularly prominent for Ir Cp^{xBip} complex **17** (IC_{50} = 0.7 μM; 15× more active than parent complex **14**, IC_{50} = 10.2 μM). The introduction of polar substituents, such as methoxy groups, may aid interaction with biological moieties inside cells which are often highly charged, such as nucleic acids and proteins.

Only slight correlation was observed between total metal accumulation in A2780 cancer cells and Log P for osmium DPEN sulfonamide series **2**-**8** (Figure 4.14, R^2 = 0.35) while no correlation is observed for BMEN complexes ($R^2 < 1 \times 10^{-5}$). This does not appear to correlate with arene ring extension, since if lipophilicity was the only factor determining cellular accumulation, the expected trend would be *m*-terphenyl (**8**) > biphenyl (**7**) > *p*-cymene (**2**). A similar lack of correlation between accumulation

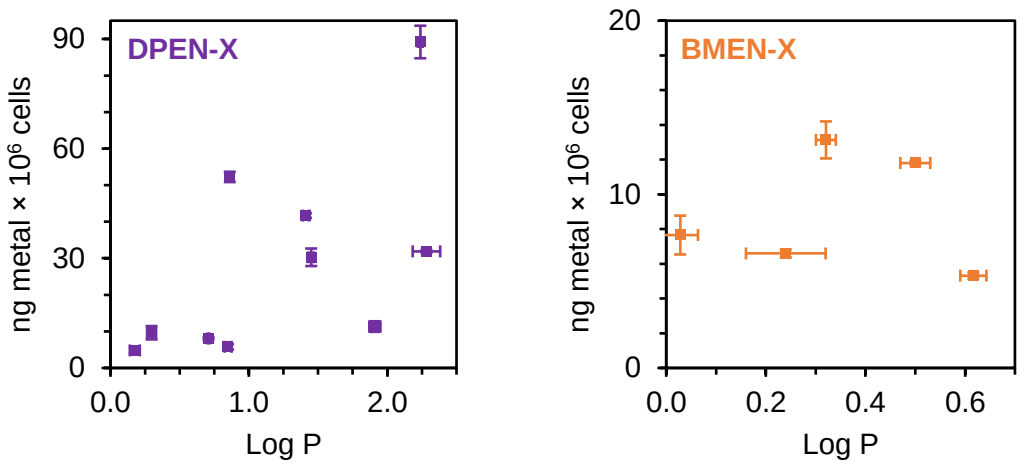

Figure 4.14. Lack of correlation between total drug accumulation (ng metal × 10^6 cells) in A2780 cancer cells and Log P for diphenylethylenediamine (DPEN). No correlation is observed for bis(4-methoxy-phenyl)ethylenediamine (BMEN) complexes. Pearson's r = 0.35 (DPEN), < 0.01 (BMEN).

and hydrophobicity was previously identified for a series of Pt complexes.[29] Complex lipophilicity may not be the only factor that governs cellular accumulation. If the complexes were only internalised in cells by passive diffusion, the accumulation trend should be linear with respect to lipophilicity. However, contribution from energy-dependent (active) mechanisms (such as ATP-dependent transporter proteins) would differ significantly from the hypothesised relationship between hydrophobicity and (passive) drug accumulation, as identified in the sulfonamide series.

4.4.3 Multi-cell line antiproliferative activity screening

Osmium tosyl (TsDPEN) **2** (*p*-cymene), **7** (biphenyl) and **8** (*m*-terphenyl), and iridium complexes **12-14** (Cp*, Cp^{xPh} and Cp^{xBip}) showed broad activity across the majority of cell lines investigated (Table 4.2), and in particular, the complexes showed promise in cancers of the reproductive organs, specifically of the breast, ovary and prostate (MCF7, A2780 and PC3, respectively). This trend could be linked to the fact that cancers of these tissues are typically hormone-responsive, and the mechanism of action may involve interactions with receptor sites or hormone-dependent pathways.

Ruthenium conjugates of the peptide hormone somatostatin have been designed to increase cancer cell selectivity by generation of $^1O_2$ upon light irradiation, utilising the overexpression of somatostatin receptors in various cancer cell types relative to healthy cells.[40] Ruthenocene complexes derived from the anticancer drug Tamoxifen were found to bind to estrogen receptor alpha (up to 85% binding, compared to 39% for hydroxytamoxifen) but did not exhibit potency towards ER-α-negative cells.[41]

Os and Ir sulfonamide complexes displayed particularly low antiproliferative activities (in some cases, >50 μM) in gastrointestinal cell lines (OE19 and HCT116), suggesting selectivity for cells of particular tissues – an important property in the design of new anti-cancer agents. In addition to specific tumour selectivity, efficacies of the complexes were investigated between cancer cells (A2780 and A549) and two non-cancerous primary cell lines, ovarian (HOF) and lung fibroblasts (MRC5) as a model for healthy cells. Ovarian fibroblasts were chosen for comparison to A2780 ovarian cancer cells, in which the complexes were highly active. In this case, Os complexes **2** (*p*-cymene), **7** (biphenyl), and **8** (*m*-terphenyl) displayed good selectivity for cancer cells over healthy cells. Many other osmium complexes have displayed similar positive selectivity towards cancerous cells.[18, 42] Iridium compounds **12-14** were not as selective, achieving only *ca.* 2× selectivity. The selectivity of iridium complexes for cancer cells over normal cells is highly dependent on the nature of the bidentate ligand.[33, 43] While cyclometalated iridium bipyridine complexes were found to possess *ca.* 11-fold selectivity for cancer cells over healthy cells, Ir(III)-curcumin complexes lack the selectivity found in structurally similar Ru(II)-curcumin derivatives.[44] In this study, both Ir(III) and Os(II) sulfonamide complexes were poorly selective between cancerous (A549) and healthy (MRC5) lung cells, largely due to the low activity in the cancerous lung cell line.

Table 4.5. Resistance factors (A2780cis/A2780) calculated for complexes of Os (**2**, **7**-**8**) and Ir (**12**-**14**).

Complex	**2**	**7**	**8**	**12**	**13**	**14**
Metal	Os	Os	Os	Ir	Ir	Ir
Arene	*p*-cym	bip	*m*-terp	Cp*	Cp^{xPh}	Cp^{xBip}
A2780	15.5 ± 0.5	6.5 ± 0.3	4.4 ± 0.3	20.9 ± 0.7	14 ± 2	10.2 ± 0.6
A2780cis	21.6 ± 0.2	25.9 ± 0.7	10.4 ± 0.5	17 ± 2	18 ± 1	6.3 ± 0.8
R.F. [a]	1.4	4.0	2.4	0.8	1.3	0.6

[a] Resistance factor (R.F.) defined as the ratio of the IC_{50} determined in A2780cis / A2780.

Osmium(II) complexes **2** (*p*-cymene), **7** (biphenyl), and **8** (*m*-terphenyl) exhibited less potency towards cisplatin-resistant cells (A2780cis) compared to cisplatin-sensitive cells (resistance factor > 1; Table 4.5). Less cross-resistance was observed with iridium complexes **12**-**14** and in fact Ir complexes **12** and **14** were more potent in the resistant cell line (resistance factor = 0.8 and 0.6, respectively). This is in agreement with other iridium(III) half-sandwich complexes.[10, 30] Importantly, all sulfonamide complexes of osmium and iridium investigated exhibited less cross resistance than cisplatin (resistance factor = 11.2). This is an important finding, since the treatment of drug-resistant tumours is a problem of clinical significance, as cisplatin-resistant cells have been shown to decrease drug transport, modify apoptotic pathways and develop drug detoxification mechanisms to maintain proliferative growth.[45]

In addition to comparing between different cancer cell types, antiproliferative activities were determined in 3 ovarian cancer cell lines: A2780, SW626 and SK-OV-3. A2780 are a platinum-sensitive cell line, while SW626 and SK-OV-3 are increasingly platinum-insensitive cell lines (cisplatin: 1.2 µM, 15.7 µM and 16.8 µM, respectively). Similarly, the antiproliferative activities of both osmium sulfonamide (**2**, **7**, **8**) and iridium sulfonamide (**12**, **13**, **14**) complexes are in agreement with this trend, with complexes exhibiting highest potency in A2780 and lower potency in the

platinum-insensitive cell lines. Taken in combination with the reduced cellular metal accumulation in A2780cis (platinum-resistant) cells, a resistance mechanism is likely common to Pt drug exposure and treatment with Os / Ir complexes.

Comparing antiproliferative activities between parental HCT116 colorectal cancer cells and derived cell lines with genetically-engineered knockouts of key genes (*P21* and the tumour-suppressor gene *P53*, in HCT116-*p21*-/- cells and HCT116-*p53*-/- cells, respectively) provides an indication of the gene's involvement in the mechanism of action. If the gene is involved in the mechanism, the determined IC_{50} concentration would be higher (less active) in the knock-out cell line. Conversely, the IC_{50} determined in a knock-out cell line would not be affected if the gene is not critical to the mechanism of action. For cisplatin, antiproliferative activities are decrease in both the *p21* (9.2 μM) and *p53* (36.7 μM) knock-out cell lines, relative to the parental line (5.2 μM). This trend is also conserved in both the osmium and iridium sulfonamide series of complexes, which all exhibited the highest relative activity in the parental cell line. In each case, these data suggest that it is likely that *p21* and/or *p53* are involved in the mechanism of action, reflected in the decreased antiproliferative activities determined in the knock-out cell lines.

Since complexes **2** and **12** have been shown to carry out the catalytic oxidation of 1,4-NADH to NAD^+ under biologically-relevant conditions, it is likely that the complexes may interfere with cellular metabolic pathways, which require NADH as a hydride source for the reduction of substrates, for example, the conversion of pyruvate to lactate, which cancer cells utilise to respire (described by the Warburg Effect).[46-48] However, perturbation of the NADH/NAD^+ ratio is also known to induce the production of ROS by complex I of the mitochondrial electron transport chain.[49] In fact, other metabolic-targeting compounds have previously been associated with *p21*-

dependent cell death. While expression of the cyclin-dependent kinase inhibitor (CDK) *p21* is known to be up-regulated by *p53* in response to anticancer agents, its expression can also be regulated without functional *p53*.[50] A structurally-similar osmium(II) half-sandwich complex [Os(η^6-*p*-cymene)(4-(2-pyridylazo)-*N*,*N*-dimethylaniline)I]PF_6 generates mitochondrial ROS, leading to the up-regulation of both *p53* and *p21*, implicating their involvement in the mechanism of action.[18] Since *p53* and *p21* appear to also be involved in the mechanism of action of **2** (less activity the knock-out cell lines), which also produces ROS and superoxide in A2780 cancer cells, Os(II) arene complexes may share a common mechanism of action.

Overall, osmium(II) complexes typically exhibit higher antiproliferative activities than their Ir(III) counterparts, though at the expense of slightly increased cross-resistance against platinum-resistant cells. However, the accumulation of iridium in cells treated with Ir complexes **12**-**17** surpassed the levels of osmium internalised by cells treated with Os complexes **2**-**10**. Since examples of both Os and Ir sulfonamide complexes have been shown to convert NADH to NAD^+ under biologically relevant conditions, it may be possible that the mode of action is catalytic in cells. While both osmium and iridium complexes have been shown to be highly stable in biological media, the higher charge of Ir(III) compared to Os(II) may more readily promote catalyst deactivation by nucleophilic components in the cell, such as nucleophilic amino acid side-chains: cysteine (R-SH) serine (R-OH), histidine (R-NHR) and lysine ($R\text{-}NH_2$).

While the nature of the metal centre appears to be crucial when comparing biological activities of Os and Ir complexes (both the antiproliferative activity of the complex and the extent of metal accumulation into the cell), exchange of the arene to afford neutral complexes (for example, Os-*p*-cymene for Ir-Cp*) does mean that specific

conclusions about the role of the metal cannot be made. Even if the directly analogous complexes, $[Os(Cp^*)(diamine)]^-$ or $[Ir(p\text{-cymene})(diamine)]^+$ complexes could be synthesised, the anionic / cationic nature of the complexes would likely dramatically alter their properties; by increasing water solubility (and therefore would have a lower octanol / water partition coefficient, Log P) which may influence the antiproliferative activity towards cancer cells, cellular accumulation, and ability to carry out the catalytic oxidation of NADH.

Cellular accumulation in other cancer cell lines

The cellular metal accumulation was determined in seven cancer cell lines (Figure 4.6) treated with equipotent concentrations of either Os complex **2** or Ir complex **12**. ICP-MS was used to detect xenobiotic elements in cell pellets digested in acidic solution. Despite the lower osmium cellular accumulation compared to iridium across the range of cell lines investigated (30 ng Os × 10^6 cells for complex **2** compared to 52 ng Ir × 10^6 cells for complex **12** in A2780), osmium complexes were typically more potent than their iridium counterparts (15.5 ± 0.5 μM for Os complex **2** compared to 20.9 ± 0.7 μM for Ir complex **12** in A2780). Structurally similar osmium half-sandwich compounds have been determined to accumulate in cancer cells at similar concentrations (20-60 ng Os × 10^6 cells) to complexes **2-10** investigated in this chapter (ranging from 5-30 ng Os × 10^6 cells, depending on the nature of the arene and sulfonamide ligand),[51] while previous iridium arene complexes have been shown to accumulate rapidly in cells,[33] similarly to finding using complex **12**.

Across multiple cell lines treated equipotent concentrations of either complex **2** or **12**, increased metal accumulation in treated cells correlated with increased drug potency (ranging from 2.32-32 ng Os × 10^6 cells for **2**, and 6.2-74 ng Ir × 10^6 cells for complex

12, with corresponding IC_{50} values between 10.9-50 μM, and 14.6-50 μM respectively). Particular cell lines may be more specialised for the internalisation of hydrophobic molecules, or conversely, efflux xenobiotic species more efficiently than other types of cell. Specifically, gastrointestinal (GI) epithelial cells are particularly adapted to circumvent toxin bio-accumulation,[52] which may explain the low antiproliferative activities determined in OE19 (esophageal) and HCT116 (colorectal) cell lines. However, the cellular accumulation of anticancer compounds in GI cancers may be increased by functionalisation of molecules with substrates for nutrient transporters.[52] Additionally, vitamin B_{12} is readily absorbed via receptor-mediated endocytosis.[53] B_{12} conjugates of nanoparticles and peptides have been explored to increase GI tract drug adsorption.[53, 54] A similar strategy could be explored for accumulation of future anticancer drugs, increasing oral bio-availability.

The metal accumulation studies in this thesis were normalised by cell number but did not account for cell volume, which varies greatly between cell lines, so an accurate in-cell concentration cannot be determined. Cell volume may be determined using flow cytometry, a Coulter counter,[55] or more recently, by use of a confocal laser scanning microscope combined with 3D reconstruction software.[56] Suspended microchannel resonators have been described which measure simultaneously the volume, density and mass of single cells,[55] however this work goes beyond the scope of this thesis. Alternatively, single-cell ICP techniques could allow for the evaluation of metal accumulation in cells, providing data concerning the accumulation of metal in a population of cells, rather than whole-pellet digest.

Accumulation of Os and Ir in cisplatin-resistant cells (A2780cis) decreased to approximately ⅓ of the metal accumulation in the platinum-sensitive cell line (30 to 9.5 ng Os × 10^6 cells). Reduction in total metal accumulation has also been observed

with platinum drugs for various ovarian cancer cell lines, in many cases reduced by the same amount as observed for the sulfonamide complexes (for cisplatin, this is between 36-66% of the accumulation determined in platinum-sensitive cells, depending on the study and cell lines investigated).[57-59] Platinum resistance has been shown to result in approximately one order of magnitude fewer platinum-DNA adducts forming.[60] As well as decreased drug accumulation, resistance has also been associated with increased platinum drug efflux.[32] More detailed studies of the mechanism(s) of drug uptake and efflux may therefore help to explain the apparent absence of a trend between total accumulation and drug hydrophobicity. For example, the P-glycoprotein efflux pump (a translocating ATPase) has a broad specificity for many hydrophobic drugs, which are known to include many anticancer agents,[61] and cells from particular tissues may be better adapted for the accumulation of molecules.

4.4.4 Differences in drug accumulation between Os(II) and Ir(III) complexes

Cellular accumulations were studied in greater detail, using equipotent concentrations of either complex **2** or **12** as representative examples from the Os and Ir series, respectively, in A2780 cancer cells. Equipotent concentrations of each drug were used to directly compare the amount of metal required to achieve the same pharmacological effect.

In concentration-dependent studies, for both metal complexes, the accumulation was found to be linear with respect to concentration, with no system (e.g. transporter channel) saturation observed up to the highest concentration tested (1.5 × IC_{50}, Figure 4.7). This is comparable with other metal-based chemotherapeutics, such as cisplatin, which is known to accumulate linearly over two orders of magnitude (0.25-100 μM).[58]

It is therefore likely that the accumulation of osmium or iridium is not dependent on a single mechanism, and is likely to involve contributions from multiple mechanisms of internalisation.

Incubation of cells at 277 K (Figure 4.9) significantly decreased the accumulation of both **2** and **12** after 3 h drug exposure (to ~9% of the accumulation at 310 K for cells treated with Os-**2**, and to 50% of the accumulation at 310 K for cells treated with Ir-**12**). It is likely that the accumulation of **12** involves contributions from both energy-dependent and passive diffusion, which has also been observed for iridium Cp* benzoquinoline complexes, where Ir accumulation at 277 K was reduced to 26% of the accumulation at 310 K.[30] In contrast, the very low Os accumulation (3 ± 2 ng Os × 10^6 cells) at 277 K suggests that the accumulation of **2** is largely active in nature.

Future experimentation could confirm this hypothesis by depletion of ATP using 2-deoxyglucose or oligomycin, inhibitors of glycolysis and oxidative phosphorylation, respectively,[62] or by using copper chloride to examine the role of CTR1/CTR2 copper transporter proteins.[24] The contribution of passive diffusion is more challenging to study, since the accumulation is not affected by molecular inhibitors. However, changes to the fluidity of the cell membrane (by cholesterol depletion using methyl-β-cyclodextrin) can influence passive diffusion,[62] but this was not explored here.

Time-dependent accumulation (Figure 4.8) showed a faster rate of metal accumulation in A2780 cancer cells treated with Ir complex **12**, reaching equilibrium between drug influx and efflux (53 ± 2 ng Ir × 10^6 cells) after just 3 h drug exposure, which was maintained throughout drug exposure (52 ± 1 ng Ir × 10^6 cells after 24 h). However, the level of internalised iridium sharply decreased after removal of the drug-containing medium (17 ± 2ng Ir × 10^6 cells after 24 h recovery time), which would be consistent

with an energy-independent (passive diffusion) uptake pathway; whereby the uptake of metal is determined by the concentration gradient. In contrast, the accumulation of osmium complex **2** reached a maximum after 6 h drug exposure (42 ± 1 ng Os × 10^6 cells). After this time, the rate of drug efflux exceeded influx, and even after removal of the drug medium, the rate of efflux remained linear. These data reflect the contrasting biological interactions experienced by complexes **2** (Os) and **12** (Ir). Similar gradual detoxification of osmium from the cell has previously been observed with [Os(η^6-*p*-cymene)(4-(2-pyridylazo)-*N*,*N*-dimethylaniline)I]PF_6 in A549 cells,[51] which appears to be a common trait for Os *p*-cymene complexes. Multi-drug resistant (MDR) transporter proteins MRP1-3 are known to transport neutral molecules,[63] and may more readily efflux Ir compared to Os, reflected in the rapid rate of efflux.

P-glycoprotein (P-gp) is a drug efflux transporter which is widely selective for many hydrophobic compounds.[61] Cisplatin exposure is known to increase the expression of P-gp, while Pt-sensitivity can be restored by administration of verapamil, a P-gp inhibitor. The effect of P-gp inhibition on the efflux of metal from cells treated with **2** or **12** was examined by allowing cells, treated with complex for 24 h, to recover in culture medium containing 20 μM verapamil (Figure 4.10). Verapamil was found to significantly reduce the efflux of **2** and **12** (p<0.05).

While this effect has been previously described for similar Ir(III) and Ru(II) complexes,[30, 37] this work appears to be the first example of efflux inhibition by verapamil in cells treated with an Os(II) complex. The remaining metal in the cell after recovery time might not be excreted due to binding with various cellular components (e.g. membrane proteins, formation of adducts with GSH). Future work may explore the efflux of **2** and **12** from cisplatin-resistant cells to assess the contribution efflux has on the observed drug resistance.

4.4.5 Contrasting cellular metal distribution

Cellular distributions of **2** and **12** were investigated in A2780 cancer cells. Interestingly, the cellular distributions significantly differed between the Os / Ir complexes. Membrane accumulation was decreased in the case of **12** (48%) compared to Os complex **2** (26%). Other organo-osmium complexes have been shown to accumulate highly in the mitochondria of A549 lung cancer cells (leading to mitochondria mediated apoptosis and S-phase cell cycle arrest), suggesting a possible sub-cellular target.[51] For complexes **2** and **12**, the differences between cytoplasmic (47% and 63%, respectively) and membrane (48% and 26%, respectively) distributions may also be attributed to the hydrophobicity of the complexes, as **12** was found to be less lipophilic than complex **2** (log P = 0.86 ± 0.02 compared to 1.45 ± 0.02) and may not cross the lipid bilayer as readily. Though nucleic fractions did not contain large quantities of Os and Ir (**2**: 1.6 ± 0.5 %, **12**: 2.3 ± 0.3 %) and did not significantly differ between the complexes (p = 0.1982), the low nucleic accumulation should not discount DNA interaction as a possible mechanism of action. The generally accepted mechanism of action of cisplatin involves the formation of intra and interstrand cross-links with DNA, and despite its low (~1%) nucleic accumulation, cisplatin is still a DNA targeting agent.[64] Overall, the wide cellular dispersion of **2** and **12** in the cytoplasm and membrane fractions suggests that the antiproliferative properties of the complexes may not rely on a single mechanism of action, and may potentially decrease the likelihood of the cancer cell acquiring drug resistance. Furthermore, the difference in metal distribution may contribute to the differing antiproliferative activities between Os and Ir sulfonamide complexes, since the sub-cellular metal distribution of similar metal-arene complexes has been previously shown to determine the cell's fate.[63]

4.4.6 Redox-targeting mechanism of sulfonamide complexes

Complexes **2** [Os(*p*-cymene)(TsDPEN)] and **12** [Ir(Cp*)(TsDPEN)] are known to be efficient catalysts for transfer hydrogenation reactions.[28, 65] In cells, The co-factor 1,4-NADH is important in maintaining redox balance, and acts as a hydride source for metabolic reductions, itself becoming oxidised to NAD^+. In fact, perturbation of the NADH/NAD^+ ratio has been implicated in the mechanism of action of other Ir(III) and Os(II) metal complexes.[33, 66]

Complex **2** and **12** were therefore explored as potential catalysts for the oxidation of NADH to NAD^+ using UV-visible spectroscopy. NADH exhibits a characteristic absorption band at 340 nm (ε = 6220 $cm^{-1}M^{-1}$), while NAD^+ does not absorb at 340 nm. Both complexes were found to catalyse the oxidation of NADH, though oxidation was found to proceed at a significantly faster rate when using Ir catalyst **12** than when using Os catalyst **2** (TOF = 0.12 h^{-1} for Os complex **2**; TOF = 0.30 h^{-1} for Ir complex **12**).

While the Os-catalysed oxidation (using complex **2**) exhibited first order kinetics with respect to 1,4-NADH throughout the reaction, non-first order kinetics were observed in the first 6 h of NADH oxidation by Ir complex **12**, followed by first order kinetics up to 24 h (Figure 4.5). The metal-NADH adduct formation has been implicated as the rate-determining step for NADH oxidation by metal complexes,[67] and the same non-first order kinetic profile seen here with complex **12** (later becoming first-order) has been observed with other Ir(III) catalysts for the oxidation of NADH.[8] The mechanism for similar iridium complexes has been shown to proceed via the formation of a metal-hydride species, which were detected in aqueous solution by ^{1}H-NMR.[8, 68] However, the hydride species was not readily identifiable for the sulfonamide complexes, owing to their low aqueous solubility.

Perturbation of the NADH/NAD^+ ratio has been linked to the generation of reactive oxygen species in living cells.[69] Complex I (NADH:ubiquinone oxidoreductase) of the mitochondrial electron transport chain is known to produce reactive oxygen species (ROS), and the production of which is strongly dependent on the ratio of NADH/NAD^+.[70] Cancer cells, in particular, are under high levels of redox stress to maintain uncontrolled proliferation.[71] However, high levels of reactive oxygen species (ROS) can cause damage to DNA, mitochondrial dysfunction, or oxidation of cysteine residues in proteins,[72] ultimately leading to cell death. It may be possible that Os complex **2** and Ir complex **12** may carry out NADH oxidation inside cells, as a means of inducing ROS production by mitochondrial complex I.

To explore whether the complexes could generate ROS *in vitro*, cells were treated with either complex **2** (Os) or **12** (Ir) at IC_{50} concentration. A large burst of reactive oxygen species was detected after 24 h drug exposure (Q2 population for superoxide and total ROS: 96% for cells treated with either complex **2** or **12**; Figure 4.12) suggesting that ROS are likely to be involved in the mechanism of action *in vitro*. Many other metallodrugs have been shown to alter the redox balance in cells by generation of reactive oxygen species.[72, 73] A structurally similar iridium transfer hydrogenation catalyst $[Ir(Cp^{xBip})(2\text{-phenylpyridine})(pyridine)]^+$ has been shown to catalyse the formation of hydrogen peroxide, via hydride transfer from NADH to O_2.[33] Importantly, significantly less ROS/superoxide were detected in non-cancerous HOF ovarian fibroblasts, compared to A2780 cancer cells, treated with complex **2** (Table 4.3). Rapid and unregulated proliferation places cancer cells under heightened redox stress, unlike healthy cells.[71] The decrease in the levels of reactive oxygen species and superoxide in non-cancerous cells suggests that targeting the inherent redox vulnerability of cancer cells may present an opportunity for the design of novel

chemotherapy drugs with higher selectivity for cancerous tissues over healthy proliferating cells. Furthermore, the catalytic nature of the sulfonamide complexes (e.g. for oxidation of NADH) facilitate preferential generation of ROS in cancer cells whilst administering lower concentrations.

The activity of osmium complex **2** was found to be enhanced by co-administration with L-BSO, a known inhibitor of γ-glutamylcysteine synthetase. This enzyme catalyses the rate-limiting step in the synthesis of GSH,[73] an important cellular antioxidant,[74] making cancer cells more vulnerable to redox stress. The IC_{50} was reduced to 64% in the presence of L-BSO (15.07 ± 0.07 μM to 10.0 ± 0.7 μM; Table 4.4). This is consistent with a mechanism of action that exploits the redox-sensitivity of the cancer cell, and has previously been observed for other half-sandwich complexes of Os(II) as well as structurally-similar Ir(III) complexes.[33, 63, 73]

4.5 Conclusions

A series of highly stable 16-electron Ir(III) sulfonamide complexes were synthesised for comparison to structurally-similar Os(II) catalysts reported in Chapter 3 (section 3.3.1, page 78). This chapter demonstrates that in a biological context, the metal centre is not purely structural. Hydrophobicities were found to correlate with antiproliferative activities towards cancer cells, determined in fourteen human cell lines, which in turn were found to correlate with the amount of metal internalised by the cells. Though iridium accumulation was greater than that of osmium, osmium complexes typically exhibited greater activities towards cancer cells, albeit at the expense of greater cross-resistance towards platinum-resistant cells, unlike their iridium counterparts. Furthermore, the antiproliferative activity of osmium complex **2** towards A2780

cancer cells was enhanced by co-adminstration with the γ-glutamylcysteine synthase inhibitor, L-BSO, suggesting that the important cellular antioxidant, GSH, may be involved in the detoxification of such metal complexes inside cells.

Further metal accumulation studies in A2780 cancer cells focused on Os complex **2** and Ir complex **12** as representative examples from each series. Ir accumulation and efflux were found to be particularly rapid. Conversely, the efflux of Os was gradual, irrespective of the extracellular drug concentration. Both complexes exhibited temperature-dependent accumulation, and efflux was decreased by co-administration of a known PgP inhibitor. Os complex **2** showed significantly more membrane (and organelle) distribution, compared to Ir complex **12** which was mainly found in the cytoplasm, in agreement with its lower partition coefficient (Log P).

In this chapter, the known Os and Ir transfer hydrogenation catalysts were demonstrated to catalytically oxidise the co-factor 1,4-NADH to NAD^+ under biologically-relevant conditions in a model system at pH 7.4. Though turnover frequencies were modest in the model system, it is expected that the same process occurs in cells likely contributes to the catalytic generation of reactive oxygen species observed in cancer cells.

Overall, once internalised, the osmium and iridium complexes appear to act catalytically inside cells. The transfer hydrogenation of NADH explored in this chapter, in combination with data showing that inhibition of GSH synthesis increases potency (using L-BSO), strongly implicates a mechanism of action involving catalytic redox-modulation to achieve cancer cell death. Crucially, the inherent redox stress experienced by cancer cells makes them more vulnerable to such a mechanism, thereby generating mechanistic selectivity for cancer cells over non-cancerous cells, which are better-equipped to adapt to drug-induced redox stress.

4.6 References

1. S. Dasari and P. Bernard Tchounwou, *Eur. J. Pharmacol.*, 2014, **740**, 364-378.
2. T. C. Johnstone, G. Y. Park and S. J. Lippard, *Anticancer Res.*, 2014, **34**, 471-476.
3. E. S. Antonarakis and A. Emadi, *Cancer Chemother. Pharmacol.*, 2010, **66**, 1-9.
4. W. Han Ang and P. J. Dyson, *Eur. J. Inorg. Chem.*, 2006, **2006**, 4003-4018.
5. W. M. Motswainyana and P. A. Ajibade, *Adv. Chem.*, 2015, **2015**, 21.
6. I. Kostova, *Curr. Med. Chem.*, 2006, **13**, 1085-1107.
7. R. Trondl, P. Heffeter, C. R. Kowol, M. A. Jakupec, W. Berger and B. K. Keppler, *Chem. Sci.*, 2014, **5**, 2925-2932.
8. A. J. Millett, A. Habtemariam, I. Romero-Canelón, G. J. Clarkson and P. J. Sadler, *Organometallics*, 2015, **34**, 2683-2694.
9. J. J. Soldevila-Barreda, I. Romero-Canelón, A. Habtemariam and P. J. Sadler, *Nat. Commun.*, 2015, **6**, 6582.
10. V. Novohradsky, L. Zerzankova, J. Stepankova, A. Kisova, H. Kostrhunova, Z. Liu, P. J. Sadler, J. Kasparkova and V. Brabec, *Metallomics*, 2014, **6**, 1491-1501.
11. Y. Geldmacher, M. Oleszak and W. S. Sheldrick, *Inorg. Chim. Acta*, 2012, **393**, 84-102.
12. L. He, Y. Li, C.-P. Tan, R.-R. Ye, M.-H. Chen, J.-J. Cao, L.-N. Ji and Z.-W. Mao, *Chem. Sci.*, 2015, **6**, 5409-5418.

13. S. D. Shnyder, Y. Fu, A. Habtemariam, S. H. van Rijt, P. A. Cooper, P. M. Loadman and P. J. Sadler, *Med. Chem. Commun.*, 2011, **2**, 666-668.

14. S. J. Dougan, A. Habtemariam, S. E. McHale, S. Parsons and P. J. Sadler, *Proc. Natl. Acad. Sci. U. S. A.*, 2008, **105**, 11628-11633.

15. W. Kandioller, E. Balsano, S. M. Meier, U. Jungwirth, S. Goschl, A. Roller, M. A. Jakupec, W. Berger, B. K. Keppler and C. G. Hartinger, *Chem. Commun.*, 2013, **49**, 3348-3350.

16. A. Maillet, S. Yadav, Y. L. Loo, K. Sachaphibulkij and S. Pervaiz, *Cell Death Dis.*, 2013, **4**, e653.

17. K. K. Kim, R. K. Singh, R. M. Strongin, R. G. Moore, L. Brard and T. S. Lange, *PLOS ONE*, 2011, **6**, e19049.

18. J. M. Hearn, I. Romero-Canelón, A. F. Munro, Y. Fu, A. M. Pizarro, M. J. Garnett, U. McDermott, N. O. Carragher and P. J. Sadler, *Proc. Natl. Acad. Sci. U. S. A.*, 2015, **112**, E3800-E3805.

19. C. Sanchez-Cano, I. Romero-Canelón, Y. Yang, I. J. Hands-Portman, S. Bohic, P. Cloetens and P. J. Sadler, *Chem. Eur. J.*, 2017, **23**, 2512-2516.

20. K. Mashima, T. Abe and K. Tani, *Chem. Lett.*, 1998, **27**, 1201-1202.

21. Y. Fu, A. Habtemariam, A. M. B. H. Basri, D. Braddick, G. J. Clarkson and P. J. Sadler, *Dalton Trans.*, 2011, **40**, 10553-10562.

22. C. Venzago, M. Popp, J. Kovac and A. Kunkel, *J. Anal. At. Spectrom.*, 2013, **28**, 1125-1129.

23. C. A. Puckett and J. K. Barton, *J. Am. Chem. Soc.*, 2007, **129**, 46-47.

24. I. Romero-Canelón, Doctor of Philosphy, University of Warwick, 2012.

25. R. Noyori and S. Hashiguchi, *Acc. Chem. Res.*, 1997, **30**, 97-102.

26. S. Hashiguchi, A. Fujii, J. Takehara, T. Ikariya and R. Noyori, *J. Am. Chem. Soc.*, 1995, **117**, 7562-7563.

27. K.-J. Haack, S. Hashiguchi, A. Fujii, T. Ikariya and R. Noyori, *Angew. Chem., Int. Ed.*. 1997, **36**, 285-288.

28. K. Murata, T. Ikariya and R. Noyori, *J. Org. Chem.*, 1999, **64**, 2186-2187.

29. A. M. Pizarro, R. J. McQuitty, F. S. Mackay, Y. Zhao, J. A. Woods and P. J. Sadler, *Chem. Med. Chem.*, 2014, **9**, 1169-1175.

30. V. Novohradsky, Z. Liu, M. Vojtiskova, P. J. Sadler, V. Brabec and J. Kasparkova, *Metallomics*, 2014, **6**, 682-690.

31. J. J. Wilson and S. J. Lippard, *J. Med. Chem.*, 2012, **55**, 5326-5336.

32. S. W. Johnson, D. W. Shen, I. Pastan, M. M. Gottesman and T. C. Hamilton, *Exp. Cell Res.*, 1996, **226**, 133-139.

33. Z. Liu, I. Romero-Canelón, B. Qamar, J. M. Hearn, A. Habtemariam, N. P. E. Barry, A. M. Pizarro, G. J. Clarkson and P. J. Sadler, *Angew. Chem. Int. Ed.*, 2014, **53**, 3941-3946.

34. M. Rimoldi, D. Fodor, J. A. van Bokhoven and A. Mezzetti, *Chem. Commun.*, 2013, **49**, 11314-11316.

35. M. W. Drover, H. C. Johnson, L. L. Schafer, J. A. Love and A. S. Weller, *Organometallics*, 2015, **34**, 3849-3856.

36. J. W. Corcoran and F. E. Hahn, *Mechanism of Action of Antimicrobial and Antitumor Agents*, Springer-Verlag, 1975.

37. R. E. Aird, J. Cummings, A. A. Ritchie, M. Muir, R. E. Morris, H. Chen, P. J. Sadler and D. I. Jodrell, *Br. J. Cancer*, 2002, **86**, 1652-1657.

38. A. Habtemariam, M. Melchart, R. Fernández, S. Parsons, I. D. H. Oswald, A. Parkin, F. P. A. Fabbiani, J. E. Davidson, A. Dawson, R. E. Aird, D. I. Jodrell and P. J. Sadler, *J. Med. Chem.*, 2006, **49**, 6858-6868.

39. Z. Liu, A. Habtemariam, A. M. Pizarro, S. A. Fletcher, A. Kisova, O. Vrana, L. Salassa, P. C. A. Bruijnincx, G. J. Clarkson, V. Brabec and P. J. Sadler, *J. Med. Chem.*, 2011, **54**, 3011-3026.

40. T. Wang, N. Zabarska, Y. Wu, M. Lamla, S. Fischer, K. Monczak, D. Y. W. Ng, S. Rau and T. Weil, *Chem. Commun.*, 2015, **51**, 12552-12555.

41. P. Pigeon, S. Top, A. Vessières, M. Huché, E. A. Hillard, E. Salomon and G. Jaouen, *J. Med. Chem.*, 2005, **48**, 2814-2821.

42. E. Păunescu, P. Nowak-Sliwinska, C. M. Clavel, R. Scopelliti, A. W. Griffioen and P. J. Dyson, *Chem. Med. Chem.*, 2015, **10**, 1539-1547.

43. J.-J. Cao, C.-P. Tan, M.-H. Chen, N. Wu, D.-Y. Yao, X.-G. Liu, L.-N. Ji and Z.-W. Mao, *Chem. Sci.*, 2017, **8**, 631-640.

44. R. Pettinari, F. Marchetti, C. Pettinari, F. Condello, A. Petrini, R. Scopelliti, T. Riedel and P. J. Dyson, *Dalton Trans.*, 2015, **44**, 20523-20531.

45. B. Köberle, M. T. Tomicic, S. Usanova and B. Kaina, *Biochim. Biophys. Acta.*, 2010, **1806**, 172-182.

46. M. V. Liberti and J. W. Locasale, *Trends Biochem. Sci.*, 2016, **41**, 211-218.

47. M. G. Vander Heiden, L. C. Cantley and C. B. Thompson, *Science*, 2009, **324**, 1029-1033.

48. O. Warburg, *Science*, 1956, **123**, 309-314.

49. N. Li, K. Ragheb, G. Lawler, J. Sturgis, B. Rajwa, J. A. Melendez and J. P. Robinson, *J. Biol. Chem.*, 2003, **278**, 8516-8525.

50. K. F. Macleod, N. Sherry, G. Hannon, D. Beach, T. Tokino, K. Kinzler, B. Vogelstein and T. Jacks, *Genes Dev.*, 1995, **15**, 935-944.

51. S. H. van Rijt, I. Romero-Canelon, Y. Fu, S. D. Shnyder and P. J. Sadler, *Metallomics*, 2014, **6**, 1014-1022.

52. J. H. Hamman, P. H. Demana and E. I. Olivier, *Drug Target Insights*, 2007, **2**, 71-81.

53. G. J. Russell-Jones, *Adv. Drug Deliv. Rev.*, 1996, **20**, 83-97.

54. A. Habberfield, K. Jensen-Pippo, L. Ralph, S. W. Westwood and G. J. Russell-Jones, *Int. J. Pharm.*, 1996, **145**, 1-8.

55. A. K. Bryan, V. C. Hecht, W. Shen, K. Payer, W. H. Grover and S. R. Manalis, *Lab Chip*, 2014, **14**, 569-576.

56. D. Hevia, A. Rodriguez-Garcia, M. Alonso-Gervós, I. Quirós-González, H. M. Cimadevilla, C. Gómez-Cordovés, R. M. Sainz and J. C. Mayo, *Protocol Exchange*, 2011.

57. S. C. Mann, P. A. Andrews and S. B. Howell, *Cancer Chemother Pharmacol.*, 1990, **25**, 236-240.

58. P. A. Andrews, S. Velury, S. C. Mann and S. B. Howell, *Cancer Res.*, 1988, **48**, 68-73.

59. R. A. Hromas, J. A. North and C. P. Burns, *Cancer Lett.*, 1987, **36**, 197-201.

60. D.-W. Shen, L. M. Pouliot, M. D. Hall and M. M. Gottesman, *Pharmacol. Rev.*, 2012, **64**, 706-721.

61. F. J. Sharom, *J. Membrane Biol.*, 1997, **160**, 161-175.

62. C. A. Puckett, R. J. Ernst and J. K. Barton, *Dalton Trans.*, 2010, **39**, 1159-1170.

63. I. Romero-Canelón and P. J. Sadler, *Inorg. Chem.*, 2013, **52**, 12276-12291.

64. A. Mandic, J. Hansson, L. S and M. C. Shoshan, *J. Biol. Chem.*, 2003, **278**, 9100-9106.

65. J. P. C. Coverdale, C. Sanchez-Cano, G. J. Clarkson, R. Soni, M. Wills and P. J. Sadler, *Chem. Eur. J.*, 2015, **21**, 8043-8046.

66. Y. Fu, M. J. Romero, A. Habtemariam, M. E. Snowden, L. Song, G. J. Clarkson, B. Qamar, A. M. Pizarro, P. R. Unwin and P. J. Sadler, *Chem. Sci.*, 2012, **3**, 2485-2494.

67. S. Betanzos-Lara, Z. Liu, A. Habtemariam, A. M. Pizarro, B. Qamar and P. J. Sadler, *Angew. Chem. Int. Ed.*, 2012, **51**, 3897-3900.

68. M. Soetens, F. Drouet and O. Riant, *Chem. Cat. Chem.*, 2017, **9**, 929-933.

69. Michael P. Murphy, *Biochem. J.*, 2009, **417**, 1-13.

70. L. Kussmaul and J. Hirst, *Proc. Natl. Acad. Sci. U. S. A.*, 2006, **103**, 7607-7612.

71. E. O. Hileman, J. Liu, M. Albitar, M. J. Keating and P. Huang, *Cancer Chemother. Pharmacol.*, 2004, **53**, 209-219.

72. U. Jungwirth, C. R. Kowol, B. K. Keppler, C. G. Hartinger, W. Berger and P. Heffeter, *Antioxid. Redox Signal.*, 2011, **15**, 1085-1127.

73. I. Romero-Canelón, M. Mos and P. J. Sadler, *J. Med. Chem.*, 2015, **58**, 7874-7880.

74. H. J. Forman, H. Zhang and A. Rinna, *Mol. Aspects. Med.*, 2009, **30**, 1-12.

Chapter 5

Os(II)-catalysed *in cell* asymmetric transfer hydrogenation

Some of the work in this chapter has been published.

J. P. C. Coverdale, I. Romero-Canelón, C. Sanchez-Cano, G. J. Clarkson, M. Wills, P. J. Sadler, Asymmetric transfer hydrogenation catalysts in cancer cells, *Nature Chemistry,* Manuscript accepted.

5. Osmium(II)-catalysed *in cell* asymmetric transfer hydrogenation

5.1 Introduction

The catalytic properties of many metal complexes are well understood,[1-3] and the role of catalysts in medicine is a rapidly-expanding field of research. Catalytic medicines would facilitate lower dosages, with a view to circumventing deleterious side effects.[4] This builds on pioneering research surrounding the design of traditional non-catalytic metallodrugs, and notably the success story of cisplatin;[5] a widely established Pt(II) chemotherapy complex,[6] used to treat soft tissue, bone, muscle, and blood vessel cancers.[7] While many platinum drugs are known, the only example of an osmium compound in the clinic is osmium tetroxide, which acts to catalyse the conversion of the superoxide anion radical to oxygen and hydrogen peroxide, and is used in the treatment of arthritis.[8] However, Os(II) arene complexes have shown *in vivo* activity against human cancer xenografts in mice, with negligible toxicity, suggesting that Os(II) complexes may warrant further exploration as anticancer agents.[9]

A catalytic metallodrug is likely to have a unique or even range of mechanisms of action, potentially avoiding drug resistance – a problem inherently associated with platinum-based treatments.[6, 7] Compared to metalloenzymes, which protect the metal centre from unfavourable substitution or redox chemistry involving large proteins, the catalytic centre of a small-molecule metal complex is easily accessible to cellular components, increasing the likelihood of catalyst deactivation (poisoning) in a biological system.[4] By rational design of kinetically stable complexes, metallodrugs can catalyse a range of bio-orthogonal reactions, such as the modification of functional

groups and carbon-carbon bond formation.[4] Previous research from Sadler *et al.* has shown that transfer hydrogenation reactions may be carried out in cancer cells, using sodium formate as a biologically-compatible alternative to the formic acid triethylamine hydrogen donor system traditionally used for the reduction of ketone substrates.[4, 10] Sodium formate was found to increase the potency of ruthenium(II) compounds, enabling the complexes to catalyse the formation of the co-enzyme NADH and perturb the already sensitised redox balance in the cell.[10]

It is well established that the metabolism of cancerous tissue differs from that of healthy tissue.[11] The 'Warburg Effect' summarises the observation that cancer cells (and other rapidly proliferating tissues) show a preference for the production of lactate from glucose, independent of oxygen availability.[12] In the presence of oxygen, non-proliferating tissues metabolise glucose to pyruvate (via glycolysis) and then oxidise pyruvate to carbon dioxide by oxidative phosphorylation. Only in the absence of oxygen would such cells utilise lactate production as a means of acquiring energy.[13] A key step in the Warburg Effect is the reduction of pyruvate to lactate (a chiral alcohol) – a process that may also be achieved using transfer hydrogenation.

In Chapter 3, a series of osmium(II) compounds were reported to catalyse asymmetric transfer hydrogenation (ATH) reactions of ketones.[14] This chapter details *in cell* transfer hydrogenation, including the reduction of pyruvate to lactate, whilst retaining enantioselectivity. Using Os(II) complexes in combination with a hydride source, the extent of the catalytic effect is compared between cancer cells (A2780 ovarian carcinoma) and normal cells (HOF ovarian and MRC5 lung fibroblasts). Additionally, enzymes that produce formate are overexpressed in certain cancer cells, and this was explored as a potential mechanism of increasing drug selectivity. This, to the best of our knowledge, represents the first report of enantioselective *in cell* ATH catalysis.

5.2 Experimental

5.2.1 Materials

Cisplatin (*cis*-diaminedichloroplatinum(II)), separate enantiomers of complex **11** [RuCl(TsDPEN)(*p*-cymene)], *N*-acetyl-methionine, *N*-formyl-methionine, sodium acetate, sodium formate, sodium pyruvate, pyruvic acid, propidium iodide, Annexin V-FITC conjugate and all other reagents were purchased from Sigma Aldrich and used directly without previous purification or modification, unless indicated otherwise. Enzymatic assay kits for L-lactate and D-lactate were purchased from Cayman and stored at 255 K before use. Phosphate buffered saline (PBS) and cell culture media were purchased from Lonza. Cell maintenance, *in vitro* growth inhibition assays, metal accumulation experiments, and methods used for ICP-OES / ICP-MS are described in Chapter 2 (section 2.2.8, page 54).

5.2.2 Transfer hydrogenation reduction of pyruvate to lactate

Reduction of pyruvic acid in formic acid / triethylamine azeotrope (5:2). The reduction of pyruvic acid was performed as described for acetophenone reductions (Chapter 3, section 3.2.5, page 83), using ^{1}H-NMR to monitor % conversion (1 mmol substrate, 500 μL formic acid : triethylamine azeotrope, 100 μL C_6D_6). Data were processed using TopSpin 3.2 (Bruker, UK). Final solution concentrations: pyruvate, 1.4M; catalyst, 6.9 mM. Reactions were monitored for 1 h unless specified otherwise, and were carried out in triplicate. Turnover frequencies (TOF / h^{-1}) are reported and their standard deviations calculated.

Reduction of pyruvate by (*R*,*R*)-2 in phosphate buffered saline (PBS). **C**oncentrations of D- and L-lactate were determined individually using enantio-specific detection assay kits (Cayman Chemical) as described in the manufacturer's instructions. Either complex **(*R*,*R*)-2** or **(*S*,*S*)-2** (15 μM, IC_{50} concentration) was incubated in PBS solution (supplemented with 5% v/v DMSO to aid solubility of the complexes) with sodium pyruvate (1 mM) for 24 h at 310 K. The experiment was repeated in the presence of sodium formate (2 mM). Using instrumental duplicates of duplicates, fluorescence measurements were acquired using a Promega GloMax Multi+ microplate reader (λ_{ex}: 530-540 nm, λ_{em}: 585-595 nm) and averages and standard deviations were calculated.

Determination of the enantiomeric excess (ee) for the reduction of pyruvate. In phosphate-buffered saline (PBS, containing 5% v/v DMSO) were prepared stock solutions of: sodium formate (100 mM), sodium pyruvate (100 mM) and complex **(*R*,*R*)-2** (saturated solution, which was filtered and osmium concentration determined using ICP-OES). Solutions were added independently to clean sterile 15 mL Falcon tubes with the addition of D_2O (10% v/v) to achieve final working concentrations: catalyst, 10 μM; pyruvate, 2 mM; formate 4 mM or 30 mM. ^{1}H-NMR data were acquired using a Bruker AV 600 spectrometer (600 MHz, 90% H_2O / 10% D_2O, 310 K) at 11 min time intervals using water suppression techniques (ZGGPW5) and data were processed using Topspin 3.2 (Bruker UK). Spectra baseline-correction was performed using the SPLINE algorithm. Percentage conversion (and turnover frequency, TOF / h^{-1}) for the reduction of pyruvate to lactate was determined using peak integrals: δ = 2.40 ppm (CH_3, pyruvate) and lactate (δ = 1.36 ppm, (CH_3, lactate).

5.2.3 Biological studies

Biological experiments and cell maintenance were carried out at the School of Life Sciences and the Department of Engineering (University of Warwick, UK) as described in Chapter 2 (section 2.3.2, page 57) under the guidance of Dr. Isolda Romero-Canelon (University of Warwick, UK) with kind assistance from Dr. Anthony Knight, Mrs Hannah Bridgewater, Mrs Ji-Inn Song and Mrs Sukhbinder Heer (University of Warwick, UK).

Cell viability modulation experiments with sodium formate. A 96-well plate was seeded using 5000 cells (A2780, HOF or MRC5 cells of ovarian and lung origin) per well using 150 μL, and incubated at 310 K for 48 h in drug-free medium. Solutions of osmium complexes **2** and **7** were freshly prepared in culture medium (containing 5% v/v DMSO) and exact Os concentrations were determined using ICP-OES (Chapter 2, section 2.2.8). After removal of the supernatant, cells were exposed to equipotent concentrations of either osmium complex, equal to 0.5 × IC_{50} concentration in A2780 cancer cells (15.5 μM and 6.5 μM for **2** and **7**, respectively), by dilution from stock solutions using culture medium. Sodium formate was independently added to the wells at three concentrations (final concentration: 0.5, 1.0 and 2.0 mM) within 5 min of drug exposure. Positive control cells were treated with cisplatin, and negative controls were established with 0-2 mM sodium formate. After 24 h drug exposure, cells were washed with PBS and further incubated for 72 h in drug-free cell culture medium. After this time, viability was determined using the SRB assay as described in Chapter 2 (page 59). The experiment was carried out as duplicates of triplicates, as part of two independent experiments. The experiment was repeated using sodium acetate in place

of formate in all cell lines. Statistics were calculated using a two-tailed *t*-test with unequal variances (Welch's *t*-test) at the 95% confidence level.

Cell viability modulation experiments with *N*-formylmethionine. The above cell viability modulation experiments were repeated using PC3 prostate cancer cells. In this case, Os complexes **2** and **7** were co-administered with a non-toxic concentration of *N*-formylmethionine (fMet) or *N*-acetylmethionine at (0.25, 0.5 and 1 mM). PC3 cancer cells are known to overexpress human peptide deformylase which is responsible for the cleavage of the formyl moiety from formylmethionine,[15] hence fMet could be enzymatically converted into formate and act as an *in situ*-generated hydride source in the transfer hydrogenation process.

Formate-dependent metal accumulation in cancer cells. Osmium accumulation was determined in A2780 human ovarian cancer cells as described in Chapter 2 (page 61) using 4.0×10^6 cells seeded in P100 petri dishes using 10 ml culture medium, 24 h pre-incubation, 24 h drug exposure and no recovery time in drug-free medium. The experiment was carried out with the following modifications: cells were exposed to equipotent concentrations of complexes **(*S*,*S*)-2** or **(*S*,*S*)-7** equal to $1/3 \times IC_{50}$ (IC_{50} concentration in A2780 cancer cells: 15.5 μM and 6.5 μM for **2** and **7**, respectively) in the presence of sodium formate (2 mM). Data were obtained in triplicate, and compared to the Os-free negative control experiments (0 mM formate or 2 mM formate, respectively). These data followed the same experimental procedure as the cellular accumulation data presented in Chapter 4 (section 4.3.5; obtained at $1 \times IC_{50}$ concentration) and hence will be discussed together.

Cell cycle analysis. A 6-well plate was seeded using 1.0×10^6 A2780 cancer cells in 2 ml of culture medium. After 24 h at 310K and in drug-free medium, the supernatant was removed and cells were exposed to complex **2** ($1.0 \times IC_{50}$ concentration in A2780: 15.5 μM) both in the presence and absence of sodium formate (2 mM) for 24 h (310 K). After treatment, the drug solution was removed and cells were washed twice with PBS. Cell pellets were harvested using trypsin/EDTA (1 ml), washed and re-suspended in PBS, then centrifuged (1000 rpm, 5 min, 277 K). Pellets were re-suspended in ice-cold ethanol to fix the cells (30 min, on ice). After this time, cells were washed again with PBS to remove ethanol, then stained using 500 μL of staining buffer in the dark for 30 min (staining buffer contains: 50 μgmL^{-1} of propidium iodide (PI) and 80 μgmL^{-1} of RNAse in phosphate-buffered saline). After centrifugation (1000 rpm, 5 min, 277 K) excess staining buffer was removed by suction and cells were re-suspended in PBS. A single cell solution was obtained in PBS, which was analysed by flow cytometry using a Becton Dickinson FACScan Flow Cytometer (PI red fluorescence detected using FL2 channel, $\lambda_{ex/em}$ = 535/617 nm). Samples were measured as instrumental triplicates and cell cycle parameters determined using the Watson (pragmatic) model in FlowJo V10 for Windows. Statistics were analysed using a two-tailed *t*-test with unequal variances (Welch's *t*-test).

Induction of Apoptosis. A 6-well plate was seeded using 1.0×10^6 A2780 cancer cells. After 24 h, the supernatant was removed and cells were exposed to complex **2** ($1.0 \times IC_{50}$, 15.5 μM) both in the presence and absence of sodium formate (2 mM) for 24 h (310 K). The drug solution was removed and cells were washed twice with PBS. Cells were harvested using trypsin/EDTA, re-suspended in PBS, then centrifuged (1000 rpm, 5 min, 277 K). Positive control samples were treated with staurosporine (1

μgml^{-1}).[16] Pellets were stained with 0.5% v/v Annexin V FITC conjugate and 0.5% v/v propidium iodide in PBS for 30 min in the dark, and then analysed by flow cytometry using a Becton Dickinson FACScan Flow Cytometer (Annexin V-FITC green fluorescence detected using FL1 channel, $\lambda_{ex/em}$ = 488/518 nm; PI red fluorescence detected using FL2 channel, $\lambda_{ex/em}$ = 535/617 nm). Data were processed using FlowJo V10 for Windows and reported as percentage populations and statistics calculated using a two-tailed *t*-test assuming unequal variances (Welch's *t*-test).

Membrane integrity. A 6 well-plate was seeded using 1.0 × 10^6 A2780 cancer cells. After 24 h, cells were exposed to complex **2** (1.0 × IC_{50}, 15.5 μM) both in the presence and absence of sodium formate (2 mM) for 24 h (310 K). After treatment, the drug solution was removed and cells were washed twice with PBS. Cell pellets were harvested using trypsin/EDTA (1 ml), re-suspended in PBS, then centrifuged (1000 rpm, 5 min, 277 K). Pellets were stained (without fixation) using 500 μL of staining buffer in the dark for 30 min (containing 50 μgmL^{-1} of propidium iodide (PI) and 80 μgmL^{-1} of RNAse), excess dye removed after centrifugation (1000 rpm, 5 min, 277 K) and samples re-suspended in PBS for analysis by flow cytometry as instrumental triplicates using a Becton Dickinson FACScan Flow Cytometer. Data were processed using FlowJo V10 for windows and statistics calculated using a two-tailed *t*-test assuming unequal variances (Welch's *t*-test).

5.2.4 In-cell reduction of pyruvate to lactate

Briefly, 30×10^6 A2780 ovarian cancer cells were seeded using 15 ml culture medium in T75 flasks and incubated for 24 h (310 K). Separately, stock solutions of osmium complexes **(*R*,*R*)-2** and **(*S*,*S*)-2** were prepared in culture medium containing 5% v/v DMSO. The metal concentration in the stock solutions was determined and adjusted by ICP-OES prior to drug exposure to cells. In triplicate flasks, supernatant solutions were removed and cells were exposed to equipotent concentrations ($1.0 \times IC_{50}$ concentration) of either complex **(*R*,*R*)-2** or **(*S*,*S*)-2**, either in the presence and absence of sodium formate (2 mM). Control experiments were also obtained in triplicate (either treated with 2 mM formate, or untreated). After 24 h, the supernatant was collected for analysis of extracellular D-lactate, and cells were washed twice with PBS and harvested using trypsin/EDTA. Cells were counted, and equal sized cell pellets (40×10^6 cells) were obtained by centrifugation (1000 rpm, 5 min, 277 K). Intracellular and extracellular D-lactate were determined using the D-lactate assay kit (Cayman Chemical) as described in the manufacturer's instructions. Samples were deproteinated by addition of MPA reagent (0.25 M) with vortexing, then placed on ice (5 min). Proteins were pelleted by centrifugation (1000 rpm, 5 min, 277 K) and the supernatant neutralised with potassium carbonate (25 μL). Samples were re-centrifuged to remove precipitated salts (1000 rpm, 5 min, 277 K) and the supernatant extracted (20 μL) for the final assay, which was carried out with a calibration range of D-lactate: 0, 25, 50, 100, 250, 500, 1000 μM (R^2 =0.995). Fluorescence was measured using a Promega GloMax Multi+ microplate reader (λ_{ex}: 530-540 nm, λ_{em}: 585-595 nm). Data were normalised to the respective complex-free control, and averages and standard deviations were calculated. Statistics were calculated using a two-tailed *t*-test assuming unequal variances (Welch's unpaired *t*-test) at the 95% confidence level.

5.3 Results

5.3.1 Reduction of pyruvic acid using formic acid

Pyruvate was selected as a target substrate for catalysis as the molecule is pro-chiral, is present at millimolar concentrations inside cells, and is a key metabolic intermediate in glycolysis. To initially confirm whether Os sulfonamide catalysts could reduce pyruvate, the reduction of pyruvic acid was studied using formic acid: triethylamine azeotrope, as described in Chapter 3 (section 3.2.5) for acetophenone-derived ketones. (5 μmol catalyst, 500 μL formic acid / triethylamine azeotrope, 100 μL d^6-benzene, 1 mmol pyruvate; 1:200 catalyst loading). Using either enantiomer of *p*-cymene complex **2** or biphenyl complex **7**, rapid turnover (TOF ~ 300 h^{-1}) was observed using time-dependent ^{1}H-NMR spectroscopy to observe the conversion to lactic acid by the formation a new quartet at 4.17 ppm (Table 5.1), relative to the singlet CH_3 signal from pyruvate (2.26 ppm). The experiment was monitored in triplicate for 1 h, with data acquired every 73 s. Due to the limitations of ^{1}H-NMR, this technique could not resolve the enantioselectivity of the complexes. Furthermore, the enantiomeric excess (*ee*) could not be determined using chiral GC-FID due to the high chemical similarity of pyruvate, lactate and formate.

Table 5.1. Reduction of pyruvic acid by Os complexes **2** or **7**, or Ru complex **11** in formic acid : triethylamine azeotrope (5:2 mol ratio), studied by time-dependent ^{1}H-NMR (C_6D_6, 310 K). Final concentration: Os catalyst, 6.9 mM; pyruvic acid, 1.4 M.

	Complex	(*R*,*R*) TOF / h^{-1}	(*S*,*S*) TOF / h^{-1}
2	[Os(*p*-cymene)((*R*,*R*)-TsDPEN)]	303.2 ± 0.8	298 ± 2
7	[Os(biphenyl)((*S*,*S*)-TsDPEN)]	103 ± 2	102 ± 1
11	[RuCl(*p*-cymene)((*S*,*S*)-TsDPEN)]	N.D.	132 ± 1

The rate of ketone reduction was equal between enantiomers. Similarly to data obtained in Chapter 3 (section 3.2.5), the initial rate of reduction (TOF_{max}) was significantly faster using Os catalyst **2** than Ru catalyst **11** (TOF = 132 h^{-1}). However, the TOF obtained with Os catalyst **7** was significantly lower (TOF ~ 100 h^{-1}). These data suggested that complex **2** was a worthy candidate for further exploration as a catalyst for pyruvate reduction in aqueous media and inside cells.

5.3.2 Aqueous-phase reduction of pyruvate using sodium pyruvate

The aqueous-phase reduction of sodium pyruvate was explored in phosphate-buffered saline (PBS) with 5% v/v DMSO to aid solubility, in which the Os catalysts are known to be stable (Chapter 3, section 3.3.4). Solutions of either **(*R*,*R*)-2** or (***S*,*S*)-2** were prepared independently, and sodium formate was used as a biologically-compatible hydride source.

Conversion of pyruvate to lactate was observed using time-dependent ^{1}H-NMR (600 MHz, 90% H_2O / 10% D_2O, 310 K) using 0.05 mol% catalyst and sodium formate (Table 5.2). Though less rapid than in formic acid : triethylamine azeotrope, the reduction was observed to occur in aqueous media (TOF_{max} = 16.4 h^{-1}), further confirming the potential for detecting *in cell* catalysis.

Table 5.2. Reduction of sodium pyruvate to lactate by osmium sulfonamide catalyst **(*R*,*R*)-2** (0.05 mol%) using sodium formate (4 mM or 30 mM) as a hydride source, in PBS (10% D_2O). Turnover number (TON) and turnover frequency (TOF_{max}, h^{-1}) determined using time-dependent ^{1}H-NMR (600 MHz, 90% H_2O / 10% D_2O, 310 K) using water-suppression techniques.

catalyst / mM	pyruvate / mM	formate / mM	TON	TOF_{max} / h^{-1}
0.01	2	4	21 (14 h)	1.5 ± 0.1
0.01	2	30	65 (4 h)	16.4 ± 0.7

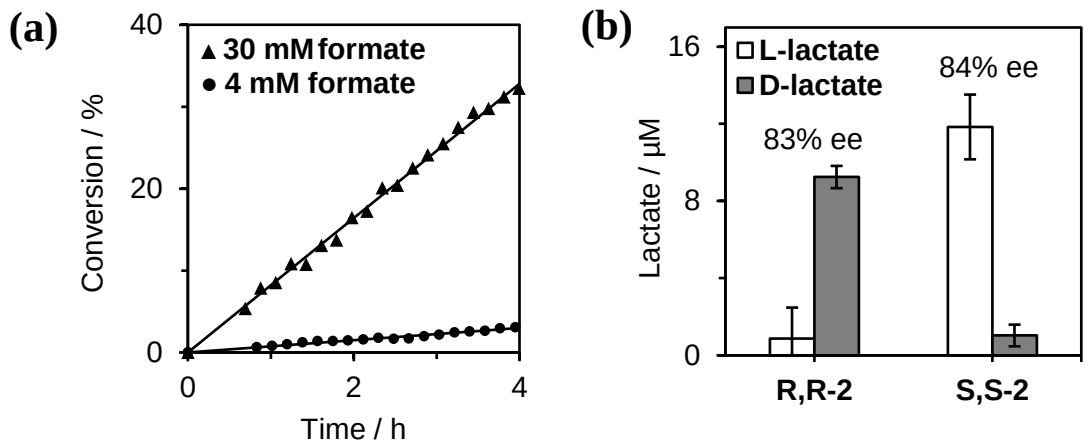

Figure 5.1. (a) Formate-dependence (2 or 15 mol equiv) for the reduction of pyruvate by osmium complex **(*R*,*R*)-2** in PBS monitored by time-dependent ^{1}H-NMR (600 MHz, 90% H_2O / 10% D_2O, 310 K); (b) Enantioselectivity for the reduction of pyruvate to lactate by complex **(*R*,*R*)-2** or **(*S*,*S*)-2**, determined using enantioselective enzymatic assay kits. Os complex, 15 µM; pyruvate, 1 mM; formate, 2 mM (24 h, 310 K).

The turnover frequency was found to be highly dependent on the concentration of formate, with 10× enhancement of turnover frequency upon increasing formate from 2 equiv to 15 equiv with respect to pyruvate (Figure 5.1a). This explains the rapid rate observed in the formic acid azeotrope, whereby the hydride source (formic acid) is acting as a solvent for the reaction, and is therefore in the greatest possible excess. Reduction rate may also be influenced by the pH of the reaction, however this goes beyond the scope of this thesis, since *in cell* reductions must occur under physiologically-relevant conditions (pH = 7.4) which is why phosphate-buffered saline was chosen as the solvent.

Similarly to reductions carried out in formic acid : triethylamine azeotrope, the enantioselectivity of the reduction could not be readily determined by chiral gas chromatography (as for acetophenone-derived ketones in Chapter 3, section 3.2.5, page 83) due to the high chemical similarity and subsequent similar retention times of the substrate and sodium formate. Instead, enantioselective enzymatic assay kits were used to evaluate independently the concentration of each enantiomer of lactate, taking

advantage of the high specificity of the enzyme for a particular enantiomer of lactate (which have also been shown to be specific for lactate, compared to other monocarboxylates, such as pyruvate and formate).

Remarkably, the enantioselectivity of the catalysts is conserved for pyruvate reduction, achieving ~83% enantiomeric excess (*ee*) for the production of lactate in aqueous solution (Table 5.3 and Figure 5.1b). D-lactate was selectively obtained using catalyst **(*R*,*R*)-2** (9.2 ± 0.6 μM D-lactate, compared to 1 ± 2 μM L-lactate; 83% *ee*), and L-lactate using catalyst **(*S*,*S*)-2** (1.0 ± 0.6 μM D-lactate, compared to 12 ± 2 μM L-lactate; 84% *ee*).The selection for the *Re*-face reduction by **(*R*,*R*)-2** (and *Si*-face reduction by catalyst **(*S*,*S*)-2**, respectively) is in agreement with reductions carried out using complex **2** for the ATH aromatic ketone substrates in formic acid (Chapter 3, section 3.3.5, page 95). These data demonstrate that, while pyruvate lacks the large aromatic substituent of acetophenone-type ketones studied in Chapter 3 (page 96), the methyl and carboxylate substituents of pyruvate sufficiently differ enough in their chemical structure (sterics) and electronic effects (anionic carboxylate, compared to neutral methyl moiety) to facilitate enantioselective reduction by the Os catalyst, depending on the chiral configuration of the diamine. Importantly, these experiments provide comparative data for *in cell* reductions carried out in section 5.3.4.

Table 5.3. Determination of enantiomeric excess (*ee*) for the reduction of sodium pyruvate by osmium complex **(*R*,*R*)-2** or **(*S*,*S*)-2** in PBS, using enantioselective enzymatic assay kits for L-lactate and D-lactate (Cayman Chemical). Os complex, 15 μM; pyruvate, 1 mM; formate, 2 mM (24 h, 310 K).

Complex	L-Lactate / μM	D-Lactate / μM	Major product	ee / %
(*R*,*R*)-2	1 ± 2	9.2 ± 0.6	D-lactate	83
(*S*,*S*)-2	12 ± 2	1.0 ± 0.6	L-lactate	84

5.3.3 Transfer hydrogenation reactions in cancer cells

To initially explore the potential for *in cell* catalytic activity, Os complexes were administered to A2780 cancer cells at 0.5 × IC_{50} concentration (determined in Chapter 4, section 4.3.4. IC_{50} concentrations: 15.5 μM and 6.5 μM for **2** and **7**, respectively) with co-administration of sodium formate (2 mM), in order to observe any increase in potency due to an *in cell* catalytic effect. For precise concentrations to be administered to cells, stock solutions of the complexes in culture medium (*ca*. 100 μM) were analysed by ICP-OES to determine the osmium concentration before addition. Sodium formate is known to be non-toxic to cells at concentrations up to 2 mM.[10] Cells were treated with the osmium with independent co-administration of sodium formate, achieving final working concentrations of formate from 0-2 mM. Negative control samples were also treated with sodium formate in the same manner.

Importantly, the proliferation of A2780 ovarian cancer cells was significantly decreased by treatment of cells with sodium formate in combination with an osmium complex; either **(*R*,*R*)-2**, **(*S*,*S*)-2, (*R*,*R*)-7** or **(*S*,*S*)-7** (P<0.001 when co-administered with 2 mM formate). Conversely, the proliferation of cells treated with sodium formate, but without an osmium catalyst, was not affected at the 95% confidence level (Welch's *t*-test). These data suggest that the mechanism of cell death may involve a catalytic component with respect to the osmium catalyst and sodium formate (Figure 5.2), utilising transfer hydrogenation chemistry to increase the potency of the catalyst towards cancer cells. Both enantiomers of *p*-cymene complex **2** displayed comparable potency enhancement (reducing the normalised cell proliferation to 20% of the catalyst-free control), suggesting that the mechanism of action does not depend on the enantioselectivity of the catalyst (i.e. neither enantiomer exhibited higher potency enhancement than the other). Interestingly, the potency of biphenyl catalyst **(*S*,*S*)-7**

was increased by over one order of magnitude (*ca*. 13×) compared to the formate-free experiment using complex **7** alone. Here, the nature of the arene appears to be an important factor in determining the catalytic properties of the complex in a biological system. This is in agreement with ATH reductions carried out in Chapter 3 (section 3.3.5) whereby arene extension yielded higher turnover frequencies for the reduction of aromatic ketones (*p*-cymene < biphenyl < *m*-terphenyl).

The experiment was repeated using HOF ovarian fibroblasts and MRC5 lung fibroblasts. Such primary cell lines are routinely used as models of non-cancerous proliferating cells, and provide an indication of drug and/or mechanism selectivity for cancer cells over healthy cells. In both cases, the proliferation of non-cancerous cells was not affected by co-administration of the osmium complex with sodium formate at the 95% confidence level (Welch's *t*-test) relative to the catalyst-free negative control. These data provide evidence for a highly selective specific enhancement of potency against ovarian cancer cells, which is both selective between cells from different organs (ovarian cancer vs. lung fibroblasts) and between cells obtained from the same tissue (ovarian cancer vs. ovarian fibroblasts).

In order to confirm the specific role of sodium formate for the modulation of antiproliferative activity, the experiments were all repeated using sodium acetate in place of sodium formate. Substitution of the formyl moiety prevents sodium acetate from acting as a hydride donor for transfer hydrogenation reactions,[10] therefore no modulation of cellular proliferation should be observed in such cases if the mechanism is synergistic with respect to both the osmium complex and formate. The antiproliferative activities of complexes **(*R*,*R*)-2**, **(*S*,*S*)-2** and **(*S*,*S*)-7** were unaffected ($P>0.05$) by co-administration of acetate, indicating that transfer hydrogenation chemistry appeared to be occurring inside cells, resulting in cell death (Figure 5.3).

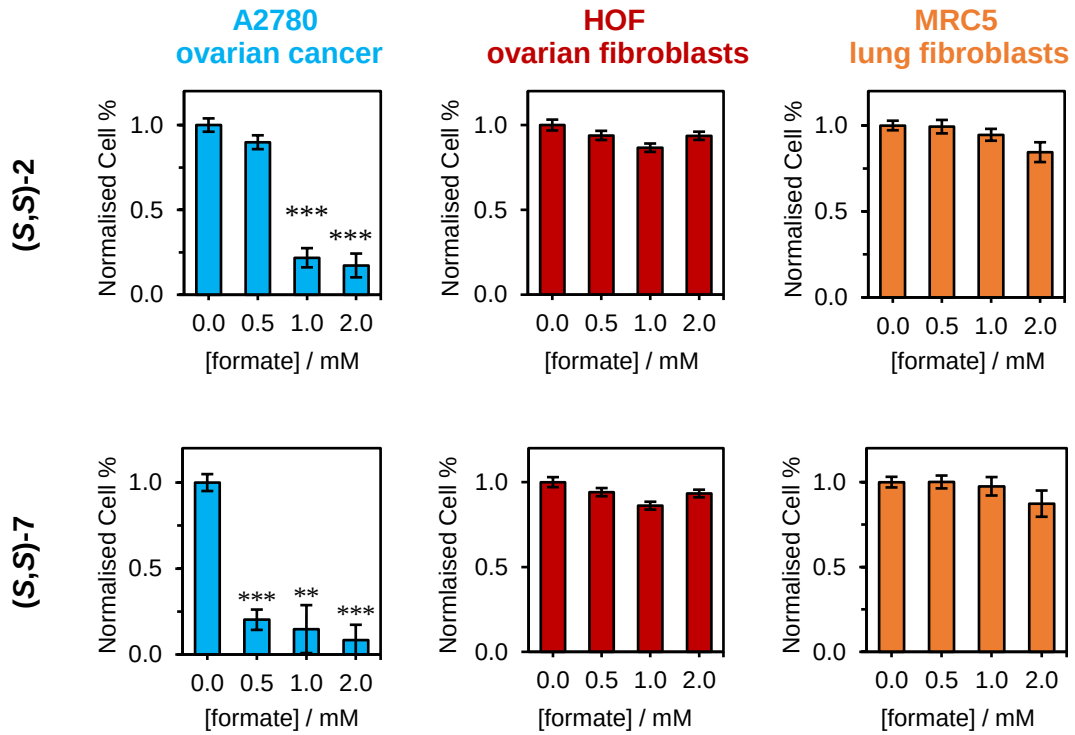

Cell line	Formate / mM	Normalised cellular proliferation			
		(*R*,*R*)-2	**(*S*,*S*)-2**	**(*S*,*S*)-7**	**No Os complex**
A2780	0.0	1.00 ± 0.03	1.00 ± 0.04	1.00 ± 0.05	1.00 ± 0.09
	0.5	0.76 ± 0.05	0.90 ± 0.04	0.20 ± 0.06	1.00 ± 0.07
	1.0	0.3 ± 0.1	0.22 ± 0.06	0.2 ± 0.1	0.98 ± 0.07
	2.0	0.2 ± 0.1	0.17 ± 0.07	0.08 ± 0.09	0.99 ± 0.07
HOF	0.0	1.00 ± 0.04	1.00 ± 0.03	1.00 ± 0.03	1.00 ± 0.02
	0.5	1.03 ± 0.04	0.94 ± 0.03	0.94 ± 0.02	0.99 ± 0.03
	1.0	1.00 ± 0.05	0.87± 0.03	0.87 ± 0.02	0.92 ± 0.02
	2.0	1.03 ± 0.03	0.94 ± 0.02	0.94 ± 0.02	0.90 ± 0.03
MRC5	0.0	1.00 ± 0.03	1.00 ± 0.03	1.00 ± 0.03	1.00 ± 0.09
	0.5	0.99 ± 0.04	0.99 ± 0.04	0.98 ± 0.04	0.96 ± 0.07
	1.0	0.90 ± 0.06	0.95 ± 0.03	0.98 ± 0.05	0.93 ± 0.08
	2.0	0.72 ± 0.04	0.85 ± 0.06	0.88 ± 0.08	0.95 ± 0.08

Figure 5.2. Normalised proliferation of: A2780 ovarian cancer cells, HOF ovarian fibroblasts and MRC5 lung fibroblasts, treated with catalyst **2** or **7** and sodium formate (0.5, 1.0, 2.0 mM) with 24 h drug exposure + 72 h recovery. Statistics using Welch's *t*-test. * $p < 0.05$, ** $p < 0.01$, *** $p < 0.001$.

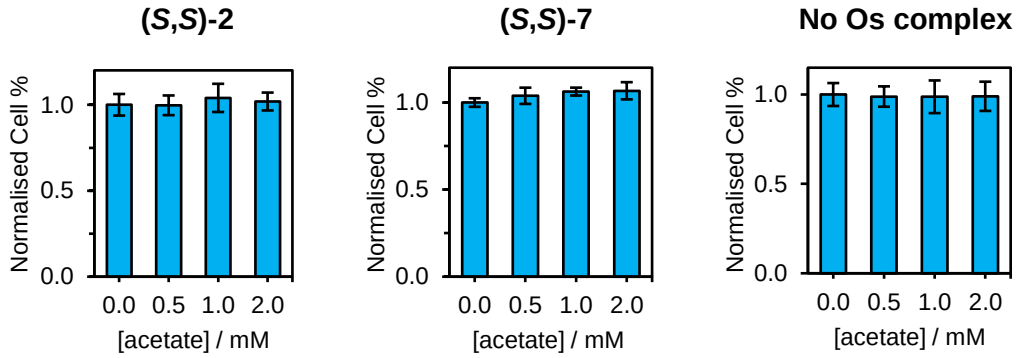

Cell line	Acetate / mM	Normalised cellular proliferation			
		(*R*,*R*)-2	**(*S*,*S*)-2**	**(*S*,*S*)-7**	**No Os complex**
A2780	0.0	1.00 ± 0.06	1.00 ± 0.02	1.00 ± 0.04	1.00 ± 0.06
	0.5	1.00 ± 0.06	0.95 ± 0.03	1.04 ± 0.04	0.99 ± 0.06
	1.0	1.04 ± 0.08	1.04 ± 0.03	1.08 ± 0.05	0.99 ± 0.09
	2.0	1.02 ± 0.05	0.98 ± 0.03	1.11 ± 0.04	0.99 ± 0.08

Figure 5.3. Normalised proliferation of A2780 human cancer cells treated with complex **2** or **7** with independent co-administration of with sodium acetate at various concentrations (0.5, 1.0 and 2.0 mM). Cells were treated for 24 h and allowed 72 h recovery time in drug-free culture medium.

The cellular accumulation of osmium in A2780 cancer cells treated with osmium sulfonamide complexes **2** and **7** was studied in depth in Chapter 4 (section 4.3.5). To investigate whether sodium formate influenced the internalisation of osmium (i.e. potency increase due to increased drug accumulation, rather than transfer hydrogenation reactions) the metal accumulation experiments were repeated based on the experimental procedure used in Chapter 4 (section 4.3.5) using cells that were co-treated with either complex **2** or **7** (1/3 × IC_{50} concentration, 5.2 µM and 2.2 µM for complexes **2** and **7**, respectively) in the presence of 2 mM formate. Cell pellets were digested in concentrated nitric acid (72%) and the metal content in samples was quantified using ICP-MS as described in Chapter 2 (section 2.2.8, page 54).

Table 5.4. Osmium accumulation in A2780 ovarian cancer cells treated with osmium complex **2** or **7** with co-administration of sodium formate (2 mM). Cells were treated for 24 h and allowed 72 h recovery time in drug-free culture medium. Osmium accumulation determined (after digesting cells) by ICP-MS. Internal metal concentration reported as ng Os × 10^6 cells.

Cell line	Formate / mM	Cellular metal accumulation (ng Os × 10^6 cells)		
		(*S*,*S*)-2	**(*S*,*S*)-7**	**No Os complex**
A2780	0.0	11 ± 2	7 ± 1	0.059 ± 0.003
	2.0	10 ± 2	8 ± 2	0.009 ± 0.009

Importantly, after treatment with Os complexes at 1/3 IC_{50} concentration, the accumulation of metal into the cell was not affected by the formate concentration (P>0.77, Table 5.4) indicating that the potency increase was not caused by greater influx of metallodrug into the cell. Rather, the potency enhancement is dependent on both the osmium complex and sodium formate in combination, since the cellular osmium accumulation was unchanged (11 ± 2 ng compared to 10 ± 2 ng in the presence of sodium formate for **(*S*,*S*)-2**; 7 ± 1 ng compared to 8 ± 2 ng in the presence of sodium formate for **(*S*,*S*)-7**). Importantly, the presence of sodium formate did not reduce the internalisation of the complex, however successful internalisation of the osmium transfer hydrogenation catalyst provides further evidence for the likelihood of an *in cell* catalytic mechanism.

Overall, to the best of our knowledge, these experiments provide the first example of osmium-catalysed transfer hydrogenation chemistry in cells. Treatment of cancer cells with an osmium transfer hydrogenation catalyst and a hydride source (sodium formate) can catalytically increase the potency of the Os complex to achieve decreased cellular proliferation via a mechanism that is likely to involve transfer hydrogenation chemistry, while also generating selectivity for cancer cells over healthy cells.

5.3.4 In-cell reduction of pyruvate to lactate

In cells, pyruvate is either utilised for oxidative phosphorylation, or reduced to L-lactate by lactate dehydrogenase, the major enantiomer in cells. On the contrary, the intracellular concentration of D-lactate inside cells is low,[17] and so the generation of additional D-lactate by an external catalyst would be readily detectable. To observe the reduction of pyruvate in cells using the enantioselective osmium sulfonamide catalysts, cancer cells were treated with either enantiomer of complex **2** (1 × IC_{50}) and sodium formate for 24 h. After drug exposure, excess drug and formate were removed with PBS washes, cell pellets obtained, and the intracellular D-lactate concentration was determined using an enantioselective enzymatic assay kit, according to the manufacturer's instructions.

Upon co-administration of either Os catalyst and sodium formate, the intracellular D-lactate concentration was found to increase, relative to the catalyst-free control (79 ± 10 μM and 51 ± 4 μM, for complex **(*R*,*R*)-2** and **(*S*,*S*)-2**, respectively, Figure 5.4). In the absence of sodium formate, neither complex significantly increased the intracellular concentration of D-lactate at the 95% confidence level relative to the osmium-free untreated control. Furthermore, co-administration of formate alone did not affect D-lactate concentration in A2780 cancer cells (31 μM and 29 μM, respectively; P=0.7259) confirming the role of the catalyst in the modulation of D-lactate concentration. The involvement of formate was confirmed by comparing D-lactate levels in cells treated with **(*R*,*R*)-2** alone, and **(*R*,*R*)-2** with formate, which was found to be significantly greater (47.6 μM compared to 79 μM; P=0.0474).

These data suggest that the transfer hydrogenation of pyruvate, catalysed by Os complexes, occurs inside cells, and represents the first example of Os-catalysed in-cell transfer hydrogenation.

Importantly, cells treated with **(*R*,*R*)-2** and formate were found to have significantly greater levels of D-lactate than those treated with **(*S*,*S*)-2** and formate (79 μM compared to 51 μM; P=0.0452) signifying that catalyst enantioselectivity is retained inside cells during pyruvate reduction. This process allows for selective generation of D-lactate inside cells depending on the chosen enantiomer of osmium catalyst **2** (Figure 5.4). The antiproliferative activities of L-lactate and D-lactate were determined using the SRB assay as described in Chapter 2 (page 59).[18] Both enantiomers were found to be non-toxic towards A2780 cancer cells up to 2 mM (highest concentration investigated), suggesting that the production of lactate is unlikely to be the direct cause of cell death.

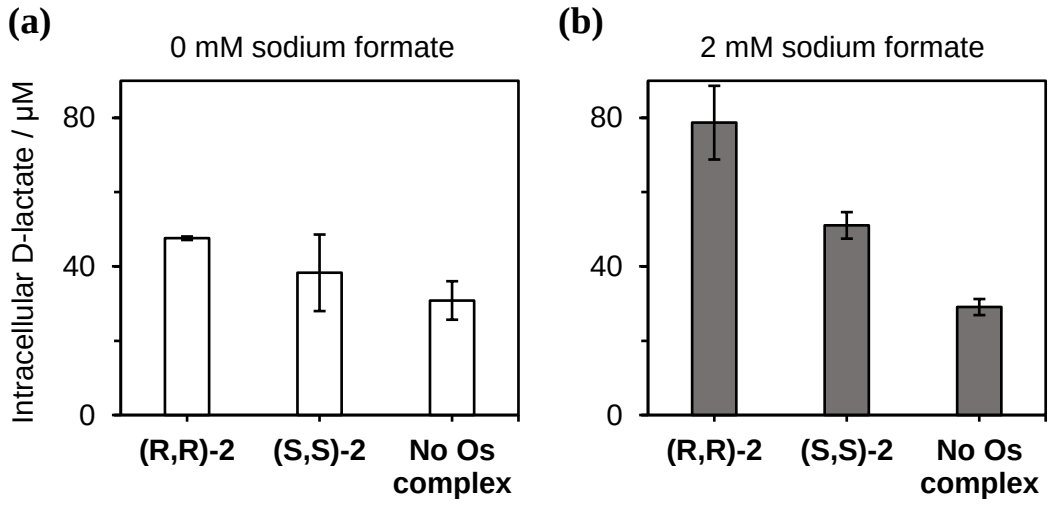

	Intracellular D-lactate / μM		
	(*R*,*R*)-2	**(*S*,*S*)-2**	No Os complex
0.0 mM formate	47.6 ± 0.5	38 ± 10	31 ± 5
2.0 mM formate	79 ± 10 *	51 ± 4	29 ± 2

Figure 5.4. Intracellular D-lactate (μM) in A2780 ovarian cancer cells exposed to either complex **(*R*,*R*)-2** or **(*S*,*S*)-2** for 24 h (1.0 × IC_{50}, 310 K, no recovery time): (a) Os complex only; (b) Independent co-adminstration of 2 mM sodium formate (within 5 min of drug addition). All statistics (*) were calculated using a two-tailed *t*-test assuming unequal variances between samples (Welch's *t*-test).

To confirm that the reduction of pyruvate occurred inside cancer cells, and not in the culture medium, extracellular lactate concentrations were determined in the same manner, per the lactate detection kit manufacturer's instructions. In this case, extracellular D-lactate levels were not statistically different ($P > 0.1$ using a two-tailed *t*-test assuming unequal variances) between the complex-free, or formate-free negative control experiments (Table 5.5). Since the culture medium used in the experiments did not contain pyruvate, these data suggest that pyruvate export from cells into the extracellular matrix is not significant, and reduction does not occur in the culture medium. Rather, the enantioselective reduction of pyruvate to D-lactate catalysed by complex (***R,R*)-2** only occurs inside cells.

Table 5.5. Extracellular D-lactate (μM) in A2780 ovarian cancer cells exposed to either complex **(*R,R*)-2** or **(*S,S*)-2** for 24 h (1.0 × IC_{50}, 310 K, no recovery time). All statistics were calculated using a two-tailed *t*-test assuming unequal variances between samples (Welch's *t*-test).

	Extracellular D-lactate / μM		
	(*R,R*)-2	**(*S,S*)-2**	No Os complex
0.0 mM formate	32 ± 4	35 ± 5	38 ± 4
2.0 mM formate	32 ± 4	36 ± 5	36 ± 6

5.3.5 Alternative in-cell hydrogenation using *N*-formylmethionine

N-formylmethionine was explored as a formate precursor in PC3 prostate cancer cells, which are known to over-express the peptide deformylase enzyme. We hypothesised that this would result in the *in situ* generation of formate in PC3 cells after enzymatic cleavage from methionine.

Co-administration of *N*-formylmethionine (fMet) with either osmium *p*-cymene complex **2** or biphenyl complex **7** decreased the normalised cellular proliferation of PC3 cancer cells (Table 5.6). Similarly to experiments using sodium formate as a hydride source in A2780 cells, the potency of biphenyl complex **7** was enhanced to a greater degree than *p*-cymene complex **2** (*ca*. 20% decrease in normalised proliferation by complex **7** and formate, compared to *ca*. 10% by complex **2** and formate).

Table 5.6. Normalised cell proliferation for PC3 prostate cancer cells treated with osmium catalyst (**2** or **7**; 0.5 × IC_{50}) with co-administration of either *N*-formyl-methionine or *N*-acetyl-methionine (0.0, 0.25, 0.5 and 1.0 mM). All experiments using 24 h drug exposure time +72 h recovery in drug-free medium (310 K). Statistics calculated using a two-tailed *t*-test assuming unequal variances (Welch's t-test). **P* < 0.05, ***P* < 0.01.

Hydride source	Conc. / mM	Normalised cellular proliferation		
		(*S*,*S*)-2	**(*S*,*S*)-7**	**No Os complex**
Formyl-Met	0.00	1.00 ± 0.09	1.00 ± 0.08	1.00 ± 0.07
	0.25	0.96 ± 0.07	0.98 ± 0.08	1.00 ± 0.08
	0.50	0.91 ± 0.10	0.88 ± 0.09 *	1.0 ± 0.1
	1.00	0.87 ± 0.06 **	0.80 ± 0.06 **	1.0 ± 0.1
Acetyl-Met	0.00	1.00 ± 0.02	1.00 ± 0.03	1.00 ± 0.07
	0.25	1.01 ± 0.06	1.01 ± 0.08	1.0 ± 0.2
	0.50	1.04 ± 0.07	1.03 ± 0.05	1.1 ± 0.2
	1.00	0.98 ± 0.02	0.96 ± 0.09	1.1 ± 0.1

The extent of potency increase was not as dramatic when using formylmethionine in PC3 prostate cancer cells, compared to co-administration of sodium formate in A2780 cancer cells. Both the antiproliferative activities of **2** and **7** (IC_{50} in A2780: 15.5 ± 0.5 μM and 6.5 ± 0.3 μM for **2** and **7**, respectively; IC_{50} in PC3: 12.0 ± 0.3 μM and 9.9 ± 0.2 μM for **2** and **7**, respectively) and the cellular accumulation of **2** (30 ± 2 ng × 10^6 cells in A2780; 32 ± 2 ng × 10^6 cells in PC3) were found to be similar between the cell lines (Chapter 4, sections 4.3.4 and 4.3.5). It is therefore likely that the lesser increase in potency, compared to those observed upon co-administration of sodium formate (achieving over one order of magnitude greater potency in the case of complex **7** in combination with formate), is related to the efficiency of either (a) formylmethionine accumulation, and/or (b) formyl cleavage by the peptide deformylase enzyme.

Similarly to studies for the co-administration of sodium acetate in A2780 cancer cells to confirm the specific role of formate, the ability of *N*-formylmethionine to provide a source of formate was confirmed by co-administration of *N*-acetylmethionine in place of formylmethionine. *N*-acetylmethionine cannot release formate, and therefore cannot act as a hydride donor (even if the acetyl residue was cleaved, this cannot act to donate hydride).

No significant change in the normalised cellular proliferation of PC3 cancer cells was observed upon treatment of cells with *N*-acetylmethionine in combination with either *p*-cymene osmium complex **2** or biphenyl complex **7**. These data confirm that (a) *N*-formylmethionine is internalised by PC3 cells, whereby the peptide deformylase can cleave the formyl residue; (b) *N*-formylmethionine was able to provide an alternative source of formate, and therefore act as an alternative hydride source for *in cell* transfer hydrogenation reactions.

5.3.6 Mechanism of action for formate-activated catalysis

To investigate the impact of formate-modulated anticancer activity, mechanistic studies of the cell cycle, induction of apoptosis and the integrity of the cell membrane were undertaken for cells treated with osmium complex **(*R*,*R*)-2** in both the presence and absence of sodium formate (2 mM). Additionally, experiments were repeated to include recovery time in drug-free culture medium to observe any late-onset effects (such as late-onset apoptosis).

Cell cycle arrest in A2780 cancer cells

A2780 cancer cells were treated with Os complex **(*R*,*R*)-2** in both the presence and absence of sodium formate (2 mM) for 24 h. The cell cycle analysis was conducted by fixing the cells using ethanol (making the cells permeable, thereby allowing the dye to cross the cell membrane) and staining with propidium iodide (PI, a DNA intercalating agent). Treated samples were analysed using flow cytometry using the FL2 (red) channel to detect propidium iodide fluorescence, which is greatly enhanced upon DNA intercalation (Figure 5.5). The G_1, G_2/M and S-phase populations were fitted to experimental data using FlowJo V10. The experiment was repeated allowing 72 h recovery time in complex and formate-free culture medium to observe any late-onset cell cycle arrest.

Cells treated with **2** showed slight G_1 phase arrest relative to the untreated control immediately after drug exposure time (66.0 % in Os-treated cells compared to 52 % in the untreated control). While sodium formate was not found to greatly modify the cell cycle, co-administration of the hydride source did statistically enhance G_1 arrest after 72 h recovery time, from 66 % to 71.4 %, respectively (P=0.0046).

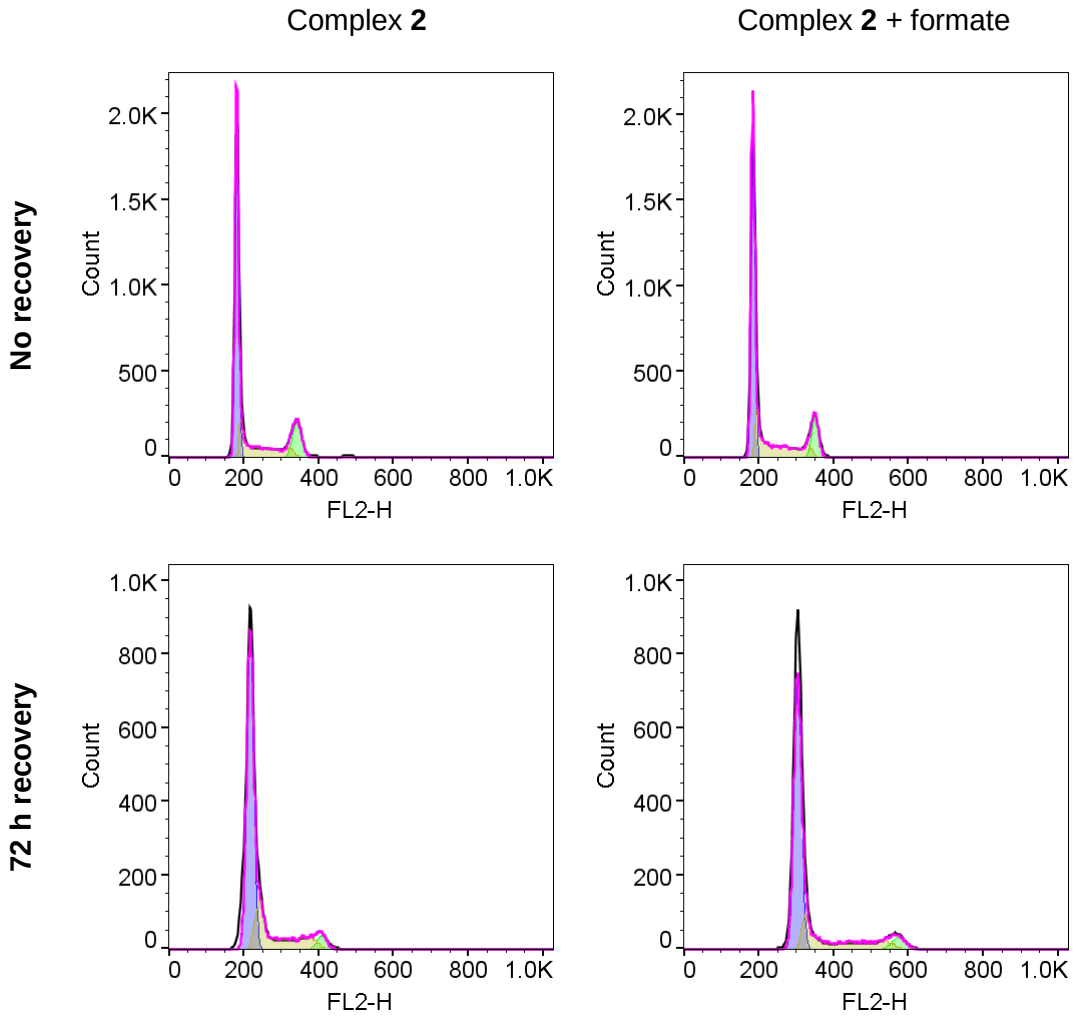

Normalised population / %		Untreated	Complex **2**	Complex **2** + 2mM formate
0 h	G_1 phase	52 ± 2	66.0 ± 0.9	63 ± 3
	S phase	24 ± 1	18.1 ± 0.3	17 ± 1
	G_2/M phase	24.3 ± 0.5	16.0 ± 0.6	20 ± 2
72 h	G_1 phase	62 ± 1	66 ± 1	71.4 ± 0.7
	S phase	30.0 ± 0.8	22.3 ± 0.4	20.4 ± 0.4
	G_2/M phase	5.0 ± 0.6	5 ± 1	6.3 ± 0.7

Figure 5.5. Cell cycle analysis for A2780 cancer cells treated with complex **2** (1.0 × IC_{50} concentration, 310 K, 24 h drug exposure) in the presence / absence of sodium formate (2 mM). The experiment was repeated with 72 h recovery time in drug-free medium. Data fitted using Watson (pragmatic) model (●) in FlowJo V10. Representative data shown from instrumental triplicates for complex **(*R*,*R*)-2** in the presence and absence of sodium formate. G_1 phase population (●); S phase population (●); G_2M phase population (●). Statistical analysis were carried out using a two-tailed *t*-test assuming unequal variances in the sample populations (Welch's *t*-test).

Induction of apoptosis in A2780 cancer cells

Treated cells were stained using a solution of propidium iodide (PI, a red DNA intercalating agent) and Annexin V-FITC (phosphatidylserine-binding protein, conjugated to the green FITC fluorophore) to allow for two-colour detection. Since cells were not fixed in this experiment, propidium iodide only permeates late-apoptotic (FL1+, FL2+) and non-viable (FL1-, FL2+) cells, resulting in the intercalation of DNA, enhancing the PI fluorescence. On the other hand, early-apoptotic cells (FL1+, FL2-) undergo membrane-flip, translocating phosphatidylserine to the exterior of the cell membrane, where it may be bound by Annexin V. Late-apoptotic cells are both permeable to propidium iodide, and have undergone membrane-flip, facilitating the binding of both dyes (FL1+, FL2+).

After 24 h exposure to complex **(*R*,*R*)-2**, no early/late-stage apoptotic cells were detectable, irrespective of the formate concentration (early/late-apoptotic populations for treated cells < 0.4 %) relative to the untreated control. The populations of early/late-stage apoptotic cells were re-determined after 72 h recovery time in drug and formate-free culture medium. Interestingly, while the non-viable cell population was significantly increased (P=0.0057), the early/late-stage apoptotic populations (< 0.03%) were statistically similar to the untreated control population (0.01% and 0.02% for early- and late-stage apoptotic populations, respectively).

In all cases, apoptotic cells were not detected, irrespective of the formate concentration or recovery time. These data suggest that cell death resulting from treatment with complex **2** may have occurred via a non-apoptotic alternative mechanism (Figure 5.6). Furthermore, the increase in the non-viable population after 72 h recovery time in drug-free culture medium may be due to over-confluency of cells.

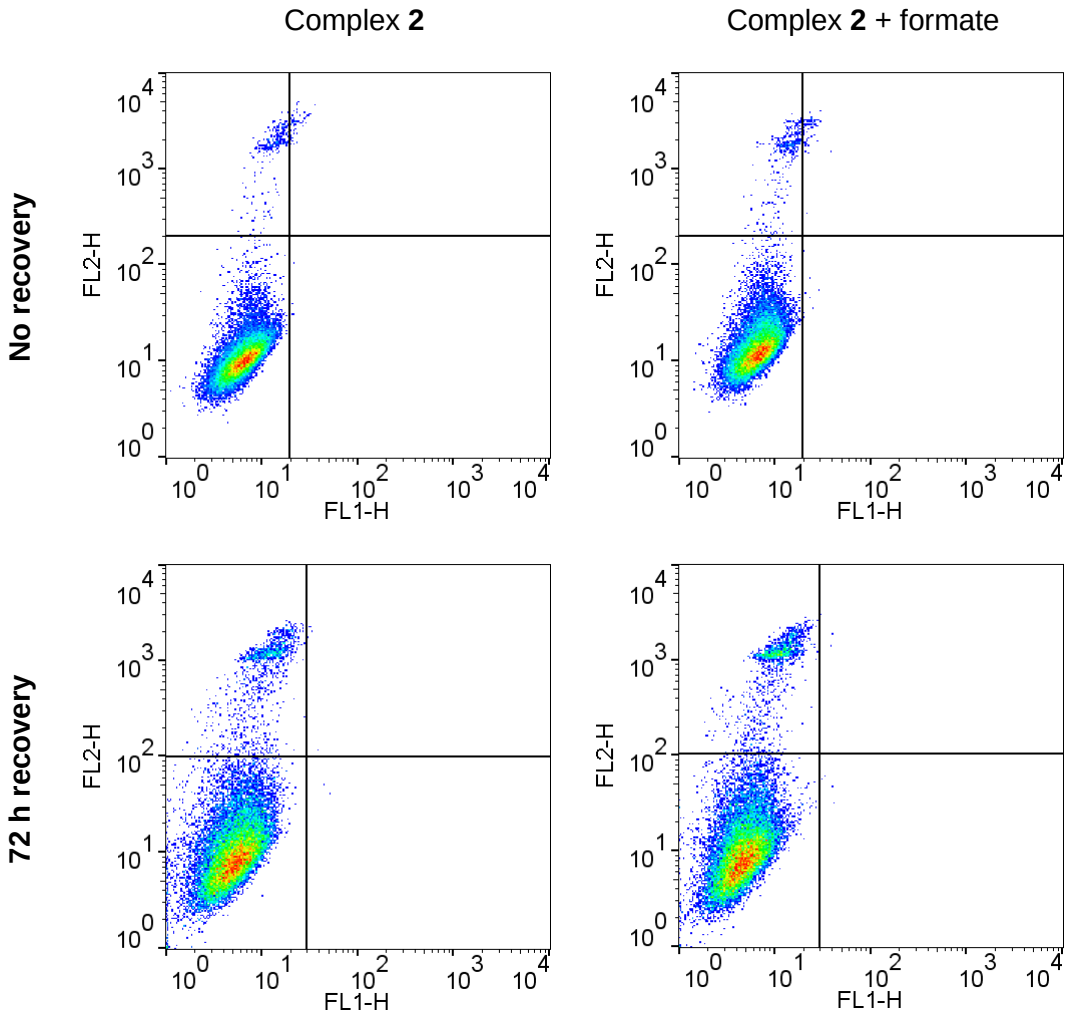

Normalised population / %		Untreated	Complex **2**	Complex **2** + 2mM formate
No recovery	Viable	96.2 ± 0.2	96.6 ± 0.3	96.1 ± 0.1
	Early-apoptotic	0.03 ± 0.01	0.01 ± 0.01	0.02 ± 0.01
	Late-apoptotic	1.1 ± 0.2	0.2 ± 0.1	0.4 ± 0.2
	Non-viable	2.6 ± 0.1	3.3 ± 0.2	3.5 ± 0.2
72 h recovery	Viable	93.2 ± 0.3	92.6 ± 0.5	94.2 ± 0.5
	Early-apoptotic	0.01 ± 0.01	0.03 ± 0.01	0.01 ± 0.01
	Late-apoptotic	0.02 ± 0.01	0.01 ± 0.01	0.02 ± 0.01
	Non-viable	6.8 ± 0.2	7.4 ± 0.5	5.8 ± 0.5

Figure 5.6. Detection of apoptosis by dual staining of A2780 cells using Annexin V-FITC (FL1) and propidium iodide (FL2). Cells were treated with complex ***(R,R)*-2** (1.0 × IC_{50}) for 24 h in the presence and absence of sodium formate (2 mM). The experiment was repeated with 72 h recovery time in drug-free medium. Data were gated and processed using FlowJo V10 for Windows: viable (FL1-Fl2-), early-apoptotic (FL1+FL2-), late-apoptotic (FL1+FL2+) and non-viable (FL1-FL2+) cells.

Membrane integrity of A2780 cancer cells

The cellular membrane integrity was determined for A2780 cancer cells treated with complex **2** in the presence and absence of sodium formate (2 mM). Cells were stained using propidium iodide, without fixation. In this experiment, A2780 cells with a compromised cell membrane would allow propidium iodide to permeate into the cell, intercalate into DNA, resulting in increased fluorescence. Stained cells were analysed using flow cytometry (FL2 channel) to detect PI fluorescence. Data were gated using FlowJo V10 into two populations, FL2- and FL2+, representing non-compromised and compromised cell membranes, respectively.

The membrane integrity of cancer cells exposed to complex **2** was not significantly affected after 24 h drug exposure ($P>0.05$) relative to the untreated control (97.4 ± 0.2 % viable cell membrane population). Furthermore, co-administration of sodium formate did not affect the membrane integrity (97.8 ± 0.1 % and 98.4 ± 0.1 % viable cell membrane population, for cells treated with complex **2** in the absence and presence of formate, respectively).

While loss of integrity was observed in Os-treated cells after 72 h recovery time in drug-free medium when compared to those determined without recovery time ($P<0.001$), the effect was also apparent in the negative control sample (untreated cells: 94.4 ± 0.5 %; complex **2** only: 95.6 ± 0.4 %; complex **2** with formate: 93.1 ± 0.2 %). This effect was also observed in the above study for the induction of apoptosis, and is likely a result of cells becoming over-confluent during the recovery time, resulting in a greater number of non-viable cells. These data suggest that complex **2**, regardless of the concentration of sodium formate or recovery time in drug-free medium, does not affect the viability of the cell membrane in A2780 cancer cells.

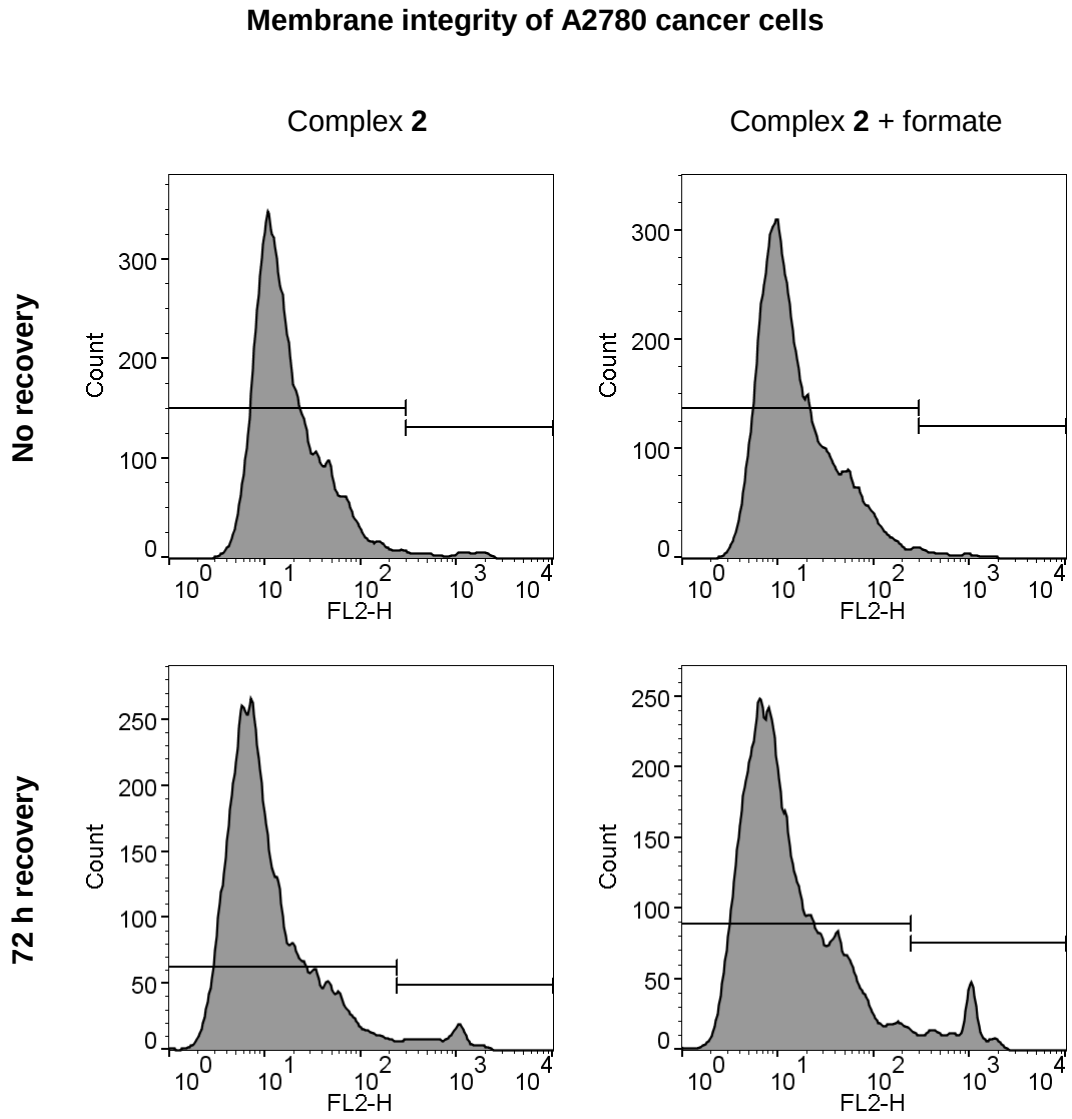

Normalised population / %		Untreated	Complex **2**	Complex **2** + 2mM formate
0 h	Viable	97.4 ± 0.2	97.8 ± 0.1	98.4 ± 0.1
	Non-viable	2.6 ± 0.1	2.2 ± 0.1	1.6 ± 0.1
72 h	Viable	94.4 ± 0.5	95.6 ± 0.4	93.1 ± 0.2
	Non-viable	5.6 ± 0.4	4.4 ± 0.3	6.9 ± 0.2

Figure 5.7. The membrane integrity of A2780 ovarian cancer cells was determined by staining with propidium iodide (FL2). Cells were treated with complex **(*R*,*R*)-2** (1.0 × IC_{50}) in the presence and absence of sodium formate (2 mM) for 24 h. The experiment was repeated with 72 h recovery time in drug-free medium. Data were gated (viable membrane, FL2-; non-viable membrane, FL2+) and processed using FlowJo V10 for Windows. Statistical analysis was carried out using a two-tailed *t*-test assuming unequal variances (Welch's *t*-test).

5.4 Discussion

5.4.1 Transfer hydrogenation as a novel approach to achieving cell death

A series of Os complexes were explored for activity as transfer hydrogenation catalysts (Chapter 3, section 3.3.5, page 95) and for antiproliferative activity against A2780 cancer cells (Chapter 4, section 4.3.4). Sulfonamide substitution was not beneficial to the catalytic activity of complexes **3**-**6** for the reduction of acetophenone (TOF ranging from 40-61.4 h^{-1}, compared to 63.9 h^{-1} using complex **2**). While arene extension increased the activity of complex **8** (4.4 μM in A2780), a useful catalyst for *in cell* reactions should be minimally potent before activation.

Co-administration of an osmium complex with sodium formate significantly decreased the proliferation of A2780 cancer cells (Figure 5.2), to *ca*. 20% of the formate-free proliferation for cells treated with **2**, and reduced to 8% for cells treated with **7**. Comparing the results to Os-free experiments (100% normalised proliferation in the presence of 2 mM formate) and those using sodium acetate (100% normalised proliferation in the presence of 2 mM acetate, with or without Os complex), the effect is dependent on both formate and the osmium catalyst (Figure 5.3, section 5.3.3). For cells treated with complex **2**, normalised proliferation decreased to 76% at 0.5 mM formate (which is in excess of the catalyst concentration) however potency was further enhanced at 1.0 and 2.0 mM formate, achieving a decrease to 30% and 20% of the original formate-free proliferation, respectively. This is suggestive of the fact that the mechanism is likely to be catalytic. Cellular Os accumulation experiments demonstrated that the potency increase is not due to a formate-enhanced drug accumulation (10 ± 2 and 11 ± 2 ng Os × 10^6 cells for cells treated with complex **2** in the presence and absence of formate, respectively; Table 5.4).

This mechanism generated high selectivity for cancer cells, achieving up to 83% decrease in normalised proliferation for cells treated with complex (***R,R*)-2**, compared to only a small decrease in healthy ovarian (6%) and lung (15%) cells in the presence of formate. The origin of this selectivity is likely due to the heightened redox stress in cancer cells, resulting from the high metabolic rate required to maintain rapid proliferation.[19] Conversely, non-cancerous cells are known to not only readily recover from redox stress,[20] but also possess functional mitochondria which can generate ATP by oxidative phosphorylation, a more efficient process than glycolysis alone, on which cancer cells are reliant as a result of commonly dysfunctional mitochondria.[13]

5.4.2 Asymmetric reduction of pyruvate in cells

The *in cell* reduction of NAD^+ to NADH has been comprehensively studied using ruthenium(II) complexes,[10] however the lack of a stereogenic centre would not allow for the investigation of any *in cell* enantioselectivity that may occur when using chiral Os catalysts. Pyruvate, the simplest of the alpha-keto acids, is a vital pro-chiral molecule in cellular metabolism, is present at millimolar concentrations in the cytoplasm, and was selected as a target compound.

Transfer hydrogenation of acetophenone-derived ketones by Os complexes using formic acid as a hydride source was studied in Chapter 3 (section 3.4.3, page 95). The reduction of pyruvate to lactate was studied in the same manner (5:2 mol ratio formic acid : triethylamine azeotrope, 310 K), achieving rapid turnover (TOF ~300 h^{-1}) when using complex **2** (Table 5.1). This is, to the best of our knowledge, the first example of the production of lactate by a Noyori-type ATH catalyst (Figure 5.8). Interestingly, the reduction using catalyst **7** proceeded at a slower rate (TOF ~102 h^{-1}) while the

Noyori Ru(II) catalyst proceeded with TOF=132 h^{-1}. Reduction of pyruvate in aqueous solution, using sodium formate as an alternative hydride source to formic acid, proceeded at a slower rate than in the organic solvent system (1.5-16.4 h^{-1}), however lactate formation was readily identified by ^{1}H-NMR (Figure 5.1). Using an enantioselective assay kit, the aqueous reduction of pyruvate by either enantiomer of complex **2** was found to proceed with high enantioselectivity (83% *ee*). The rate of catalysis was found to be highly dependent on the concentration of sodium formate (Table 5.2), with an order of magnitude rate enhancement observed upon increasing the formate concentration from 4 mM (TOF = 1.5 h^{-1}) to 30 mM (TOF = 16.4 h^{-1}).

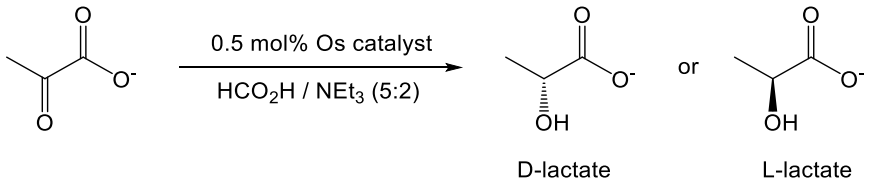

Figure 5.8. Reduction of pyruvate to L / D lactate by Os complex **2** or **7**

Though no direct evidence for the proposed transition state was obtained in this study, the substrate carboxylate group may interact with the catalyst arene (*p*-cymene or biphenyl for complex **2** or **7**, respectively) in an electrostatic manner, to orientate pyruvate for subsequent enantioselective reduction to lactate (Figure 5.9).[21] This hypothesised transition state is based on previous mechanistic and computational studies undertaken for the transfer hydrogenation of aromatic ketones, where the transition state is determined by a C-H--π interaction between the catalyst arene and the aromatic group of the substrate. However, it is unclear whether the transfer of hydride occurs via a concerted 6-membered transition state, or in a step-wise fashion involving solvent participation.[22, 23]

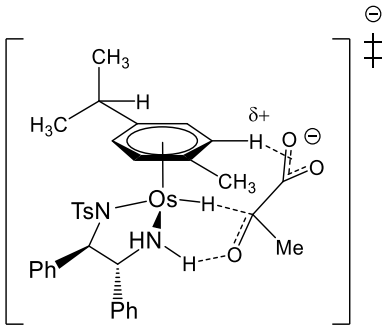

Figure 5.9. Proposed transition state for the reduction of pyruvate to D-lactate by complex ***R,R*-2**.

The enantioselectivity for the reduction of pyruvate likely occurs in the same manner as the original Noyori asymmetric transfer hydrogenation transition state, which is governed by steric effects involving the pendent phenyl groups of the chirally-pure diamine.[24, 25] This favours carbonyl reduction on a specific face; in the case of the (*R,R*) configured catalyst, reduction occurs on the *Re* face, yielding D-lactate (and *Si* face reduction to yield L-lactate for the (*S,S*) configured catalyst). In addition to steric effects and arene interaction between the catalyst and the substrate, the less-favoured transition state may be further destabilised by unfavourable interactions between the substrate and the sulfonyl group on the catalyst.[22, 23, 26]

Generation of lactate in cells using osmium sulfonamide complexes

In cells, the conversion of pyruvate to L-lactate is catalysed by lactate dehydrogenase (LDH).[27] This process is particularly prevalent in cancer cells, which up-regulate glycolysis to meet the metabolic demands of rapid growth and proliferation, as described by the Warburg Effect.[28] The exclusivity of this process to cancer cells makes depletion of pyruvate (and other glycolytic pathway-targeting methods) an attractive strategy for the development of novel anti-cancer therapies.

The significantly greater production of D-lactate by the chiral (*R*,*R*) osmium complex, compared to the (*S*,*S*) complex (79 μM compared to 51 μM, Figure 5.4), offers the first example of *in cell* enantioselective reduction by a synthetic catalyst. Though the apparent *in cell* turnover frequency (TOF) is low, lactate and pyruvate homeostasis is tightly regulated in cells by monocarboxylate transporters (MCT1-4),[27, 29] and therefore the concentration of lactate determined after 24 h drug exposure is likely not to reflect the true extent of conversion. Furthermore, though cells were treated using 15 μM of complex **2**, the concentration of active catalyst in the cytoplasm is likely to be significantly lower. In fact, compartmentalisation studies using complex **2** in Chapter 4 (section 4.3.6) showed that only *ca.* 50% of the total metal accumulated remains in the cytoplasmic fraction. Though ICP-MS was used to investigate osmium accumulation in treated cells, the technique does not distinguish between active and deactivated catalyst. Small molecules have been shown to deactivate metal complexes inside cells.[30] Co-administration of complex **2** with a glutathione synthetase inhibitor (L-BSO) was found to increase the activity of the complex (from IC_{50} = 15.5 μM, to IC_{50} = 10.0 μM in the presence of 5 μM L-BSO; Figure 4.11), and therefore it is likely that glutathione may deactivate the catalyst (Chapter 4, section 4.3.8).

In addition to the availability of active catalyst inside the cell, the intracellular formate concentration may be limited by homeostatic feedback mechanisms involving the same monocarboxylate transporters described above.[27, 29] In addition, formate has been linked to the activity of mitochondrial electron transport chain Complex I.[31] Exploration of Complex I inhibitors may therefore be beneficial in order to modulate intracellular formate levels. Overall, the depletion of formate is expected to reduce the turnover frequency, as demonstrated in aqueous model system experiments. Strategies to counteract homeostatic mechanisms may improve *in cell* catalytic activities.

5.4.3 Enzymatic activation of N-formylmethionine

The first amino acid of newly synthesised polypeptide chains is commonly formylated methionine (*N*-formyl-methionine, fMet). After assembly, the formyl residue is usually cleaved as part of post-translational modification. The enzyme responsible for catalysing the hydrolysis, peptide deformylase (PDF) has been identified in human cells, and is known to be over-expressed in some cancer cell lines, including PC3 prostate cancer cells.[15] Though many studies have explored the inhibition of human peptide deformylase, resulting in the inhibition of mitochondrial function and the induction of apoptosis,[32-34] few have explored the potential of utilising its over-expression, and none have used the enzyme for *in cell* hydrogenation. By co-administration of additional *N*-formylmethionine, it was hoped that formate could be generated *in situ* inside cells that are prone to deformylase over-expression.

Co-administration of either complex **2** or **7** with fMet in PC3 cells resulted in a significant reduction (20% reduction, P=0.003) in normalised proliferation relative to the Os-free control (Table 5.6, section 5.3.5). Conversely, co-administration of *N*-acetyl-methionine did not affect the cellular proliferation (~2% decrease normalised proliferation), as was similarly observed in experiments conducted using A2780 cancer cells co-treated with an Os complex and sodium acetate. Though the decrease in proliferation was not as prominent as in A2780 cancer cells treated with sodium formate, the maximum dose of fMet was only 1 mM (compared to 2 mM formate) and the formate availability was likely further limited by the rate of hydrolysis by peptide deformylase. Considering that the rate of catalysis was shown to be highly dependent on the formate concentration, the results obtained by co-administration of *N*-formyl-methionine demonstrate that formate precursors may warrant further exploration for *in cell* reductions.

5.5 Conclusions

Osmium complexes **2** [Os(*p*-cymene)(TsDPEN)] and **7** [Os(biphenyl)(TsDPEN)] have been shown to reduce pyruvate to lactate in both *in vitro* and *in cell* experiments. The reduction was found to be dependent on the concentration of sodium formate available, and was found to proceed with high enantioselectivity (~83% *ee*) in the aqueous model system. Selective treatment of cancer cells with a particular enantiomer of catalyst **2** allowed for the specific production of un-natural D-lactate; providing the first example of an asymmetric *in cell* transformation catalysed by a synthetic compound.

N-formyl-methionine was explored as an alternative hydride source to sodium formate, and when co-administered to PC3 cancer cells alongside an osmium complex led to a ~20% reduction in normalised cell proliferation. PC3 cancer cells are known to over-express the peptide deformylase enzyme,[15] and the process appears to generate formate *in situ*. While further work is required to determine the precise mechanism of action, these preliminary data are promising. We hypothesise that exploration of alternative hydride sources may further increase the selectivity between cancer cells and healthy cells, based on cell phenotypes (e.g. enzyme over-expression).

While it is unlikely that the generation of lactate causes cell death (since neither D-lactate or L-lactate were found to be toxic towards A2780 cancer cells up to 2 mM), the Os(II) catalysts demonstrate manipulation of key metabolic components while retaining enantioselectivity. The interactions between chiral biomolecules and chiral active sites in enzymes are crucial to the maintenance of cell proliferation, and may present a novel target for future drug design for many diseases beyond the treatment of cancer.

In contrast to cisplatin, which damages DNA by the formation of inter- and intra-strand adducts leading to G_2/M cell cycle arrest,[7, 35] treatment of A2780 cancer cells with osmium complex **2** induced G_1 cell cycle arrest with no significant sub-G_1 population. Cellular distribution studies found low nucleic Os accumulation (1.6% of total accumulated Os, see Chapter 4, section 4.3.6), and in combination with the cell cycle analysis, we conclude that complex **2** is unlikely to target DNA. Co-administration of formate enlarged the G_1 population after 72 h recovery (66% to 71.4%, Figure 5.5, section 5.3.6), suggesting that the mechanism of action may be enhanced, rather than altered. Treated cells were also not found to be apoptotic (early / late apoptotic populations <1%, Figure 5.6, section 5.3.6). In the absence of apoptosis, G_1 arrest has been linked to a cellular response to metabolic stress,[36] which is consistent with the postulate that the osmium complexes are targeting pyruvate, a key metabolic intermediate in the glycolytic pathway. Interestingly, a half-sandwich rhodium(III) sulfonamide complex has also been shown to induce G_0/G_1 arrest without induction of apoptosis.[37] The apparent cytostatic nature of osmium complex **2** may result from pyruvate depletion. In addition, the observation of G_1 arrest without a significant population of non-viable cells (by dual FITC-Annexin V / PI staining) is suggestive of a highly cytostatic component of the mechanism of action, which has previously been observed for other osmium(II) half-sandwich complexes.[38]

Relative to the untreated control, no significant membrane disruption (P>0.05) was observed upon treatment with **2** and formate, excluding membrane-targeting as a potential mechanism of action (Figure 5.7). Though the population of cells with non-viable membranes was increased after 72 h, this was also observed in untreated cells (Figure 5.7, section 5.3.6).

5.6 References

1. I. Bauer and H.-J. Knölker, *Chem. Rev.*, 2015, **115**, 3170-3387.
2. G. Chelucci, S. Baldino and W. Baratta, *Acc. Chem. Res.*, 2015, **48**, 363-379.
3. R. H. Crabtree, *Chem. Rev.*, 2015, **115**, 127-150.
4. J. J. Soldevila-Barreda and P. J. Sadler, *Curr. Opin. Chem. Biol.*, 2015, **25**, 172-183.
5. B. Rosenberg, L. Van Camp and T. Krigas, *Nature*, 1965, **205**, 698-699.
6. K. D. Mjos and C. Orvig, *Chem. Rev.*, 2014, **114**, 4540-4563.
7. A. M. Florea and D. Büsselberg, *Cancers*, 2011, **3**, 1351-1357.
8. S. Goldstein, G. Czapski and A. Heller, *Free Radical Bio. Med.*, 2005, **38**, 839-845.
9. S. D. Shnyder, Y. Fu, A. Habtemariam, S. H. van Rijt, P. A. Cooper, P. M. Loadman and P. J. Sadler, *Med. Chem. Commun.*, 2011, **2**, 666-668.
10. J. J. Soldevila-Barreda, I. Romero-Canelón, A. Habtemariam and P. J. Sadler, *Nat. Commun.*, 2015, **6**, 6582.
11. Y. Zhao, E. B. Butler and M. Tan, *Cell Death Dis.*, 2013, **4**, e532.
12. O. Warburg, *Science*, 1956, **123**, 309-314.
13. M. G. Vander Heiden, L. C. Cantley and C. B. Thompson, *Science*, 2009, **324**, 1029-1033.
14. J. P. C. Coverdale, C. Sanchez-Cano, G. J. Clarkson, R. Soni, M. Wills and P. J. Sadler, *Chem. Eur. J.*, 2015, **21**, 8043-8046.
15. H. Randhawa, S. Chikara, D. Gehring, T. Yildirim, J. Menon and K. M. Reindl, *BMC Cancer*, 2013, **13**, 321-321.

16. S. J. Martin, C. P. Reutelingsperger, A. J. McGahon, J. A. Rader, R. C. van Schie, D. M. LaFace and D. R. Green, *J. Exp. Med.*, 1995, **182**, 1545-1556.

17. B. Ling, F. Peng, J. Alcorn, K. Lohmann, B. Bandy and G. A. Zello, *Nutr. Metab.*, 2012, **9**, 6-14.

18. V. Vichai and K. Kirtikara, *Nat. Protocols*, 2006, **1**, 1112-1116.

19. E. O. Hileman, J. Liu, M. Albitar, M. J. Keating and P. Huang, *Cancer Chemother. Pharmacol.*, 2004, **53**, 209-219.

20. J. D. Pennington, T. J. C. Wang, P. Nguyen, L. Sun, K. Bisht, D. Smart and D. Gius, *Drug Resist. Update*, 2005, **8**, 322-330.

21. C. M. Bligh, L. Anzalone, Y. C. Jung, Y. Zhang and W. A. Nugent, *J. Org. Chem.*, 2014, **79**, 3238-3243.

22. P. A. Dub and J. C. Gordon, *Dalton Trans.*, 2016, **45**, 6756-6781.

23. P. A. Dub and T. Ikariya, *J. Am. Chem. Soc.*, 2013, **135**, 2604-2619.

24. R. Noyori, M. Yamakawa and S. Hashiguchi, *J. Org. Chem.*, 2001, **66**, 7931-7944.

25. P. Brandt, P. Roth and P. G. Andersson, *J. Org. Chem.*, 2004, **69**, 4885-4890.

26. J. W. Handgraaf and E. J. Meijer, *J. Am. Chem. Soc.*, 2007, **129**, 3099-3103.

27. J. R. Doherty and J. L. Cleveland, *J. Clin. Invest.*, 2013, **123**, 3685-3692.

28. F. Hirschhaeuser, U. G. A. Sattler and W. Mueller-Klieser, *Cancer Res.*, 2011, **71**, 6921-6925.

29. A. P. Halestrap, *IUBMB Life*, 2012, **64**, 1-9.

30. R. J. Needham, C. Sanchez-Cano, X. Zhang, I. Romero-Canelón, A. Habtemariam, M. S. Cooper, L. Meszaros, G. J. Clarkson, P. J. Blower and P. J. Sadler, *Angew. Chem. Int. Ed.*, 2017, **56**, 1017-1020.

31. J. Meiser, S. Tumanov, O. Maddocks, C. F. Labuschagne, D. Athineos, N. Van Den Broek, G. M. Mackay, E. Gottlieb, K. Blyth, K. Vousden, J. J. Kamphorst and A. Vazquez, *Sci. Adv.*, 2016, **2**, e1601273.

32. S. Escobar-Alvarez, J. Gardner, A. Sheth, G. Manfredi, G. Yang, O. Ouerfelli, M. L. Heaney and D. A. Scheinberg, *Mol. Cell. Biol.*, 2010, **30**, 5099-5109.

33. M. D. Lee, Y. She, M. J. Soskis, C. P. Borella, J. R. Gardner, P. A. Hayes, B. M. Dy, M. L. Heaney, M. R. Philips, W. G. Bornmann, F. M. Sirotnak and D. A. Scheinberg, *J. Clin. Invest.*, 2004, **114**, 1107-1116.

34. A. Sheth, S. Escobar-Alvarez, J. Gardner, L. Ran, M. L. Heaney and D. A. Scheinberg, *Cell Death Dis.*, 2014, **5**, e1152.

35. S. Dasari and P. Bernard Tchounwou, *Eur. J. Pharmacol.*, 2014, **740**, 364-378.

36. L. A. Hoeferlin, N. V. Oleinik, N. I. Krupenko and S. A. Krupenko, *Genes Cancer.*, 2011, **2**, 889-899.

37. H. Dou, W. Zhong, L. Yang, T. Wang, H. Yan and Y. Hou, *Bioorg. Med. Chem.*, 2012, **20**, 4693-4700.

38. I. Romero-Canelón, M. Mos and P. J. Sadler, *J. Med. Chem.*, 2015, **58**, 7874-7880.

Chapter 6

In vivo studies of organo-osmium and organo-iridium complexes

6. *In vivo* studies of organo-Os and organo-Ir complexes

6.1 Introduction

Cell-based assays facilitate high-throughput phenotypic screening for novel compounds. In Chapters 4 and 5, cell assays were used to explore the antiproliferative activity (section 4.3.4, page 125), cellular accumulation and distribution (sections 4.3.5 and 4.3.6, pages 131 and 138), generation of reactive oxygen species (section 4.3.8, page 141), redox modulation (section 4.3.8, page 141) and catalytic activity (section 5.3.3, page 180) of Os(II) and Ir(III) complexes. However, *in vivo* studies are more complex. Administered compounds must be internalised by the host, transported to target sites (e.g. tumours), with consideration given to their metabolism, excretion, and toxicity to various organs.

Zebrafish provide a rapidly-developing vertebrate model for observation of drug toxicity over a short time period.[1] The similarities between zebrafish and human genomes has been studied in great depth.[2, 3] Despite clear physiological difference between zebrafish and humans, almost three-quarters of human genes have at least one orthologue in zebrafish.[4] Though some prominent human genes (such as *BRCA1*) do not have a direct zebrafish orthologue, zebrafish often possess genes which encode functionally similar proteins (e.g. *BARD1*).[4]

Many small molecules show conserved biological activities in zebrafish and humans,[5] and studies suggest that zebrafish assays can be used successfully and reliably to predict drug toxicity in humans.[6] Cardio-, hepato- and nephrotoxicity have been shown to correlate closely between zebrafish, preclinical mammalian models (rodents) and humans, owing to genetic similarities and common biochemical pathways.[7, 8] Both

toxicological endpoints (LC_{50}) and mechanisms of toxicity may be readily studied *in vivo*, by both qualitative and quantitative assessments.[9] As well as toxicology assays, zebrafish have been used to observe the teratogenic effects of small molecules,[10] as hosts for cancer cell xenografts[11] as well as primary human fibroblasts,[12] and both cancer mutant and transgenic oncogene lines have been investigated.[13] Interestingly, novel cell cycle inhibitors have been identified in zebrafish, which were not detected in mammalian cell experiments.[14] Another study comparing MCF7 human breast cancer cells and zebrafish successfully identified compounds which activated *P53* in zebrafish, which was shown to translate to human cells *in vitro*.[15]

Primary cell lines are frequently used in drug development as a measure of drug selectivity for target cells (e.g. cancer) over normal proliferating cells.[16-18] However, the life-span of non-immortalised cells is finite, and most enter senescence within 5-10 passages. In contrast, the zebrafish model offers a high-throughput and cost-effective *in vivo* solution to acute toxicity testing of novel pharmaceuticals.[19, 20] Zebrafish are also transparent, allowing for visualisation of many phenotypes in real-time using light microscopy.[19, 21] Furthermore, zebrafish share developmental phenotypes with mammalian species, which is particularly important when studying the embryonic organism.[22]

The study of organometallic compounds (particularly ruthenium complexes) *in vivo* using the zebrafish embryo acute toxicity test has attracted interest over recent years, likely due to the ease of embryo handling, breeding and drug administration. Ruthenium(II) N-heterocyclic carbene (NHC) anti-cancer complexes were found to impart only low toxicity in zebrafish embryos,[23] while ruthenium(II) bipyridine complexes showed a wide range of zebrafish toxicities (9-170 mg L^{-1}) along with high selectivity for cancer cells over MRC5 fibroblasts.[24] A phosphorescent Ru(II) complex

(designed for imaging cell nuclei) exhibited low toxicity in zebrafish, and only slightly inhibited growth of human breast cancer cells (MDA-MB-231) and epidermal (HaCaT) cells.[25]

More recently, complexes of iridium have also been studied using zebrafish. Making use of the transparent properties of the embryos, phosphorescent iridium(III)-ethylenediamine complexes have been visualised in fish.[26] Other chemo-sensing iridium(III) complexes have been used to track zinc(II) ions[27] and hypochlorous acid[28] *in vivo*. Photoactivatable iridium(III)-PEG complexes showed the absence of toxicity in the dark, and their potential for *in vivo* imaging.[29]

However, organometallic studies are not limited to ruthenium and iridium complexes. In fact, copper complexes of alkyl substituted-malonic acids with higher hydrophobicity (determined by octanol-water partition coefficients) were found to delay embryo hatching relative to those with lower hydrophobicity.[30] Toxicities of antimicrobial Au(III)[31] and Ag(I)[32] complexes have been evaluated in MRC5 cells and zebrafish, however no clear trend was identified in either case between mammalian and fish models. Induction of apoptosis in cancer cells by the platinum anti-cancer drug cisplatin is known to occur in human cancer cells,[33] and has also been observed in zebrafish using immuno-staining methods.[34] Cisplatin was also found to cause hair cell loss in lateral line neuromasts of zebrafish, which correlated with Pt accumulation.[35] In summary, the comprehensive use of the zebrafish embryo acute toxicity test to investigate potential organometallic compounds *in vivo* demonstrates the clear advantages the organism presents to identify potential lead compounds.

For the purposes of this work, zebrafish embryos were explored as a tool for investigating drug toxicity in a healthy model organism. To the best of my knowledge,

this is the first example of toxicity and mechanistic studies of osmium(II) complexes in zebrafish (Os complexes **2**-**8**, and **18**-**23**; Table 6.1). The findings are compared to structurally similar iridium complexes, first explored in Chapter 4 (Ir complexes **12**-**14**, see Chapter 4, section 4.3.1; and Table 6.1), and current platinum drugs, cisplatin and carboplatin. In this chapter, trends are identified between *in vitro* human cell culture experiments and current *in vivo* zebrafish research.

	arene	R^1
2	*p*-cymene	4-tolyl
3	*p*-cymene	methyl
4	*p*-cymene	4-nitrophenyl
5	*p*-cymene	4-fluorophenyl
6	*p*-cymene	phenyl
7	biphenyl	4-tolyl
8	*m*-terphenyl	4-tolyl
12	Cp*	4-tolyl
13	Cp^{xPh}	4-tolyl
14	Cp^{xBip}	4-tolyl
18	*p*-cymene	SRB [a]

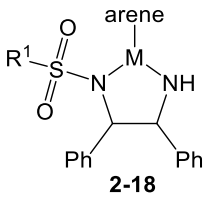

2-18

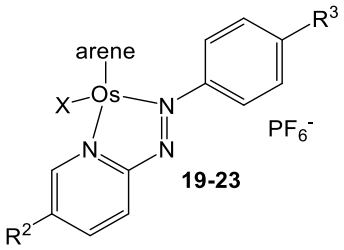

19-23

	R^1 (arene)	R^2	R^3	X
19	*p*-cymene	H	NMe_2	Cl
20	*p*-cymene	H	NMe_2	I
21	biphenyl	H	NMe_2	Cl
22	biphenyl	H	NMe_2	I
23	biphenyl	H	OH	I

Table 6.1: Os complexes **2**-**8** and Ir complexes **12**-**14** were described previously (sections 3.3.1 and 4.3.1). Chapter 6 introduces fluorescent complex **18** [Os(*p*-cymene)(SRB-DPEN)] and Os azopyridine complexes **19**-**23**.[36-38] [a] SRB = 2-(3-diethylamino-6-diethylazaniumylidene-xanthen-9-yl)-5-sulfo-benzenesulfonyl.

6.2 Experimental

6.2.1 Materials

Os complexes **2-8** were introduced in Chapter 3 (section 3.3.1, page 79). Ir complexes **12-14** and corresponding antiproliferative activities (IC_{50}) were described in Chapter 4 (sections 4.3.1 and 4.3.3, respectively). Osmium complexes **19-23** were kindly synthesised by Dr. Russell Needham (University of Warwick, UK). L-Ascorbic acid (≥99%), c*is*-diaminedichloroplatinum(II) (CDDP, cisplatin, ≥99%), carboplatin (≥99%), DMSO (> 99%, molecular biology grade), tricaine (98%, ethyl 3-aminobenzoate methanesulfonate) and thiourea (≥99%) were purchased from Sigma Aldrich and used as received. Ultrapure grade nitric acid (72% v/v) was freshly distilled before use. Hanks Balanced Salt Solutions (without phenol red), 0.05% trypsin/EDTA. ROS/superoxide detection kit was purchased from Enzo Life Sciences (UK). Three strains (AB, Singapore and TU) of wild-type zebrafish (*Danio rerio*) were maintained in reverse-osmosis water supplemented with Aquavitro salt (pH 7.5; hereon described as "egg water"). Powder food (GEMMA micro) was purchased from Skretting, and live food (*Artemia salina*) from ZM Fish Food.

Tricaine solution was prepared using 4 mg mL^{-1} tricaine powder: 400 mg (1.53 mmol) ethyl 3-aminobenzoate methanesulfonate in 97.9 mL doubly-deionised water with *ca*. 2.1 mL 1M Tris (pH 9) to adjust pH = 7. The solution was stored at 277 K and used within one month of preparation.[39] For embryo euthanisation, the tricaine stock solution was used directly. For anesthetisation, the stock solution was diluted 1:24 to achieve a final working concentration of 0.17 mg mL^{-1}.

6.2.2 Synthesis of rhodamine-tagged ligand L18 and osmium complex 18

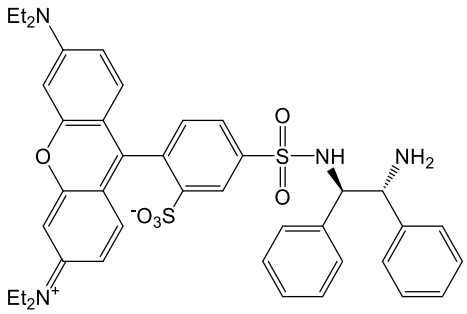

Ligand L18 (SrbDPEN)

2-(3-diethylamino-6-diethylazaniumylidene-xanthen-9-yl)-5-(*N*-(2-amino-1,2-diphenyl-ethyl)sulfonoyl)-benzenesulfonate (Ligand L18). (1*R*,2*R*)-1,2-diphenylethylenediamine (112 mg, 0.58 mmol) and triethylamine (117 mg, 160 µL, 1.16 mmol) were dissolved in dichloromethane (2 ml) at 273 K. Sulforhodamine B acid chloride (400 mg, 0.69 mmol) in dichloromethane (2 ml) was added dropwise over 3 h. The solution was washed with water (10 × 25 ml) and aqueous fractions extracted with dichloromethane (3 × 10 ml). Organic fractions were dried over magnesium sulphate and the solvent removed to yield a dark purple amorphous solid. (78.6 mg, 0.104 mmol, 18%). ^{1}H NMR (500 MHz, CD_3CN, 25°C, TMS): δ=8.43 (s, 1H, ArH), 7.49 (m, 1H, ArH), 7.38 (m, 1H, ArH), 6.88-7.35 (m, 14H, ArH), 6.81 (m, 2H, ArH), 4.55 (d, ^{3}J(H,H)=7.4 Hz, 1H, C*H*NH), 4.15 (d, ^{3}J(H,H)=7.4 Hz, 1H, C*H*NH), 3.58-3.73 (m, 8H, CH_2), 1.24-1.33 (m, 12H, CH_3); ^{13}C NMR (125 MHz, CD_3CN, 25°C, TMS) δ 158.8, 158.2, 156.0, 148.4, 143.0, 142.6, 139.6, 133.5, 133.4, 130.0, 128.6, 128.5, 128.3, 128.2, 127.8, 127.6, 127.5, 127.4, 127.4, 127.3, 127.0, 126.8, 113.6, 95.9, 65.1, 61.2, 60.2, 59.8, 50.0, 12.2; UV/Vis: λ_{max} 557, 399, 353, 307, 281, 258 nm; HRMS (*m/z*): $[M+H]^+$ calcd. for $C_{41}H_{45}N_4O_6S_2$, 753.2775; found, 753.2769; analysis: (calcd. for $C_{41}H_{44}N_4O_6S_2$, found): C (65.40, 65.05), H (5.89, 6.04), N (7.44, 7.62).

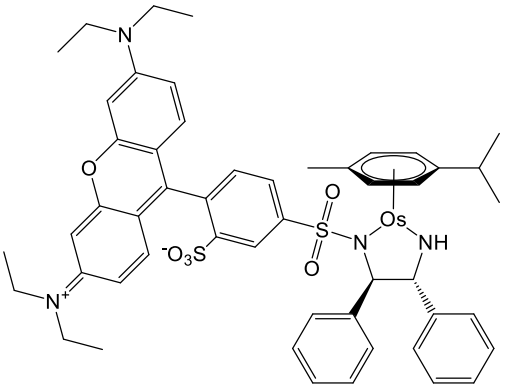

(*R*,*R*)-18

[Os(η^6-*p*-cymene)(SrbDPEN)] (18). This complex was synthesised following the method described for **2**,[40] using osmium *p*-cymene dimer [Os(η^6-biphenyl)Cl$_2$]$_2$ (15.7 mg, 0.02 mmol) and ligand **L18** (1*R*,2*R*)-SrbDPEN (30 mg, 0.04 mmol). The organic layer was washed with water and concentrated *in vacuo* to yield a purple oil, which was precipitated as a dark purple solid by addition of *n*-pentane. (13 mg, 0.012 mmol, 61%). ^{1}H NMR (500 MHz, CD$_3$CN, 25°C, TMS): δ=6.70-8.64 (m, 19H, ArH), 6.14 (d, ^3J(H,H)=5.5 Hz, 1H, Os-ArH), 6.03 (d, ^3J(H,H)=5.5 Hz, 1H, Os-ArH), 5.90 (m, 2H, Os-ArH), 4.40 (s, 1H, C*H*NTs), 3.96 (d, ^3J(H,H)=4.4 Hz, 1H, C*H*NH), 3.55-3.74 (m, 8H, CH$_2$), 2.90 (sept, ^3J(H,H)=7.0 Hz, 1H, C*H*(CH$_3$)$_2$), 2.31 (s, 3H, CH$_3$), 1.25-1.35 (m, 12H, CH$_3$), 1.23 (d, ^3J(H,H)=7.0 Hz, 6H, CH(C*H*$_3$)$_2$); ^{13}C NMR (125 MHz, CD$_3$CN, 25°C, TMS) δ 159.7, 158.2, 156.0, 133.9, 133.7, 133.5, 129.5, 129.3, 128.9, 128.6, 128.5, 128.4, 128.3, 128.2, 128.0, 127.9, 127.7, 127.5, 127.2, 126.9, 126.7, 126.6, 126.1, 113.6, 113.5, 113.4, 95.8, 91.6, 83.6, 81.0, 77.0, 74.1, 73.1, 69.7, 71.2, 68.2, 63.8, 63.2, 58.7, 58.5, 46.0, 45.9, 33.9, 33.0, 31.2, 23.8, 23.3, 23.2, 20.6, 18.6, 12.3; UV/Vis: λ_{max} 555, 398, 352, 281, 258 nm; HRMS (*m/z*): [M+H]$^+$ calcd. for $C_{51}H_{57}N_4O_6OsS_2$, 1077.3329; found, 1077.3337.

6.2.3 *In vivo* studies and husbandry of zebrafish (*Danio rerio*)

Experiments were carried out using three strains of wild-type zebrafish embryos (AB, Singapore and Tubingen) in collaboration with Dr. Karuna Sampath (Warwick Medical School) under project AWERB.10/16-17. Warwick University are members of the Institute of Animal Technology and the Laboratory Animal Science Association. Zebrafish were maintained in accordance with ASPA 1986 by Mr. Ian Bagley, using 3.5 L tanks (checked daily for water quality) in a 14 h light cycle, and provided with food (live and powder) four times a day during the week and twice a day during weekends. Fish were mated in breeding tanks fitted with a divider. Two mating pairs were used per breeding tank, and the divider was removed at dawn.

6.2.4 Acute toxicity assessment in zebrafish (*Danio rerio*)

Twenty-four-well plates were prepared with solutions of test compounds (20 wells per plate per concentration using 1 ml per well, 4 negative control wells per plate, Figure 6.1). DMSO did not exceed 1% v/v. Plates were seeded using at least one (and a maximum of 3) embryos per well, and incubated at 301.5 K for 96 h. Mortality was assessed by (a) embryo coagulation, (b) somite formation, (c) tail detachment, (d) heartbeat.[41] Dose-response curves were obtained by plotting % survival against the logarithm of the drug concentration, and were fitted using Origin 9.1 for Windows. LC_{50} values were determined from two independent experiments and standard deviations calculated.

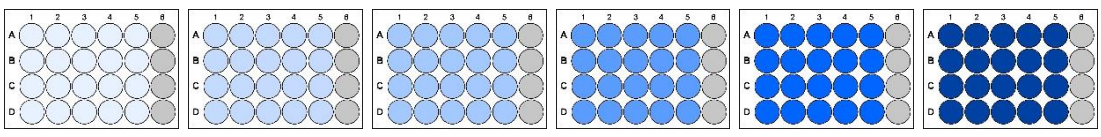

Figure 6.1. Typical 24-well plate experiment for LC_{50} determination of a compound in zebrafish (*Danio rerio*). Six concentrations (**low** to **high**, 0.01-100 μM) with four **untreated** controls per plate.

6.2.5 Fluorescence imaging in zebrafish (*Danio rerio*)[39]

This method was adapted from an existing literature procedure.[39, 42] Approximately 10-20 zebrafish embryos were seeded in a P100 petri dish containing *ca*. 30 mL of either complex **1**, **18** or **20** (at concentrations equal to either 1× or 2× LC_{50}) for 96 h at 301.5 K. Untreated embryos were also incubated for 96 h for use as either negative or positive control samples.

Low-melting point agarose was prepared (1% w/v) using HBSS, and tricaine was diluted to anaesthetising concentrations (0.2 mg mL^{-1}) using egg water. After drug exposure, embryos were collected and washed with HBSS three times to remove the metal complex. Additionally, 20 untreated embryos were exposed to rotenone (positive control: 50 μM, 2 min) then washed three times with HBSS to remove the rotenone.[42] Embryos were then stained using an ROS Detection Kit (Enzo Life Sciences) using 500 μL of stain solution in the dark for 20 min (20 μM ROS reagent). Embryos were washed three times using HBSS to remove the stain, then anaesthetised using tricaine (0.2 mg mL^{-1}) for 5-10 min at 298 K.

Approximately three viable anesthetised embryos were transferred individually to a glass-bottom slide and mounted laterally using *ca*. 200 μL of 1% agarose, which was covered with approximately 200 μL egg water. Embryos were analysed by confocal microscopy using a LSM880 confocal microscope (Argon laser; excitation: 458, 488, 561 nm; green emission for ROS: 493-550 nm; red emission for complex **18**: 568-750 nm). Data were obtained and processed using Zen 2.3 for Windows.

6.3 Results

6.3.1 Acute toxicity in zebrafish embryos (LC_{50})

The *in vivo* toxicity (LC_{50}, μM) of Os and Ir complexes (sections 3.3.1 and 4.3.1), cisplatin, carboplatin and previously reported highly potent Os azopyridine complexes[37, 38] were evaluated using zebrafish embryos. Three wild-type strains (SG, AB and TU) were studied to evaluate continuity between wild-type strains. The zebrafish embryo acute toxicity test is a live/dead assay, reliant on four observable parameters: (a) embryo coagulation, (b) lack of somite formation, (c) tail detachment, (d) lack of heartbeat. If any one of the four observations are made, the fish is recorded as dead. Viable embryos are required to not exhibit any of the four aforementioned developmental phenotypes.

Cisplatin was found to exhibit the highest toxicity (LC_{50} 0.6 ± 0.2 μM) of all compounds investigated (Figure 6.2), whilst carboplatin was found to have *ca*. ten-fold less toxicity (LC_{50} 5.7 ± 0.9 μM) than cisplatin. The toxicity of Os compounds was not significantly affected by variation of the sulfonamide substituent (Table 6.1) in compounds **3**-**6** relative to complex **2**. Arene extension in both Os (**2**, **7**-**8**) and Ir complexes **(12**-**14**) increased toxicity (LC_{50} Os: 2.4, 2.2, 0.7 μM; Ir: 1.8, 1.6, 0.71 μM, respectively). Ir complexes were found to exhibit higher toxicities than structurally-similar Os analogues (Ir-Cp^{xPh} > Os-biphenyl). Interestingly, Os azopyridine complexes **19**-**23** showed remarkably low toxicities (LC_{50} 6.6-24.3 μM) compared to both Os / Ir sulfonamides (LC_{50} 0.7-3.5 μM) and Pt agents (LC_{50} 0.6-5.7 μM). Furthermore, all trends in toxicity between series of compounds were found to be conserved in all three wild-type zebrafish strains investigated.

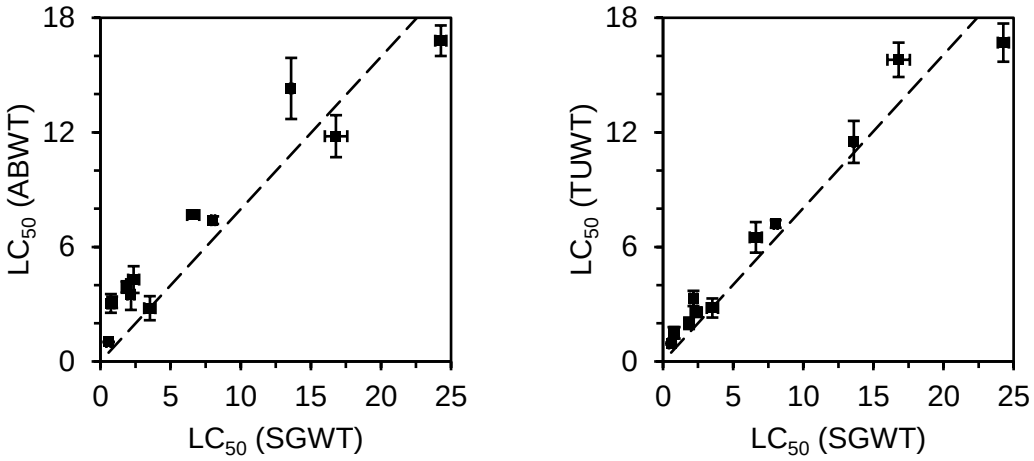

				LC_{50} / μM		
	Metal	Arene	Ligand	SG-WT	AB-WT	TU-WT
2	Os	*p*-cym	TsDPEN	2.4 ± 0.4	4.3 ± 0.7	2.6 ± 0.3
3	Os	*p*-cym	MsDPEN	3.5 ± 0.4	2.8 ± 0.6	2.8 ± 0.5
4	Os	*p*-cym	NsDPEN	1.9 ± 0.3	3.9 ± 0.3	2.2 ± 0.3
5	Os	*p*-cym	FbDPEN	0.7 ± 0.2	3.0 ± 0.5	1.5 ± 0.3
6	Os	*p*-cym	BsDPEN	0.8 ± 0.2	3.1 ± 0.3	1.5 ± 0.3
7	Os	biphenyl	TsDPEN	2.2 ± 0.2	3.5 ± 0.8	3.3 ± 0.4
8	Os	*m*-terphenyl	TsDPEN	0.7 ± 0.2	N.D.[d]	N.D.[d]
12	Ir	Cp*	TsDPEN	1.8 ± 0.1	6.4 ± 0.3	6.5 ± 0.6
13	Ir	Cp^{xPh}	TsDPEN	1.6 ± 0.3	5.5 ± 0.7	1.9 ± 0.3
14	Ir	Cp^{xBip}	TsDPEN	0.71 ± 0.07	3.8 ± 0.1	1.3 ± 0.2
18	Os	*p*-cym	SrbDPEN	2.2 ± 0.1	4.0 ± 0.1	3.1 ± 0.1
19	Os	*p*-cym	AzPy-NMe_2	13.61 ± 0.09	14 ± 2	12 ± 1
20	Os	*p*-cym	AzPy-NMe_2	24.3 ± 0.4	16.8 ± 0.8	17 ± 1
21	Os	biphenyl	AzPy-NMe_2	16.8 ± 0.8	12 ± 1	15.8 ± 0.9
22	Os	biphenyl	AzPy-NMe_2	6.6 ± 0.4	7.7 ± 0.1	6.5 ± 0.8
23	Os	biphenyl	AzPy-OH	8.0 ± 0.1	7.4 ± 0.2	7.2 ± 0.2
CDDP	Pt	-	-	0.6 ± 0.2	1.02 ± 0.03	0.94 ± 0.05
CBP	Pt	-	-	5.7 ± 0.9	10 ± 1	7.1 ± 0.7

Figure 6.2. LC_{50} concentrations (μM) determined for Os / Ir sulfonamide complexes (Chapters 3 and 4), and previously reported Os azopyridine complexes[37, 38] in three wild-type (WT) zebrafish embryo stains: SG (Singapore), AB and TU. (96 h exposure, with no recovery time in drug-free solution). All trends in toxicity are conserved in all three embryonic strains investigated. CDDP = cisplatin; CBP = carboplatin. $R^2 = 0.81$ (SG-WT / AB-WT). $R^2 = 0.94$ (SG-WT / TU-WT). N.D. = not determined.

6.3.2 ROS induction in whole-mount zebrafish

Chapter 4 demonstrated that the generation of reactive oxygen species (ROS) generation likely contributes to the *in vitro* mechanism of action of sulfonamide complexes in cancer cells (section 4.3.7, page 139). In this Chapter, a method to visualise *in vivo* ROS generation in zebrafish was adapted and optimised in collaboration with Mrs Hannah Bridgewater, based on an adapted literature procedure.[39] Zebrafish embryos were treated with a known zebrafish ROS-inducer (rotenone, 96 hpf embryos exposed to 50 μM for 2 min), after which time, embryos (treated and untreated) were stained using the ROS Detection Kit (Enzo Life Sciences). Comparison between rotenone-treated and untreated embryos (which exhibit low fluorescence due to basal signalling levels of ROS) confirmed the efficacy of the dye for ROS detection in anesthetised whole-mount embryos.

To explore ROS production by Os complexes *in vivo*, newly fertilised embryos were treated with equipotent concentrations of Os sulfonamide complex **2** or Os azopyridine complex **20** (1× or 2× LC_{50} concentration) for 96 hours to replicate experiments for LC_{50} determination. Both complex **2** and **20** induced the generation of ROS in whole-mount zebrafish embryos. In both cases, the generation of reactive oxygen species appears to be proportional to the concentration of drug administered (Figure 6.3), however those treated with sulfonamide complex **2** exhibit tightly localised ROS (likely to be the swim bladder) whereas ROS in samples treated with azopyridine complex **20** display broader ROS production throughout the organism. Furthermore, levels of *in vivo* ROS appear to be greater in embryos treated with sulfonamide complex **2**, compared to azopyridine complex **20**, based on evidence from confocal microscopy.

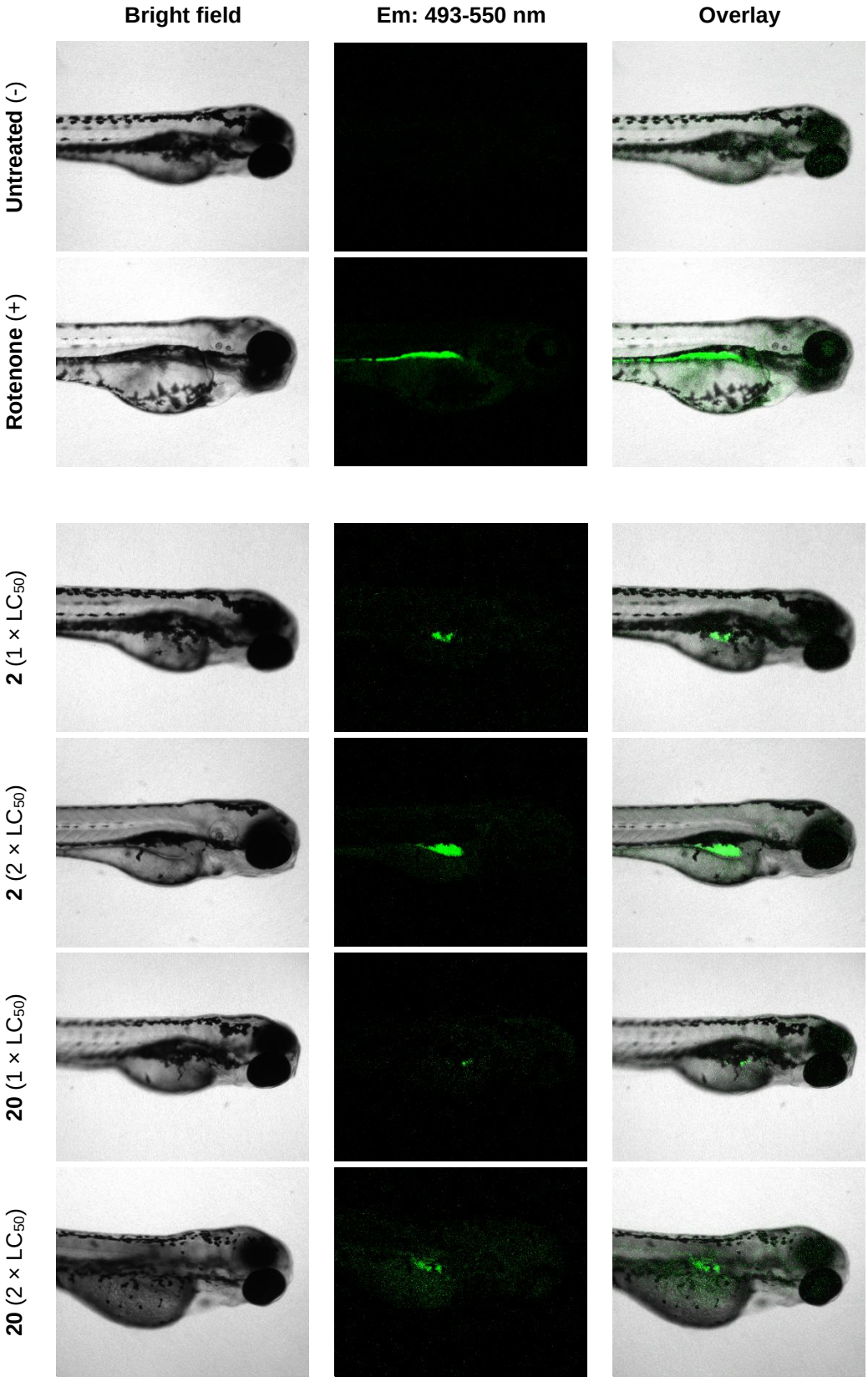

Figure 6.3. Whole-mount SG-WT zebrafish treated with Os complex **2** or **20** for 96 h (1 or 2× LC_{50}), stained using ROS detection kit (Enzo life science). Data acquired using a Zeiss LSM880 confocal microscope. Fluorescence for ROS (**green**) shown superimposed onto transmitted light images. Excitation: 458, 488 nm; Emission: 493-550 nm. Rotenone (positive control; 50 μM, 2 min).

6.3.3 Synthesis and biological properties of a fluorescent osmium complex

To confirm that the location of *in vivo* ROS correlated with the distribution of the complex inside the zebrafish, a red-fluorescent derivative of complex **2** was designed. Previous ligand substitutions at the sulfonamide did not significantly impact either the catalytic (Chapter 3, section 3.3.5, page 88) or biological (Chapter 4, section 4.3.4, page 125) properties. Substitution of the tosyl moiety for a sulforhodamine (SRB) group, which is known to be highly fluorescent,[43] was readily achieved using the same synthetic procedure described in Chapter 3 (section 3.3.1, page 79) for other sulfonamide ligands studied in this thesis. Addition of the corresponding sulfonyl chloride to a solution of an enantio-pure diamine in basic solution afforded the highly fluorescent ligand **L18**, which was reacted with Os *p*-cymene dimer to obtain **18** [Os(*p*-cymene)(SrbDPEN)] as a purple solid (Figure 6.4).

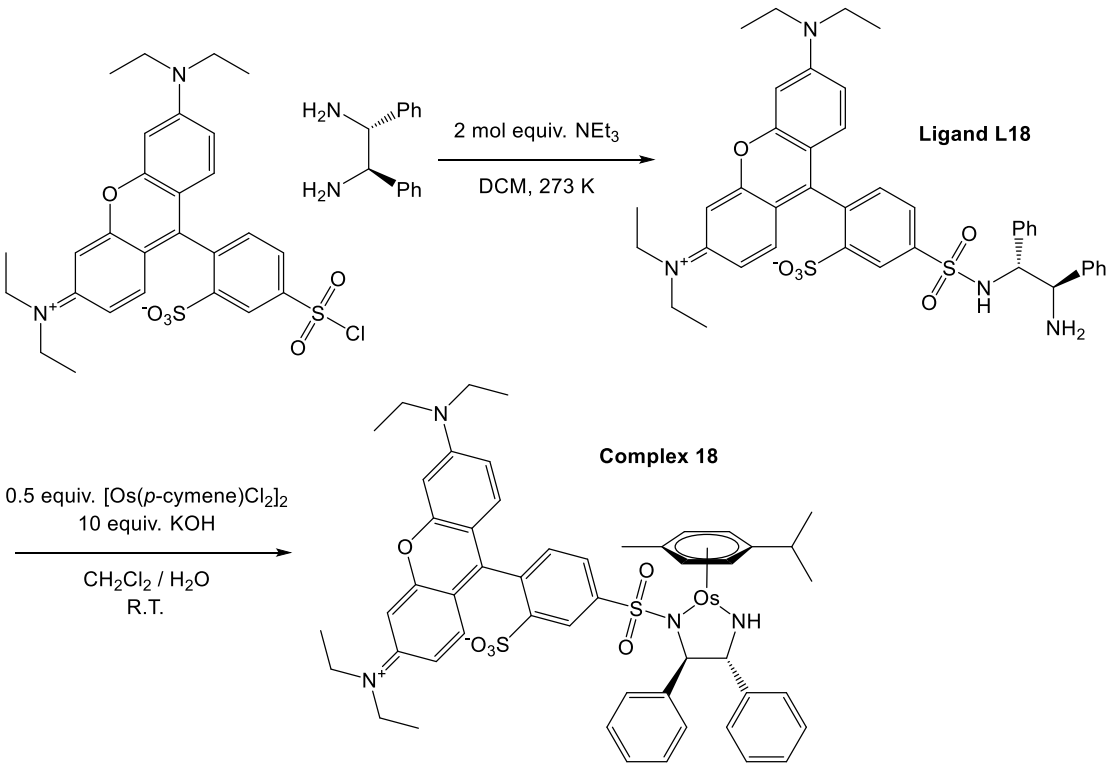

Figure 6.4. Two-step synthesis using sulforhodamine acid chloride and diphenylethylenediamine (forming intermediate **L18**) which was reacted with Os *p*-cymene chlorido dimer to obtain **18**.

The ^{1}H-NMR spectrum of complex **18** in d^{6}-DMSO was acquired after 24 incubation at 310 K, and no change was observed. Complex **18** was also studied in aqueous solution (95% PBS / 5% DMSO) by UV-visible spectroscopy for 24 h (spectra acquired at 1 h intervals) and no change in the spectrum was observed. These data suggest that **18** remains highly stable in both DMSO and in aqueous solution, similarly to findings using complex **2** (Chapter 3, section 3.3.4, page 86), from which **18** is derived.

Os(II) sulfonamide complex **18** was characterised using 3D fluorescence mapping. Complex **18** exhibited an optimal excitation at 560 nm, with red light emission at 580 nm (Figure 6.5). Unlike many metal complexes,[44] fluorescence of ligand **L18** (Ex / Em = 560 / 580 nm) was not quenched upon coordination to the osmium metal centre. Complex **18** was found to be highly fluorescent in both organic solvents (dichloromethane and acetonitrile) but importantly also retained fluorescence in phosphate-buffered saline solution.

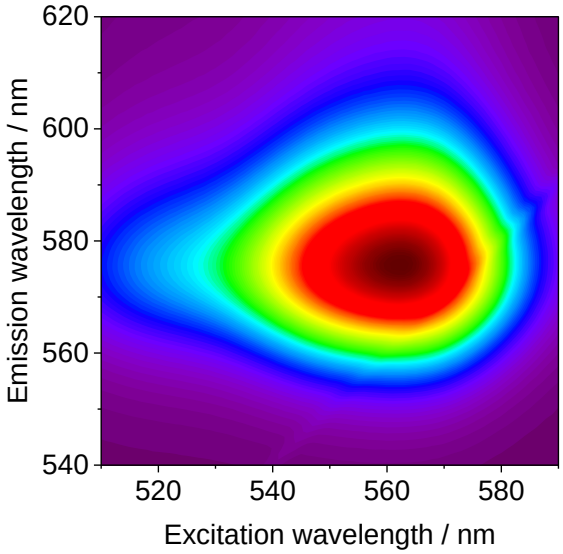

Figure 6.5. Representative three-dimensional (peak excitation / emission) fluorescence spectra for complex **18** (~0.01 mM) in acetonitrile acquired using a Jasco FP-6500 Fluorimeter. Ex / Em = 560 / 580 nm. Ligand **L18** retains fluorescence upon coordination to osmium.

To evaluate the impact of rhodamine substitution, the antiproliferative activity of complex **18** was assessed towards A2780 cancer cells (Figure 6.6). Interestingly, the complex displayed highly similar antiproliferative activity (18 ± 3 μM) as parent tosyl compound **2** [Os(*p*-cymene)(TsDPEN)] in A2780 cancer cells (15.5 ± 0.5 μM).

Zebrafish embryos allow the facile study of highly coloured or fluorescent compounds *in vivo* due to the transparency of the zebrafish in the early stages of development, before pigment formation. Complex **18** was observed to retain fluorescence in aqueous media and therefore studies were continued in the animal model. The LC_{50} of osmium SRB complex **18** (2.2 ± 0.1 μM) was found to be similar to that of parent osmium tosyl complex **2** (2.4 ± 0.4 μM), suggesting that the rhodamine substituent, while sterically demanding and highly lipophilic, did not significantly affect the acute toxicity of **18** compared to **2** (Figure 6.6).

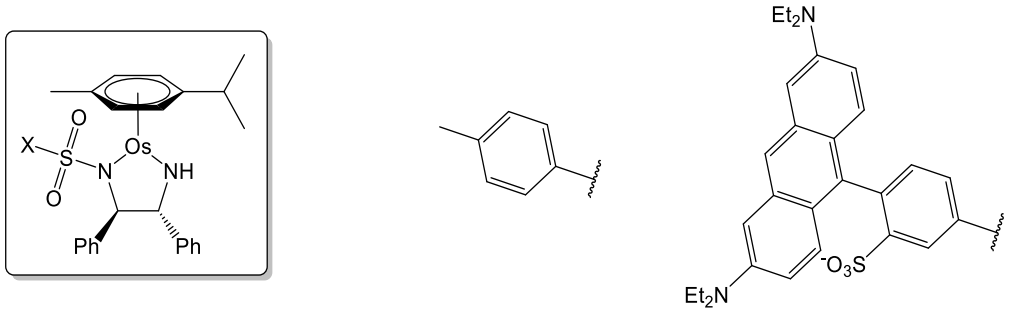

X = 4-tolyl **X = SRB**

	X	A2780 cells IC_{50} / μM	SG-WT zebrafish LC_{50} / μM
2	4-tolyl	15.5 ± 0.5	2.4 ± 0.4
18	SRB	18 ± 3	2.2 ± 0.1

Figure 6.6. Comparison between the antiproliferative activity (IC_{50} / μM) of **2** and **18** in A2780 cancer cells (24 h drug exposure, 72 h recovery time in drug-free medium) and acute toxicity (LC_{50} / μM) in Singapore wild-type (SG-WT) zebrafish embryos. Modification of the sulfonamide group does not significantly impact the biological properties.

Investigation of *in vivo* ROS generation by complex **18** was carried out as previously described for studies with complex **2**. The difference between the emission wavelengths of fluorescence for **18** and the ROS dye allowed for dual imaging of reactive oxygen species (green) and the fluorescent osmium complex (red). By superimposing green and red fluorescence, the merged image (co-localisation in yellow) shows high similarity in the position of metal complex and ROS localisation (Figure 6.7). Reactive oxygen species were confined to a small area, likely to be the swim bladder, as was also found for embryos treated with complex **2** (Figure 6.3).

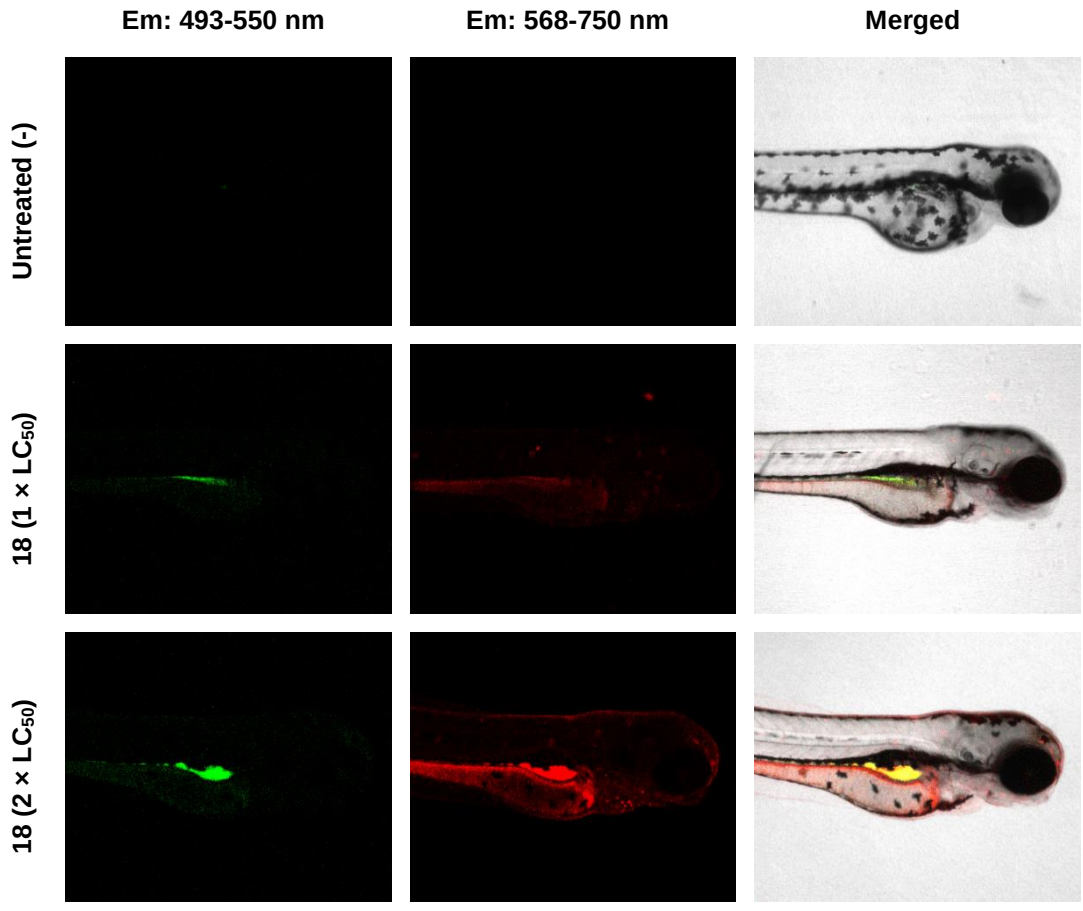

Figure 6.7. Dual-colour confocal microscopy of Singapore wild-type zebrafish treated with **18** (96 h drug exposure, 1 or 2× LC_{50} concentration) and stained using ROS detection kit (Enzo life sciences). Data acquired using a Zeiss LSM880 confocal microscope. Fluorescence for ROS (**green**) and complex **18** (**red**) shown superimposed onto transmitted light images; co-localisation shown in overlay (**yellow**). Excitation: 458, 488, 561 nm; Green emission: 493-550 nm; Red emission: 568-750 nm.

6.4 Discussion

6.4.1 Acute aquatic toxicity of osmium complexes

All Os and Ir complexes investigated were found to be less toxic than the well-established platinum anticancer complex, cisplatin. Clinical studies in humans have previously demonstrated the lower toxicity of carboplatin, compared to cisplatin,[45] which was also observed in zebrafish (5.7 μM compared to 0.6 μM, respectively). While no significant trends in toxicity were observed upon substitution on the sulfonamide, arene extension was found to increase toxicity (**2** < **7** < **8**), in agreement with higher antiproliferative activities observed for arene-extended complexes in Chapter 4 (15.5 μM, 6.5 μM and 4.4 μM against A2780 cancer cells, respectively). Toxicity trends (arene extension, Os complexes less toxic than Ir complexes) were maintained in all three wild-type strains investigated, showing that no given phenotype presents significantly advantageous properties when compared to the other wild-type strains. For this reason, further studies were pursued using only Singapore (SG) wild-type embryos.

Os complexes typically exhibited less toxicity than their Ir counterparts, but were more active against cancer cells (Chapter 4, section 4.3.4, page 125), which may encourage future development of novel Os therapies. While previously reported Ru(II) arene complexes bearing *N*,*O*-bidentate ligands have been found to be less toxic under the same experimental conditions (LC_{50} = 20.0 ± 1.8 μM) whilst achieving similar antiproliferative activities against A2780 cancer cells (IC_{50} = 13 ± 1 μM) compared to Os complex **2** (LC_{50} = 2.4 ± 0.4 μM; IC_{50} = 15.5 ± 0.5 μM), the Ru complex was not shown to act catalytically (e.g. to carry out the oxidation of NADH). Therefore, though more toxic than the Ru-arene complex, the catalytic nature of Os complex **2** may facilitate dose minimisation, circumventing potential toxicity to the host organism.

While Os-azopyridine complexes are known to be highly potent towards cancer cells, achieving nanomolar potencies,[36-38] the acute toxicities of **19**-**23** were generally an order of magnitude less than those of Os-sulfonamide complexes. In agreement with the low acute aquatic toxicity against zebrafish embryos, complex **20** has previously been shown to delay the growth of colorectal cancer xenografts in mice, with negligible toxicity to the host.[46] Comparison of the sulfonamide and azopyridine series demonstrates that the *N*,*N*-chelating ligand is crucial not only to **20** achieving potent antiproliferative activity towards mammalian cancer cells, but also to the low aquatic toxicity, upon comparison to **2** (Figure 6.2).

6.4.2 *In vivo* generation of reactive oxygen species

Detection of reactive oxygen species *in vivo* using the ROS detection kit (Enzo Life Sciences) was validated using a known ROS inducer, rotenone (inhibitor of complex I in mitochondria). The positive control experiment showed even distribution of ROS over the entire organism, suggesting that the dye was able to permeate the embryo and was evenly dispersed in the zebrafish. The ROS dye detects a range of reactive species, including hydroxyl radicals, peroxynitrite, and hydrogen peroxide.

Internalisation of the osmium complex was confirmed by administering a highly fluorescent derivative of complex **2**; complex **18**. Complex **18** is red-fluorescent, and was readily prepared using Sulforhodamine B acid chloride in combination with diphenylethylenediamine in the presence of a base (TEA), as previously described for the synthesis of structurally similar ligands in Chapter 3 (section 3.2.2, page 61). The intense fluorescence in water allows for the dual-imaging of red-fluorescence from the Os complex, and the green ROS probe. The internalisation of **18** was readily observed

(Figure 6.7) and the localisation appeared to coincide with the generation of ROS *in vivo*. Structurally similar phosphorescent iridium(III) diamine complexes have also been used in zebrafish,[26] however this work appears to be the first example of a fluorescent osmium(II) complex studied using zebrafish.

Interestingly, the generation of ROS by **2** [Os(*p*-cymene)(TsDPEN)] was greater than that generated by osmium azopyridine complex **20** [Os(*p*-cymene)(4-(2-pyridylazo)-*N*,*N*-dimethylaniline)I]PF_6, despite the administered dose of **2** being an order of magnitude less than that administered of **20** (LC_{50} concentration administered: 2.4 μM compared to 24.3 μM, respectively). This observation may be rationalised by the structure and properties of the complexes. Osmium sulfonamide complex **2** is a transfer hydrogenation catalyst, and both oxidises NADH to NAD^+ (Chapter 4, section 4.3.2, page 122) and reduces pyruvate to lactate when co-administered with a hydride source (Chapter 5, section 5.3.4, page 185). Conversely, the generation of ROS *in vitro* by azopyridine complex **20** is not catalytic.[36] It is likely that the generation of ROS by **2** *in vivo* is catalytic, which may involve the oxidation of NADH to NAD^+ (by hydride transfer from NADH to the catalyst; described in section 4.3.2, page 122), which has previously been linked to the generation of reactive oxygen species in cells.[47, 48] The catalytic nature of the sulfonamide complexes would allow lower doses to be administered in order to achieve the same effect (to achieve the same level of ROS). These data suggest that the zebrafish are a useful tool for translating mechanistic experiments from *in vitro* to *in vivo*. Live whole-organism imaging make zebrafish particularly suited to such an application, providing further mechanistic evidence for new compounds.

6.5 Conclusions

While Ir(III) complexes have been previously studied in zebrafish,[27-29] to the best of my knowledge, this work presents the first example of toxicity studies using osmium(II) complexes in zebrafish. While toxicities of Os sulfonamide complexes did not significantly differ despite sulfonamide substitution, Os azopyridine complexes displayed low toxicities in zebrafish, in contrast to their potency towards human cancer cell lines.[36] This chapter highlights the importance of the *N*,*N*-chelating ligand, which appears crucial to the aquatic toxicity of osmium(II) and iridium(III) complexes. Furthermore, Os complexes are shown to accumulate in zebrafish, using fluorescent Os complex **18**, imaged using confocal microscopy. Complex **18** was further utilised to generate ROS in zebrafish, allowing for the dual imaging of the red-fluorescent complex and green ROS-detection probe.

The ease of throughput, handling and drug administration make the zebrafish a useful experimental tool for toxicity screening of lead compounds. It is envisaged that the methods established in this Chapter: (i) determination of the acute aquatic toxicities, and (ii) detection of ROS in treated embryos; may be readily adopted to become a common experimental step as part of future metallodrug development, before considering translation to mammalian models (e.g. rodents).

Additionally, future research may employ genetic manipulation techniques (e.g. CRISPR) to develop transgenic zebrafish strains to study to the mechanism of organometallic complexes in greater depth *in vivo*. Such work may include knocking-out genes which have been associated with the antiproliferative activity *in vitro* (for example, *P21* and *P53*) in order to examine whether experimental observations translate to an *in vivo* model.

6.6 References

1. S. Zhao, J. Huang and J. Ye, *J. Exp. Clin. Canc. Res.*, 2015, **34**, 80.
2. G. J. Lieschke and P. D. Currie, *Nat. Rev. Genet.*, 2007, **8**, 353-367.
3. W. B. Barbazuk, I. Korf, C. Kadavi, J. Heyen, S. Tate, E. Wun, J. A. Bedell, J. D. McPherson and S. L. Johnson, *Genome Res.*, 2000, **10**, 1351-1358.
4. K. Howe, M. D. Clark, C. F. Torroja, J. Torrance, C. Berthelot, M. Muffato, J. E. Collins, S. Humphray, K. McLaren, L. Matthews, S. McLaren, I. Sealy, M. Caccamo, C. Churcher, C. Scott, J. C. Barrett, R. Koch, G.-J. Rauch, S. White, W. Chow, B. Kilian, L. T. Quintais, J. A. Guerra-Assuncao, Y. Zhou, Y. Gu, J. Yen, J.-H. Vogel, T. Eyre, S. Redmond, R. Banerjee, J. Chi, B. Fu, E. Langley, S. F. Maguire, G. K. Laird, D. Lloyd, E. Kenyon, S. Donaldson, H. Sehra, J. Almeida-King, J. Loveland, S. Trevanion, M. Jones, M. Quail, D. Willey, A. Hunt, J. Burton, S. Sims, K. McLay, B. Plumb, J. Davis, C. Clee, K. Oliver, R. Clark, C. Riddle, D. Eliott, G. Threadgold, G. Harden, D. Ware, B. Mortimer, G. Kerry, P. Heath, B. Phillimore, A. Tracey, N. Corby, M. Dunn, C. Johnson, J. Wood, S. Clark, S. Pelan, G. Griffiths, M. Smith, R. Glithero, P. Howden, N. Barker, C. Stevens, J. Harley, K. Holt, G. Panagiotidis, J. Lovell, H. Beasley, C. Henderson, D. Gordon, K. Auger, D. Wright, J. Collins, C. Raisen, L. Dyer, K. Leung, L. Robertson, K. Ambridge, D. Leongamornlert, S. McGuire, R. Gilderthorp, C. Griffiths, D. Manthravadi, S. Nichol, G. Barker, S. Whitehead, M. Kay, J. Brown, C. Murnane, E. Gray, M. Humphries, N. Sycamore, D. Barker, D. Saunders, J. Wallis, A. Babbage, S. Hammond, M. Mashreghi-Mohammadi, L. Barr, S. Martin, P. Wray, A. Ellington, N. Matthews, M. Ellwood, R. Woodmansey,

G. Clark, J. Cooper, A. Tromans, D. Grafham, C. Skuce, R. Pandian, R. Andrews, E. Harrison, A. Kimberley, J. Garnett, N. Fosker, R. Hall, P. Garner, D. Kelly, C. Bird, S. Palmer, I. Gehring, A. Berger, C. M. Dooley, Z. Ersan-Urun, C. Eser, H. Geiger, M. Geisler, L. Karotki, A. Kirn, J. Konantz, M. Konantz, M. Oberlander, S. Rudolph-Geiger, M. Teucke, K. Osoegawa, B. Zhu, A. Rapp, S. Widaa, C. Langford, F. Yang, N. P. Carter, J. Harrow, Z. Ning, J. Herrero, S. M. J. Searle, A. Enright, R. Geisler, R. H. A. Plasterk, C. Lee, M. Westerfield, P. J. de Jong, L. I. Zon, J. H. Postlethwait, C. Nusslein-Volhard, T. J. P. Hubbard, H. R. Crollius, J. Rogers and D. L. Stemple, *Nature*, 2013, **496**, 498-503.

5. A. J. Rennekamp and R. T. Peterson, *Curr. Opin. Chem. Biol.*, 2015, **24**, 58-70.
6. P. M. Eimon and A. L. Rubinstein, *Expert Opin. Drug Metab. Toxicol.*, 2009, **5**, 393-401.
7. C. A. MacRae and R. T. Peterson, *Nat. Rev. Drug Discov.*, 2015, **14**, 721-731.
8. J.-W. Lu, Y. Hsia, H.-C. Tu, Y.-C. Hsiao, W.-Y. Yang, H.-D. Wang and C.-H. Yuh, *Birth Defects Res. C Embryo Today*, 2011, **93**, 157-172.
9. A. J. Hill, H. Teraoka, W. Heideman and R. E. Peterson, *Toxicol. Sci.*, 2005, **86**, 6-19.
10. J. B. Veselinović, G. M. Kocić, A. Pavic, J. Nikodinovic-Runic, L. Senerovic, G. M. Nikolić and A. M. Veselinović, *Chem. Biol. Interact.*, 2015, **231**, 10-17.
11. C. Zhao, X. Wang, Y. Zhao, Z. Li, S. Lin, Y. Wei and H. Yang, *PLOS ONE*, 2011, **6**, e21768.

12. A. O. Benyumov, P. Hergert, J. Herrera, M. Peterson, C. Henke and P. B. Bitterman, *Zebrafish*, 2012, **9**, 38-43.

13. G. Gao, L. Chen and C. Huang, *Curr. Mol. Pharmacol.*, 2014, **7**, 44-51.

14. R. D. Murphey, H. M. Stern, C. T. Straub and L. I. Zon, *Chem. Biol. Drug. Des.*, 2006, **68**, 213-219.

15. Y. Li, W. Huang, S. Huang, J. Du and C. Huang, *Biochem. Biophys. Res. Commun.*, 2012, **422**, 85-90.

16. T. Bhowmik, P. P. Saha, A. Sarkar and A. Gomes, *Chem. Biol. Interact.*, 2017, **261**, 35-49.

17. W. Gamal, P. Treskes, K. Samuel, G. J. Sullivan, R. Siller, V. Srsen, K. Morgan, A. Bryans, A. Kozlowska, A. Koulovasilopoulos, I. Underwood, S. Smith, J. del-Pozo, S. Moss, A. I. Thompson, N. C. Henderson, P. C. Hayes, J. N. Plevris, P.-O. Bagnaninchi and L. J. Nelson, *Sci. Rep.*, 2017, **7**, 37541.

18. N. L. Ignjatović, K. M. Penov-Gaši, V. M. Wu, J. J. Ajduković, V. V. Kojić, D. Vasiljević-Radović, M. Kuzmanović, V. Uskoković and D. P. Uskoković, *Colloids Surf., B*, 2016, **148**, 629-639.

19. T. V. Bowman and L. I. Zon, *ACS Chem. Biol.*, 2010, **5**, 159-161.

20. J. L. Tan and L. I. Zon, in *Methods in Cell Biology*, eds. M. W. H. William Detrich and I. Z. Leonard, Academic Press, 2011, vol. Volume 105, pp. 491-516.

21. C. Chiranjib, H. Chi Hsin, W. Zhi Hong, L. Chang Shing and A. Govindasamy, *Curr. Drug Metab.*, 2009, **10**, 116-124.

22. N. S. Sipes, S. Padilla and T. B. Knudsen, *Birth Defects Res. C Embryo Today*, 2011, **93**, 256-267.

23. J. M. Alfaro, A. Prades, M. del Carmen Ramos, E. Peris, J. Ripoll-Gómez, M. Poyatos and J. S. Burgos, *Zebrafish*, 2010, **7**, 13-21.

24. O. A. Lenis-Rojas, A. R. Fernandes, C. Roma-Rodrigues, P. V. Baptista, F. Marques, D. Perez-Fernandez, J. Guerra-Varela, L. Sanchez, D. Vazquez-Garcia, M. L. Torres, A. Fernandez and J. J. Fernandez, *Dalton Trans.*, 2016, **45**, 19127-19140.

25. Z.-P. Zeng, Q. Wu, F.-Y. Sun, K.-D. Zheng and W.-J. Mei, *Inorg. Chem.*, 2016, **55**, 5710-5718.

26. T. S.-M. Tang, K.-K. Leung, M.-W. Louie, H.-W. Liu, S. H. Cheng and K. K.-W. Lo, *Dalton Trans.*, 2015, **44**, 4945-4956.

27. D.-L. Ma, H.-Z. He, H.-J. Zhong, S. Lin, D. S.-H. Chan, L. Wang, S. M.-Y. Lee, C.-H. Leung and C.-Y. Wong, *ACS Appl. Mater. Interfaces*, 2014, **6**, 14008-14015.

28. F. Zhang, X. Liang, W. Zhang, Y.-L. Wang, H. Wang, Y. H. Mohammed, B. Song, R. Zhang and J. Yuan, *Biosens. and Bioelectron.*, 2017, **87**, 1005-1011.

29. S. P.-Y. Li, C. T.-S. Lau, M.-W. Louie, Y.-W. Lam, S. H. Cheng and K. K.-W. Lo, *Biomaterials*, 2013, **34**, 7519-7532.

30. F. B. Palmer, C. A. Butler, M. H. Timperley and C. W. Evans, *Environ. Toxicol. Chem.*, 1998, **17**, 1538-1545.

31. B. D. Glisic, N. D. Savic, B. Warzajtis, L. Djokic, T. Ilic-Tomic, M. Antic, S. Radenkovic, J. Nikodinovic-Runic, U. Rychlewska and M. I. Djuran, *Med. Chem. Commun.*, 2016, **7**, 1356-1366.

32. N. D. Savic, B. D. Glisic, H. Wadepohl, A. Pavic, L. Senerovic, J. Nikodinovic-Runic and M. I. Djuran, *Med. Chem. Commun.*, 2016, **7**, 282-291.

33. Z. H. Siddik, *Oncogene*, 2003, **22**, 7265-7279.

34. H. J. De Jesus, J. Podratz, T. M. Greenwood, S. C. Ekker and A. J. Windebank, *FASEB J.*, 2011, **25**, 943-947.

35. H. C. Ou, D. W. Raible and E. W. Rubel, *Hear. Res.*, 2007, **233**, 46-53.

36. J. M. Hearn, I. Romero-Canelón, A. F. Munro, Y. Fu, A. M. Pizarro, M. J. Garnett, U. McDermott, N. O. Carragher and P. J. Sadler, *Proc. Natl. Acad. Sci. U. S. A.*, 2015, **112**, 3800-3805.

37. Y. Fu, A. Habtemariam, A. M. Pizarro, S. H. van Rijt, D. J. Healey, P. A. Cooper, S. D. Shnyder, G. J. Clarkson and P. J. Sadler, *J. Med. Chem.*, 2010, **53**, 8192-8196.

38. Y. Fu, M. J. Romero, A. Habtemariam, M. E. Snowden, L. Song, G. J. Clarkson, B. Qamar, A. M. Pizarro, P. R. Unwin and P. J. Sadler, *Chem. Sci.*, 2012, **3**, 2485-2494.

39. A. Rissone and F. Candotti, *Bio-protocol*, 2016, **6**, 1941.

40. J. P. C. Coverdale, C. Sanchez-Cano, G. J. Clarkson, R. Soni, M. Wills and P. J. Sadler, *Chem. Eur. J.*, 2015, **21**, 8043-8046.

41. OECD, *Test No. 236: Fish Embryo Acute Toxicity (FET) Test*, OECD Publishing, Paris, 2013.

42. V. Mugoni, A. Camporeale and M. M. Santoro, *J. Vis. Exp.*, 2014, **89**, 51328.

43. V. Vichai and K. Kirtikara, *Nat. Protocols*, 2006, **1**, 1112-1116.

44. in *Principles of Fluorescence Spectroscopy*, ed. J. R. Lakowicz, Springer US, Boston, MA, 2006, DOI: 10.1007/978-0-387-46312-4_8, pp. 277-330.

45. S. R. McWhinney, R. M. Goldberg and H. L. McLeod, *Mol. Cancer Ther.*, 2009, **8**, 10-16.

46. S. D. Shnyder, Y. Fu, A. Habtemariam, S. H. van Rijt, P. A. Cooper, P. M. Loadman and P. J. Sadler, *Med. Chem. Commun.*, 2011, **2**, 666-668.

47. Michael P. Murphy, *Biochem. J.*, 2009, **417**, 1-13.

48. L. Kussmaul and J. Hirst, *Proc. Natl. Acad. Sci. U. S. A.*, 2006, **103**, 7607-7612.

Chapter 7

Conclusions and future work

7. Conclusions and future work

7.1 Conclusions

Catalytic pharmaceuticals would allow for dose-minimisation, with a view to decreasing the number of off-target effects in the patient, as well as reducing the cost of medication. Catalysts that are activated by co-administration of a second compound (such is the case for transfer hydrogenation catalysts, which require a hydride source) may gain additional selectivity for diseased cells over healthy cells through dual-targeting methods. This thesis focusses on the potential medicinal applications of chiral half-sandwich osmium catalysts. While Sadler *et al.* have previously reported a series of similar osmium complexes that generate reactive oxygen species in cancer cells, the mechanism was not catalytic.[1] In fact, few other examples of osmium bioorthogonal catalysts exist. In this work, novel osmium(II) 16-electron complexes of the general formula [Os(arene)(diamine)] have been described. They are structurally-related to a non-chiral Ru(II) complex which was previously explored as a catalytic metallodrug. By co-administration of the Ru(II) complex with sodium formate, the NAD^+/NADH ratio was catalytically modulated in cancer cells.[2] Here, new Os(II) catalysts are shown, in an analogous way, to carry out asymmetric transfer hydrogenation reactions in cancer cells as a new strategy for selectively targeting cancer cells.

In Chapter 3, a series of novel osmium(II) 16-electron complexes, analogous to the well-established ruthenium(II) Noyori active catalyst, were synthesised and fully characterised. The complexes were found to be highly stable in atmospheric air, and in aqueous solution.[3] Additional methoxy-substituted derivatives were synthesised

with the aim of increasing the water solubility (which was investigated further in later chapters). The transfer hydrogenation of acetophenone-derived ketones was readily catalysed by the osmium complexes using formic acid as a hydride source, achieving high conversions and enantioselectivities (>99%).[3] The synthesis proceeded via a novel di-chlorido intermediate complex, which was also found to be active for transfer hydrogenation catalysis.[3] Importantly, the turnover frequency (TOF) for acetophenone reduction by Os(II) catalysis was significantly higher than that achieved by the analogous Ru(II) catalyst under identical conditions (63.9 h^{-1} and 23 h^{-1}, respectively). The nature of the η^6-arene was found to considerably modulate the rate of catalysis. Substituting *p*-cymene (**2**) for biphenyl (**7**) increased the catalytic rate from 63.9 h^{-1} to 78 h^{-1}, whereas *m*-terphenyl substitution caused rate reduction (43 h^{-1}), likely due to steric hindrance in the transition state. In contrast, variation of the sulfonamide substituent of the diamine in complexes **3**-**6** [Os(*p*-cymene)(diamine)] did not enhance the rate of catalysis, which was confirmed by the similarity between the calculated electrostatic potential surfaces using DFT, as charge effects were localised only at the site of substitution. Osmium is a third-row transition metal, and its ligand exchange kinetics are typically slower than second-row ruthenium, perhaps accounting for the lack of development of osmium catalysts. These data, however, suggest that osmium(II) catalysts may provide a useful alternative to ruthenium(II) complexes.[3]

Chapter 4 explored the biological properties of the arene osmium(II) complexes in cancer cells. For comparison between metal centres, a series of Cp* iridium(III) sulfonamide complexes were synthesised by the similar method as described for the osmium complexes in Chapter 3, and were readily isolated as dark purple solids which were fully characterised using NMR, mass spectrometry, UV-visible spectroscopy and elemental analysis. Antiproliferative activities (half-maximal inhibitory

concentration, IC_{50}) towards a series of human cancer cell lines were determined for both Os(II) and Ir(III) complexes. It was found that the lipophilicity of the complexes (determined by the octanol / water partition coefficient, Log P) correlated well with antiproliferative activities, and that osmium(II) complexes were typically more potent than their iridium counterparts. Antiproliferative activities ranged from moderate to good (IC_{50} 4-30 μM), however none of the catalysts were highly potent (i.e. nanomolar potency) when administered to cells alone, which may be advantageous for the development of catalytic therapies (Chapter 5). Osmium complexes showed better selectivity for cancerous ovarian cells over healthy ovarian fibroblasts, while the selectivity of iridium was much lower. However, iridium complexes did not display evidence of cross-resistance when antiproliferative activities were evaluated in cisplatin-resistant A2780cis cancer cells. Cellular accumulation of osmium / iridium in cancer cells exposed to equipotent concentrations of the complexes were determined in all cell lines using 1 × IC_{50} concentration and 24 h exposure. The cellular accumulation in A2780 cells did not correlate with either drug lipophilicity or antiproliferative activity. However when the accumulation of complex **2** [Os(*p*-cymene)(TsDPEN)] or **12** [Ir(Cp*)(TsDPEN)] was examined across a range of cell lines, a clear trend between antiproliferative activity and metal accumulation was observed; higher antiproliferative activities (lower IC_{50} concentrations) were determined for cells in which a greater amount of drug (metal) accumulated.

Representative compounds from each series (Os complex **2** and Ir complex **12**) were further investigated for the time, temperature and concentration dependence of cell accumulation, as well as cellular compartmentalisation. The accumulation profiles for **2** [Os(*p*-cymene)(TsDPEN)] and **12** [Ir(Cp*)(TsDPEN)] significantly differed, with rapid accumulation and efflux of the iridium complex compared to the osmium

counterpart, for which detoxification from the cell was significantly more gradual. The compartmentalisation of metal in the cell was also different, with a greater amount of osmium from complex **2** localising in the membrane / particulate fraction, compared to iridium from complex **12** which mainly located in the cytoplasmic fraction.

Reactive oxygen species (ROS) are known to be produced in cells by Os and Ir complexes,[1, 4, 5] and so the induction of oxidative stress was assessed in cells treated with **2** [Os(*p*-cymene)(TsDPEN)] or **12** [Ir(Cp*)(TsDPEN)], which both produced a large burst of ROS after drug exposure, which remained prevalent in cells even after 72 h recovery in drug-free medium. Furthermore, the tripeptide glutathione (GSH) is an important antioxidant in cells, and co-administration of osmium complex **2** with a non-toxic concentration of a glutathione synthetase inhibitor (L-BSO) was found to enhance the potency of the compound. Overall, Chapter 4 highlights that the role of the metal centre is not purely structural. Rather, the biological properties of the complexes may be greatly altered by exchange of osmium for iridium (and *p*-cymene for Cp* to still obtain neutral complexes), consequently affecting the oxidation state of the metal centre.

Chapter 5 examines the potential for osmium complexes to carry out transfer hydrogenation chemistry inside cancer cells. By co-administration of a non-toxic concentration of sodium formate (as an alternative hydride source to formic acid) cell proliferation was decreased catalytically with respect to both formate and the osmium catalyst. The effects were found to be more prominent in A2780 ovarian cancer cells than in healthy HOF (fibroblast) and MRC5 (lung) cells, enhancing the selectivity of the complexes for cancerous cells. *N*-formyl-methionine was explored as an alternative hydrogen source, and formate precursor, for use in cells that over-express for deformylase enzyme, thereby selectively generating formate *in situ* in cancer cells.

Most importantly, it was shown that both aqueous and *in cell* reductions proceeded with high enantioselectivity (83% *ee*). This was demonstrated for the reduction of pyruvate (a key metabolic intermediate) to D-lactate, which is normally only present at very low concentrations in eukaryotic cells.[6] The catalytic rate (TOF) was found to be highly dependent on the concentration of formate, using a model aqueous system which was studied using time-dependent ^{1}H-NMR. Mechanistic studies showed that the complex caused G_1 cell cycle arrest but did not induce apoptosis which, in combination, has previously been associated with metabolic interference.[7] Furthermore, the cell membrane viability was not affected by treatment of cancer cells with the complex (nor by the complex in combination with sodium formate). Chiral recognition between biological components (enzymes, substrates, DNA helical chirality) are crucial to cellular proliferation and therefore the manipulation of enantiomeric ratios of important molecules (such as lactate) in the cell are anticipated to play a vital role in the development of future catalytically-targeting therapies.

In Chapter 6, *in vivo* experiments were undertaken using the zebrafish (*Danio rerio*) model. Osmium and iridium sulfonamide catalysts from previous chapters were compared to highly potent osmium azopyridine drug candidates and existing platinum-based drugs, cisplatin and carboplatin. This work presents the first example of osmium complexes investigated using the zebrafish model. While the sulfonamide complexes showed a broad activity range against A2780 cancer cell proliferation (IC_{50} 4-30 μM), the toxicity range in zebrafish was particularly narrow (LC_{50} 0.7-3.5 μM), though all complexes investigated were found to be either equally or less toxic than cisplatin (LC_{50} 0.7 μM). Interestingly, while osmium(II) azopyridine complexes are highly potent towards human cancer cells *in vitro*,[4] they displayed negligible toxicity in zebrafish (notably for Os complex **20** [Os(η^6-*p*-cymene)(4-(2-pyridylazo)-*N*,*N*-

dimethylaniline)I]PF_6, LC_{50} 24.3 μM). The simple screening process allows for rapid identification of compounds which possess low toxicity and is promising for further study and development. Confocal microscopy was used to visualise the internalisation of a fluorescent derivative of complex **2**, which was synthesised using methods described in Chapter 3. The antiproliferative activity and toxicity of fluorescent complex **18** [Os(*p*-cymene)(SrbDPEN)] were not statistically different from those of **2** [Os(*p*-cymene)(TsDPEN)] (IC_{50} 18 μM, LC_{50} 2.2 μM), suggesting that the probe did not significantly affect the biological properties of the complex. Complex **18** was found to internalise in zebrafish, and appeared to concentrate in the swim bladder. Following ROS detection *in vitro* (Chapter 4), the generation of ROS *in vivo* was observed using a commercially-available green fluorescent probe for oxidative stress. Dual-colour imaging of fluorescent osmium complex **18** and the green oxidative stress probe confirmed high co-localisation of the signals, indicative of direct ROS generation by the osmium complex.

7.2 Future work

The work in this thesis describes the progress achieved in osmium-catalysed asymmetric transfer hydrogenation reactions, including those carried out inside living cells. 16-electron osmium complexes [Os(η^6-arene)(diamine)] are highly stable and reductions proceed with high enantioselectivity, yet the complexes are very poorly water soluble, and the pharmacokinetics, pharmacodynamics and further *in vivo* studies are still to be explored.

7.2.1 Increasing the water-solubility of sulfonamide catalysts

In Chapter 4, substitution of methoxy-groups onto the phenyl backbone of the sulfonamide ligand greatly improved the hydrophilicity of the Os and Ir sulfonamide series (lower octanol / water partition coefficients). Introduction of additional polar substituents may further increase the water solubility of the complexes. Surface-active ruthenium(II) and rhodium(III) sulfonamide catalysts have been reported which were found to form micelles in aqueous solution, achieved by functionalization with trialkyl ammonium side groups.[8] Imidazolium-functionalised TsDPEN catalysts of rhodium have been shown to achieve up to 98% *ee* for the transfer hydrogenation of various ketones in water, using sodium formate as a hydride source (Figure 7.1).[9]

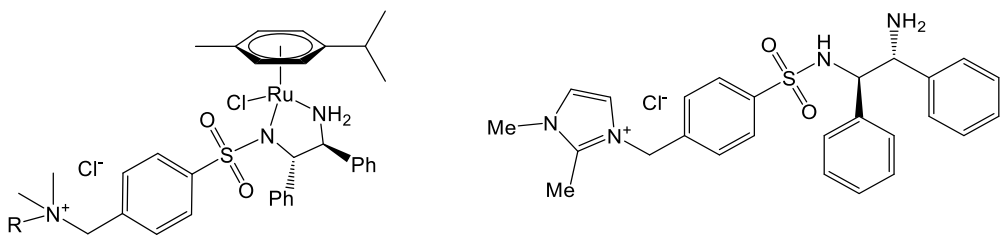

Surface-active Ru(II) catalysts[8] **Imidazolium-functionalised ligand[9]**

Figure 7.1. Surface-active Ru(II) catalysts (Peruzzini *et al.*)[8] and imidazolium-tethered catalysts (Ni *et al.*)[9] have been developed to increase the water solubility of transfer hydrogenation catalysts.

7.2.2 Enhancement of anti-cancer efficacy and *in cell* catalysis

The circadian rhythm, and other rhythmic cycles, have been shown to be important for the time-dependent efficacy and toxicity of drugs.[10] Particularly, the liver has been shown to possess its own regulatory clock, and the disruption of which has been shown to modulate the rate of xenobiotic detoxification in mice.[11] Future *in vivo* investigation of osmium and iridium sulfonamide complexes, and indeed other anti-cancer metal complexes, may greatly benefit from such an approach to further reduce off-target effects and lower toxicity. Similarly, studies of the time-dependence of in cell catalytic reductions may prove advantageous to improve potency. For example, by administering the hydride source at a given time-period before exposure to the catalyst (e.g. treatment with formate 24 h prior to drug introduction), the intracellular formate concentration may be increased, subsequently increasing the rate of catalysis.

Combination therapy is a well-known strategy to improve drug efficacy and potency. In Chapter 5, complex **2** [Os(*p*-cymene)(TsDPEN)] was shown to catalyse the conversion of pyruvate to lactate with high enantioselectivity inside cells by co-administration of the Os catalyst with a hydride source. This approach may be further enhanced as part of a combination therapy with an inhibitor of lactate transport. AZD3965 is a novel inhibitor of the monocarboxylate transporter protein MCT1, which acts by blocking lactate transport, and is currently undergoing clinical trials for the treatment of solid cancers.[12] A multi-drug combination therapy of Os catalyst **2**, a source of hydride and AZD3965 would be expected to increase the lactate concentration by way of Os(II)-catalysed transfer hydrogenation of pyruvate, raising the intracellular concentration beyond the tolerance threshold, leading to cell death. Since Os(II)-catalysed ATH in cells was shown to be selective for cancer cells over healthy cells, this approach may also increase the efficacy of AZD3965.

7.2.3 Sulfonamide ligand modification

The apparent inert site of substitution on the sulfonamide ligand was identified in Chapters 3 and 4, whereby catalytic activities and antiproliferative activities towards cancer cells were relatively unchanged, compared to parent osmium complex **2** [Os(*p*-cymene)(TsDPEN)]. A modification was utilised in Chapter 6 to track a fluorescent-derivative of **2** bearing a sulforhodamine-based fluorophore in transparent zebrafish embryos. Further work could be carried out to explore additional functionalization at this position, including the introduction of an atom (such as bromine) that is readily detected by ICP-MS, or synchrotron x-ray fluorescence spectroscopy,[13] to observe the co-localisation of the osmium metal centre and the ligand (Figure 7.2).

The site of substitution could also be explored for conjugation of the sulfonamide complex to existing pharmaceuticals (similarly to Ferroquine, and osmium-derivatives of Tamoxifen)[14-16] or to polymeric supports for either increased solubility, drug delivery[17] or for the development of heterogeneous asymmetric reduction systems (which have been extensively studied for ruthenium(II) Noyori-type catalysts).[18-20]

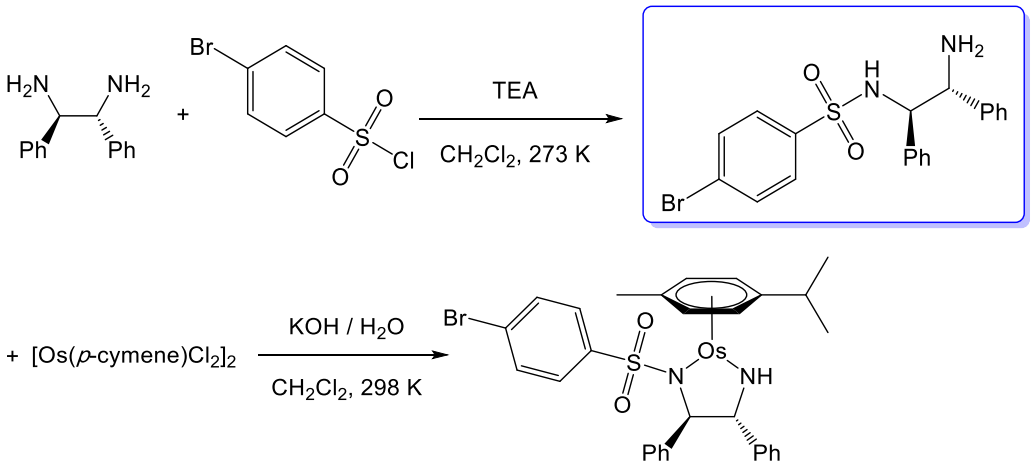

Figure 7.2. Functionalisation of the sulfonamide ligand (•) by substitution of a hydrogen atom by bromine would facilitate dual tracking of Os and Br in the final complex by ICP-MS.

7.2.4 Further utilisation of the zebrafish (*Danio rerio*) model

In vitro and *in vivo* screening assays provide complementary approaches to examining large chemical libraries which, in combination, provide a robust method of identifying lead compounds,[21] and zebrafish in particular facilitate high-throughput, low-cost *in vivo* testing. In this thesis, acute toxicities were determined for Os(II), Ir(III) and Pt(II) complexes. While this work focussed on early-stage embryo toxicity, future work may investigate toxicity in adult zebrafish, with a view to develop a better understanding of the efficacy of lead compounds before undertaking further *in vivo* studies.

Chapter 6 investigated the *in vivo* generation of reactive oxygen species (ROS), after previously observing their generation *in vitro* in cells treated with Os(II) complexes. Future work using zebrafish may examine whether other mechanistic observations from *in vitro* cell culture studies also translate to the animal model. This may include the activity-dependence of Os(II) complexes on key genes such as *P21* and *P53* using zebrafish with knockout-mutation(s). In fact, the wild-type zebrafish *p53* protein is 48% identical to human *p*53, and is highly expressed in the early developmental stages of zebrafish growth (< 48 hours post-fertilisation).[22] Apoptotic cell death has also been observed in zebrafish using immuno-staining methods, and so such an experiment may be adapted to explore the *in vivo* induction of apoptosis by novel anti-cancer complexes that have been previously shown activity *in vitro*.[23] More advanced screenings have identified behavioural changes after exposure to neuro-active compounds,[24] as well as specific organ toxicities (liver, heart and kidney).[25, 26] More recently, zebrafish bearing green-fluorescent protein (GFP) have been developed to aid the prediction of organ toxicities.[27] Such an approach could be complemented by visualising both GFP and a fluorescent complex (such as **18**, described in Chapter 6).

7.2.5 Involvement of the mitochondrial electron transport chain

Osmium azopyridine complex **20** [Os(*p*-cymene)(AzPy-NMe_2)]PF_6 (investigated for acute toxicity and ROS generation in zebrafish in Chapter 6) has been previously shown to shift cellular metabolism from oxidative phosphorylation to glycolysis.[4] Complex **20** increases in the production of mitochondrial ROS, causes the up-regulation of *p21* and *p53*, and does not induce apoptosis.[4] Such mechanistic observations were similarly recorded for cells treated with Os sulfonamide complex **2** [Os(*p*-cymene)(TsDPEN)] in Chapter 4, suggesting that the two complexes may share a similar mechanism of action. Complex I of the electron transport chain (ETC) was implicated as a potential target of complex **20** in cancer cells.[4] Preliminary experiments have attempted to determine the involvement of ETC complexes in the mechanism of **2** by determining its antiproliferative activity as previously described, with co-administration of known inhibitors at a non-lethal concentrations, including: rotenone (complex I),[28] 2-thenoyltrifluoroacetone (complex II),[29] Antimycin A (complex III),[30] potassium cyanide (complex IV)[31] and CCCP (*p*-trichloromethoxy carbonyl cyanide phenyl hydrazine, a mitochondrial uncoupling agent).[32]

Preliminary data appear to show that both ETC complexes I and II are affected by exposure of cells to complex **2**. While complex I was also identified as a potential target for osmium azopyridine complex **20**,[4] complex II (succinate dehydrogenase) is redox-active, catalysing the oxidation of succinate to fumarate and concurrent reduction of ubiquinone to ubiquinol.[33] Since complex **2** was shown to carry out transfer hydrogenation reactions in cells, if **2** can catalyse succinate oxidation and/or ubiquinone reduction in a model system, such redox chemistry may be involved in its mechanism of action. In fact, complex II has been associated with the generation of ROS, and has been implicated as a potential target for future anticancer therapies.[33, 34]

7.3 References

1. Y. Fu, M. J. Romero, A. Habtemariam, M. E. Snowden, L. Song, G. J. Clarkson, B. Qamar, A. M. Pizarro, P. R. Unwin and P. J. Sadler, *Chem. Sci.*, 2012, **3**, 2485-2494.
2. J. J. Soldevila-Barreda, I. Romero-Canelón, A. Habtemariam and P. J. Sadler, *Nat. Commun.*, 2015, **6**, 6582.
3. J. P. C. Coverdale, C. Sanchez-Cano, G. J. Clarkson, R. Soni, M. Wills and P. J. Sadler, *Chem. Eur. J.*, 2015, **21**, 8043-8046.
4. J. M. Hearn, I. Romero-Canelón, A. F. Munro, Y. Fu, A. M. Pizarro, M. J. Garnett, U. McDermott, N. O. Carragher and P. J. Sadler, *Proc. Natl. Acad. Sci. USA*, 2015, **112**, E3800-E3805.
5. Z. Liu, I. Romero-Canelón, B. Qamar, J. M. Hearn, A. Habtemariam, N. P. E. Barry, A. M. Pizarro, G. J. Clarkson and P. J. Sadler, *Angew. Chem. Int. Ed. Engl.*, 2014, **53**, 3941-3946.
6. B. Ling, F. Peng, J. Alcorn, K. Lohmann, B. Bandy and G. A. Zello, *Nutr. Metab.*, 2012, **9**, 6-14.
7. L. A. Hoeferlin, N. V. Oleinik, N. I. Krupenko and S. A. Krupenko, *Genes Cancer.*, 2011, **2**, 889-899.
8. A. M. Kalsin , T. y. A. Peganova, V. V. Novikov, A. I. Zhamoytina, L. Gonsalvi and M. Peruzzini, *Chem. Eur. J.*, 2014, **20**, 846-854.
9. G. Kang, S. Lin, A. Shiwakoti and B. Ni, *Catal. Commun.*, 2014, **57**, 111-114.
10. R. Dallmann, A. Okyar and F. Lévi, *Trends Mol. Med.*, **22**, 430-445.

11. J. P. DeBruyne, D. R. Weaver and R. Dallmann, *J. Biol. Rhythms*, 2014, **29**, 277-287.

12. R. Polański, C. L. Hodgkinson, A. Fusi, D. Nonaka, L. Priest, P. Kelly, F. Trapani, P. W. Bishop, A. White, S. E. Critchlow, P. D. Smith, F. Blackhall, C. Dive and C. J. Morrow, *Clin. Cancer. Res.*, 2014, **20**, 926-937.

13. C. Sanchez-Cano, I. Romero-Canelón, Y. Yang, I. J. Hands-Portman, S. Bohic, P. Cloetens and P. J. Sadler, *Chem. Eur. J.*, 2017, **23**, 2512-2516.

14. H. Z. S. Lee, O. Buriez, F. Chau, E. Labbé, R. Ganguly, C. Amatore, G. Jaouen, A. Vessières, W. K. Leong and S. Top, *Eur. J. Inorg. Chem.*, 2015, **2015**, 4217-4226.

15. W. A. Wani, E. Jameel, U. Baig, S. Mumtazuddin and L. T. Hun, *Eur. J. Med. Chem.*, 2015, **101**, 534-551.

16. L. Delhaes, C. Biot, L. Berry, P. Delcourt, L. A. Maciejewski, D. Camus, J. S. Brocard and D. Dive, *Chem. Bio. Chem.*, 2002, **3**, 418-423.

17. E. Pérez-Herrero and A. Fernández-Medarde, *Eur. J. Pharm. Biopharm.*, 2015, **93**, 52-79.

18. Y. Li, Z. Li, F. Li, Q. Wang and F. Tao, *Org. Biomol. Chem.*, 2005, **3**, 2513-2518.

19. X. Li, W. Chen, W. Hems, F. King and J. Xiao, *Org. Lett.*, 2003, **5**, 4559-4561.

20. X. Li, X. Wu, W. Chen, F. E. Hancock, F. King and J. Xiao, *Org. Lett.*, 2004, **6**, 3321-3324.

21. K. L. Taylor, N. J. Grant, N. D. Temperley and E. E. Patton, *J. Cell Commun. Signal.*, 2010, **8**, 11.

22. N. Y. Storer and L. I. Zon, *Cold Spring Harb. Perspect. Biol.*, 2010, **2**, 1123.

23. H. J. De Jesus, J. Podratz, T. M. Greenwood, S. C. Ekker and A. J. Windebank, *FASEB J.*, 2011, **25**, 943-947.

24. J. Rihel and A. F. Schier, *Dev. Neurobiol.*, 2012, **72**, 373-385.

25. A. D. B. Vliegenthart, C. S. Tucker, J. Del Pozo and J. W. Dear, *Br. J. Clin. Pharmacol.*, 2014, **78**, 1217-1227.

26. C. A. MacRae and R. T. Peterson, *Nat. Rev. Drug Discov.*, 2015, **14**, 721-731.

27. K. L. Poon, X. Wang, S. G. P. Lee, A. S. Ng, W. H. Goh, Z. Zhao, M. Al-Haddawi, H. Wang, S. Mathavan, P. W. Ingham, C. McGinnis and T. J. Carney, *Toxicol. Sci.*, 2017, **156**, 133-148.

28. N. Li, K. Ragheb, G. Lawler, J. Sturgis, B. Rajwa, J. A. Melendez and J. P. Robinson, *J. Biol. Chem.*, 2003, **278**, 8516-8525.

29. H.-O. Byun, H. Y. Kim, J. J. Lim, Y.-H. Seo and G. Yoon, *J. Cell. Biol.*, 2008, **104**, 1747-1759.

30. N. S. Sipes, S. Padilla and T. B. Knudsen, *Birth Defects Res. C Embryo Today*, 2011, **93**, 256-267.

31. I. P. Hargreaves, A. J. Duncan, L. Wu, A. Agrawal, J. M. Land and S. J. R. Heales, *Mitochondrion*, 2007, **7**, 284-287.

32. Y.-Q. Zhang, X. Shen, X.-L. Xiao, M.-Y. Liu, S.-L. Li, J. Yan, J. Jin, J.-L. Gao, C.-L. Zhen, N. Hu, X.-Z. Zhang, Y. Tai, L.-S. Zhang, Y.-L. Bai and D.-L. Dong, *Br. J. Pharmacol.*, 2016, **173**, 3145-3158.

33. A. Bezawork-Geleta, J. Rohlena, L. Dong, K. Pacak and J. Neuzil, *Trends Biochem. Sci.*, **42**, 312-325.

34. C. L. Quinlan, A. L. Orr, I. V. Perevoshchikova, J. R. Treberg, B. A. Ackrell and M. D. Brand, *J. Biol. Chem.*, 2012, **287**, 27255-27264.

Appendix

Table A1. Fractional atomic coordinates ($\times 10^4$) for the crystallographic structure of **(*R*,*R*)-2**

Atom	x	y	z	Atom	x	y	z
Os 1	4210(2)	5956.4(2)	2857.9(2)	C 17	9333(10)	4526(7)	3934(6)
S 8	5744(2)	7762.1(1)	3559.2(9)	C 18	8782(8)	4936(6)	3345(5)
O 8A	4682(5)	8375(4)	3388(3)	C 19	7041(7)	7040(5)	2018(4)
O 8B	6978(5)	8202(4)	3523(3)	C 20	6037(8)	7443(5)	1650(4)
N 9	5748(6)	6781(4)	3104(3)	C 21	6196(9)	7803(6)	974(4)
N 12	5562(6)	5176(4)	2507(4)	C 22	7368(10)	7812(6)	670(4)
C 1	5074(9)	6600(9)	6631(5)	C 23	8393(9)	7457(7)	1041(5)
C 2	5239(8)	6890(7)	5862(4)	C 24	8210(8)	7074(6)	1703(5)
C 3	6015(8)	6358(6)	5413(5)	C 25	2633(8)	6789(6)	3353(5)
C 4	6163(8)	6607(6)	4709(4)	C 26	2624(9)	6915(5)	2615(5)
C 5	5500(7)	7408(5)	4447(4)	C 27	2638(7)	6095(5)	2151(4)
C 6	4739(8)	7951(6)	4887(5)	C 28	2590(8)	5152(6)	2447(4)
C 7	4606(9)	7671(7)	5590(5)	C 29	2661(8)	5040(6)	3179(5)
C 10	6913(7)	6550(5)	2721(4)	C 30	2688(7)	5864(5)	3649(4)
C 11	6868(7)	5434(5)	2623(4)	C 31	2783(8)	5718(7)	4436(4)
C 13	7477(7)	4912(5)	3255(4)	C 32	2656(8)	6248(6)	1357(4)
C 14	6767(8)	4461(6)	3768(5)	C 33	1327(9)	6040(15)	1079(6)
C 15	7322(8)	4047(7)	4352(5)	C 34	3634(8)	5656(6)	979(4)
C 16	8608(9)	4090(7)	4448(5)				

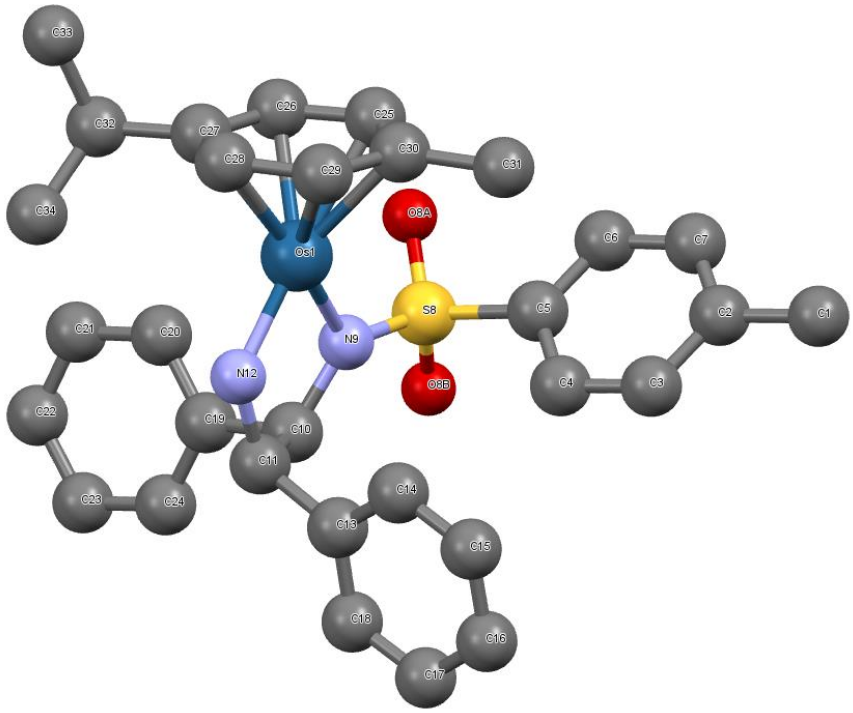

Table A2. Fractional atomic coordinates ($\times 10^4$) for the crystallographic structure of **(*R*,*R*)-7**

Atom	x	y	z	Atom	x	y	z
C 1	-2944(7)	3136(3)	1517.6(2)	C 13	3075(4)	1880(2)	3233.0(2)
C 01	6872(4)	4775(3)	5151.9(2)	C 14	3168(5)	1461(2)	2781.6(2)
Cl 1	4716(1)	4711.1(8)	5018.3(5)	C 15	2619(5)	1828(2)	2349.9(1)
Os 1	2290(1)	4905.5(7)	3644.9(5)	C 16	1951(4)	2609(2)	2369.2(1)
C 02	3059(6)	6835(3)	5707.0(2)	C 17	1869(4)	3024(2)	2818.6(1)
C 2	-2678(5)	3440(2)	2040.3(2)	C 18	511(4)	3282(2)	4497.1(1)
Cl 2	7734(2)	5663.3(7)	4900.5(4)	C 19	371(5)	2518(3)	4720.2(2)
C 3	-1812(5)	4166(2)	2127.7(2)	C 20	504(6)	2426(3)	5229.2(2)
Cl 3	7170(2)	4744.2(9)	5801.1(4)	C 21	784(5)	3099(3)	5526.1(2)
C 4	-1558(5)	4451(2)	2604.2(1)	C 22	859(5)	3864(3)	5311.0(2)
Cl 4	1398(2)	6256.8(7)	5458.5(5)	C 23	733(5)	3950(3)	4799.7(1)
C 5	-2121(4)	4002(2)	3010.3(1)	C 24	3375(4)	4893(3)	2275.0(1)
Cl 5	4406(2)	7170.0(1)	5238.0(7)	C 25	3224(5)	4724(3)	1773.6(2)
C 6	-2972(4)	3274(2)	2929.7(2)	C 26	2236(5)	5210(3)	1470.0(1)
Cl 6	2278(2)	7678.2(8)	6034.1(5)	C 27	1405(5)	5872(3)	1672.9(2)
C 7	-3239(5)	3001(3)	2448.6(2)	C 28	1552(5)	6045(3)	2173.2(2)
O 8A	-2796(3)	3906.9(2)	3949.8(9)	C 29	2533(4)	5556.8(2)	2484.3(1)
O 8B	-1918(3)	5235.5(1)	3597.4(1)	C 30	2678(4)	5742.1(2)	3024.4(1)
S 8	-1706(1)	4364.3(5)	3619.6(4)	C 31	1255(4)	6040(2)	3295.6(1)
N 9	219(3)	4159.8(2)	3736.1(1)	C 32	1340(5)	6155(3)	3816.0(1)
C 10	570(4)	3334(2)	3930.7(1)	C 33	2854(5)	5994(2)	4069.1(1)
C 11	2356(4)	3103.1(2)	3753.3(1)	C 34	4319(5)	5753(2)	3803.5(1)
N 11	3311(3)	3867.5(2)	3740.4(1)	C 35	4225(4)	5620(2)	3288.3(1)
C 12	2423(4)	2665.1(2)	3257.1(1)				

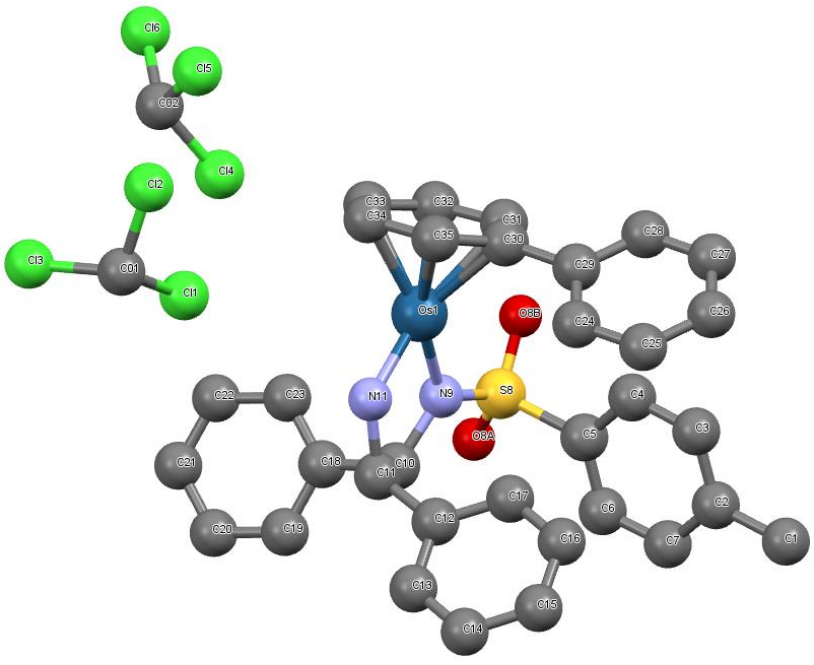

Table A3. Cartesian coordinates calculated for **(*R*,*R*)-2** at the PBE0/Lanl2DZ/6-31+G** level.

Atom	x	y	z
Os 1	-0.6332	-0.8017	-0.6446
S 2	0.6975	0.3027	2.1219
O 3	0.0166	-0.7797	2.8536
O 4	0.8776	1.5738	2.8500
N 5	0.0026	0.6088	0.6836
N 6	-0.9153	0.8162	-1.6189
C 7	6.3369	-1.6442	0.9417
H 8	6.3201	-2.5678	0.3509
H 9	6.8768	-1.8655	1.8677
H 10	6.9085	-0.9016	0.3788
C 11	4.9415	-1.1656	1.2244
C 12	4.3812	-0.1072	0.5000
H 13	4.9723	0.3883	-0.2681
C 14	3.0813	0.3226	0.7445
H 15	2.6487	1.1272	0.1584
C 16	2.3236	-0.3151	1.7240
C 17	2.8598	-1.3674	2.4638
H 18	2.2592	-1.8542	3.2297
C 19	4.1622	-1.7863	2.2082
H 20	4.5806	-2.6104	2.7861
H 21	-1.2312	0.8592	-2.5898
C 22	-0.4724	1.9729	0.4301
H 23	0.2345	2.6964	0.8500
C 24	-0.4775	2.0997	-1.1070
H 25	-1.2104	2.8743	-1.3799
C 26	0.8730	2.5477	-1.6588
C 27	1.7221	1.6819	-2.3499
H 28	1.4083	0.6540	-2.5076
C 29	2.9590	2.1224	-2.8233
H 30	3.6093	1.4307	-3.3578
C 31	3.3613	3.4391	-2.6163
H 32	4.3257	3.7841	-2.9864
C 33	2.5150	4.3163	-1.9370
H 34	2.8147	5.3513	-1.7766
C 35	1.2821	3.8729	-1.4687
H 36	0.6267	4.5715	-0.9481
C 37	-1.8447	2.2681	1.0238
C 38	-2.6245	1.2853	1.6346
H 39	-2.2325	0.2758	1.7116
C 40	-3.8819	1.5930	2.1544
H 41	-4.4757	0.8106	2.6260
C 42	-4.3753	2.8926	2.0783
H 43	-5.3555	3.1344	2.4868
C 44	-3.5970	3.8867	1.4845
H 45	-3.9647	4.9108	1.4309
C 46	-2.3440	3.5744	0.9647
H 47	-1.7448	4.3645	0.5119
C 48	0.0124	-2.7517	0.3346
H 49	0.6462	-2.8294	1.2110
C 50	-1.3758	-2.5599	0.5089
H 51	-1.7862	-2.5172	1.5142
C 52	-2.2233	-2.2730	-0.6141
C 53	-1.6507	-2.2886	-1.9254
H 54	-2.2595	-2.0415	-2.7917
C 55	-0.2475	-2.3888	-2.0802
H 56	0.1956	-2.2487	-3.0649
C 57	0.6136	-2.6025	-0.9426
C 58	2.0946	-2.7114	-1.1303
H 59	2.4408	-2.0272	-1.9094
H 60	2.3559	-3.7317	-1.4374
H 61	2.6291	-2.4810	-0.2067
C 62	-3.6990	-2.0348	-0.3836
H 63	-3.7906	-1.6612	0.6448
C 64	-4.4483	-3.3686	-0.4750
H 65	-4.3869	-3.7803	-1.4888
H 66	-5.5067	-3.2282	-0.2328
H 67	-4.0367	-4.1099	0.2174
C 68	-4.3037	-0.9870	-1.3137
H 69	-3.7256	-0.0584	-1.2773
H 70	-5.3324	-0.7698	-1.0095
H 71	-4.3390	-1.3371	-2.3514

Table A4. Cartesian coordinates calculated for **(*R*,*R*)-3** at the PBE0/Lanl2DZ/6-31+G** level.

Atom	x	y	z
Os 1	-0.6396	-0.8226	-0.2781
S 2	0.6574	0.2446	2.5389
O 3	-0.6506	-0.1115	3.0990
O 4	1.3472	1.4392	3.0244
N 5	0.5624	0.2989	0.8967
N 6	0.5256	-0.0107	-1.5620
H 7	0.5237	-0.2204	-2.5532
C 8	1.2969	1.3747	0.2292
H 9	2.2196	1.5961	0.7771
C 10	1.6521	0.8126	-1.1622
H 11	1.7488	1.6620	-1.8519
C 12	2.9809	0.0700	-1.1710
C 13	3.0700	-1.2996	-0.9162
H 14	2.1541	-1.8601	-0.7503
C 15	4.3084	-1.9370	-0.8862
H 16	4.3613	-3.0041	-0.6859
C 17	5.4762	-1.2157	-1.1182
H 18	6.4410	-1.7147	-1.0998
C 19	5.3979	0.1497	-1.3827
H 20	6.3021	0.7210	-1.5740
C 21	4.1596	0.7828	-1.4097
H 22	4.1053	1.8493	-1.6212
C 23	0.5086	2.6752	0.1213
C 24	-0.7997	2.7987	0.5865
H 25	-1.2713	1.9443	1.0620
C 26	-1.4858	4.0057	0.4641
H 27	-2.5032	4.0852	0.8382
C 28	-0.8717	5.1094	-0.1185
H 29	-1.4060	6.0510	-0.2092
C 30	0.4422	5.0019	-0.5695
H 31	0.9403	5.8614	-1.0098
C 32	1.1231	3.7959	-0.4462
H 33	2.1553	3.7296	-0.7861
C 34	-1.6969	-2.1749	1.1961
H 35	-1.3931	-2.3033	2.2284
C 36	-2.5311	-1.0805	0.8759
H 37	-2.8387	-0.4118	1.6709
C 38	-2.8040	-0.7427	-0.4880
C 39	-2.2929	-1.5961	-1.5181
H 40	-2.4477	-1.3326	-2.5580
C 41	-1.4027	-2.6490	-1.1983
H 42	-0.9142	-3.2038	-1.9927
C 43	-1.0667	-2.9332	0.1739
C 44	-0.1226	-4.0506	0.4972
H 45	0.6778	-4.1222	-0.2444
H 46	-0.6629	-5.0048	0.5028
H 47	0.3295	-3.9188	1.4829
C 48	-3.6634	0.4622	-0.7998
H 49	-3.5228	1.1612	0.0347
C 50	-5.1364	0.0399	-0.8281
H 51	-5.3230	-0.6687	-1.6428
H 52	-5.7796	0.9111	-0.9874
H 53	-5.4366	-0.4378	0.1094
C 54	-3.2646	1.1897	-2.0805
H 55	-2.1985	1.4354	-2.0746
H 56	-3.8309	2.1214	-2.1702
H 57	-3.4847	0.5930	-2.9732
C 58	1.7403	-1.1430	2.8622
H 59	1.8454	-1.2357	3.9449
H 60	1.2959	-2.0460	2.4424
H 61	2.7075	-0.9470	2.3975

Table A5. Cartesian coordinates calculated for **(*R*,*R*)-4** at the PBE0/Lanl2DZ/6-31+G** level.

Atom	x	y	z	Atom	x	y	z
Os 1	-0.8711	-0.8049	-0.6773	C 36	-4.1888	1.3267	2.2969
S 2	0.4431	0.3458	2.0815	H 37	-4.6786	0.5242	2.8422
O 3	-0.0688	-0.8608	2.7393	C 38	-4.8173	2.5598	2.1609
O 4	0.5076	1.5983	2.8338	H 39	-5.8014	2.7251	2.5900
N 5	-0.3171	0.6128	0.6571	C 40	-4.1654	3.5882	1.4836
N 6	-1.2942	0.8116	-1.6140	H 41	-4.6372	4.5621	1.3857
C 7	4.7528	-0.6040	1.0239	C 42	-2.9038	3.3735	0.9401
C 8	4.1160	0.4330	0.3501	H 43	-2.4000	4.1912	0.4274
H 9	4.6575	1.0007	-0.3971	C 44	-0.0208	-2.7072	0.2179
C 10	2.7906	0.7110	0.6545	H 45	0.6760	-2.7374	1.0473
H 11	2.2667	1.5047	0.1326	C 46	-1.4023	-2.6209	0.4975
C 12	2.1310	-0.0572	1.6128	H 47	-1.7273	-2.5961	1.5310
C 13	2.7834	-1.0873	2.2880	C 48	-2.3498	-2.3859	-0.5536
H 14	2.2418	-1.6576	3.0357	C 49	-1.8745	-2.3446	-1.9027
C 15	4.1123	-1.3686	1.9916	H 50	-2.5655	-2.1275	-2.7092
H 16	4.6568	-2.1615	2.4906	C 51	-0.4843	-2.3470	-2.1664
H 17	-1.6465	0.8531	-2.5630	H 52	-0.1266	-2.1705	-3.1757
C 18	-0.8871	1.9481	0.4434	C 53	0.4713	-2.5009	-1.0975
H 19	-0.2279	2.7029	0.8854	C 54	1.9401	-2.4938	-1.3904
C 20	-0.9129	2.1083	-1.0876	H 55	2.1785	-1.7922	-2.1941
H 21	-1.6862	2.8478	-1.3371	H 56	2.2620	-3.4931	-1.7074
C 22	0.4111	2.6274	-1.6398	H 57	2.5188	-2.2140	-0.5076
C 23	1.2443	1.8441	-2.4384	C 58	-3.8178	-2.2523	-0.2144
H 24	0.9356	0.8309	-2.6782	H 59	-3.8588	-1.8672	0.8128
C 25	2.4590	2.3443	-2.9072	C 60	-4.4709	-3.6386	-0.2352
H 26	3.0958	1.7194	-3.5280	H 61	-4.4460	-4.0659	-1.2438
C 27	2.8570	3.6374	-2.5836	H 62	-5.5185	-3.5711	0.0746
H 28	3.8038	4.0271	-2.9464	H 63	-3.9613	-4.3345	0.4381
C 29	2.0270	4.4330	-1.7946	C 64	-4.5676	-1.2648	-1.1039
H 30	2.3250	5.4461	-1.5396	H 65	-4.0593	-0.2961	-1.1258
C 31	0.8147	3.9324	-1.3338	H 66	-5.5801	-1.1126	-0.7185
H 32	0.1739	4.5631	-0.7203	H 67	-4.6677	-1.6355	-2.1305
C 33	-2.2713	2.1312	1.0544	O 68	6.6830	-0.2311	-0.1670
C 34	-2.9242	1.1146	1.7501	O 69	6.6863	-1.8141	1.3100
H 35	-2.4260	0.1593	1.8817	N 70	6.1485	-0.9055	0.6980

Table A6. Cartesian coordinates calculated for **(*R*,*R*)-5** at the PBE0/Lanl2DZ/6-31+G** level.

Atom	x	y	z	Atom	x	y	z
Os 1	-0.6540	-0.7843	-0.6626	H 35	-2.1229	0.3546	1.8677
S 2	0.7115	0.2380	2.1218	C 36	-3.7600	1.7012	2.2537
O 3	0.0200	-0.8779	2.7792	H 37	-4.3343	0.9584	2.8013
O 4	0.8909	1.4910	2.8562	C 38	-4.2570	2.9913	2.1021
N 5	0.0344	0.5768	0.6629	H 39	-5.2224	3.2611	2.5208
N 6	-0.8765	0.8563	-1.6271	C 40	-3.4964	3.9406	1.4228
C 7	4.8976	-1.2587	1.2232	H 41	-3.8640	4.9572	1.3122
C 8	4.4061	-0.1790	0.4999	C 42	-2.2585	3.5918	0.8940
H 9	5.0303	0.2991	-0.2473	H 43	-1.6680	4.3487	0.3805
C 10	3.1141	0.2636	0.7541	C 44	-0.1004	-2.7557	0.3184
H 11	2.7022	1.0948	0.1913	H 45	0.5294	-2.8456	1.1955
C 12	2.3380	-0.3848	1.7132	C 46	-1.4752	-2.4890	0.4993
C 13	2.8472	-1.4611	2.4362	H 47	-1.8639	-2.4001	1.5071
H 14	2.2233	-1.9400	3.1843	C 48	-2.3165	-2.1701	-0.6209
C 15	4.1416	-1.9094	2.1885	C 49	-1.7516	-2.2266	-1.9334
H 16	4.5695	-2.7456	2.7310	H 50	-2.3546	-1.9494	-2.7905
H 17	-1.1952	0.9232	-2.5864	C 51	-0.3561	-2.3953	-2.0967
C 18	-0.3919	1.9608	0.4335	H 52	0.0872	-2.2852	-3.0813
H 19	0.3366	2.6472	0.8788	C 53	0.5010	-2.6387	-0.9616
C 20	-0.3833	2.1137	-1.0993	C 54	1.9775	-2.8007	-1.1502
H 21	-1.0820	2.9207	-1.3600	H 55	2.3403	-2.1619	-1.9598
C 22	0.9861	2.5123	-1.6403	H 56	2.2123	-3.8407	-1.4071
C 23	1.7889	1.6338	-2.3681	H 57	2.5203	-2.5390	-0.2399
H 24	1.4249	0.6281	-2.5578	C 58	-3.7743	-1.8475	-0.3796
C 25	3.0415	2.0334	-2.8340	H 59	-3.8208	-1.3884	0.6164
H 26	3.6528	1.3355	-3.4005	C 60	-4.5851	-3.1478	-0.3515
C 27	3.5084	3.3188	-2.5793	H 61	-4.5564	-3.6450	-1.3274
H 28	4.4833	3.6308	-2.9431	H 62	-5.6324	-2.9395	-0.1113
C 29	2.7117	4.2068	-1.8579	H 63	-4.1980	-3.8484	0.3946
H 30	3.0639	5.2145	-1.6556	C 64	-4.3567	-0.8449	-1.3709
C 31	1.4624	3.8058	-1.3989	H 65	-3.7412	0.0586	-1.4177
H 32	0.8466	4.5074	-0.8390	H 66	-5.3648	-0.5568	-1.0586
C 33	-1.7578	2.2925	1.0247	H 67	-4.4417	-1.2685	-2.3783
C 34	-2.5191	1.3547	1.7215	F 68	6.1412	-1.6882	0.9780

Table A7. Cartesian coordinates calculated for **(*R*,*R*)-6** at the PBE0/Lanl2DZ/6-31+G** level.

Atom	x	y	z	Atom	x	y	z
Os 1	-0.5964	-0.7581	-0.6495	H 35	-2.0268	0.7210	1.7628
S 2	0.7414	0.1293	2.1898	C 36	-3.4347	2.3367	1.9838
O 3	-0.1521	-0.8503	2.8213	H 37	-4.1594	1.7257	2.5155
O 4	1.0677	1.3606	2.9105	C 38	-3.6974	3.6824	1.7512
N 5	0.2068	0.5261	0.6870	H 39	-4.6288	4.1272	2.0900
N 6	-0.4932	0.8615	-1.6694	C 40	-2.7463	4.4601	1.0941
C 7	4.7129	-2.0340	1.5799	H 41	-2.9299	5.5171	0.9215
C 8	4.4190	-0.9015	0.8213	C 42	-1.5541	3.8867	0.6665
H 9	5.1372	-0.5229	0.0998	H 43	-0.8135	4.5108	0.1692
C 10	3.2009	-0.2488	0.9801	C 44	-0.3412	-2.7568	0.3790
H 11	2.9589	0.6223	0.3802	H 45	0.2599	-2.9109	1.2669
C 12	2.2781	-0.7450	1.8980	C 46	-1.6724	-2.3093	0.5298
C 13	2.5637	-1.8706	2.6672	H 47	-2.0560	-2.1386	1.5288
H 14	1.8260	-2.2251	3.3804	C 48	-2.4413	-1.8986	-0.6094
C 15	3.7871	-2.5166	2.5023	C 49	-1.8686	-2.0538	-1.9115
H 16	4.0168	-3.3961	3.0969	H 50	-2.4142	-1.7097	-2.7828
H 17	-0.7276	0.9406	-2.6519	C 51	-0.5105	-2.4260	-2.0498
C 18	0.0358	1.9507	0.3900	H 52	-0.0421	-2.4027	-3.0287
H 19	0.8408	2.5239	0.8630	C 53	0.2875	-2.7544	-0.8944
C 20	0.1603	2.0439	-1.1432	C 54	1.7295	-3.1268	-1.0518
H 21	-0.3861	2.9399	-1.4686	H 55	2.1905	-2.5698	-1.8719
C 22	1.6030	2.2035	-1.6122	H 56	1.8168	-4.1966	-1.2773
C 23	2.2935	1.1819	-2.2646	H 57	2.2927	-2.9200	-0.1396
H 24	1.7854	0.2388	-2.4428	C 58	-3.8473	-1.3788	-0.4089
C 25	3.6150	1.3622	-2.6721	H 59	-3.8717	-0.9499	0.6009
H 26	4.1367	0.5549	-3.1798	C 60	-4.8329	-2.5515	-0.4560
C 27	4.2645	2.5692	-2.4347	H 61	-4.8360	-3.0179	-1.4475
H 28	5.2933	2.7111	-2.7535	H 62	-5.8494	-2.2047	-0.2451
C 29	3.5818	3.5994	-1.7895	H 63	-4.5771	-3.3219	0.2777
H 30	4.0771	4.5481	-1.6022	C 64	-4.2416	-0.2746	-1.3854
C 31	2.2637	3.4165	-1.3876	H 65	-3.5010	0.5308	-1.3820
H 32	1.7384	4.2284	-0.8877	H 66	-5.2097	0.1469	-1.0990
C 33	-1.2883	2.5297	0.8773	H 67	-4.3468	-0.6537	-2.4085
C 34	-2.2384	1.7648	1.5531	H 68	5.6656	-2.5401	1.4526

Table A8. Cartesian coordinates calculated for **(*R*,*R*)-7** at the PBE0/Lanl2DZ/6-31+G** level.

Atom	x	y	z
C 1	-4.5564	3.7862	-1.5444
H 2	-4.7751	3.9225	-0.4783
H 3	-5.4151	3.2743	-1.9891
H 4	-4.4831	4.7807	-1.9925
Os 5	0.6971	-1.5221	0.3491
C 6	-3.2888	3.0021	-1.7351
C 7	-3.2898	1.6057	-1.6252
H 8	-4.2213	1.0814	-1.4249
C 9	-2.1189	0.8744	-1.7713
H 10	-2.1356	-0.2070	-1.6884
C 11	-0.9213	1.5408	-2.0282
C 12	-0.8977	2.9258	-2.1552
H 13	0.0402	3.4199	-2.3873
C 14	-2.0802	3.6454	-2.0088
H 15	-2.0629	4.7274	-2.1128
O 16	1.5918	1.5597	-2.7050
O 17	0.2982	-0.6115	-2.8901
S 18	0.6051	0.6241	-2.1681
N 19	1.0056	0.2289	-0.6185
C 20	1.7309	1.2650	0.1239
H 21	1.3934	2.2604	-0.1904
C 22	1.3643	1.0745	1.6139
H 23	2.2475	1.3530	2.2049
N 24	1.0981	-0.3437	1.7950
C 25	0.2140	1.9403	2.0965
C 26	0.4499	2.9609	3.0195
H 27	1.4598	3.1195	3.3932
C 28	-0.5889	3.7741	3.4681
H 29	-0.3873	4.5603	4.1904
C 30	-1.8816	3.5753	2.9931
H 31	-2.6939	4.2076	3.3406
C 32	-2.1269	2.5602	2.0695
H 33	-3.1306	2.3999	1.6846
C 34	-1.0891	1.7460	1.6291
H 35	-1.2847	0.9594	0.9075
C 36	3.2416	1.2128	-0.0665
C 37	4.0178	2.2562	0.4483
H 38	3.5289	3.0956	0.9403
C 39	5.4031	2.2429	0.3298
H 40	5.9881	3.0663	0.7305
C 41	6.0370	1.1803	-0.3106
H 42	7.1189	1.1675	-0.4087
C 43	5.2718	0.1440	-0.8358
H 44	5.7563	-0.6811	-1.3512
C 45	3.8836	0.1623	-0.7180
H 46	3.2837	-0.6335	-1.1467
C 47	-2.8909	-1.5040	1.4117
H 48	-2.1314	-1.1276	2.0920
C 49	-4.2179	-1.1211	1.5661
H 50	-4.4961	-0.4713	2.3908
C 51	-5.1832	-1.5546	0.6585
H 52	-6.2199	-1.2540	0.7794
C 53	-4.8124	-2.3732	-0.4047
H 54	-5.5588	-2.7180	-1.1144
C 55	-3.4835	-2.7595	-0.5596
H 56	-3.1998	-3.4114	-1.3812
C 57	-2.5096	-2.3283	0.3465
C 58	-1.1002	-2.7562	0.1783
C 59	-0.4905	-2.7673	-1.1119
H 60	-1.0155	-2.3472	-1.9603
C 61	0.8768	-3.0948	-1.2659
H 62	1.3518	-2.9181	-2.2221
C 63	1.6513	-3.4304	-0.1254
H 64	2.7218	-3.5744	-0.2192
C 65	1.0351	-3.5322	1.1615
H 66	1.6414	-3.7482	2.0339
C 67	-0.3300	-3.1884	1.3175
H 68	-0.7831	-3.1792	2.3025
H 69	1.0364	-0.6001	2.7737

Table A9. Cartesian coordinates calculated for **(*R*,*R*)-8** at the PBE0/Lanl2DZ/6-31+G** level.

Atom	x	y	z	Atom	x	y	z
C 1	-6.5773	-0.4502	1.2249	C 41	1.9186	5.6683	-1.2013
H 2	-6.3303	-0.5441	2.2895	H 42	2.4833	6.5336	-1.5368
H 3	-6.9660	-1.4168	0.8924	C 43	2.0468	4.4481	-1.8579
H 4	-7.3809	0.2871	1.1426	H 44	2.7117	4.3597	-2.7130
Os 5	1.0600	-0.2980	-0.5498	C 45	1.3181	3.3389	-1.4350
C 6	-5.3695	-0.0389	0.4312	H 46	1.4019	2.3929	-1.9603
C 7	-4.5215	-0.9983	-0.1334	C 47	-1.1288	-3.3103	0.4457
H 8	-4.7568	-2.0543	-0.0261	H 48	-0.6594	-2.7494	1.2493
C 9	-3.3827	-0.6277	-0.8385	C 49	-2.2484	-4.0897	0.7103
H 10	-2.7401	-1.3799	-1.2843	H 50	-2.6253	-4.1595	1.7268
C 11	-3.0831	0.7249	-0.9856	C 51	-2.8936	-4.7672	-0.3233
C 12	-3.9230	1.6994	-0.4527	H 52	-3.7691	-5.3757	-0.1159
H 13	-3.6936	2.7470	-0.6200	C 53	-2.4073	-4.6599	-1.6231
C 14	-5.0572	1.3114	0.2526	H 54	-2.9002	-5.1860	-2.4355
H 15	-5.7156	2.0717	0.6654	C 55	-1.2809	-3.8863	-1.8881
O 16	-1.7904	2.6337	-2.1890	H 56	-0.8952	-3.8249	-2.9016
O 17	-1.3568	0.2433	-2.8975	C 57	-0.6295	-3.1984	-0.8584
S 18	-1.6003	1.2264	-1.8427	C 58	0.5768	-2.3919	-1.1509
N 19	-0.3997	1.0931	-0.7113	C 59	0.7045	-1.6712	-2.3649
C 20	-0.3152	2.2411	0.2068	H 60	-0.1517	-1.5817	-3.0193
H 21	-1.3231	2.5871	0.4697	C 61	1.8128	-0.8297	-2.5836
C 22	0.3647	1.7211	1.4895	H 62	1.8195	-0.1597	-3.4344
H 23	0.9267	2.5568	1.9271	C 63	2.8682	-0.7742	-1.6140
N 24	1.2967	0.6912	1.0587	H 64	3.6790	-0.0664	-1.7469
C 25	-0.5908	1.2161	2.5575	C 65	2.8591	-1.6170	-0.4596
C 26	-0.5800	1.7936	3.8281	C 66	1.6638	-2.3444	-0.1995
H 27	0.1139	2.6050	4.0392	H 67	1.5781	-2.9151	0.7180
C 28	-1.4440	1.3458	4.8262	H 68	1.9967	0.4724	1.7594
H 29	-1.4175	1.8050	5.8107	C 69	3.9573	-1.5702	0.5303
C 30	-2.3387	0.3148	4.5595	C 70	5.2828	-1.4550	0.0976
H 31	-3.0162	-0.0345	5.3338	C 71	3.7066	-1.6627	1.9060
C 32	-2.3616	-0.2654	3.2914	C 72	6.3293	-1.4273	1.0137
H 33	-3.0654	-1.0628	3.0672	H 73	5.4961	-1.4084	-0.9668
C 34	-1.4909	0.1758	2.3015	C 74	4.7534	-1.6356	2.8206
H 35	-1.5150	-0.2757	1.3145	H 75	2.6826	-1.7399	2.2623
C 36	0.4545	3.4328	-0.3457	C 76	6.0687	-1.5166	2.3781
C 37	0.3256	4.6643	0.3031	H 77	7.3521	-1.3420	0.6584
H 38	-0.3574	4.7559	1.1462	H 78	4.5397	-1.7016	3.8835
C 39	1.0496	5.7744	-0.1179	H 79	6.8857	-1.4947	3.0931
H 40	0.9294	6.7249	0.3949				

Table A10. Cartesian coordinates calculated for **(*R*,*R*)-9** at the PBE0/Lanl2DZ/6-31+G** level.

Atom	x	y	z	Atom	x	y	z
Os 1	-0.4996	-1.0063	-0.8531	C 41	-4.4714	2.8596	1.2366
S 2	0.2103	-0.2307	2.2332	C 42	-3.5186	3.7858	0.7985
O 3	-0.6906	-1.3160	2.6433	H 43	-3.8224	4.8196	0.6674
O 4	0.3005	0.9657	3.0721	C 44	-2.2178	3.3784	0.5562
N 5	-0.0932	0.2338	0.6861	H 45	-1.4907	4.1219	0.2340
N 6	-0.4028	0.6934	-1.7307	C 46	-0.2707	-3.0617	0.0862
C 7	5.8069	-2.6240	2.2081	H 47	0.1363	-3.2411	1.0745
H 8	5.8499	-3.5393	1.6061	C 48	-1.6381	-2.7310	-0.0347
H 9	6.1184	-2.8912	3.2228	H 49	-2.2462	-2.6786	0.8609
H 10	6.5424	-1.9255	1.8009	C 50	-2.1806	-2.2975	-1.2921
C 11	4.4249	-2.0334	2.1993	C 51	-1.3289	-2.3057	-2.4410
C 12	4.1414	-0.8701	1.4765	H 52	-1.7040	-1.9435	-3.3914
H 13	4.9348	-0.3772	0.9198	C 53	0.0582	-2.5420	-2.2916
C 14	2.8608	-0.3287	1.4541	H 54	0.7237	-2.3973	-3.1368
H 15	2.6525	0.5682	0.8798	C 55	0.6158	-2.9029	-1.0107
C 16	1.8401	-0.9622	2.1562	C 56	2.0856	-3.1536	-0.8726
C 17	2.0978	-2.1165	2.8923	H 57	2.6603	-2.4834	-1.5174
H 18	1.2881	-2.5848	3.4435	H 58	2.3154	-4.1851	-1.1668
C 19	3.3844	-2.6451	2.9072	H 59	2.4191	-3.0062	0.1565
H 20	3.5856	-3.5459	3.4825	C 60	-3.6416	-1.9163	-1.3774
H 21	-0.4655	0.8276	-2.7330	H 61	-3.9201	-1.5576	-0.3783
C 22	-0.3748	1.6541	0.4552	C 62	-4.4747	-3.1638	-1.6913
H 23	0.2659	2.2624	1.1033	H 63	-4.2215	-3.5611	-2.6805
C 24	0.0078	1.8889	-1.0191	H 64	-5.5421	-2.9211	-1.6903
H 25	-0.5752	2.7470	-1.3814	H 65	-4.3052	-3.9569	-0.9567
C 26	1.4812	2.2301	-1.2068	C 66	-3.9271	-0.7883	-2.3644
C 27	2.4001	1.3325	-1.7578	H 67	-3.2888	0.0765	-2.1605
H 28	2.0514	0.3527	-2.0710	H 68	-4.9714	-0.4735	-2.2787
C 29	3.7395	1.6689	-1.8995	H 69	-3.7718	-1.1049	-3.4023
H 30	4.4541	0.9728	-2.3284	C 70	-6.6975	2.4569	1.9247
C 31	4.1982	2.9246	-1.4923	H 71	-6.8771	1.6355	1.2178
C 32	3.2937	3.8396	-0.9475	H 72	-6.4210	2.0318	2.8986
H 33	3.6171	4.8233	-0.6263	H 73	-7.6146	3.0376	2.0361
C 34	1.9539	3.4833	-0.8166	C 74	6.0243	4.4135	-1.2667
H 35	1.2621	4.2083	-0.3910	H 75	5.8813	4.5832	-0.1915
C 36	-1.8214	2.0454	0.7289	H 76	7.0930	4.3988	-1.4862
C 37	-2.7765	1.1411	1.1804	H 77	5.5559	5.2363	-1.8226
H 38	-2.4867	0.1113	1.3644	O 78	5.5234	3.1606	-1.6683
C 39	-4.0928	1.5329	1.4330	O 79	-5.7208	3.3502	1.4492
H 40	-4.8020	0.7972	1.7965				

Table A11. Cartesian coordinates calculated for **(*R*,*R*)-10** at the PBE0/Lanl2DZ/6-31+G** level.

Atom	x	y	z
C 1	4.9268	2.4211	2.8020
H 2	5.3488	2.6279	1.8107
H 3	5.6122	1.7322	3.3055
H 4	4.9213	3.3619	3.3585
Os 5	-0.6993	-1.5607	-0.6114
C 6	3.5459	1.8384	2.6907
C 7	3.3663	0.4978	2.3260
H 8	4.2337	-0.1311	2.1388
C 9	2.0955	-0.0474	2.2056
H 10	1.9703	-1.0889	1.9307
C 11	0.9788	0.7523	2.4472
C 12	1.1326	2.0835	2.8193
H 13	0.2509	2.6790	3.0336
C 14	2.4135	2.6163	2.9380
H 15	2.5333	3.6551	3.2353
O 16	-1.5723	1.0488	2.8663
O 17	-0.6176	-1.2965	2.7633
S 18	-0.6649	0.0772	2.2586
N 19	-0.9207	0.0209	0.6329
C 20	-1.3973	1.2682	0.0242
H 21	-0.9782	2.1306	0.5575
C 22	-0.8550	1.2859	-1.4249
H 23	-1.6135	1.7801	-2.0476
N 24	-0.7361	-0.1039	-1.8396
C 25	0.4410	2.0502	-1.6143
C 26	0.4588	3.2353	-2.3572
H 27	-0.4638	3.5993	-2.8054
C 28	1.6289	3.9575	-2.5383
H 29	1.6454	4.8747	-3.1184
C 30	2.8230	3.5049	-1.9699
C 31	2.8256	2.3239	-1.2235
H 32	3.7329	1.9515	-0.7606
C 33	1.6413	1.6103	-1.0573
H 34	1.6555	0.6960	-0.4722
C 35	-2.9129	1.4087	0.0382
C 36	-3.4848	2.6233	-0.3628
H 37	-2.8399	3.4527	-0.6486
C 38	-4.8574	2.8010	-0.3926
H 39	-5.3008	3.7443	-0.6957
C 40	-5.7056	1.7550	-0.0127
C 41	-5.1543	0.5430	0.3998
H 42	-5.7871	-0.2785	0.7171
C 43	-3.7678	0.3842	0.4244
H 44	-3.3435	-0.5536	0.7683
C 45	2.9465	-1.8923	-1.3309
H 46	2.3214	-1.2764	-1.9719
C 47	4.3227	-1.6999	-1.2993
H 48	4.7743	-0.9527	-1.9457
C 49	5.1162	-2.4490	-0.4316
H 50	6.1915	-2.2973	-0.4069
C 51	4.5244	-3.3914	0.4048
H 52	5.1358	-3.9811	1.0816
C 53	3.1462	-3.5868	0.3729
H 54	2.6879	-4.3333	1.0159
C 55	2.3442	-2.8392	-0.4950
C 56	0.8792	-3.0665	-0.5259
C 57	0.1404	-3.1974	0.6894
H 58	0.6278	-3.0164	1.6388
C 59	-1.2671	-3.3372	0.6723
H 60	-1.8106	-3.2482	1.6039
C 61	-1.9552	-3.3519	-0.5665
H 62	-3.0391	-3.3426	-0.5868
C 63	-1.2252	-3.3252	-1.7982
H 64	-1.7606	-3.2934	-2.7404
C 65	0.1841	-3.1836	-1.7820
H 66	0.7355	-3.0779	-2.7097
H 67	-0.5661	-0.1909	-2.8354
C 68	-7.9225	1.0082	0.3372
H 69	-7.7630	0.7281	1.3868
H 70	-8.9279	1.4179	0.2262
H 71	-7.8313	0.1095	-0.2876
C 72	5.1381	3.8634	-1.6361
H 73	5.0871	3.8299	-0.5394
H 74	5.4488	2.8774	-2.0071
H 75	5.8791	4.6061	-1.9358
O 76	-7.0372	2.0212	-0.0724
O 77	3.9181	4.2742	-2.2018